High Rate, Large Area Laser-assisted Chemical Vapor Deposition of Nickel from Nickel Carbonyl

by

Vlad Paserin

A thesis
presented to the University of Waterloo
in fulfillment of the
thesis requirement for the degree of

Doctor of Philosophy

in

Physics

Waterloo, Ontario, Canada, 2009

AUTHOR'S DECLARATION

I hereby declare that I am the sole author of this thesis. This is a true copy of the thesis, including any required final revisions, as accepted by my examiners.

I understand that my thesis may be made electronically available to the public.

ABSTRACT

High-power diode lasers (HPDL) are being increasingly used in industrial applications. Deposition of nickel from nickel carbonyl ($Ni(CO)_4$) precursor by laser-induced chemical vapor deposition (CVD) was studied with emphasis on achieving high deposition rates. An HPDL system was used to provide a novel energy source facilitating a simple and compact design of the energy delivery system. Nickel deposits on complex, 3-dimensional polyurethane foam substrates were prepared and characterized. The resulting "nickel foam" represents a novel material of high porosity (>95% by volume) finding uses, among others, in the production of rechargeable battery and fuel cell electrodes and as a specialty high-temperature filtration medium. Deposition rates up to ~19 μm/min were achieved by optimizing the gas precursor flow pattern and energy delivery to the substrate surface using a 480W diode laser. Factors affecting the transition from purely heterogeneous decomposition to a combined hetero- and homogeneous decomposition of nickel carbonyl were studied. High quality, uniform 3-D deposits produced at a rate more than ten times higher than in commercial processes were obtained by careful balance of mass transport (gas flow) and energy delivery (laser power). Cross-flow of the gases through the porous substrate was found to be essential in facilitating mass transport and for obtaining uniform deposits at high rates. When controlling the process in a transient regime (near the onset of homogenous decomposition), unique morphology features formed as part of the deposits, including textured surface with pyramid-shape crystallites, spherical and non-spherical particles and filaments.

Operating the laser in a pulsed mode produced smooth, nano-crystalline deposits with sub-100 nm grains. The effect of H_2S, a commonly used additive in nickel carbonyl CVD, was studied using both polyurethane and nickel foam substrates. H_2S was shown to improve the substrate coverage and deposit uniformity in tests with polyurethane substrate, however, it was found to have no effect in improving the overall deposition rate compared to H_2S-free deposition process.

Deposition on other selected substrates, such as ultra-fine polymer foam, carbon nanofoam and multi-wall carbon nanotubes, was demonstrated.

The HPDL system shows good promise for large-scale industrial application as the cost of HPDL energy continues to decrease.

ACKNOWLEDGMENTS

DEDICATION

I dedicate this work to Bill Nowosiadly, a colleague and friend whose untimely departure from this life surprised us all, and who was immensely helpful in the project discussions and in preparing and imaging numerous SEM samples.

TABLE OF CONTENTS

LIST OF TABLES

LIST OF FIGURES

GLOSSARY

CVD Chemical Vapor Deposition

CFD Computational Fluid Dynamics

CFX CFD software marketed by Ansys Inc.

CW Continuous-wave (laser beam operation)

DTR Differential Thickness Ratio

DVD Directed Vapor Deposition

FIB Focused Ion Beam (microscopy)

FTIR Fourier Transfer Infra Red (spectroscopy)

FWHM Full-Width Half-Maximum

GM-effect Giant Magnetoresistance effect

HEV Hybrid Electric Vehicle

HP-LCVD High-Pressure Laser Chemical Vapor deposition

HPDL High Power Diode Laser

IR Infrared

LCVD Laser Chemical Vapor Deposition

MCFC Molten Carbonate Fuel Cell

Ni(CO)$_4$ Nickel carbonyl

NiCd Nickel Cadmium

NiMH Nickel Metal Hydride

PEMFC Proton Exchange Membrane Fuel Cell

ppb parts per billion

PPI Pores per inch

PU Polyurethane

PVD Physical Vapor Deposition

QCW Quasi-Continuous Wave

reticulated (foam) open-cell foam (cell membranes removed)

SALD Selected Area Laser Deposition

SEM Scanning Electron Microscope

SHEDS Super-High Efficiency Diode Sources

SOFC Solid Oxide Fuel Cell

SQW Single Quantum Well

TEM Transmission Electron Microscopy

TGA Thermal Gravimetric Analysis

TLV Threshold Limit Value

UV Ultraviolet

XRD X-ray diffraction

YAG Yttrium-Aluminum Garnet (laser)

1 INTRODUCTION

1.1   Laser deposition

Laser-induced film deposition processes have been studied extensively over the past ~25 years, mainly due to their potential applications in the electronics industry. In spite of this, lasers have had only small, although growing presence in manufacturing. This is changing rapidly since the advent of high-power lasers. While applications of such lasers (mainly CO_2) in cutting, drilling, marking and heat treating abound, the use of lasers in deposition processes has been limited to specialized applications in manufacturing of electronic materials and parts (mask-less patterning and microfabrication) and in laser cladding.   However, the growing availability and decreasing production costs of high-power lasers (particularly diode lasers) will undoubtedly lead to new uses. *Large-area* laser-driven material deposition represents one of such emerging uses.   More specifically, laser-induced chemical vapor deposition (LCVD) is a good candidate for large-area metal deposition utilizing nickel carbonyl, a precursor yielding high-purity nickel deposits.   Nickel carbonyl is available industrially in tonnage quantities as part of the nickel refining process.

The LCVD process is particularly suitable for high-rate metal deposition on complex, 3-dimensional substrates forming structures that belong to the general category of *cellular metals*, the subject of this thesis.

1.2 Nickel carbonyl

One of the unique properties of metallic nickel is its ability to react with carbon monoxide at near room temperature to form nickel carbonyl, a covalent compound. The molecular structure of $Ni(CO)_4$ is shown in Figure 1.1. It is a highly symmetric molecule with tetrahedral symmetry and two distinct chemical bonds: Ni-C and C-O.

Since 1902, nickel carbonyl has been used commercially in the nickel refining process. At ambient pressure, $Ni(CO)_4$ is a volatile liquid with a boiling point of 43 °C. It is readily decomposed into elemental nickel and CO upon heating to 100 – 200°C via the following reaction:
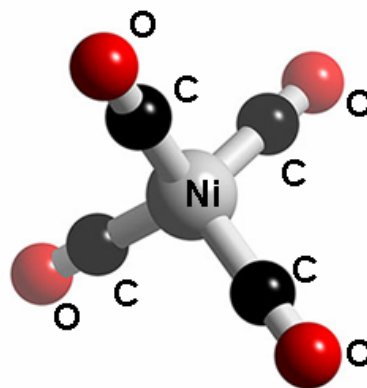
Figure 1.1 $Ni(CO)_4$ molecule structure

$$Ni(CO)_4 \Rightarrow Ni + 4\ CO \quad \text{(heat of reaction 160.4 kJ/mol)} \qquad (1.1)$$

The low decomposition temperature is unique among metal carbonyls and makes this reaction particularly suitable for nickel deposition on temperature-sensitive substrates, such as polymer foams.

The main difficulty in working with nickel carbonyl is its extreme toxicity (the U.S. TLV is 1 ppb). Additional information on chemical and physical properties of nickel carbonyl, including a brief historical note on its discovery in the late 1800's, is given in Appendix 1.

1.3 Thesis objectives and outline

The objective of this thesis is the investigation of the use of high power diode lasers in large-area nickel CVD process leading to improvements in deposition rates and continuous production equipment design. An additional objective is the study of the effects of various deposition control regimes on the deposit morphology and characteristics.

This thesis is divided into six chapters and three appendices. The rest of this chapter outlines the problem statement and objectives of the thesis, and provides introduction to the general topics of cellular metals and their uses, conventional nickel foam production processes (electrodeposition and nickel carbonyl CVD), laser-material interaction and laser CVD, reaction kinetics and thermodynamics and specific applications of nickel foam. Chapter two is a brief literature survey on nickel carbonyl decomposition kinetics, deposit morphology effects, and a fairly complete coverage of work to-date on laser CVD using nickel carbonyl as a precursor. Brief review of literature on the general subject of metal foams is also included. Chapter three covers the experimental part of this work, including deposition on substrates other than polyurethane foams, and the general subject of high-power diode lasers and their emerging use in materials processing. Chapter four provides analysis of experimental results and discussion of the physical and chemical processes affecting the deposition process kinetics and deposit morphology. Chapter five covers CFD modeling of the laboratory reactor and includes a discussion on possible process scale-up options to industrial scale. Summary of conclusions and some recommendations for future work are given in Chapter six.

Appendices 1-3 include additional data on nickel carbonyl properties, details of experiments and a discussion of nickel carbonyl and laser safety, respectively.

1.4 Nickel carbonyl uses in industry

Chemical vapor deposition with nickel carbonyl as a precursor has been used to produce high purity nickel products since the beginning of the 20th century. The present carbonyl nickel product range includes Ni powders, Ni pellets (solid nickel spheres with a diameter from a few mm to ~1 cm - this is the dominant form of bulk carbonyl nickel with nickel purity > 99.95%), Ni-coated particles, Ni-coated carbon fibres and high-porosity Ni foams (Figure 1.2). Another use of nickel carbonyl is in the petroleum, plastic and rubber industries as a catalyst.

Products produced using Ni refinery intermediate - $Ni(CO)_4$

PELLET CVD REACTOR — *nickel pellets*

POWDER CVD REACTOR — *nickel powders*

FOAM / FIBRE CVD REACTOR

$Ni(CO)_4$

specialty products:
- Ni foams and felts
- Ni coated fibres
- Ni coated powders
- etc.
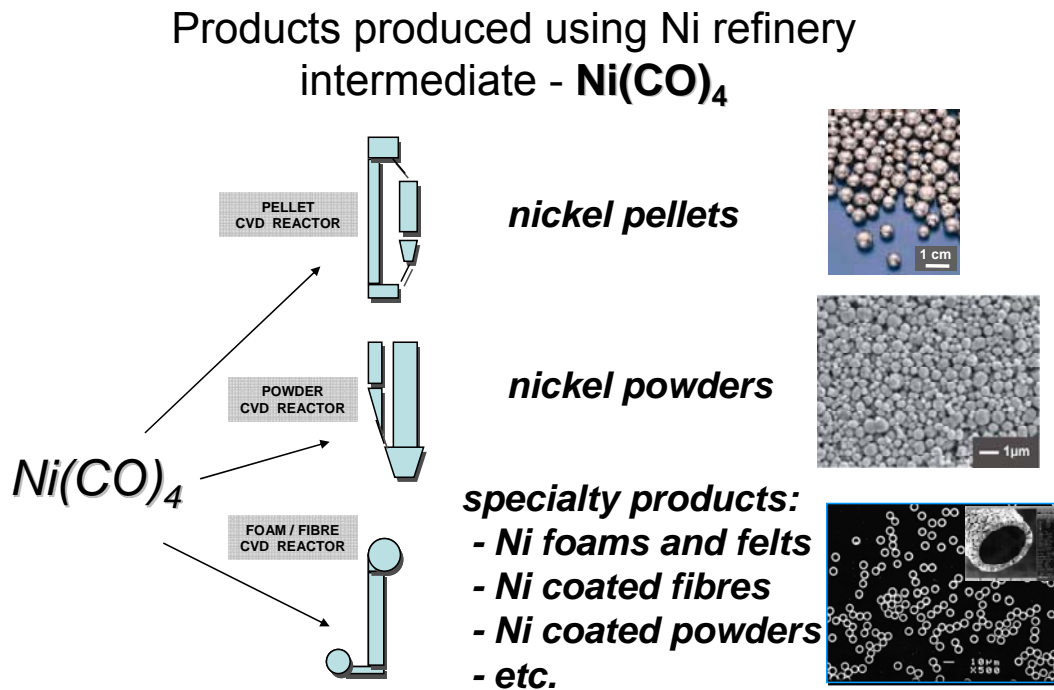
Figure 1.2   Typical Ni carbonyl vapor deposition – based products

In all cases the nickel metal in the final product originates from the thermal decomposition of nickel carbonyl. Nickel carbonyl is most economically available

on a large scale as a nickel refinery intermediate in the plants of at least two major nickel producers (Vale Inco in Canada and the United Kingdom and Norilsk Nickel in Russia).

1.5 Cellular metals

A cellular metal or "metal foam" is a porous metal structure comprising an interconnected network of struts or ligaments and plates forming the edges and nodes of three-dimensional cells. Cellular metals represent a relatively new class of materials receiving increasing attention and finding new applications in recent years due to their unique combination of useful properties: light weight, good electrical and thermal conductivity, high surface area, high strength, corrosion resistance and good thermal stability. They can be categorized by the cell type (open or closed), cell size and relative density (ratio of the cellular metal density and density of the same metal in bulk). The relative density values can be as low as few percent [Ashby, 2000 and Wadley, 2002].

Various methods of manufacturing cellular metals are being developed. Foaming techniques starting from liquid metal and injecting a gas or gas-releasing particles (chemical blowing agents) can produce both open and closed cell foams with cell sizes in the ~0.5 to ~15 mm range and relative densities of ~4 to 40%. The final structure depends on the rheology and surface tension of the fluids in the melt. Open-cell metal foams with uniform cells are usually made using open-cell polymer foam templates by "templated deposition". The metal can be deposited on the polymer substrate by a variety of processes such as metal slurry application, electrodeposition or by chemical vapor deposition [Wadley, 2001].

1.5.1 Nickel foam – a unique form of high-porosity nickel

The focus of this thesis is the high-rate deposition of nickel by IR laser-driven nickel carbonyl CVD process onto polymer foam templates to produce "nickel

foam". The resulting material represents a unique category of cellular metals consisting of a relatively regular, 3-dimensional skeleton of high porosity, honeycomb-like structure (Figure 1.3).
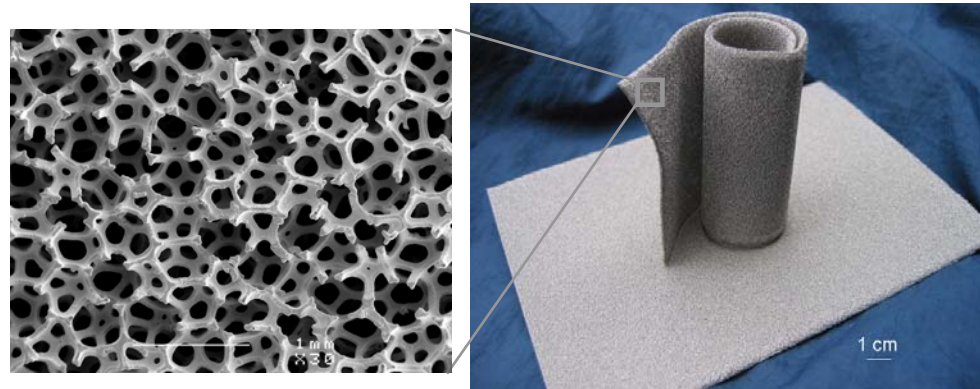
Figure 1.3   SEM image of nickel foam surface (30x magnification) and samples of battery electrode - grade Ni foams

1.6   Nickel foam manufacturing processes

To produce nickel foam by the templated deposition process, nickel metal is deposited onto polymer substrates such as polyurethane (PU) foam and heat-treated afterwards in a controlled atmosphere to remove the substrate and to anneal the nickel deposit.

The earliest literature reference to sponge-like metallic materials based on PU foam templates known to the author is found in the US patent by B.B. Ball granted in 1963. The patent describes metallization of a PU foam by application of a metal slurry and subsequent burning of the polymer template in a sintering furnace [Ball, 1963].

The first known reference to a nickel foam-like material produced from nickel carbonyl (at least on a laboratory scale) can be found in the work of William C. Jenkin in mid-1960's [Jenkin, 1964 and 1990]. Commercially, nickel foam was first produced in the early 1980's by Sumitomo Electric Industries of Japan using electroless deposition on polyurethane substrates, followed by electroplating

6

[Matsumoto et al., 1981]. Polyurethane foam structure-based nickel foam is often used as a representative example of the general category of metal foam materials. Driven mainly by use as a battery electrode material, the world annual production now exceeds 5,000 tons (>10 million square meters). In 2005, Inco Limited became a leading producer of nickel foam with a total annual production capacity of some 4 million square meters (~ 2,000 tons) of battery-grade nickel foam, using both carbonyl CVD and electroplating processes [Paserin et al., 2006].

1.6.1   Ni deposition

In general, nickel coating can be applied by means of sputtering, electroless (chemical) deposition, directed vapor deposition, electroplating, powder slurry application, and CVD processes [Wadley, 1996]. For mass production of nickel foams, electroplating and CVD have been the main industrial processes. The production process flowsheets for these two dominant processes as practiced by Vale Inco in 2006 are schematically shown in Figure 1.4.
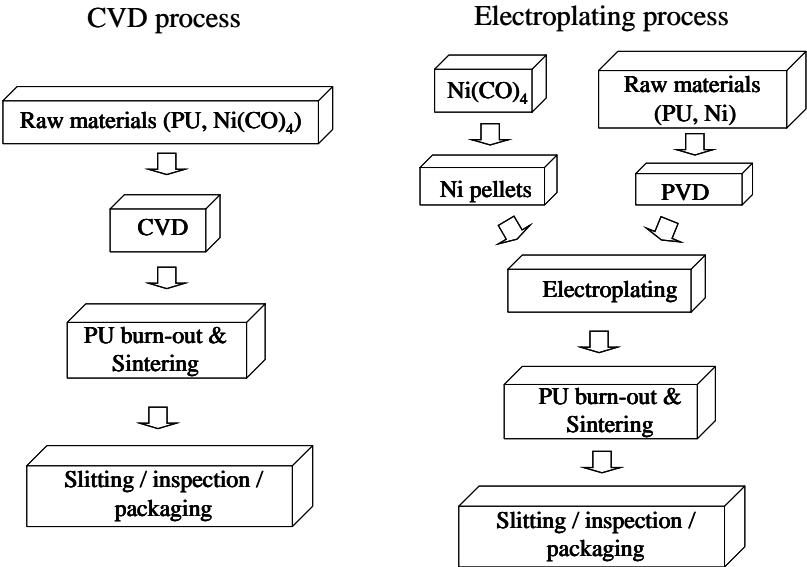
Figure 1.4 Comparison of Vale Inco CVD and electroplating process flowsheets

7

The carbonyl-based CVD process involves direct deposition of Ni on the non-conducting polymer substrate, which is relatively stable at nickel carbonyl atmospheric pressure decomposition temperature (see TGA data in Section 3.5).

1.6.2   Annealing step

Subsequent to the Ni deposition operation, the as-deposited foam is subjected to a high-temperature heat treatment in a controlled atmosphere, electric or gas-fired belt furnace. This step is common to both CVD and electroplating production methods. The material enters the high temperature heat treatment with the polymer substrate still present inside the nickel shell. Typical flexible polyurethane foam starts to decompose at approximately 250 °C. The PU burn-out is essentially complete at 350 °C in an oxidizing atmosphere [Olurin et al., 2003]. The polymer thus melts and vaporizes within the nickel shell, building up internal pressure until the shell ruptures and the organic vapor escapes (Figure 1.5). Upon additional heating, the ruptured nickel deposit becomes continuous again by the sintering action of the high temperature treatment (typical conditions are 1000°C for 5 minutes). Thus, following the high temperature anneal, the individual struts are hollow.
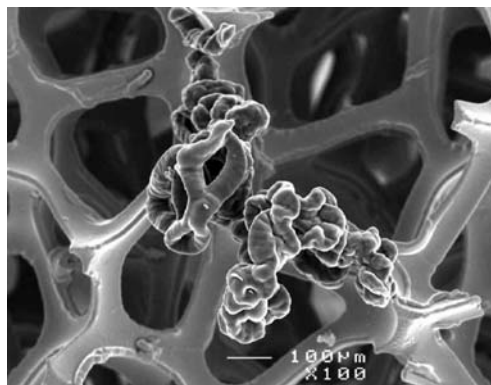
Figure 1.5 Polyurethane foam burn-out

In the Vale Inco CVD process, the PU foam burnout and high-temperature anneal were performed as a single step operation in a partially oxidizing atmosphere of water vapor, nitrogen and hydrogen [Cushnie and Campbell, 1998]. Figure 1.6 shows a fracture cross-section of a hollow strut after high-temperature treatment, with the PU template removed.
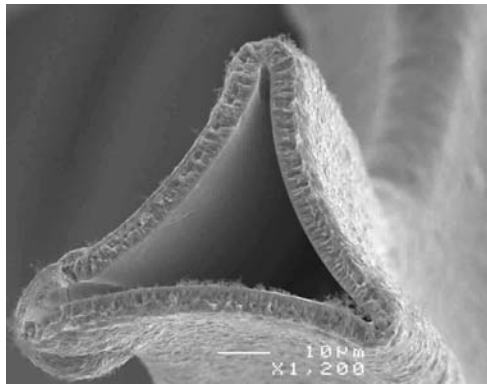
Figure 1.6 Hollow strut after sintering

1.7 Parameters affecting deposition rate

Nickel carbonyl has been used as a refinery intermediate and a precursor for the production of high-purity nickel for many decades. Its potential for high rate deposition of Ni coatings was recognized already during the early stages of CVD process development in the 1960's: *"Very high deposition rates can be obtained by thermal decomposition of nickel tetracarbonyl – several hundred times as rapid as those obtained in conventional nickel electrodeposition"* [Powell et al., 1966].

Nickel foam for battery applications, including batteries for hybrid electric vehicles, has been produced by electrolytic plating or by chemical vapor deposition process of Ni on polyurethane foam substrate. Both methods of metal deposition involve delivering the metal precursor and the required energy to the surface of the foam substrate. In case of the electroplating process,

$$\text{Ni}^{++} + 53.6 \text{ Ah x V} \rightarrow \text{Ni}^{\text{o}} \qquad (1.2)$$
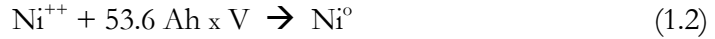
corresponding to the following energy value for a typical cell voltage of 12V:

$$\text{Ni}^{++} + 2315 \text{ kJ} \rightarrow \text{Ni}^{\text{o}} \qquad (1.3)$$

And for the carbonyl CVD:

$$\text{Ni(CO)}_4 + 160 \text{ kJ} + \text{heating energy} \rightarrow \text{Ni}^{\text{o}} + 4\text{CO} \qquad (1.4)$$

An estimate of the heating energy required to raise the temperature of a sample of Ni foam by ΔT is calculated by

$$Q = c_{pNi} \cdot m_{Ni} \cdot \Delta T \qquad (1.5)$$

For a ~1cm^2 nominal (projected) area coupon of standard, battery grade Ni foam with 5 micron thick Ni deposit (0.03 g) and ΔT of 200 deg C, this energy is about 2.7 J. The corresponding energy required for decomposition of carbonyl to form the same deposit (0.03 g) of Ni is about 83 J – i.e. during the deposition process, significantly higher amount of the absorbed energy is used to drive the decomposition reaction. Another major consumer of energy in the high-rate CVD process is the energy required to counteract the cooling effect of the precursor gas, particularly in the forced flow configuration discussed earlier. The gas flow cooling effect is further discussed in Section 3.12.

The production rate of both industrial processes is constrained by rate limitations of the fundamental mass and heat transport processes (Figure 1.7). The rate-limiting stages are also influenced by the unusual form of the product – a three dimensional, open pore skeleton structure of very low density and high porosity. In commercial grades of foam used as battery electrode material, the porosity approaches 97% by volume.
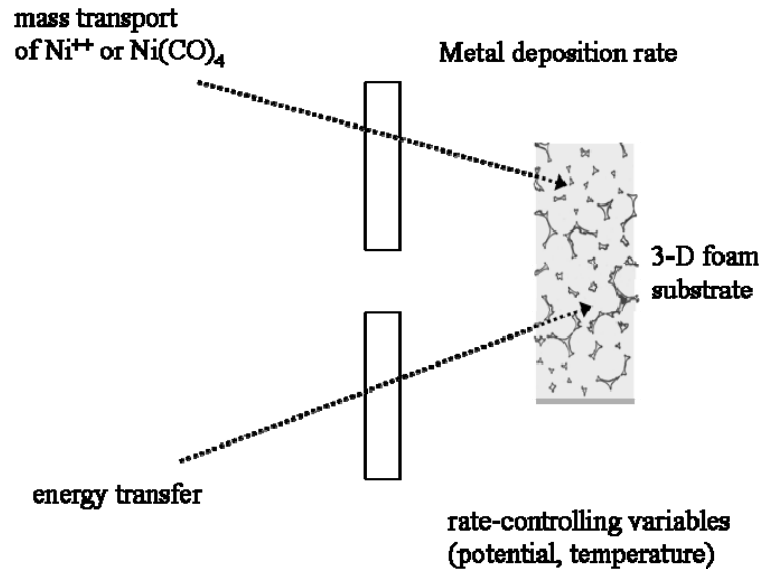
Figure 1.7 Energy and mass transfer concept in electrolytic and CVD processes

To achieve a high metal deposition rate, the energy delivery and mass transport must be balanced and both must be controlled at a level that supports the desired deposition rate *throughout* the 3-D structure of the foam.

Mass transport

The mass transport limitation presents similar problem in both processes: under typical industrial conditions it involves a combination of natural convection – driven by the density gradient between the bulk phase and the depleted electrolyte or gas outside the foam layer – and mainly concentration-driven diffusion inside the foam structure (Figure 1.8).

For 3-dimensional substrates, the precursor diffusion rate inside the 3-D structure is the most serious constraint to the mass transport. In case of the carbonyl process the diffusion rate is additionally inhibited by the net gas flow away from the plated surface as one mole of decomposed nickel carbonyl

11

produces four moles of CO. The diffusion rate of the nickel ion in the liquid phase is, on the other hand, severely inhibited by the slow diffusion in high viscosity electrolyte.
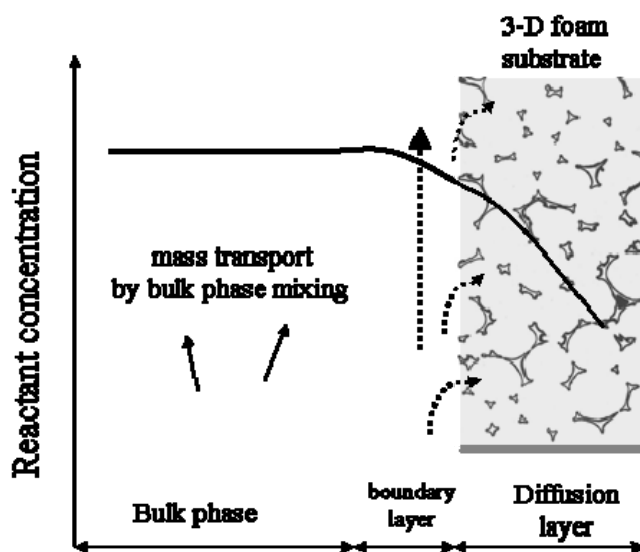
Figure 1.8 Mass transport in electrolytic and CVD processes

The diffusion rate constraint can be alleviated by forcing the gas or electrolyte through the 3-D structure at a sufficient rate to minimize the depletion of the plating precursor inside the foam. There will still be a thin diffusion layer around each strut, but the concentration gradient and diffusion rate are increased by an order of magnitude and may no longer limit the rate of deposition. The flow-through (or "cross-flow", "forced convection") concept to increase mass transport is not usually employed commercially because it complicates the process and does not eliminate the deposition rate limitation caused by the energy transfer process. The cross-flow concept is further discussed in Sections 3.7, 3.13 and 5.1.

Energy Transfer

Energy transfer to the complex 3-D deposition surface is equally difficult, although it is of fundamentally different nature for the two deposition processes.

In case of the **electrolytic process**, the plating energy delivery path involves passing electric current to the plating area via the foam structure and electrolyte, both of which have relatively low conductivity. Delivering the electric energy from the current contact above the solution level to the plated area below the surface therefore involves significant voltage losses in the foam, across the electrolyte and in the soluble anode. Because these energy losses are mostly of ohmic nature, they will increase nearly proportionally with the plating rate (current) making energy cost of high-rate electrolytic process prohibitive, even if the mass transport rate limitation is overcome by forced convection (e.g. forced flow of electrolyte across the foam). The electrolytic process with typical operating conditions is illustrated in Figure 1.9.
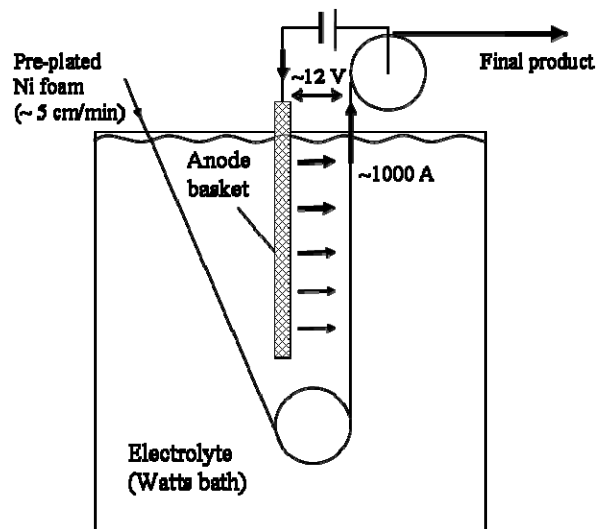
Figure 1.9   Schematic of electrolytic Ni foam production process with typical operating conditions

In the case of the **carbonyl CVD process** the energy is delivered in a direction perpendicular (or nearly perpendicular) to the foam sheet surface by radiation from a source placed near the surface. The main radiant energy barrier involved in the vapor deposition process is the partition between the gas phase inside the reactor and the radiant energy source which is usually outside the reactor. In the conventional process this function is performed by a double-glazed window made from IR transparent glass with an IR transparent coolant circulating between the two panes to keep the inner surface below plating temperature [Paserin et al., 1992]. A schematic of this reactor configuration is shown in Figure 1.10. Additional description of the conventional IR window technology is found in Section 1.11.2.
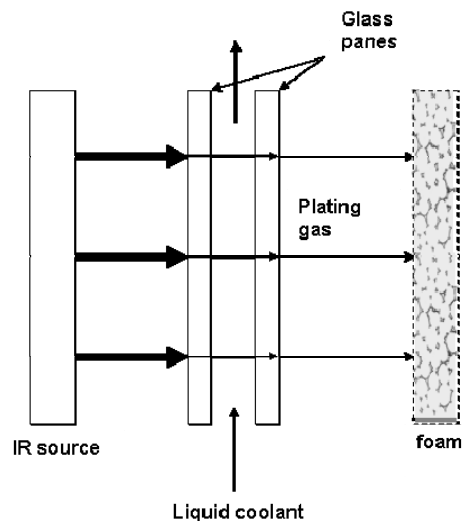
Figure 1.10   Energy transfer schematic for Ni foam production by carbonyl CVD

The diagram in Figure 1.10 illustrates that the energy transfer in the carbonyl plater is limited by the performance characteristics of the IR energy source and of the energy transmitting partition. Readily available assemblies of IR lamps with reflectors (e.g. model 5209 Hi-Temp IR heater from Research Inc.) can produce

14

IR energy flux in excess of 50 W/cm^2 – much higher than typically used in the conventional process. Unfortunately, the glass windows absorb most energy above the ~2 µm wavelength and this energy has to be removed by the window coolant. Quartz has somewhat better transparency range than IR transparent (low-iron) glass and has been used in smaller reactors (including the one in the present experimental setup). However, quartz windows are not used in the conventional commercial carbonyl CVD plater due to the lower strength and high cost of large quartz panes.

In the conventional carbonyl CVD foam plating, the immediate limiting factor in deposition rate is the loss of deposit uniformity for deposition rates exceeding about ~ 1.5 microns/min. However, because of the high absorption of IR lamp energy in the reactor window assembly (double-glazed glass with circulating liquid coolant), the window cooling requirement represents another limitation in the amount of energy that can be delivered to the foam substrate. The energy efficiency of the carbonyl plating process using IR lamps and liquid-cooled windows is thus only about 10%. The window coolant losses represent about 40%, energy required to heat the foam and reactor gases to the deposition temperature of ~ 180 $^{\circ}$C is ~30%, while the remaining energy (~20%) is lost to the lamp and reactor surroundings. Even at this low overall energy efficiency, the CVD process is still more energy efficient compared to electroplating (see Figure 1.15 later in this chapter).

1.7.1   Problem statement and objectives summary

1. Both electroplating and CVD conventional processes used in production of nickel foam in industrial practice are operating near the practical limits of the mass and energy transfer.

2. The mass transport rate limitation of both processes can be significantly improved by the flow of metal-carrying medium across the foam (forced convection). This can be achieved more easily with the low viscosity gas than with aqueous electrolyte.

3. The energy transfer in the electrolytic process represents a serious barrier as the energy delivery path involves the relatively poorly conductive nickel foam product and the electrolyte. Current densities in excess of about $10A/dm^2$ result in impractically high Ohmic losses in electrolyte, requiring large cooling systems that further reduce the overall energy efficiency of the process.

4. The energy transfer in the carbonyl process is limited only by the properties of the IR radiation source and by the transparency of the partition between the nickel foam inside the deposition chamber and the IR energy source.

5. **This opens the possibility of using an advanced energy source of suitable wavelength, such as a high power diode laser, which can deliver much higher energy flux while minimizing energy losses in the windows.**

Investigating the possibility of using this new energy source to substantially increase nickel foam production rate is the main objective of this thesis. An additional objective is the study of various deposition control regimes and the morphology of the resulting deposits.

1.8   Principles and Advantages of Ni foam CVD process

The principle of the pyrolytic Ni carbonyl CVD process involves the heating of a thermally stable substrate to the decomposition temperature of nickel carbonyl and simultaneously exposing the substrate to the plating gas mixture. The

process can be operated at atmospheric pressure. This contrasts with the electroplating method which requires electrically conducting substrates, and with various sub-atmospheric processes requiring vacuum equipment (e.g. sputtering).

A schematic of the polyurethane foam-based CVD process principle, demonstrated with simple laboratory equipment using a quartz tube reactor and IR lamp heaters, is shown in Figure 1.11. The external IR source provides energy for substrate heating to the nickel carbonyl decomposition temperature and for the decomposition reaction itself. The reactor window must be either highly transparent to IR radiation or it must be actively cooled to prevent window overheating. Alternatively, it must have a provision for "sweep gas" to keep the Ni carbonyl away from the internal window surface.

The substrate is used as a sacrificial template, providing the desired geometry for the metal foam structure. The technique is sometimes referred to as the "replication method" or "templated condensation" [Wadley, 2002].
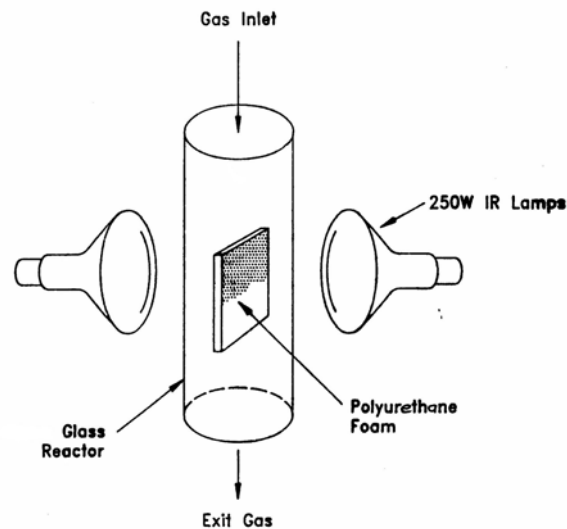
Figure 1.11 Principle of nickel deposition onto polyurethane substrates by carbonyl CVD process (1989)

A schematic of a complete semi-continuous laboratory demonstration system is shown in Figure 1.12 [Babjak et al., 1990]. The system consisted of a nickel carbonyl source delivered to the reactor by a CO gas carrier, a CVD deposition chamber with IR windows, external IR heaters, source of inert purge gas, polyurethane foam feeding and transport mechanism and off-gas treatment system. The system operated at atmospheric pressure.

The main advantage of the carbonyl CVD process thus lies in its simplicity, low energy requirement due to the low decomposition temperature of the precursor, and the potential for a high specific deposition rate. The nickel is deposited directly onto the non-conductive polymer substrate in a single step, using a nickel refinery intermediate. The deposition rates range from about 1 μm/min in conventional, large area carbonyl CVD to hundreds of μm/min in specialized, laser-driven nickel carbonyl CVD processes [Herman et al., 1983].
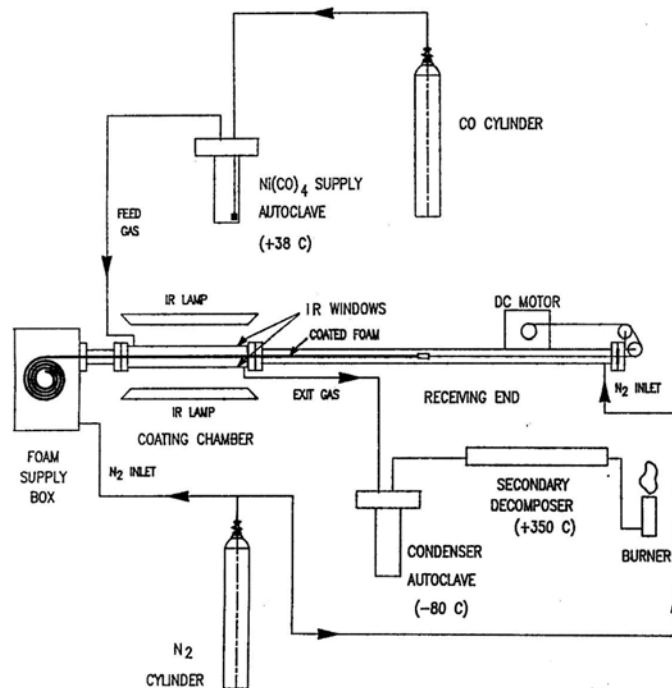
Figure 1.12 Semi-continuous laboratory CVD foam plating system (US Patent #4,957,543)

18

The requirement of the conductive substrate in the competing electroplating process is usually addressed by an initial, thin coating via electroless plating, sputtering or carbon coating. Typical deposition rate during the main electrolytic deposition in the commercial electroplating process is ~0.5 μm/minute or less. While both processes are capable of producing high-quality battery-grade nickel foam, the foam made by the CVD process generally exhibits greater degree of transverse (across the thickness) density uniformity. This is illustrated in SEM images of polished metallographic cross-sections of two nickel foam specimens produced by the two different methods, Figure 1.13.
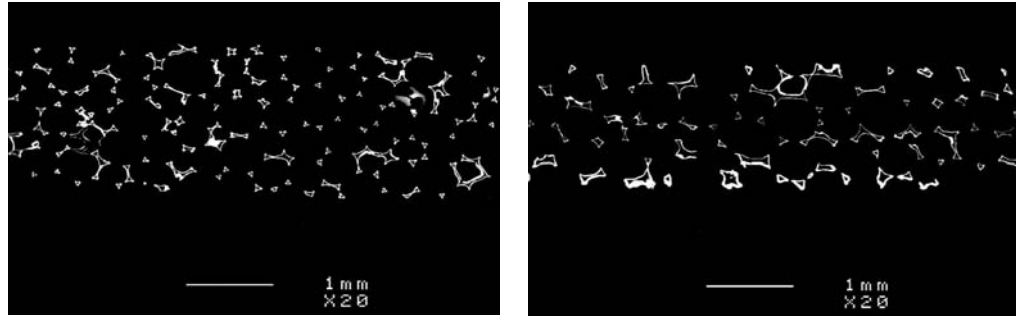
Figure 1.13 Typical SEM cross-sections of CVD (left.) and electroplated (right) Ni foams

The cross-section on the right (electrolytic foam) has clearly visible thicker struts on the outer 2 surfaces. Such deposit thickness gradient can be important in the control of properties and structure (compressibility) during the battery electrode manufacturing process. An example of a finished electrode cross-section produced with electrolytic foam is shown in Figure 1.14. Because of the non-uniform compression, the strut-to-strut distances in the middle part of the electrode are quite different from those near the surfaces. For comparison, Figure 1.37 later in this chapter shows a cross-section of a battery electrode made with CVD foam.
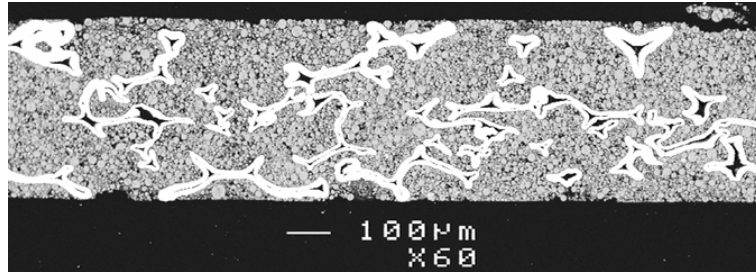
Figure 1.14 Typical SEM cross-section of a compressed battery electrode made with electroplated Ni foam

The main complication of the carbonyl process is in the need for robust engineering and production control protocols to deal with the highly toxic nature of the plating gas.

1.9 Feasibility of high-rate CVD deposition process

A thermally-driven CVD process is particularly suitable for rapid building of porous, three-dimensional structures. As discussed earlier, the rate of material delivery can be maximized simply by providing high flow of gas precursor against the substrate surface, and by matching this delivery rate with the corresponding amount of energy required for the precursor decomposition and for maintaining the desired surface temperature. In the case of thin porous substrates (such as foam for battery electrodes), the reaction by-products can be effectively removed by the high gas flow penetrating the open structure of the substrate. Thus in practice the deposition rate limit is ultimately determined by the mechanical strength and integrity of the substrate to withstand high gas flow and by the ability to deliver the required, controlled amount of energy to the substrate surface. The potential for high deposition rates and comparison between electroplating and carbonyl CVD processes using data from this work and from current industrial practice is shown in Figure 1.15.

Deposition rates and energy consumption of Ni Foam Processes
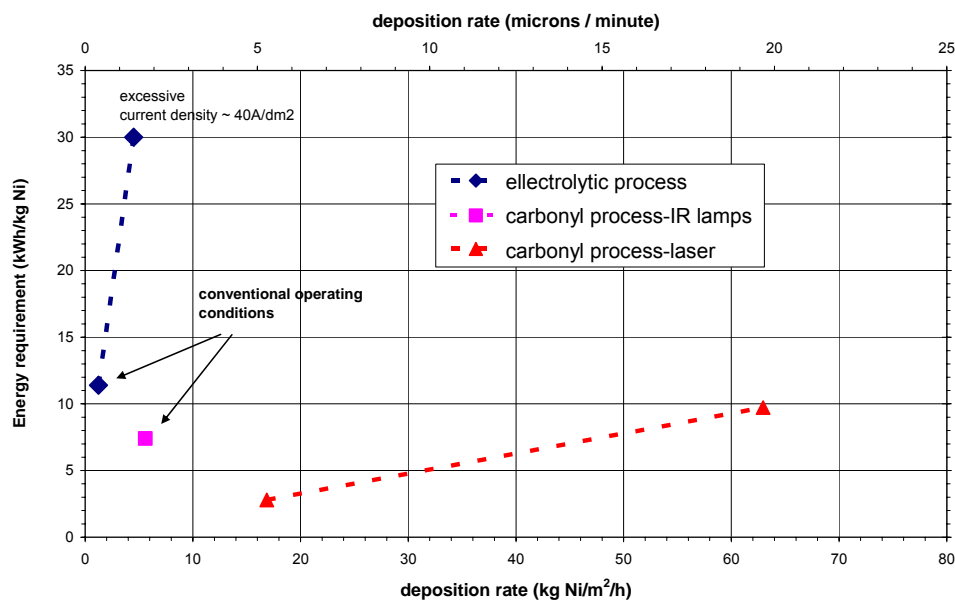
Figure 1.15   Energy requirement and deposition rate potential in Ni foam production

1.9.1   Energy delivery considerations in the deposition process

A key aspect of the pyrolytic CVD process is the method of energy delivery required to drive the decomposition reaction.   To facilitate a purely heterogeneous decomposition of the precursor (deposition of a film), care must be taken not to exceed certain critical temperature on any of the reactor internal surfaces, including the substrate.   This temperature depends on the thermodynamic properties of the precursor, its concentration (partial pressure), type and concentration of the carrier gas (typically CO or inert gases) and the presence of impurities or chemical additives.   For intermediate concentration (~30%) of nickel carbonyl in CO at atmospheric pressure and in the absence of impurities, the heterogeneous decomposition temperature range is about 110 to 220 $^{\circ}$C.

There are several methods by which substrate surfaces can be heated to this moderate temperature range inside a CVD reactor.   For stationary, bulk

substrates such as plating mandrels, heating by hot fluid channeled through the mounting assembly or the substrate itself is one option [Weber, 1995]. Another option is to introduce the substrate into the reaction chamber at elevated temperature, by heating it outside of the reaction zone. This is how nickel pellets have been made since early days of the Mond process to this day [Howard-White, 1963]. Finally, the substrate can be heated by energy sources external to the reactor, such as IR sources and induction coils, or by resistance heating. In the case of IR radiation, commonly used sources are short-wave IR lamps (the so-called "T-3" lamps) or IR ceramic heaters. The resistance heating option [Babjak et al., 1990] can use AC or DC current which is passed directly through the substrate that was first made conductive by some other method. The resistance heating method is efficient and seems simple and attractive, however, it suffers from the difficulty of distributing the electric current uniformly in a large-area substrate, leading to non-uniform heating. Providing electrical contacts capable of supplying high currents to a moving, porous substrate also presents a challenge.

1.9.2   High-power diode laser heating

In spite of the wide-spread use of lasers in industry during the last four decades, the use of high-power lasers in materials processing is far from saturation. Part of the reason is that to date, high-power lasers have been rather bulky and costly devices, requiring niche applications to justify their use. This is starting to change as diode lasers stacks are being positioned to revolutionize the high-power laser technology. This particularly applies to materials processing.

Diode lasers have long been used as light emitters in fiber optic communications, in bar-coding technology, laser absorption spectrometry, and in optical discs. More recently (since the mid-1990's), diode lasers have also been capable of providing considerable optical power. They are thus starting to find their way

into applications such as welding, cutting, cladding, surface hardening and general heat treatment, replacing more conventional technologies. The progress of the diode laser bar power output in recent years is shown in Figure 1.16 [Mondry et al., 2005 and Bookham, 2009]. Great reliability improvements have been achieved through the use of aluminum-free active area construction, which enabled the conduction-cooled diode laser bar to exceed the 40-watt, 10,000-hour lifetime mark. The lifetime can be extended to past 20,000 hours by operating the laser at reduced power. Current development efforts involve advancing several different aspects of diode design, fabrication, cooling and packaging in order to further reduce the cost of diode laser energy.

Semiconductor Laser Bar Output
1 cm industry standard configuration with >10,000 hr lifetime
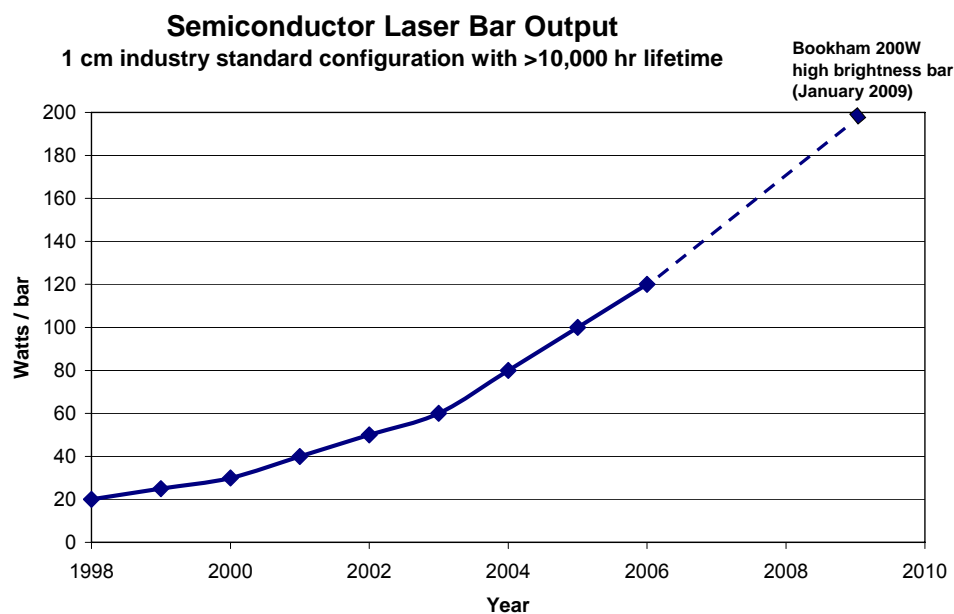
Figure 1.16   Increase in diode laser bar output in recent years [Mondry et al., 2005 and Bookham, 2009]

The key attractive features of high-power diode lasers include their compactness, easy cooling, and power efficiencies exceeding 50%. This is several times higher efficiency than other laser systems (typical power efficiency of a high-power CO_2 laser is ~ 15-20%). Furthermore, as part of the US DARPA SHEDS program

(Super-High Efficiency Diode Sources), effort is underway to improve the wall-plug efficiency of diode lasers to the ~80% level [Hitz, 2005].

In the case of a cold-wall reactor, such as the CVD process-based foam deposition system, the goal is to minimize energy absorption in the reactor window and in the reactor gases, while maximizing the absorption on the substrate surface. If conventional materials are used for reactor windows (e.g. tempered glass), any radiation heat source with wavelength longer than about ~2 μm will be strongly absorbed in the window material, requiring active window cooling or careful control of gas composition near the window internal surface (window sweep).

High-power diode lasers are candidates as possible energy sources for several reasons: the operating wavelength lies in the ideal region below 1 μm, where ordinary glass materials are highly transparent and metal surfaces exhibit higher absorption than at longer wavelengths. The ability to build diode laser stacks and arrays facilitates large area coverage for a possible industrial system. The achievable power densities can easily meet the requirement of the application. While at present the cost of this form of energy is relatively high (the cost of the 480 W system used in this study was ~US$25,000 in 2003), mass production techniques based on standard electronic component manufacturing are expected to lead to significant reduction in the cost of high-power diode lasers over time.

1.10 Laser – material interactions

1.10.1 Absorption of IR radiation

IR absorption on the nickel surface depends on the wavelength of the incident radiation and on the nickel surface condition. The radiation wavelength vs. absorption relationship for a clean, bright nickel surface is graphically shown in Figure 1.17 [Lide, 1994]. This value is also dependent on the surface texture and is likely higher for an as-deposited carbonyl Ni film. It is evident that higher absorption is obtained as the wavelength of the incident radiation is decreased.
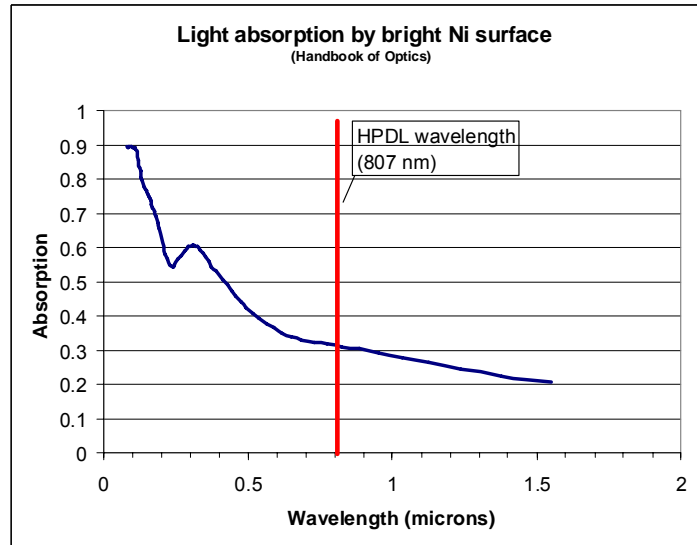
Figure 1.17 Absorption of clean, bright Ni surface as a function of wavelength

A typical spectrum for a short-wave IR lamp (filament temperature at 2500 K) is shown in Figure 1.18. The high absorption of IR radiation in a standard glass at wavelengths longer than about 2 μm (Figure 1.19) results in the need to provide active cooling of the chamber windows to prevent window overheating and
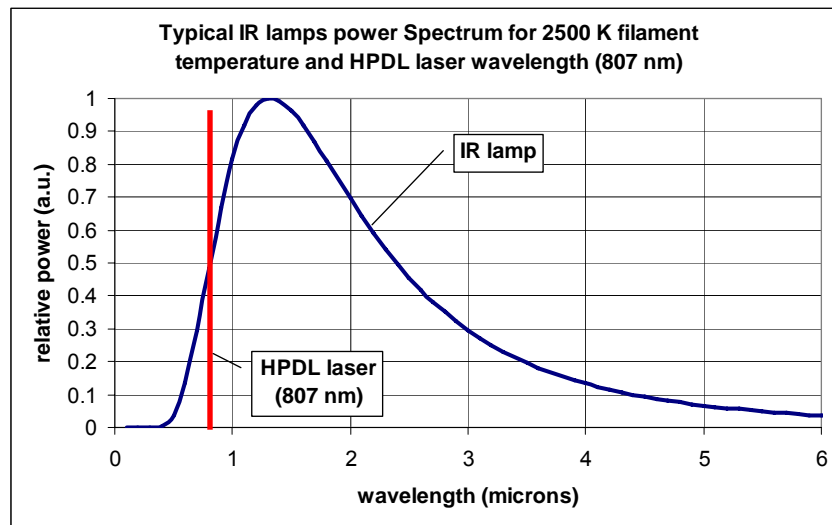
Figure 1.18 IR lamp energy spectrum. Also shown is the HPDL laser wavelength

subsequent metallic film deposition on the internal window surface. The diode laser line at ~807 nm is also shown in Figures 1.18 and 1.19. This part of the near-IR spectral region is ideal for a thermally-driven CVD process as it lies in the high-transmission range of common CVD chamber window materials, relatively high absorption of the nickel surface (compared to CO_2 laser or conventional IR lamp sources) and in the region where gaseous nickel carbonyl does not absorb (see Appendix 1 for $Ni(CO)_4$ absorption data).
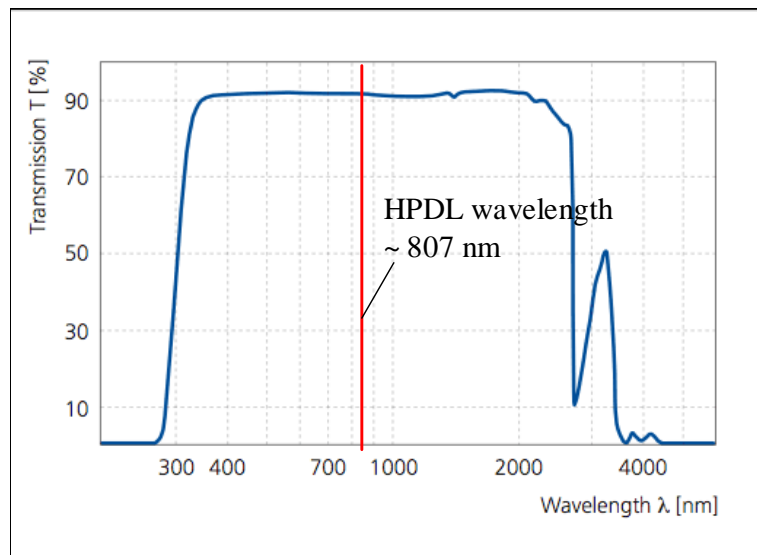
Figure 1.19 Typical borosilicate glass transmission spectrum

1.11 Limitations of the conventional CVD process

1.11.1 Deposition rate and deposit uniformity

The conventional CVD foam plating process used by Vale Inco as of 2006 operated at a specific deposition rate of about ~1.2 μm/min (0.02 μm/second). This rate resulted in a uniform distribution of nickel across the foam thickness with DTR[1] (Differential Thickness Ratio) values < ~1.2. Various attempts to increase the rate by increasing the substrate temperature and gas supply in this

---

[1] Differential Thickness Ratio concept is explained in Chapter 3, Section 3.15.

system demonstrated that rates starting at approximately ~1.5 μm/min (averaged over full thickness) resulted in unacceptable nickel distribution. Figure 1.20 shows metallographic cross-section of a sample of high-density nickel foam produced at a rate of ~1.8 μm/min in the commercial system described in Chapter five (Figures 5.11-5.16). A high DTR of ~2.1 was measured on this sample (high-end battery electrode use requires DTR values to be ≤ ~1.4). The poor Ni distribution problem arises from the fact that the fresh carbonyl feed gas does not effectively reach the middle portion of the PU foam substrate. Four moles of CO formed from each mole of nickel carbonyl during the decomposition inhibit transport of fresh carbonyl which is present in the main volume of the reactor, resulting in a significant gradient in carbonyl concentration between the foam interior and the outer surfaces. One possible way to minimize this problem in a conventional reactor is by controlling the reaction at a relatively low rate of < ~1.5 μm/min – this method was used in the commercial practice. Figure 1.21 shows a uniform nickel distribution (DTR~1.1) in a sample of high density foam produced at a rate of ~0.9 μm/min.
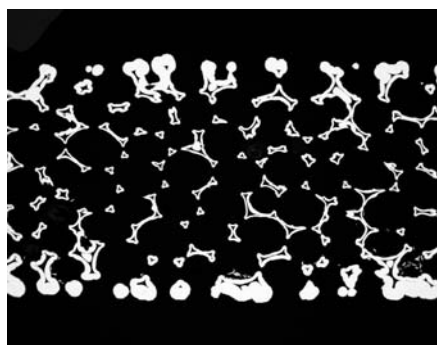
Figure 1.20 ~5,000 g/m² foam, DTR ~ 2.1
Deposition rate ~1.8 μm/min
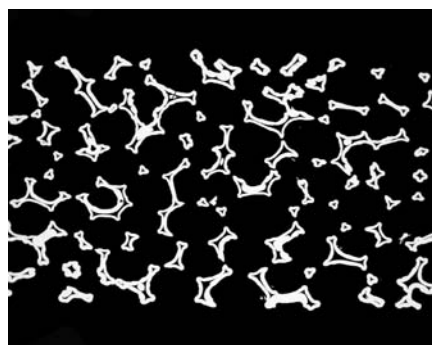
Figure 1.21 ~5,000 g/m² foam, DTR ~ 1.1
Deposition rate ~0.9 μm/min

As discussed earlier, another way to overcome the problem of poor across-thickness uniformity and simultaneously maintain high deposition rate is to force the gas *through* the highly porous substrate in a so-called "cross-flow" regime,

while providing sufficient energy to drive the decomposition reaction throughout the 3-D foam surface at a desired deposition rate. Sufficient quantity of gas must be available to minimize the concentration gradient across the foam thickness. This concept proved critical in the course of this work, leading to deposition of uniform, 3-D nickel films at rates significantly higher (demonstrated up to ~ 20x) than typically practiced in industrial CVD processes.

1.11.2 IR window

The industrial practice in Vale Inco's CVD production plant was the use of a double-pane glass with an IR-transparent liquid passed between the two panes [Paserin et al., 1992]. However, this significantly reduced the overall energy efficiency of the process (coolant heating accounted for about 40% of the total IR lamp energy), and also resulted in occasional deposition of nickel on the window, requiring periodic cleaning. An example of a window deposit due to process upset is shown in Figure 1.22. In most cases, such event necessitated premature shutdown, causing costly downtime. It is therefore desirable to develop a heating system that would minimize the need for window cooling. Diode laser radiation adequately meets this need, as most common window materials are highly transparent in the ~807 nm wavelength range.
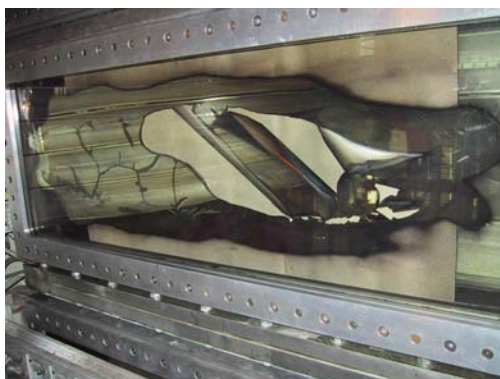
Figure 1.22 Nickel-plated internal surface of a deposition chamber window. The deposit started to crack and to peel-off at the time of the unit shutdown.

28

1.12 Large-area laser CVD

The use of laser energy sources in the CVD of $Ni(CO)_4$ has been reported in the literature by several authors. In most cases, the laser beam was focused to a small spot size to facilitate the growth of Ni microstructures [Maxwell et al., 1995], or for laser writing [Herman et al., 1983]. Thus, the high deposition rates are typically associated with small substrate areas or microstructures, enabled by the combination of 3-D diffusion paths for the gas precursor and high energy density of the laser beam. While Ni foam can be considered as a "large area" material, the term takes on a special meaning in this case owing to the unique, 3-dimensional nature of the substrate. This uniqueness lies in the combination of the relatively large surface area and small (dimensions of the order of 50-100 μm) local areas or "microstructures" acting as deposition sites, surrounded by large (hundreds of microns) voids that efficiently facilitate fluid delivery to the internal deposition surfaces. Due to the large porosity and 3-D nature of the foam structure, each square cm of nominal or 'projected' area of battery-grade foam (~2 mm thick with ~500 μm diameter cells) contains about 10 cm^2 of deposition surface. The foam can thus be viewed as a network of inter-connected microstructures, and hence represents a substrate that is quite analogous to the traditional LCVD deposit shapes (see for example metallographic cross-section images in Figures 3.29-3.33). Because of the excellent gas permeability, this structure is highly suitable for a cross-flow gas delivery, enhancing precursor mass transport throughout the foam substrate. The substrate geometry effects are further discussed in Section 1.16.

A laser energy source can provide unique advantages for a commercial, larger area carbonyl CVD process. In comparison with conventional heat sources, it could provide delivery of higher energy densities to the deposition zone, thus facilitating design of a compact deposition chamber with high material throughput. This may lead to the design of a fully continuous, atmospheric pressure process for

deposition of nickel onto continuous, web-based materials. Chapter five (Section 5.4) further discusses scale-up issues related to this process and outlines a possible design of such a laser-based production system.

1.13 Commercial CVD Ni foam production

The commercial nickel foam plating units utilizing the CVD process operated at Vale Inco nickel refinery in a semi-continuous mode to produce coils of nickel foams approximately 2500 m long, 1 m wide and 1 to 3 mm thick in a single batch. A schematic of the commercial deposition system is shown in Figure 1.23. The system was fully enclosed and operated at slightly above atmospheric pressure. The carbonyl CVD foam plating process was patented in 1990 by Vale Inco [Babjak et al., 1990]. The plating unit was essentially a cold-wall CVD reactor with multiple connected deposition chambers with IR-transparent windows providing means of substrate heating by an external energy source. The amount of nickel plated onto the substrate depended on plating gas composition, substrate temperature, substrate surface area, and residence time in the deposition chambers. In the conventional process, the reaction energy was provided by external short-wave IR lamps. In addition to the CVD process, the production involved significant amount of material handling in the substrate preparation and post-processing steps (spooling and trimming of PU foam, cutting, winding and packaging of small spools for the battery industry). Driven mainly by labor cost considerations, the commercial operation of the CVD system was discontinued in 2006 and the production of INCOFOAM® at Vale Inco was transferred to China, utilizing a combination of PVD (sputtering) metallization of the PU substrate and electroplating.
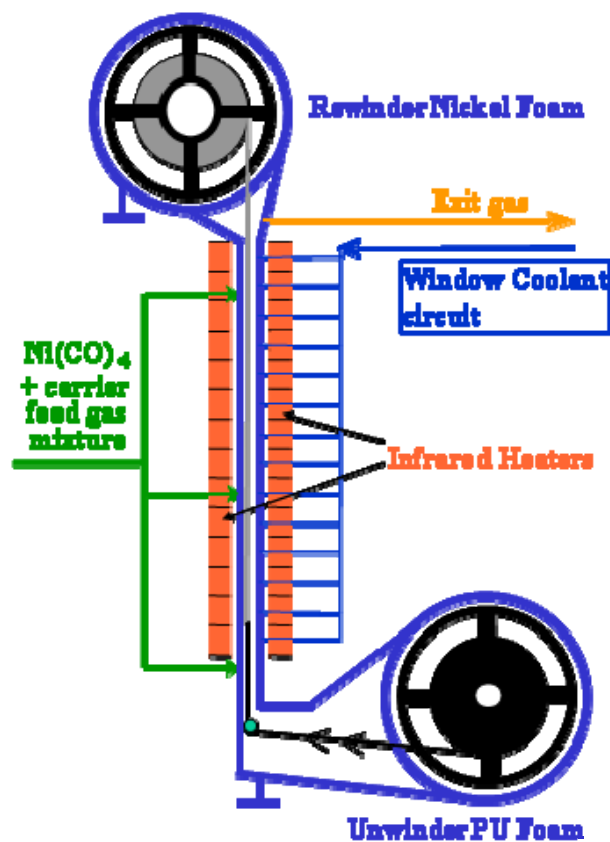
Figure 1.23 Schematic of a commercial Ni foam CVD production system (2006)[*]

The uniform foam structure can be made in a wide range of specifications – typically spanning a $0.2 - 2.6$ g/cm^3 density range and ~450 to ~3200 µm average cell diameters. Figure 1.24 shows three examples of achievable material porosity using the carbonyl CVD process: ~98%, ~91% and ~74% by volume (0.2 g/cm^3, 0.8 g/cm^3 and ~2.3 g/cm^3, respectively), all deposited on the same PU foam. The nominal cell size is the same for each of these foams. The observed density difference was achieved by adjusting the residence time (line speed) of the

[*] drawing courtesy of W.P. Leavoy

substrate inside the deposition chamber. The material exhibited excellent 3-D uniformity of the nickel coating in the entire density range.

| 0.2 g/cm3 (~98% porous) | 0.81 g/cm3 (~91% porous) | 2.3 g/cm3 (~74% porous) |
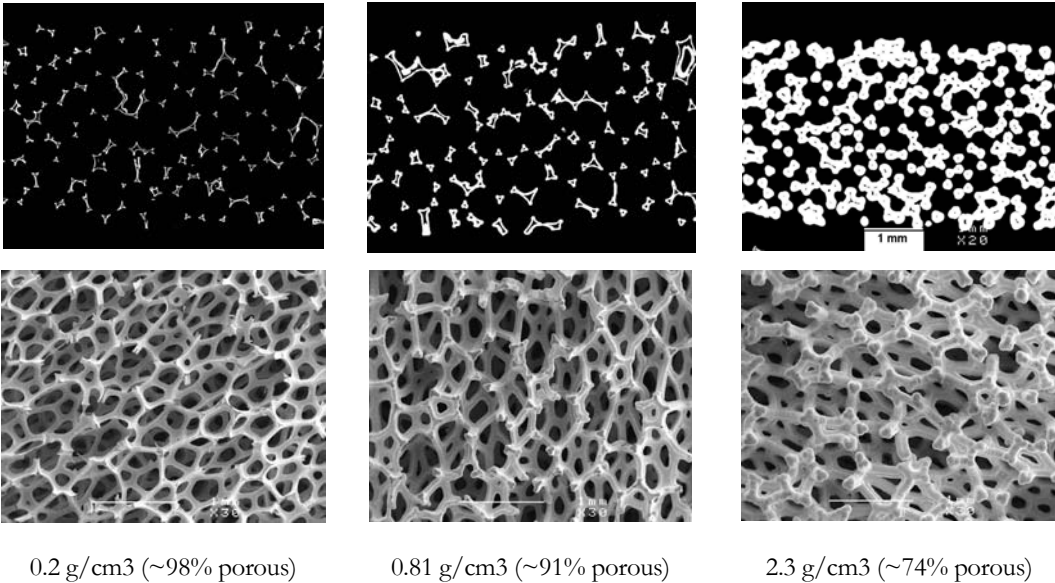
Figure 1.24 SEM cross-sections and surface micrographs of nickel foam of several porosities

The cell size of nickel foam is determined by the cell size of the polymer foam template. Reticulated polyurethane foams are available in cell sizes ranging from about 5 ppi (pores per inch) to about 130 ppi (average 3-D cell diameter ~6 mm to ~0.4 mm). Examples of 110 ppi and 20 ppi foams are shown in Figure 1.25.
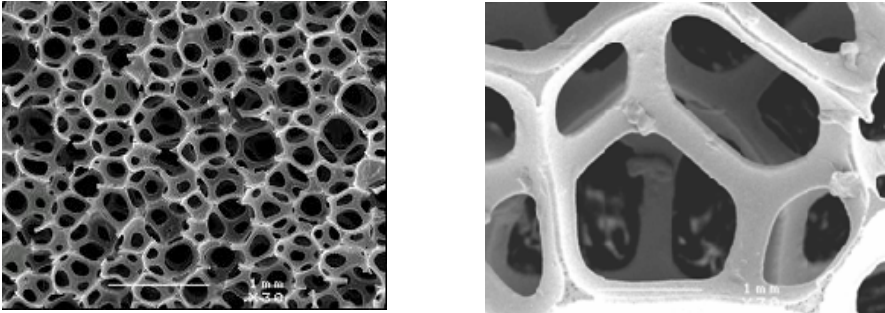
Figure 1.25   SEM images (both 30 X) of ~450 μm (left) and ~3200 μm (right) foams

1.14 Types of LCVD reactions

Laser-induced chemical processing of materials deals with deposition, patterning and general physico-chemical modification of solid surfaces, or gas-phase particle formation by laser radiation-induced chemical reactions. The reaction is termed **heterogeneous** when it is induced at or near the solid-gas interface. The product of such reaction is a solid deposit in a form of a thin or thick film or a 3-dimensional microstructure, depending on the substrate morphology and process conditions. The reaction is termed **homogeneous** if it is activated within the ambient medium itself or within the bulk of the material. The usual product of homogenous reactions is particulate matter, which can also become part of a solid deposit on a substrate, if the solid and particle surface properties are appropriate for deposit assembly. In-depth discussion of laser processing techniques, terminology and processes can be found in a recent book by D. Bäuerle *"Laser processing and Chemistry"* [Bäuerle, 2000] and in J. Mazumder's book *"Theory and Application of Laser Chemical Vapor Deposition"* [Mazumder and Kar, 1995].

Both heterogeneous and homogeneous reactions can be activated thermally (pyrolytic reaction) or photochemically (photolytic reaction). In the thermal process, the laser simply acts as a heat source (as in the present study). Photochemical processing implies selective excitation, ionization or dissociation of targeted species and can typically proceed without (substantial) temperature increase. In cases where both mechanisms play a role, the process is termed **photothermal**.

The photolytic processing appears attractive, especially for temperature-sensitive substrates such as PU foams. However, the cost of UV photons required for

large-scale processing would be prohibitive at present, and into the foreseeable future [Herman, 1983].

The use of a laser in pyrolytic CVD processes provides unique features which are difficult to obtain with conventional energy sources, such as IR lamps. This uniqueness is mainly based on the space and time localization of the laser radiation and on wavelength selectivity. As a consequence, novel reaction pathways and products, material microstructures, high deposition rates and novel surface morphologies are often possible.

In this work, the subject of investigation is diode laser-initiated thermal decomposition of nickel carbonyl on the surface of 3-dimensional substrates. The laser is used purely as a source of thermal energy which is efficiently delivered to the substrate via IR-transparent glass windows. The nickel deposition process (both rate and deposit uniformity) is controlled by the following key phenomena:

- Kinetics and thermodynamics of the carbonyl decomposition reaction

$$Ni(CO)_4 \rightarrow Ni_{(s)} + 4CO_{(g)} \qquad (1.6)$$
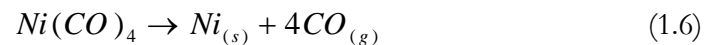
- Mass transport of nickel into the foam structure, controlled by the precursor flow rate and substrate geometry

- Heat transfer to the surface of individual foam struts

In the following sections, these individual aspects of the deposition process will be discussed in some detail.

1.15 Ni(CO)$_4$ thermodynamics

Thermodynamically, at atmospheric pressure and intermediate concentration, nickel carbonyl starts decomposing at a temperature of approximately 100 ^{o}C. Figure 1.26 shows the pure nickel carbonyl equilibrium conversion data[2] at different concentrations (balance CO) at atmospheric pressure. It can be seen that thermodynamically, the decomposition is practically complete at 200 ^{o}C and for highly concentrated mixtures it starts at temperatures as low as 50 ^{o}C.
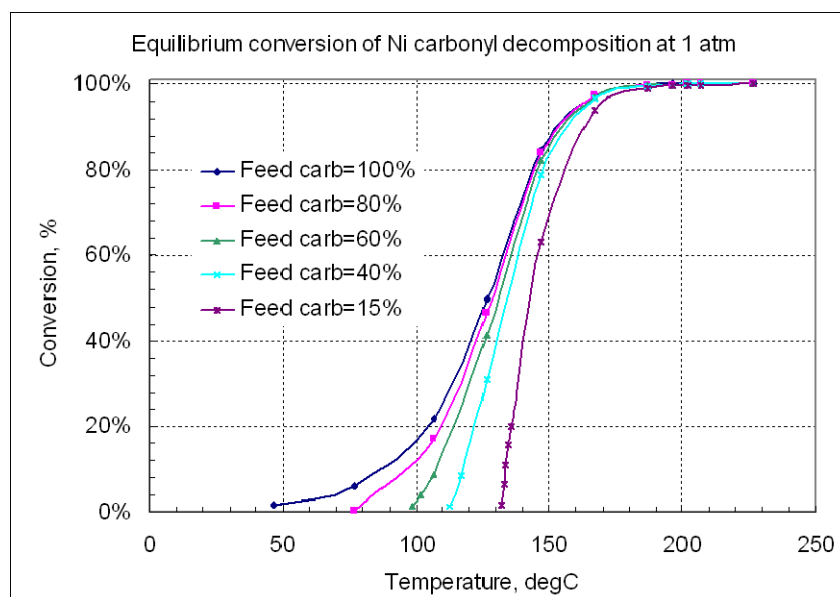
Figure 1.26 Equilibrium conversion of nickel carbonyl at atmospheric pressure

---

[2] Calculated using FACTSAGE© chemical thermodynamics software package

35

1.16 Substrate geometry effects

The uniformity of the deposit on a 3-dimensional structure such as a sheet of open-cell PU foam will depend on the balance of mass transport, energy delivery, and reaction control mode that prevails during deposition. If transport of the carbonyl precursor inside the foam becomes the slow step, the nickel will tend to grow out into the gas stream, with limited deposition within the foam interior. This situation will be favored by slower gas flow rates and faster reaction rates (higher temperature), and can be partly addressed by flowing the precursor faster. This implies that for a given gas flow rate, there will be a critical deposition temperature (and hence deposition rate), beyond which the 3-dimensional deposit will become non-uniform. Substrate geometry plays a major role in this effect. If the substrate is a large, flat surface, the precursor can reach the deposition surface from one direction only, and the reaction products must leave in the same direction. Thus competition between arriving and leaving gas molecules will limit the total exchange of fresh carbonyl molecules available for decomposition. This situation changes markedly if the substrate is a 3-dimensional object such as a fiber, rod, open-cell porous material, or other microstructure with gas arriving at the deposition surface from many directions. This is the fundamental reason for unusually high deposition rates reported in the growth of various microstructures (see literature review in Chapter two).   The 1-D vs. 3-D diffusion consideration is schematically illustrated in Figures 1.27 and 1.28.
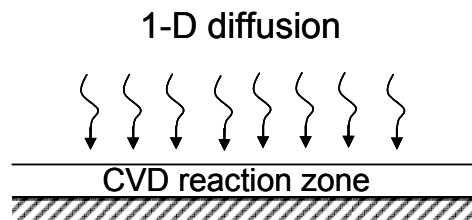
| Figure 1.27 Conventional CVD on large area flat substrate – 1D diffusion effects | Figure 1.28 Laser CVD of microstructures – 3D diffusion effects |
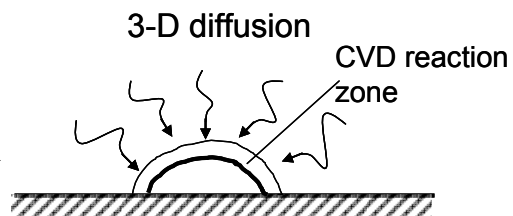
The open-cell polyurethane foam structure benefits from the 3-D diffusion effects, especially if the overall gas flow is directed to cross a sheet of foam material of some finite thickness. While the overall flow can be deliberately uni-directional, many local micro-currents are formed as the gas is making its way through the tortuous path of interconnected struts and cell openings (Figure 1.29). Thus fresh precursor molecules are arriving at the foam surfaces from many directions and similarly the byproduct CO is leaving in many directions to join the bulk flow crossing the foam sheet. The 3-D nature of mass transport to
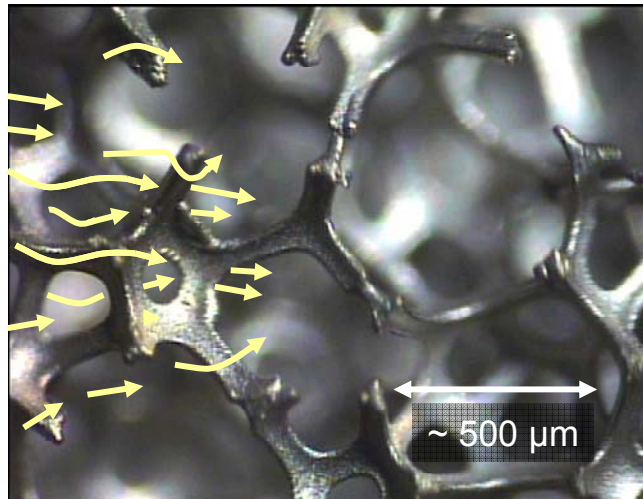
Figure 1.29 Laser CVD of porous foam – 3D effects

the foam surface is clearly manifested by high uniformity of nickel deposit on the struts, as shown in an SEM cross-section detail in Figure 1.30. The image shows a single strut of typical triangular shape with uniform, ~ 5μm thick nickel deposit formed on the original PU foam surface.
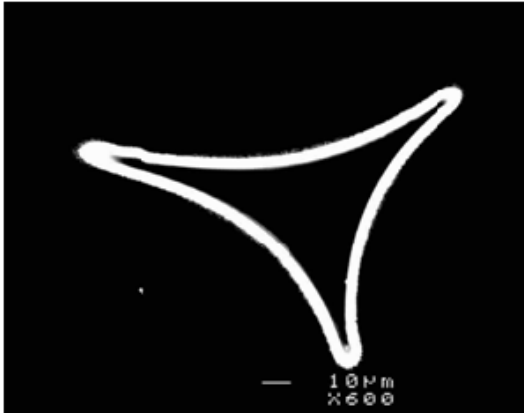
Figure 1.30 SEM cross-section detail showing excellent 3-D uniformity of Ni deposit on an individual foam strut

1.17 Nucleation and growth processes

Nucleation and growth processes control the formation and properties of solid deposits in both homogenous and heterogeneous decomposition of a CVD precursor. In this section, the principles governing these processes are reviewed and selected examples of the types of deposits obtained in the LCVD foam deposition process are presented. Figure 1.31 illustrates the fundamental sequential steps occurring in a CVD process:

1. convective and diffusive transport of reactants from the reactor inlet to the reaction zone

2. homogeneous chemical reactions in the gas phase producing reactive species and by-products

3. transport of the reactants to the substrate surface

4. adsorption (chemical and physical) and diffusion of the reactant species on the substrate surface

38

5. heterogeneous reactions catalyzed by the surface, leading to island growth and film formation

6. desorption of the by-products of the surface reactions

7. convective and diffusive transport of the reaction by-products away from the reaction zone
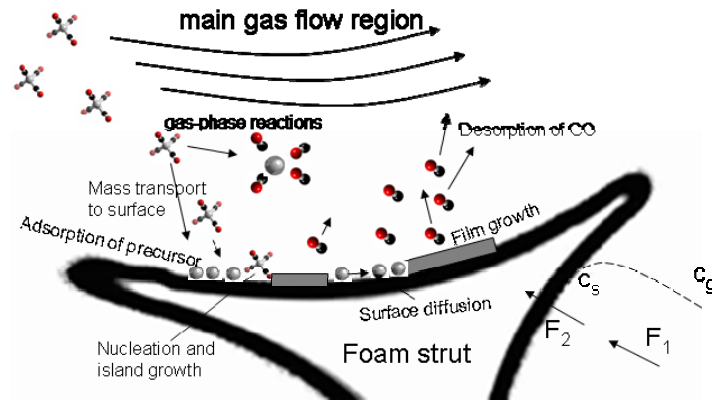
Figure 1.31 Nucleation and growth processes on the foam substrate surface

The nickel carbonyl flux F_1 arriving from the main gas flow region to the area near the surface can be approximated by

$$F_1 = h_g \cdot (c_g - c_s) \qquad (1.7)$$

where c_g and c_s are the concentrations of nickel carbonyl in the bulk of the gas and at the surface, respectively, and h_g is the mass transfer coefficient. The flux F_2 consumed by the decomposition of nickel carbonyl at the surface of the growing deposit can be approximated by

39

$$F_2 = k_s \cdot c_s \tag{1.8}$$

Where k_s is the chemical surface reaction rate constant. The flux is thus proportional to a driving force, which in the case of mass transfer is the gas concentration difference and in the case of a first-order chemical reaction, the local concentration of the reacting species. In steady state, $F_1 = F_2 = F$ and the surface concentration of nickel carbonyl at the substrate surface can be expressed as

$$c_s = \frac{c_g}{1 + \dfrac{k_s}{h_g}} \tag{1.9}$$

In this formula, the surface concentration c_s will go to zero if $h_g \ll k_s$, resulting in a *mass-transfer controlled* process. On the other hand, if $h_g \gg k_s$, the surface concentration will approach bulk gas concentration and the process becomes *surface-reaction (or kinetically) controlled.*

1.17.1 Gas-phase mass transfer

The transport of active species across the "stagnant" film of the boundary layer δ proceeds mainly by diffusion. Thus the flux F_1 across this layer can be written as

$$F_1 = D_g \frac{c_g - c_s}{\delta} \tag{1.10}$$

Where D_g is the diffusivity of the active species in the gas. This then relates the mass transfer coefficient h_g to diffusivity and boundary layer thickness δ as

$$h_g = \frac{D_g}{\delta} \qquad (1.11)$$

The internal foam surface can be approximated by a collection of small flat plates represented by the sides of the triangular struts of width L (Figure 1.32). Using the assumption that the extent of the flowing fluid is infinitely large (i.e. far away from the strut surface the fluid is flowing with a uniform velocity U), and that immediately next to the strut surface the velocity is zero, the local fluid velocity will assume certain distribution along the strut length from 0 to U. As the fluid moves along the strut surface, the disturbance will spread further towards the middle of the open foam cells, creating a boundary region δ with average thickness given by

$$\overline{\delta} \equiv \frac{1}{L}\int_0^L \delta(x)\,dx = \frac{2}{3}\cdot L\sqrt{\frac{\mu}{\rho \cdot U \cdot L}} = \frac{2}{3}\frac{L}{\sqrt{Re}} \qquad (1.12)$$

Where $\mathbf{Re} = \dfrac{\rho UL}{\mu}$ is the Reynolds number, representing the ratio of the magnitude of inertial effects to viscous effects in fluid motion. Here ρ represents fluid density in g/cm^3 and μ is the fluid viscosity in g cm^{-1}s^{-1}, L is in cm and U in cm s^{-1}.
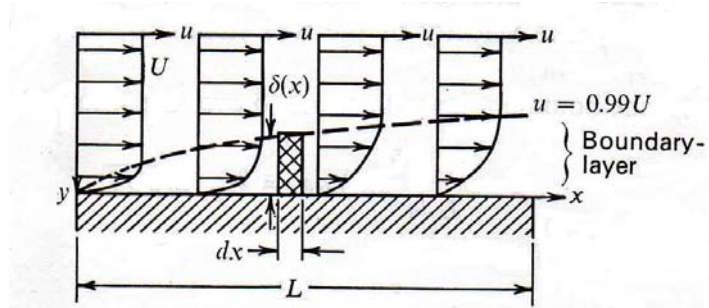
Figure 1.32 Boundary layer formation at the foam strut interface [Grove, 1967]

Numerically, taking L as ~ 150 microns, the dynamic viscosity of carbonyl/CO mixture (30:70) at 200°C as 0.0203 cP [Wasmund, 2005] and a bulk gas velocity of 25 cm/s, the boundary layer thickness is of the order of ~40 microns.

Figure 1.33 is an example of a highly textured deposit formed by creating conditions near the substrate surface that result in a growth of pointed, single-crystal cones. A common structure for carbonyl nickel is pyramid-shaped crystallites with sharp vortices protruding from the surface of the main deposit. The top image in Figure 1.33 is a fracture cross-section of such deposit and the bottom image documents the deposit surface morphology. The pyramid-shaped crystallites grow as part of the columnar morphology which is initiated near the substrate interface and maintained throughout the deposit growth. The areas between the columnar grains are filled by smaller crystallites and some porosity. The voids are formed as the grains occasionally form a bridge and limit mass transport to the tight spaces between rapidly growing vertical columns. The sample shown in Figure 1.33 was produced at 220 - 230 °C substrate temperature and in the absence of H_2S additive.

Further discussion on the subject of deposit morphology effects is included in the literature review section (2.2.4) and in Chapter four, Sections 4.4 and 4.5.
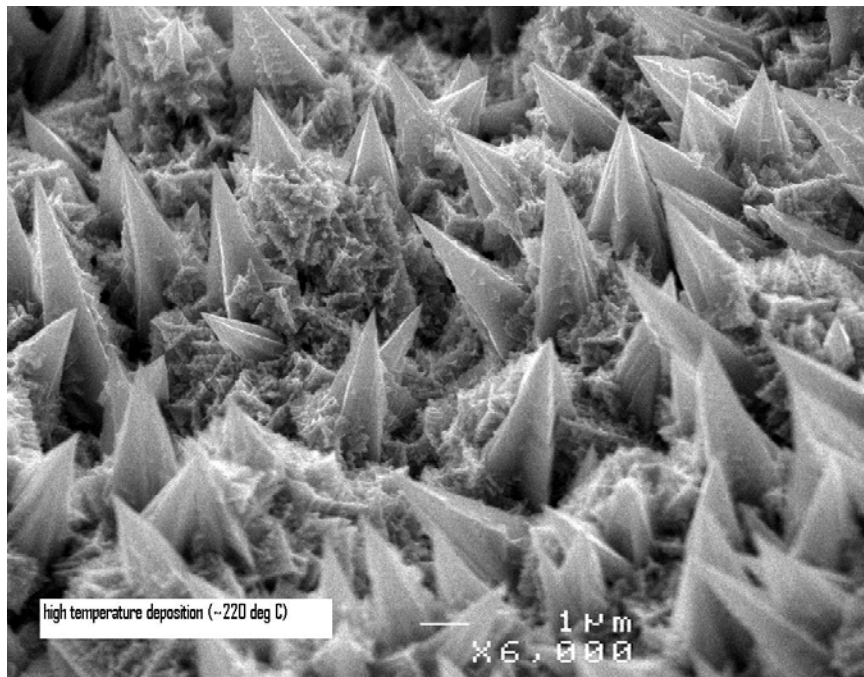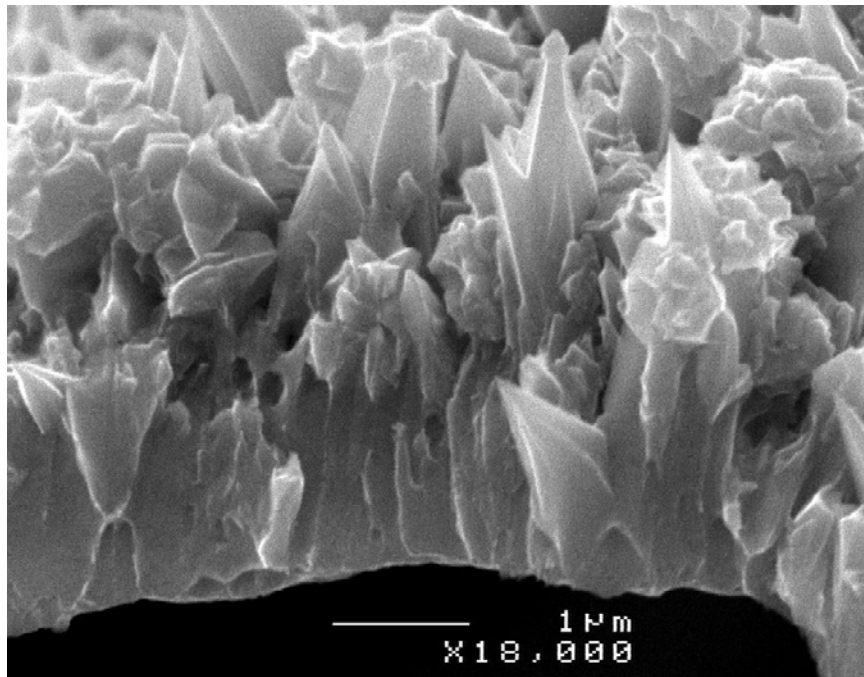
Figure 1.33 Fracture cross-section (top, 18,000 x mag.) and surface image (bottom, 20,000 x mag.) of a deposit morphology under conditions near homogeneous decomposition onset (exp. LH050308)

1.18 Reaction kinetics

As discussed in the previous section, the deposition process can operate in one of the three possible regimes: the chemical reaction rate or kinetics-controlled regime, mass transport or diffusion-controlled regime, or, for a narrow set of conditions, the process can be in an intermediate state between these two regimes. Figure 1.34 is a general Arrhenius plot of a logarithm of deposition rate plotted against inverse temperature. Ideally, to maintain high quality and maximum 3-D uniformity in complex-shape deposits, it is desirable to control the process in the kinetic regime. By enhancing mass transport using such means as forced flow through a porous substrate, it is possible to extend the kinetically-controlled region to higher temperatures, yielding high quality deposits at higher deposition rates. This is schematically illustrated in Figure 1.34.
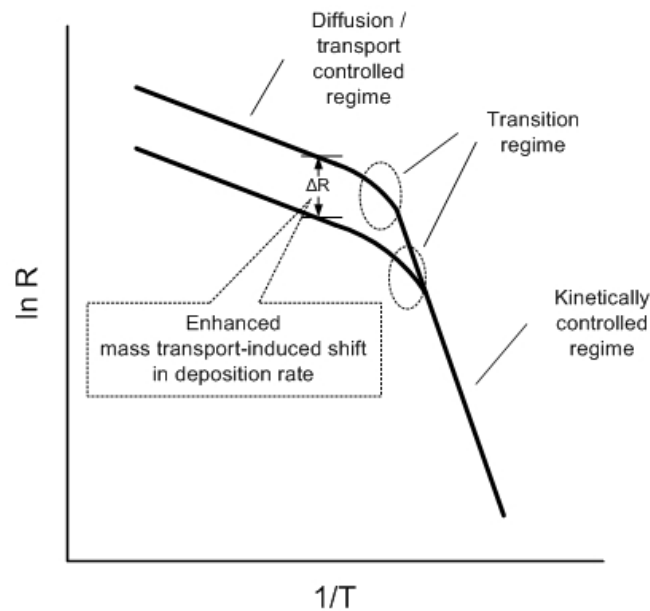
Figure 1.34 Arrhenius relationship between deposition rate and temperature

44

There are several possible approaches to enhancing the mass transport of reactants, leading to increased deposition rates. One might increase the pressure of the reactants, increase the concentration of the precursor in the carrier gas, or provide faster gas delivery to the reaction surface by increased flow over the substrate surface (forced flow or the "gas jet" concept). By using these techniques and focusing on the high pressure mode of operation, Maxwell et al. demonstrated a phenomenally high growth rate for carbon fibres by LCVD from ethylene precursor

Figure 1.35 Deposition rates of carbon in high-pressure CVD [Maxwell, 1999]

[Maxwell et al., 1999]. Figure 1.35 shows the results of this work, demonstrating highest rates in excess of ~10 cm/s in solid carbon growth at a pressure of ~1.1 MPa.

For safety reasons, carbonyl deposition is typically done at atmospheric or sub-atmospheric pressures. The experiments done as part of this thesis were carried out at slightly above atmospheric pressure (~0.2 psig).

1.19 Kinetics of CVD foam plating

Using the assumption of a first-order reaction (consistent with earlier Inco measurements as well as published work, e.g. Tsylov [1971]), the deposition rate can be written as

$$R = \frac{1}{S} \cdot \frac{dN_{Ni(CO)_4}}{dt} = k \cdot c_{Ni(CO)_4} \qquad (1.13)$$

45

where

R = reaction rate (mol cm^{-2} s^{-1})

S = gas-foam interface in cm^2 (for PU foam samples used in this study, the actual or effective surface area was ~50 cm^2 per cm^3 of foam-occupied volume)

$\dfrac{dN_{Ni(CO)_4}}{dt}$ = number of carbonyl molecules decomposing on the substrate surface per unit time

k = reaction rate constant (cm s^{-1})

$c_{Ni(CO)_4}$ = nickel carbonyl concentration (mol cm^{-3})

From the Arrhenius plot the rate and temperature are related as follows:

$$k = k_0 \cdot e^{\frac{-E}{\Re \cdot T}} \quad \rightarrow \quad \ln k = \ln k_0 - \frac{E}{\Re} \cdot \frac{1}{T} \qquad (1.14)$$

where

E = activation energy in J mol^{-1}

$\Re$ = universal gas constant (=8.314 J mol^{-1} K^{-1})

T = temperature in K

k_0 = pre-exponential constant (obtained from the vertical axis intercept at 1/T=0)

The measured values for k_0 and E using foam samples are given in Section 4.1.

1.20 Nickel foam applications

Nickel foam possesses unique features such as high porosity, light weight, exceptional 3-dimensional uniformity, intrinsic strength, corrosion resistance, and good electrical and thermal conductivity. Various existing and potential new applications are discussed next.

1.20.1 Battery electrodes

Nickel foam has been predominantly used in the production of battery electrodes, especially for the positive electrode of rechargeable nickel metal hydride (NiMH) batteries. Such batteries have found extensive applications for portable computers, cordless power tools and phones, battery-powered scooters, bicycles, emergency lighting, and more recently, hybrid electric vehicles (HEVs). The foam can be used in both cylindrical and prismatic cells. The construction of both types of batteries is schematically illustrated in Figure 1.36 [Linden, 1995].
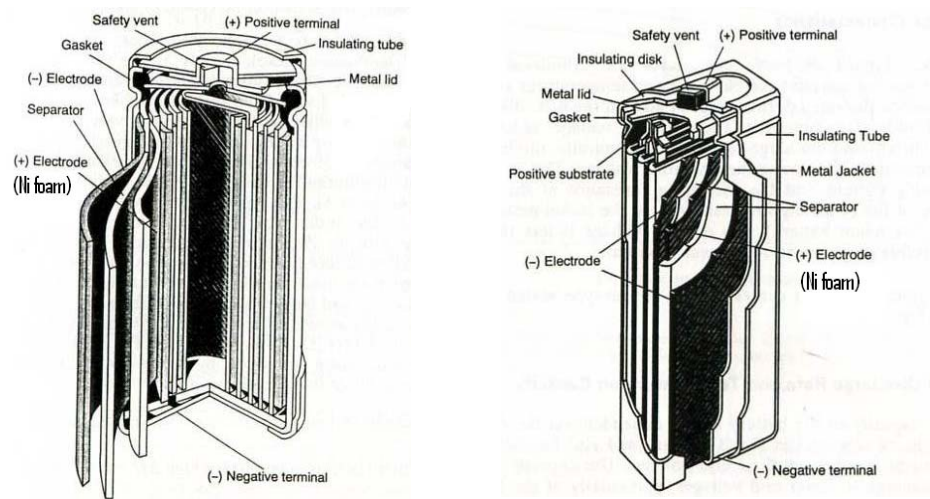
Figure 1.36   Construction of cylindrical (left) and prismatic (right) NiMH battery with Ni foam positive electrode

The CVD-derived nickel foam provides uniform compressibility to the electrode, allowing the use of a very light weight structure in electrode manufacturing. The

effective surface area of the electrode's active materials can thus be increased to enhance the high power capability. The foam also facilitates simplified and environmentally clean battery manufacturing processes where the active mass containing nickel hydroxide is mechanically pasted into the foam structure, replacing wet chemical impregnation methods used in sintered nickel electrodes. A typical cross-section of a pasted CVD Ni foam-based battery electrode is shown in Figure 1.37. The micrograph shows good uniformity of the Ni foam deposit thickness throughout the structure. Also shown is one of the first versions of assembled NiMH modules based on prismatic cells, commonly used in the construction of electric and hybrid-electric vehicle batteries, as well as typical cylindrical NiMH batteries. These batteries were produced by Panasonic, a leading supplier of rechargeable batteries.

Due to its light weight and customizable cell structure, nickel foam for use as electrode material in lithium ion batteries is also under development.
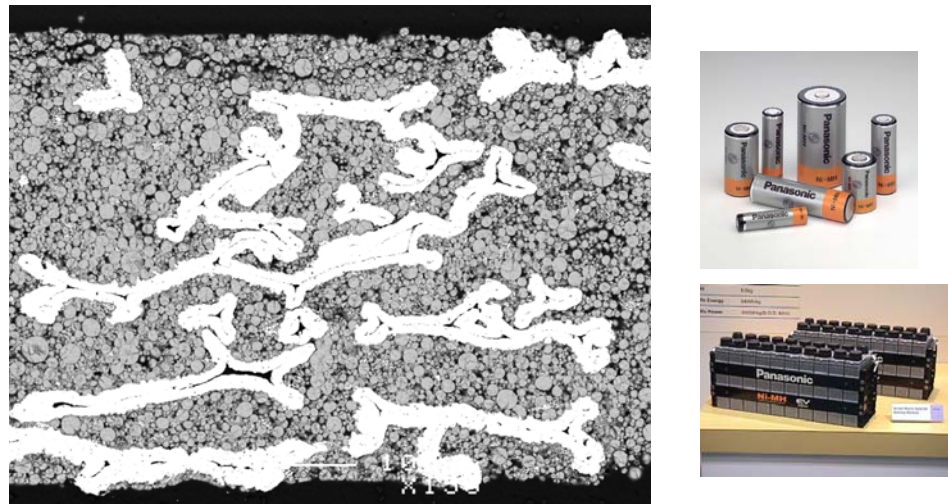
Figure 1.37   SEM image showing typical structure of a pasted nickel foam battery positive electrode (left) and examples of assembled NiMH cells (right)

1.20.2   Fuel cell applications

Nickel is active in hydrogen dissociation at elevated temperatures. This makes nickel foam a potential material as an electro catalyst in molten carbonate fuel cells (MCFC), which normally operate at 550-700 ºC. The chemical environment of MCFC fuel cells is such that nickel can be used for both electrodes. Nickel foam provides a suitable structure for these applications as it offers high porosity, good gas distribution characteristics and thermal stability.

Ni foam may find additional applications as a bipolar plate enhancement material for proton exchange membrane fuel cells (PEMFC), electrode interconnects for solid oxide fuel cells (SOFC), and electrode materials in electrolysis such as hydrogen electrolyzers. It may also provide an enhanced conductive surface area for use in steam reforming reactions to supply hydrogen or syngas for fuel cells.

1.20.3   Catalyst materials

Due to the unique open cell structure, low pressure drop, intrinsic strength and resistance to thermal shock, Ni foam has potential as a catalyst support for automotive catalytic converters and catalytic combustion, and for catalytic filters for diesel engine particulates. Its high thermal conductivity may be superior to ceramic monolith supported catalysts in low light-off conversion of carbon monoxide and hydrocarbons during engine cold start. Ni foam may be therefore comparable or superior to high temperature steels as a catalyst support. Other catalyst applications of nickel foam may include foam-supported catalysts for the Fisher-Tropsch reaction and the hydrogenation of fine chemicals.

Ni foam has been used as a substrate for carbon nanofibre catalyst support [Jarah, 2004]. The nanofibres were grown following the formation of nano-size

Ni particles on an oxidized and subsequently reduced Ni foam surface. Figure 1.38 shows the type of morphology obtained in Jarah's experiments.
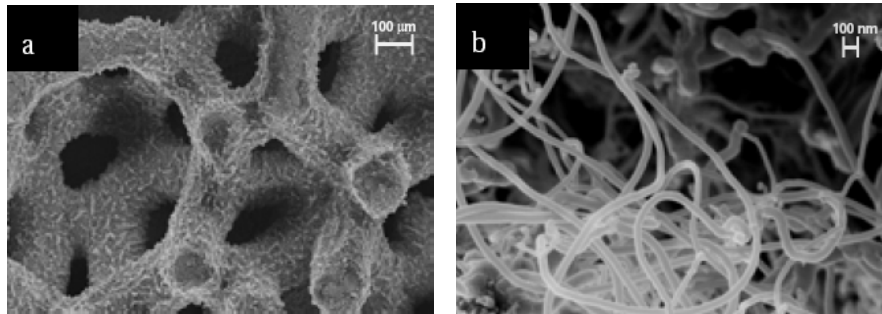
Figure 1.38 SEM micrographs of carbon nanofibres (CNF) grown on Ni foam:
(a) 25 wt% CNF synthesized at 450°C in 2 hours (b) details of the CNF layer [Jarah, 2004]

Another research group used a nickel foam substrate directly for the deposition of carbon nanotubes from acetylene gas [Kavecky, 2005].

1.20.4   Other application opportunities

While NiCd and NiMH rechargeable battery electrodes remain the dominant uses at present, the material will likely find its way to a number of new applications. Owing to its uniform 3-D structure with a broad possible range of custom porosity and high-temperature corrosion resistance, nickel foam may find applications as a high-temperature filter material. Alloying the foam with other metals, by application of a powder slurry and subsequent sintering, yields nickel superalloy materials with high porosity. One of the applications of such high temperature porous material is a diesel particulate filter [Koltsakis et al., 2006].

The ferro-magnetic properties of nickel may make it suitable as a magnetic flux conductor for handling magnetic particles in a fluid. Other applications may include hydrogen storage medium, heat exchanger medium, and even in visual

arts owing to its unique shaping capabilities, wide porosity range and environmental stability.

The flow characteristics of a metal foam media can be exploited in gas separation technology where the foam could be used as functional support for special adsorbents such as zeolites or other high-surface area functional structures.

Applying various functionalized surface coatings can result in useful 3-D structures with desirable environmental stability (owing to the high corrosion resistance of nickel) and functional properties. The idea of using Ni foam for photovoltaic application is further elaborated on in Section 4.4.2.

2 LITERATURE REVIEW

2.1 Nickel carbonyl decomposition kinetics

The first systematic study of nickel carbonyl decomposition kinetics was done by Mittasch in 1902, about a decade after Mond's discovery and initial work with this compound [Mittasch, 1902]. Mittasch concluded that the carbonyl formation and decomposition was a reversible reaction within a relatively narrow temperature range between 50 and 120^0C. He found the decomposition to be a first order reaction with respect to carbonyl concentration, affected by the type of nickel surface present.

A number of other researchers investigated the carbonyl chemistry as the compound gained in commercial importance in the production of high-purity nickel. Two of the most quoted experimental studies were conducted by Chan [1954] at the University of Toronto and Carlton and Oxley [1967] at the Battelle Memorial Institute. The latter kinetic data is the most comprehensive, covering a temperature range from 100 to 225ºC and is often quoted in more recent publications. Carlton and Oxley used a flow-through reactor with temperature-controlled filament and gas-directing orifice designed to direct the gas stream over the filament. The filament was a resistively-heated ⅛" hollow steel tube with a thermocouple inserted in the centre of the tube (Figures 2.1 and 2.2). The rate measurements were determined by the weight gain of the filament, the initial surface area and the duration of the run. The deposited thickness of nickel did not change the filament diameter by more than 2%. The experiments were done in a pressure range between 20 and 200 Torr.
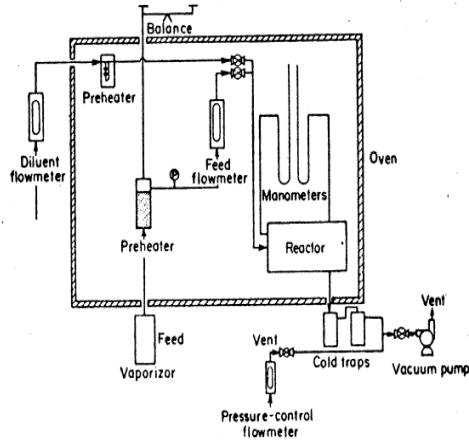
Figure 2.1 Schematic diagram of Carlton-Oxley's equipment
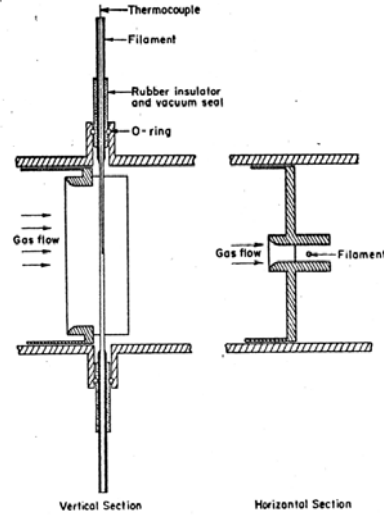
Figure 2.2 Filament and orifice detail

Carlton and Oxley arrived at the following expression for the rate of heterogeneous decomposition R (in moles cm^{-2} s^{-1}) of nickel carbonyl as a function of temperature T (in K) and partial pressures of nickel carbonyl and CO, p_1 and p_2, respectively (in Torr):

$$R(p_1, p_2, T) = 5.1 \times 10^{29} e^{-\frac{T_0}{T}} \frac{k_1^2 (p_1^2 - \left(\dfrac{p_2^4}{K_{eq}}\right)^2)}{(1 + k_1 p_1 + k_2 p_2)^2} \tag{2.1}$$

with the following values of parameters k_1, k_2, K_{eq} and T_0:

$$k_1 = 0.089 \times e^{-\frac{T_1}{T}} Torr^{-1} \quad T_1 = 352K$$

$$k_2 = 0.00152 \times e^{-\frac{T_2}{T}} Torr^{-1} \quad T_2 = 2{,}013K$$

$$K_{eq} = 1.4 \times 10^{31} \times e^{-\frac{T_3}{T}} Torr^3 \quad T_3 = 18{,}800K$$

$$T_0 = 11{,}022K$$

53

2.2 Laser-driven CVD of nickel carbonyl

A vast amount of literature on laser-driven chemical vapor deposition processes has been written since the discovery and commercial availability of practical lasers in the 1960's. Notable book-size reviews were written by Mazumder (*"Theory and Application of Laser Chemical Vapor Deposition"*) [Mazumder and Kar, 1995] and Bäuerle (*"Laser processing and Chemistry"*) [Bäuerle, 2000]. A summary of laser deposition studies, with focus on UV lasers is reviewed in chapter 9 of W. Duley's book *UV Lasers: Effects and Applications in Materials Science* [Duley, 1996]. Infrared laser effects in deposition on substrates and in gas-phase reactions are discussed in chapters 7 and 8 of W. Duley's book *CO$_2$ lasers* [Duley, 1976].

The following summary will focus on a review of laser driven processes applied specifically to nickel carbonyl decomposition. Selected references dealing with the general concept of increased deposition rate by the use of forced gas flow, or gas jet, facilitating improved mass transport of the reactants to the substrate surface, will be also briefly mentioned. The review is organized by the type of deposition process (film growth or gas phase particle formation and growth), with emphasis on film deposition. Further discussion on hetero- and homogeneous decomposition processes can be also found in Section 1.14 of Chapter one.

2.2.1 Heterogeneous decomposition processes

In several published studies describing heterogeneous decomposition processes, some considerably high deposition rates have been reported in literature by authors using laser-driven CVD of Ni(CO)$_4$. The objective was typically the growth of tapered microstructures or nickel rods, spots and lines, targeting mainly electronic circuit patterns and interconnects in large-scale integration circuits. The earliest work with laser-induced decomposition of nickel carbonyl reported in literature appears to have been done at the Centre for Laser Studies (University

of Southern California) by S.D. Allen in 1981, using a 10W, continuous-wave CO_2 laser and several different substrates [Allen, 1981]. Deposition rates approaching 1 mm/min on quartz substrates were observed in growing spots up to ~0.8 mm in diameter at sub-atmospheric pressure (~40 Torr). The thickness of the deposits ranged from ~10 nm to ~1 micron. The films were polycrystalline with a grain size below 10 nm based on SEM measurements.

I.P. Herman and colleagues, working at the Physics department of Lawrence Livermore National Laboratory, published a study describing the deposition of nickel lines on silicon substrate using low concentration $Ni(CO)_4$ (~1.5 vol% in helium) and Ar^+ laser at 514.5 nm [Herman et al., 1983]. The laser was focused to a spot up to 3 μm in diameter. Deposition rates of up to ~100 μm/s (~6 mm/min) were measured using power densities of ~ 5 MW/cm². The published study included a discussion of the theory of laser-induced pyrolytic deposition processes and rate-limiting steps. Kinetic expressions developed by Carlton & Oxley [1967] were used to predict deposition rates as a function of laser power. The rate was found to reach an asymptotic condition where gas diffusion was insufficient to maintain local concentration of reactant at the substrate surface and to disperse the forming CO. Expressed in terms of metal-bearing gas pressure and "effective interaction radius" ρ, the growth rate of the Ni deposit thickness in the mass transport limit was calculated to be

$$u_c \leq 9.1 \times 10^{-4} \frac{p_{1\infty}}{\rho} \left(\mu m / s \right) \qquad (2.2)$$

where $p_{1\infty}$ is partial pressure of $Ni(CO)_4$ far from the location of irradiated laser beam spot (in Torr) and ρ is in cm.

Small spot sizes (or small substrate deposition areas irradiated by a larger laser beam) are thus desirable in order to realize high growth rates. The above expression gives a deposition rate of ~120 μm/s for a 2 μm beam spot size and a 10 Torr carbonyl partial pressure (~1.4 vol % concentration).

Kräuter et al., working at the Johan-Kepler University in Linz, Austria published at least 2 papers on the deposition of Ni from $Ni(CO)_4$ using Kr^+ laser [Kräuter et al, 1983 and Bäuerle, 1983]. Their focus was the growth of microstructures such as Ni rods and stripes on glass, Ni and steel substrates. The deposition rate was found to be independent of the laser wavelength used (476.2, 530.9 and 647.1 nm), but strongly affected by the thermal conductivity of the substrate during the onset of the growth. During the steady-state phase the rate was independent of the substrate and function of laser irradiance, precursor concentration and the physical properties of the deposit, e.g. reflectivity and thermal conductivity. Careful control of laser power allowed the deposition of Ni stripes that were narrower than the diffraction limit of the optical system (1.3 μm vs. 2.5 μm spot size). The highest measured rate in the growth of Ni rods reached values of ~10 μm/s on a steel substrate at 933 mbar total pressure and 400 mbar partial pressure of $Ni(CO)_4$ with He carrier gas. The authors attributed the high deposition rate observations to the extension of kinetically controlled regime to much higher temperatures than in conventional CVD process. This was possible due to the strong localization of heating with laser beam and 3-dimensional diffusion of gas molecules (both precursor and reaction products) to and from the reaction zone.

Bezuk et al. of Unisys Corporation used polyimide substrates to write Ni lines by irradiation with an Ar-ion laser at 514.5 nm at sub-atmospheric pressures (~1-4.6 Torr) in a static chamber [Bezuk et al., 1987]. At low scan speeds (100 μm/s or 6 cm/min), the line shape had rounded cross-section profile, at intermediate speeds the profile was flat, and it became volcano-shaped at high scan speeds of ~200 μm/s. Powder formation was observed at pressures exceeding ~3.5 Torr.

Tonneau of Bertin Technologies in France described the deposition of Ni dots and films on Si-coated quartz substrates by Ar+ laser-induced decomposition of $Ni(CO)_4$ [Tonneau et al., 1988]. The carbonyl pressure was varied between 0.1 and 100 Torr and the deposition was demonstrated to occur via purely pyrolytic decomposition at temperatures between 200 and 400°C. For carbonyl pressures over ~10 Torr, Ni powder and carbonaceous residue formation were observed. The highest measured deposition rate of a metallic film (~200 μm diameter dots) was ~ 2 μm/s (120 μm/min) at 0.7 W laser power and 3 Torr carbonyl pressure.

The same authors reported on the deposition of nickel microstructures by CO_2 laser heating of quartz plates [Tonneau et al., 1989]. The laser power was varied from 0.1 to 3W using ~300 μm spot size. The highest measured deposition rate was 4 μm/s (240 μm/min) at a $Ni(CO)_4$ pressure of 10 Torr and 400°C substrate temperature. The required CO_2 laser power was found to be up to 5x higher than that required by the visible laser light. The higher power was necessary to compensate for the lower substrate heating efficiency due to the high surface reflectivity of nickel at 10.6 μm.

Boughaba and Auvert of Telecom France described the deposition of Ni lines on Si and SiO_2 substrates using cw Ar laser (several wavelengths around 500 nm) at up to 10 mbar pressure, with maximum observed rate of about 4 μm/s (240 μm/min) [Boughaba and Auvert, 1993]. The lines were between 1 and 4 μm wide, controlled by the scanning speed of the beam with optics-adjustable spot size ranging from 1.1 to 4.8 μm. The laser direct-writing technique was aimed at repair and prototype design of microelectronic integrated circuits, facilitating a mask-less process.

Maxwell, Pegna and Hill of the Rensselaer Polytechnic Institute reported growth rates of Ni "rods" up to 18 μm/s (1080 μm/min) using the argon ion laser-

induced pyrolysis of $Ni(CO)_4$ [Maxwell et al., 1995]. Their technique, termed SALD (Selected Area Laser Deposition, or 3D-LCVD) is described as a 3-dimensional mode of pyrolytic LCVD, and is thus akin to the concepts explored in this thesis. The Ni microstructures were ~200 μm in diameter and were grown on graphite substrates using a static fill of the deposition chamber at 200 mbar carbonyl pressure.

2.2.2 Rate increase by high pressure operation

To further increase the heterogeneous deposition rate beyond what is possible by optimized mass transport under kinetic and thermodynamic conditions in vacuum or atmospheric pressure systems, one can operate the deposition system at elevated pressure. Increasing the pressure in the reaction chamber increases the global concentration of the reagent species, hence more precursor molecules are available to react. While no such work has been reported using nickel carbonyl, the principle has been demonstrated on carbon deposition to form C fibres at a phenomenal rate of ~12 cm/s using an Ar^+ laser at pressures up to 1.1 MPa [Maxwell et al., 1999]. More details on the results obtained in this work were included in Chapter one, Section 1.18.

2.2.3 Deposition by laser breakdown

Dielectric breakdown of gas mixtures can be used for thin film CVD with appropriate control of flow and pressure conditions to suppress gas-phase nucleation and particle formation. Work done at Los Alamos National Laboratory in mid-1980's included the deposition of nickel from $Ni(CO)_4$ and molybdenum from $Mo(CO)_6$ by pulsed CO_2 laser forming a reaction zone adjacent to a cold substrate [Jervis, 1984 and Jervis, 1986]. The focused beam of a pulsed CO_2 laser created a region of high electric field sufficient to break down a mixture of metal precursor and a buffer gas, forming a plasma plume up to 1 cm in length near the substrate. The laser was pulsed at 0.5 Hz using a pulse

width of up to 0.1 ms. The metallic film deposition rate on a glass microscope slide substrate was estimated at ~1 nm/pulse. Minimizing turbulence in the area immediately above the substrate was necessary to avoid particulate formation from gas phase nucleation. The overall pressure in the chamber was held in the 10-15 Torr range with carbonyl concentration in the 1-3% range in argon – higher pressures resulted in "copious amounts of powder" and reduced film growth rate. The deposits were found to consist of very fine-grain structures, with a diffracting domain size of ~2.5 nm in the case of nickel.

2.2.4   Homogeneous decomposition processes

Studies of homogeneous decomposition of nickel carbonyl using laser beams are very limited in number in comparison to decomposition studies aimed at growth of films or microstructures. In this case the laser beam is used as a means to provide a tightly controlled residence time and thermal treatment of the carbonyl precursor and Ni particles formed by its decomposition. This facilitates the formation of highly controlled particles (in terms of size and morphology), including nickel nanopowders. The breakdown of the carbonyl molecule can be initiated either directly by photolytic decomposition, targeting CO-Ni bonds (UV lasers), or thermally using a sensitizer gas. The use of a sensitizer gas in the case of visible and IR lasers is necessary because carbonyl IR bands do not coincide with the wavelengths of commonly available, high power lasers. SF_6, ethylene or ammonia can be used with a CO_2 laser. The carbonyl group does have a reasonably strong absorption band close to the most common CO_2 laser wavelength (10.6 μm), and a tunable CO_2 laser tuned to 10.9 μm could be used directly to excite the carbonyl molecule. Unfortunately, the strongest absorption band at 2051 cm^{-1} also just misses the most common CO laser wavelength, rendering the CO laser unsuitable for direct heating of the carbonyl molecule. UV and IR absorption spectra of nickel carbonyl are included in Appendix 1.

The photonucleation technique driven by a XeCl excimer laser (308 nm) was used by He et al. at the Chemical Engineering Dept. of the University of Rochester to produce ultrafine Ni particles [H. He et al., 1997]. The particles were agglomerates consisting of 1 to 5 nm primary particles that analyzed mostly as metallic nickel with minor phases of Ni_3C and NiO. The material was shown to be a particularly active catalyst for ethane hydrogenation.

More recently, the homogeneous laser-driven pyrolysis of nickel carbonyl was demonstrated by a University of Buffalo group led by M. Swihart [Y. He et al., 2005]. A 60 W CO_2 laser was used to initiate the decomposition of a nickel carbonyl-containing gas stream via absorption of SF_6 and C_2H_4 sensitizer gases. A schematic of the reactor system and a photograph of the reactor in operation during the production of Ni nanoparticles are shown in Figure 2.4. The carbonyl vapors were generated in-situ by passing CO over a bed of H_2-reduced Ni powder.
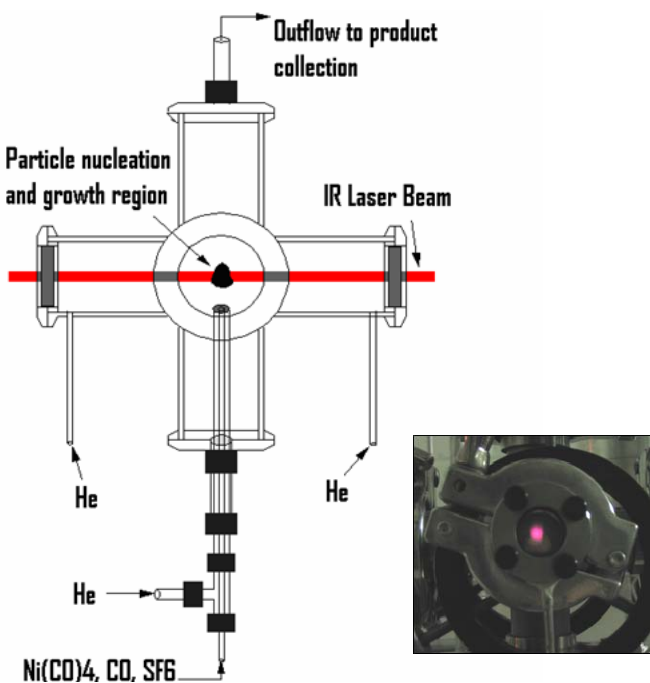
Figure 2.4 Laser pyrolysis reactor for preparation of Ni nanoparticles from Ni(CO)$_4$ (M. Swihart, Univ.of Buffalo)

By varying the precursor flow rate and concentration, the laser energy, the carrier gas flow rate (to control the residence time) and the sensitizer gas concentration, the average particle size could be controlled between 5 and 50 nm. Figure 2.5 shows a TEM image of several Ni and NiF_2 particles prepared by this process. The smallest particles (5-8 nm) exhibited superparamagnetic properties [Sahoo et al., 2005].
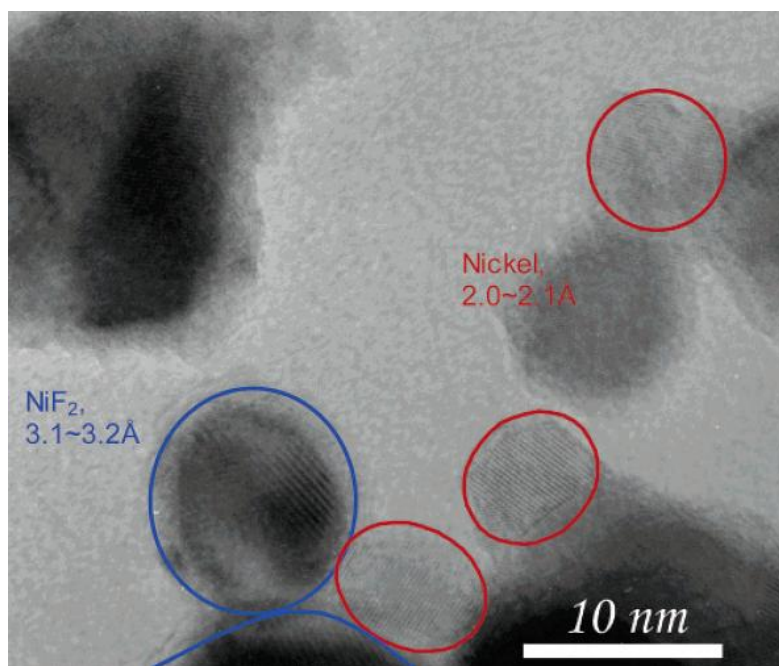
Figure 2.5 Ni and NiF_2 nanoparticles prepared by laser pyrolysis of $Ni(CO)_4$ using SF_6 as a sensitizer gas

Most studies discussing the laser-driven homogeneous decomposition of gaseous precursors are based on small-scale, laboratory systems with focus on the fundamental understanding of the process and resultant product properties. In the late 1990's, a commercial-scale equipment and process have been developed by Nanogram Corporation in San Jose, CA. The key aspects of the technology are described in a US patent by Bi and Kambe, assigned to Nanogram Corp. [Bi and Kambe, 2001]. A schematic of Nanogram's reactor described in the patent is

reproduced in Figure 2.6. This system uses CO_2 lasers and a specially designed elongated reaction chamber to facilitate the production-scale application of a laser-driven process to produce metallic and other nanopowders at a demonstrated rate of up to ~1 kg/hr.
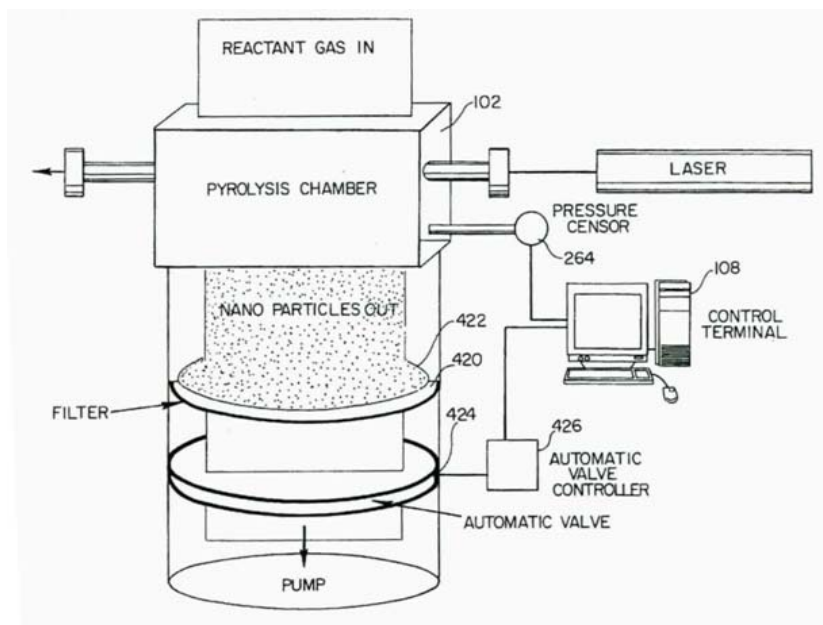
Figure 2.6 Scaled-up laser pyrolysis reactor with ~1 kg/hr production rate
(US patent # 5,958,348)

The topics of homogeneous nucleation and particle growth from nickel carbonyl decomposition in a hot tube aerosol reactor have been recently studied by E. Wasmund as part of his PhD work at Vale Inco and McMaster University [Wasmund, 2005]. The thesis includes a comprehensive literature review of past nickel carbonyl kinetic studies and proposed mechanisms.

Table 2.1 summarizes published reports dealing with heterogeneous laser-driven deposition of Ni from a nickel carbonyl precursor. Key parameters from each reference, including the maximum achieved specific deposition rates, are listed in the table.

Table 2.1   Summary of literature references on heterogeneous laser-driven deposition of Ni from Ni(CO)$_4$

Author	Publication date	Laser source	Power density used W/cm^2	Beam area (spot size, cm^2)	Substrate	Reactor Pressure mbar	Type of deposit	Reported max. deposition rate microns/min	Comments
Allen et al. USCLA	1981	10W cw CO$_2$ 10.6 μm	~440	0.01	quartz	53	Ni spots	~ 1000	
Herman et al.	1983	0.6W Ar$^+$ 514.5 nm	4.8 x 10^6	0.0000003	silicon	936	Ni lines	~6000	
Kräuter, Bäuerle J. Keppler Univ., Austria	1983	20 mW cw Kr$^+$ 530.9 nm	100,000	0.0027	steel, Ni, glass	933	Ni rods	~ 600	
Bezuk et al. Unisys Corp	1987	1W cw Ar$^+$ 514.5 nm	0.9 x 10^6	0.0000011	polyimide	1.3 – 4.6	Ni lines	~ 60	
Tonneau et al. Bertin Tech.	1988	5W cw Ar$^+$ 488 - 514 nm	10,000	0.0003	Si-coated quartz	up to 13	Ni dots and films	~ 120	powder observed at > 13 mbar pressure
Tonneau et al. Bertin Tech.	1989	3W cw CO$_2$ 10.59 μm	4,244	0.0007	quartz	up to 13	Ni dots and films	~ 240	Carbonaceous deposit observed at > 13 mbar pressure
Baughaba et al. France Telecom	1993	5W cw Ar$^+$ 488 - 514 nm	27 x 10^6	0.0000002	silicon	20	Ni lines	~ 240	laser 'direct writing', scanning beam
Maxwell et al. Rensselaer Polytechnic	1995	8W Ar$^+$ 488/514 nm	0.4 x 10^6	0.00002	Graphite Alfa/Aesar #10832	200	Ni rods	1080	
This work	2009	480W cw diode 807 nm	up to ~ 400	up to 60	PU and Ni foams	atm..	large area, porous 3D structure	~ 20	3-D porous substrates

2.3   Transport phenomena in laser-induced CVD

Several authors reviewed the role of mass transport in laser-induced chemistry. [Kodas and Comita, 1990; Kleijn, C.R., 1991]   Transport processes can in general occur by a molecular bombardment (ballistic) mechanism in a free-molecular-flow regime, or by a diffusive mechanism in the viscous-flow regime.   The relative importance of the two mechanisms depends on the Knudsen number, Kn, representing the ratio of the gas mean free path to the characteristic dimension of the system. With the mean free path at atmospheric pressure of the order of sub-micron and system dimension of the order of mm (substrate foam cell structure), the Kn<<1, meaning that the transport occurs mainly by diffusive mechanism.   In this case, physical processes such as diffusion of reactants and products, surface reactions, gas-phase cluster formation and free and forced convection can all influence the reaction rate.   For sufficiently rapid surface reaction, concentration gradients exist in the gas phase and deposition rate is limited by the rate of mass transport in the gas phase.   The deposition rate expression for a spherical deposit for the case of thermal CVD and diffusion-dominated regime is given by [Kodas and Comita, 1990]:

$$\frac{da}{dt} = \frac{D_{AB} v_1 p_1}{akT} \tag{2.3}$$

Here, a is the radius of the deposit, D_{AB} is the binary diffusion coefficient, v_1 is the volume of an atom in the deposit, p_1 is the partial pressure of the precursor gas, and kT is the molecular energy.   Note that the temperature is in the denominator – this pertains strictly to mass transport aspect of the process and is unrelated to the deposition process chemical reaction kinetics (Arrhenius relation).

Diffusive transport can strongly influence the morphology and shape of deposits by controlling the rates of growth.

Substantially different growth rates can be found within the reaction zone, resulting in irregularly shaped deposits. For example, Figure 2.3 shows gold crystallites produced under diffusional transport regime, which were found growing out radially from the nucleation site. The sample was prepared by an LCVD process using organometallic gold precursor in the

Figure 2.3 An LCVD deposit of gold under conditions of diffusional transport produced in the presence of oxygen additive

presence of small additions of oxygen [Kodas et. al, 1988]. The "buffer" gas (oxygen) effectively shortened the mean free path of the reactant, which was otherwise longer than the characteristic dimension of the deposit (at 0.35 Torr in a background pressure of 10^{-6} Torr). Without the buffer gas, the deposit was uniformly bombarded by reactant molecules and assumed a smooth, hemispherical shape of a diameter determined by the laser spot size. Upon addition of the buffer gas the deposition rate became mass-transport limited and fewer reactant molecules reached the centre of the deposit compared to the tips of the crystallites, which the reactant molecules reached first.

The same mechanism is believed to be responsible in the formation of highly textured deposits observed in the nickel carbonyl deposition under certain process conditions.

2.4 Gas-jet LCVD

A gas-jet or *forced flow* reactant delivery system is expected to aid the mass transport of reagent gases to the deposition zone, thus increasing the deposition rate. The study of gas-jet effects in LCVD processes was the focus of recent

work conducted at the Georgia Institute of Technology [Lackey et al., 2002 and Duty, 2001]. A high-velocity gas jet was used to deliver reagent gases directly to the substrate surface (Figure 2.7). By creating a forced flow environment, the momentum and concentration boundary layers were decreased, aiding diffusion and shifting the reaction rates closer to the kinetically limited range. The forced convection cooling was significant, accounting for up to 20% change in substrate temperature under the specific conditions used in the study. To minimize the cooling effect, the gas was pre-heated just prior to entry into the reaction chamber. The forced flow was found to effectively increase the concentration of reagent gases at the substrate surface, thus increasing the deposition rates.
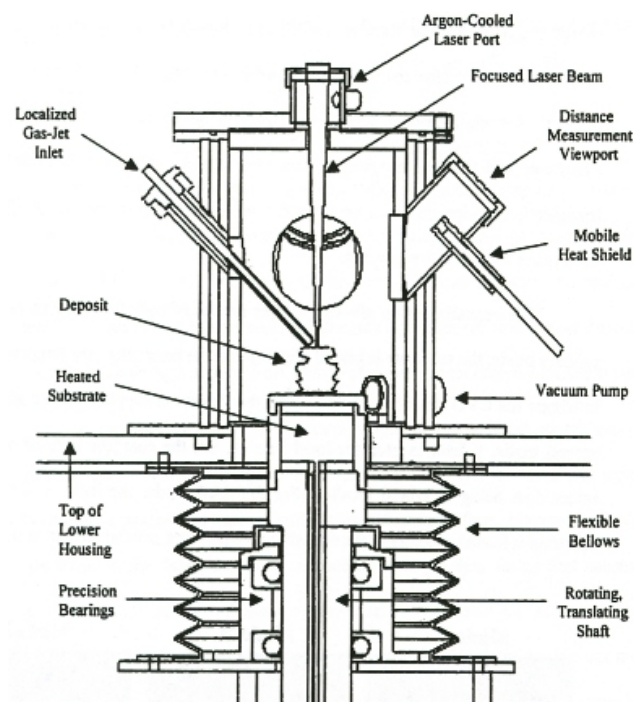
Figure 2.7 Schematic of the gas-jet LCVD chamber at Georgia Inst. of Technology

2.5 Studies in LCVD deposit morphology and process modeling

Modeling of thin film growth and morphology development effects applicable to laser-driven vapor deposition processes have been addressed in a number of papers and books.

A model that included solid-phase heat transfer, gas-phase heat and mass transfer and the transient film growth was described by Skouby and Jensen, using nickel from nickel carbonyl and a Gaussian-shaped CO_2 laser beam as a case study [Skouby and Jensen, 1987]. Volcano-like deposits were predicted for some combinations of conditions, with the following four possible causes playing a role in forming such morphology: (1) depletion of reactant molecules in the beam centre; (2) Stefan flow, in which case product molecules create a net convection away from the surface; (3) thermal diffusion, causing the diffusion of the larger reactant molecules away from the hotter beam centre, and (4) kinetics with a local maximum with respect to temperature. The dominant effects resulting in volcano-type morphology were either local reactant depletion or absorption-desorption effects linked to non-linear, Langmuir-Hinshelwood kinetics commonly found in decomposition of organometallic compounds.

Bates et al. [1989] used a growth dynamics model to show how diffusion (mass transport) and reaction kinetics effects can give rise to various observed deposit morphologies. Their model is further discussed in Section 4.4.1.

2.6 Metal foams literature review

The science and technology of metal foams have been reviewed in the book "Metal foams design guide" by M. Ashby and collaborators [Asby et al., 2000]. The text covers the preparation methods, structural and property characterization, constitutive model discussion and a number of application fields, with emphasis on exploiting the unique mechanical properties of metal foams. Another book-size coverage of the topic was published under the title

"Handbook of Cellular Metals: Production, Processing, Applications" [Degischer and Kriszt, 2002].

A comprehensive review of metal foam preparation and manufacturing methods was published by H. Wadley [2002]. The CVD deposition onto polyurethane foam substrates is described as "templated condensation". Figure 2.8 is a graphical representation of the various manufacturing routes for metal foams taken from this reference.
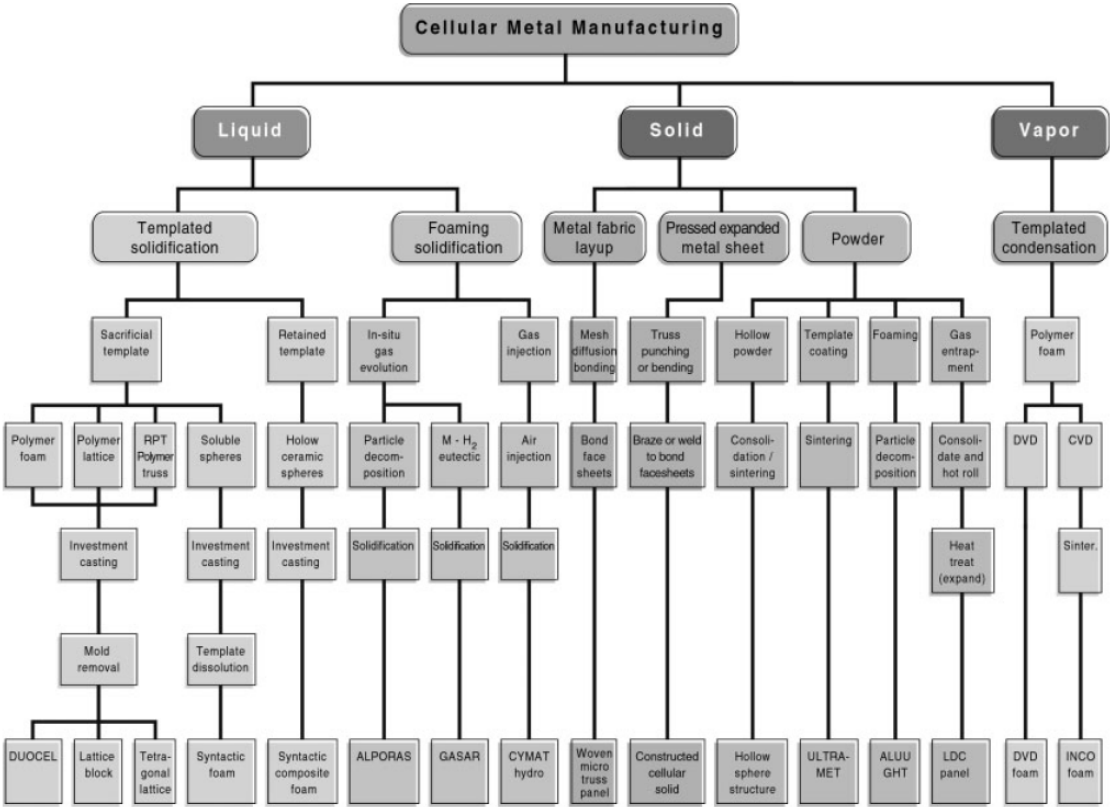
Figure 2.8 Taxonomy of cellular metal manufacturing processes [Wadley, 2002]

2.6.1 Literature on mass and heat transfer in metal foams

Forced convection in high porosity metal foams was studied experimentally (using air as the fluid medium) and by numerical modeling by Calmidi and Mahajan [2000]. They found that the predominant mode of energy transport from the heated surface (attached to the foam sample by brazing electric heaters to one surface of the foam) to the fluid (flowing across the foam in a direction parallel to the heated side) was by conduction through the solid metal foam phase and interfacial heat transfer from the solid to the fluid phase. Similar study was conducted by E.C. Ruiz, who also provided comprehensive literature review on heat transfer in porous media of metallic foams [Ruiz, 2004]. An obvious application built on the high gas permeability and good heat conductivity of the metal foam skeleton is in compact, high performance heat exchangers. This application was reviewed by Boomsma et al. [2003]. The pressure drop in a porous media such as metal foams is given by the quadratic-extended Darcy flow model:

$$\frac{\Delta P}{L} = \frac{\mu}{K}V + \rho CV^2 \qquad (2.4)$$

where ΔP is the pressure drop across the medium, L is the length of the medium in the flow direction, V is the "clear channel" (Darcian) fluid velocity, K is the permeability of the medium, μ and ρ are the dynamic viscosity and density of the fluid, respectively, and C is the coefficient related to the structure of the porous medium. The overall effective thermal conductivity of the solid-fluid system, k_{eff}, can be described by the porosity ε and conductivities of the solid and fluid phases k_s and k_f, respectively:

$$k_{eff} = \varepsilon k_f + (1-\varepsilon)k_s \qquad (2.5)$$

The open cell metal foam structure was described as having the desirable qualities of a "well-designed heat exchanger" – high specific solid-fluid interface surface area (for samples used in this work this value was ~5,000 m^2/m^3), good thermally

conducting solid phase (k_s for Ni at room temperature is ~91 Wm^{-1}K^{-1}), and a tortuous coolant flow path to promote mixing and heat transfer.

3 EXPERIMENTAL

3.1 Deposition system design and assembly

The deposition system used in this work consisted of a stainless steel cylindrical chamber (16.2 cm diameter, 8.4 cm deep, internal volume 1.73 l), a gas delivery system, 2 high-power diode laser heads, and an offgas handling system. The chamber and laser heads were mounted inside a metal enclosure providing added safety for the operation of the diode lasers. Figures 3.1 and 3.2 show the system enclosure, cylindrical reactor and the 2 high-power diode laser heads shortly after the initial system assembly.

Figure 3.1 Laser CVD system enclosure

Figure 3.2 LCVD cylindrical reactor system shown shortly after assembly

A schematic diagram of the equipment is shown in Figure 3.3. Nickel carbonyl was supplied by bubbling CO carrier gas through a volume of liquid nickel carbonyl stored in a 2-litre autoclave at room temperature. A Bomem FTIR spectrometer with a 19 cm flow-through cell connected to the reactor exit line was used to monitor the gas composition during each experiment. The large reactor windows provided good visibility inside the chamber, and an external video camera aimed at the substrate location was used to capture the progress of most experiments. A photograph of the overall deposition system taken later in the project showing the reactor system, laser heads, gas control panel and the Bomem FTIR analyzer is in Figure 3.4. The system was located in the Carbonyl II laboratory of Vale Inco Technical Services Limited, the corporate research facility of Vale Inco located in Mississauga, Ontario. The laboratory was equipped with a sensitive environmental monitoring system necessary for safe operation of the equipment handling the highly toxic nickel carbonyl.
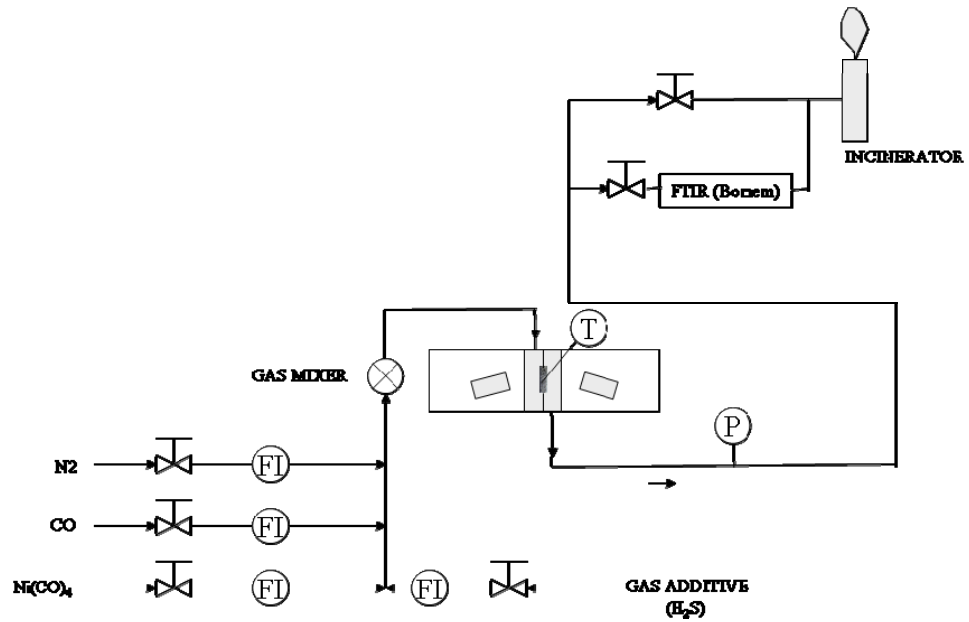
FI – flow indicator   P-pressure gauge   T-thermocouple   FTIR-gas spectrometer

Figure 3.3 Schematic diagram of the laboratory deposition system

Figure 3.4 Overall deposition system layout

The chamber windows were circular panes with a diameter of ~18 cm made of 3/8" thick quartz glass and sealed with Viton o-rings. The integrity of the seal was verified prior to each experiment by pressurizing the entire system to 5 psi and verifying that there was no appreciable pressure drop over a 60-minute time period. The substrate temperature was measured by one or two K-type thermocouples lightly pressed into the foam surface. Gases were metered by rotameters and a gas mixing chamber provided mixing of up to four gas components: nickel carbonyl/CO mixture, CO dilution gas, catalyst gas and nitrogen for purging. The off-gas was processed through a set of secondary decomposers heated to ~ 400 °C and finally a high-temperature incinerator ensuring that any traces of unused nickel carbonyl were destroyed.

3.2   High power diode laser system

A high-power diode laser purchased from Nuvonyx Inc.[3] was employed to deliver the required infrared energy to the substrate surface inside the CVD chamber. The laser consisted of two laser heads containing four high-power (60 W) laser diodes each, for a total power of 480W (Figures 3.5 and 3.6). The laser heads were oriented at an angle to avoid directing their beams at each other due to the semi-transparent nature of the porous substrate. In the initial configuration, two pairs of lenses providing horizontal and vertical beam control and a diffuser plate were used to homogenize the beam to a rectangular diverging pattern designed to illuminate a 4 x 15 cm sample area inside the chamber. Figure 3.6 shows the laser beam profile measured at 125 mm working distance. The beam profile was matched to the size of the opening in a sample holder mounted vertically inside the cylindrical plating chamber. The laser was used in this configuration for the initial set of experiments (Phase I), until it became

---

[3] Nuvonyx Inc. was acquired by Coherent Inc. in April 2007

apparent that the deposition rate could be further increased by increasing the laser beam power density and using higher gas flows.
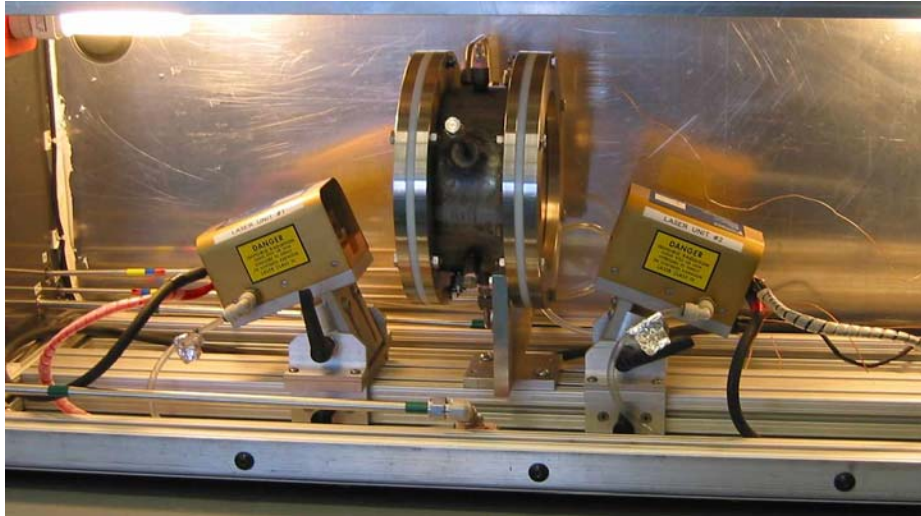
Figure 3.5 Nuvonyx laser setup and cylindrical deposition chamber inside a safety enclosure

Beam profile obtained by combination of lenses shown (measured at 125 mm working distance)

Diffuser plate

Horizontal beam shape control lenses

Vertical beam shape control lenses
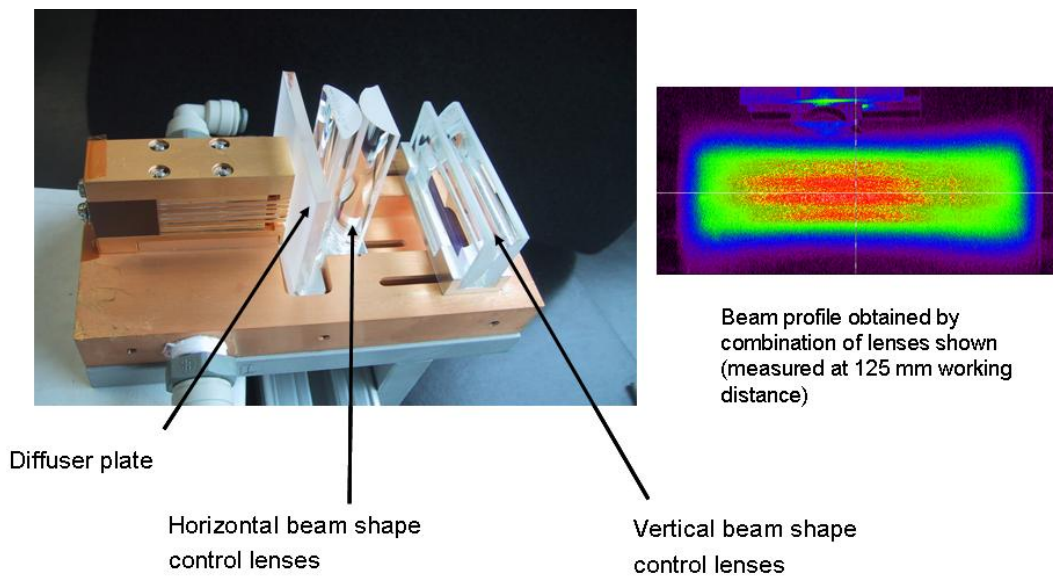
Figure 3.6 Laser head optics and beam profile at 125 mm working distance

3.2.1 Beam quality control

A typical high-power diode laser beam has a diverging slow (horizontal) axis with a ~5° angle and fast (vertical) axis with a ~20° divergence, as illustrated in Figure 3.7.
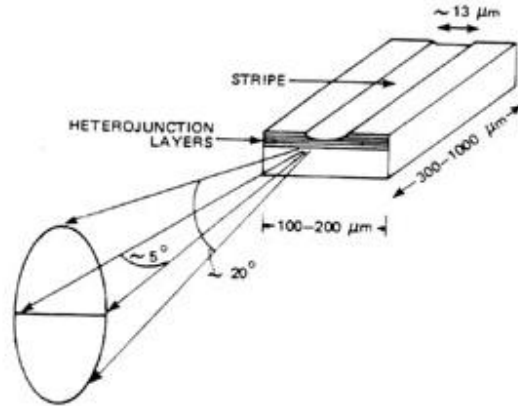
Figure 3.7 Diode laser bar beam geometry

Thus, a major drawback of a diode laser system in direct heating applications is the poor uniformity of the radiation intensity distribution at the irradiated area. With no means to adjust the distribution, the diodes produce severely diverging beam, as shown in Figure 3.7. The manufacturers often install micro lenses in front of the diode arrays, as illustrated in Figure 3.8. This provides some degree of fast axis collimation. A variety of additional
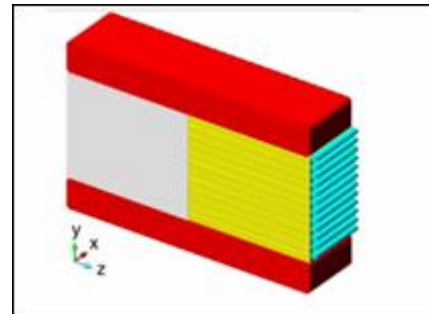
Figure 3.8 Diode laser stack with fast axis collimation (y-axis)

techniques are used to achieve the desired beam shape and quality. In this work, a combination of a homogenizer (sand-blasted quartz plate) and 2 pairs of cylindrical lenses were used to produce a large (~4x15 cm) and relatively uniform

rectangle of laser light. While not perfect, the beam resulted in a production of reasonably uniform Ni deposits of similar size. An example of the intensity profile at the edge of the beam of the 4 diode bars imaged on the View-It[®4] ceramic plate is shown in Figure 3.9. The shape of the individual beam components from the 4 laser bars is clearly visible. Another image of the laser beam profile (supplied by the laser manufacturer) is shown in Figure 3.6.

Figure 3.9 Part of the laser head beam with beam-shaping optics and homogenizer installed and imaged on the View-It® ceramic plate

3.2.2   High power diode laser construction

High-power diode lasers are usually produced in the form of ~10 x 0.6 mm bars comprising from 20 to 60 monolithic groups of up to 20 parallel, single-laser stripes. The bars are normally attached to a heat sink designed to remove excess heat. As of 2009, the output power per bar has reached 200 W (www.coherent.com and www.bookham.com). By stacking many bars, optical output power in the kilowatts range can be achieved. Stacked arrays with

---

[4] View-it® plate is made of a white ceramic material with non-linear optical properties allowing direct viewing of otherwise invisible, 807 nm diode laser IR radiation (available from KENTEK Corp.).

installed micro-optics are pushing power densities to the 10^5 W/cm^2 level, with the prospect to reach the MW/cm^2 level in the future [Diehl, 2000]. QCW power levels of 200W per bar are now available (e.g. from Jenoptik Laserdiode GmbH and Bookham Inc).

The Nuvonyx semiconductor lasers are fabricated using Metal Organic Chemical Vapor deposition to epitaxially grow InGaAsP multilayer structures. A Single Quantum Well (SQW) active region centered inside a separate confinement heterostructure forms the gain medium of the device. Semiconductor processing of the epitaxial wafer is accomplished in a full wafer format with automated processes typical of the silicon integrated circuit industry. Individual laser diode bars are cleaved from the processed wafer, optically coated, and packaged using robotic assembly methods. The laser diode bar used in the experiments described in this work consisted of 49 optically independent emitters, each 100 microns wide on 200 micron centers; spaced across a 1 cm wide bar. Each stripe operated in a single transverse (perpendicular to the plane of the active region) mode but in a multitude of lateral (parallel to the plane of the active region) and longitudinal modes. The individual emitters were incoherent. Each stack of diode laser bars was packaged in a copper block for electrical contact and heat removal. The active region is a very thin section through the InGaAsP semiconductor laser bar, parallel and close to the plane of the package anode.

The diode laser bar performance is accomplished through the use of the Nuvonyx Inc. micro-channel cooler system [Allen et al., 1983]. Cooling is provided by de-ionized, oxygen free water. Figure 3.10 is a photograph of one of the bars showing the main current contacts at the back and mounted on the microchannel cooler block, with optics components installed in front of the stack.
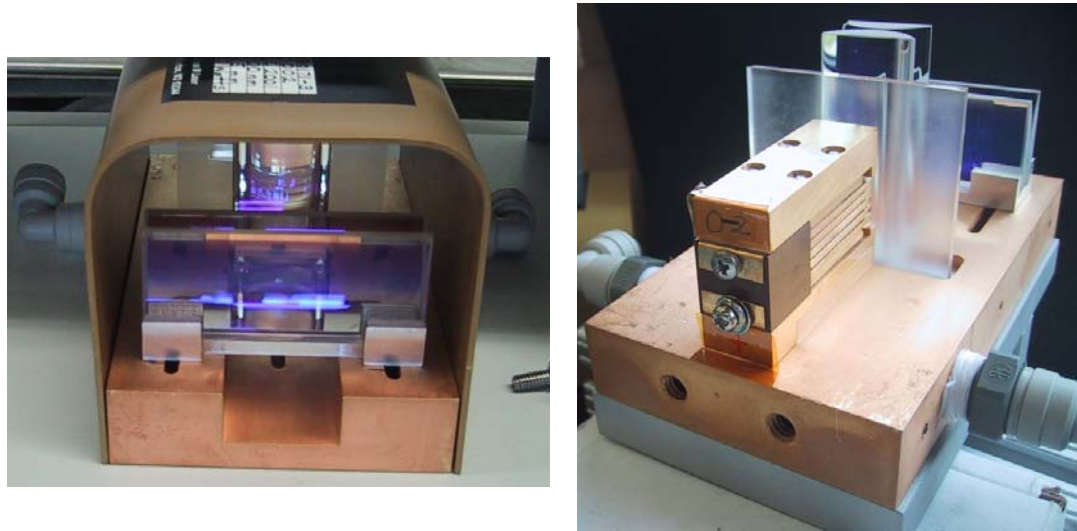
Figure 3.10   Nuvonyx 240W laser head mounted on a micro-channel cooling block

A schematic of the basic laser diode package is shown in Figure 3.11. The diode laser spectral distribution is centered at approximately 807 nm and has a FWHM about ~5 nm (Figure 3.12)
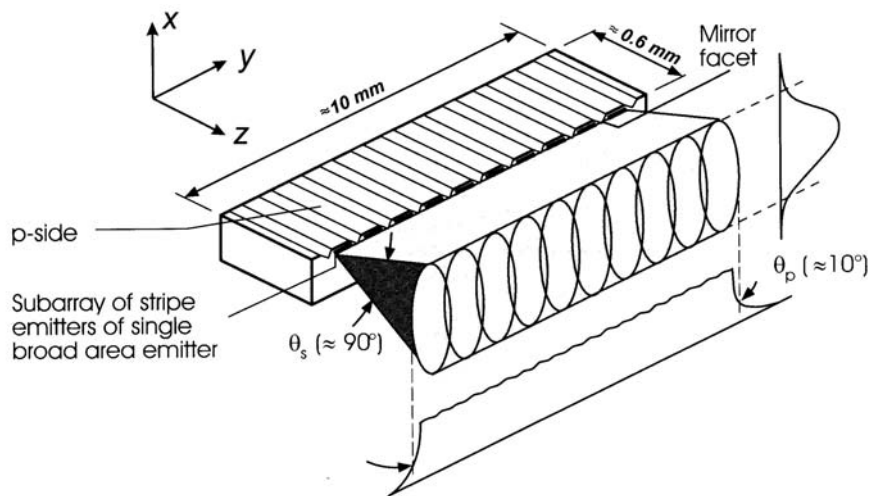
Figure 3.11   Diode laser array

79
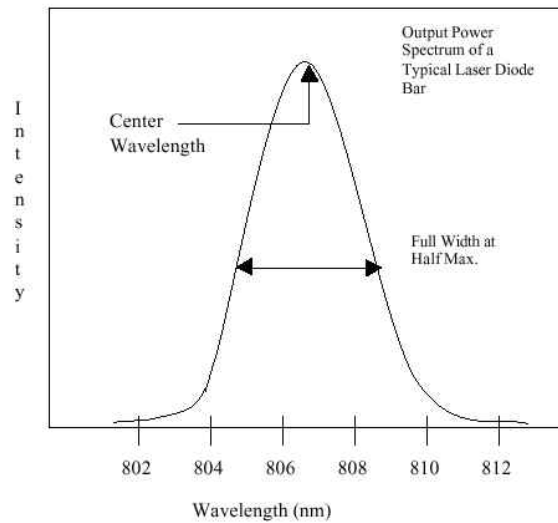
Figure 3.12 Typical diode laser power spectrum (data supplied by Nuvonyx)

3.3   Laser power calibration

Figure 3.13 shows the calibration data for the diode lasers used in this work. The lasing threshold current was about ~ 12 A. The manufacturer's calibration was done with both lenses and beam diffuser in place.
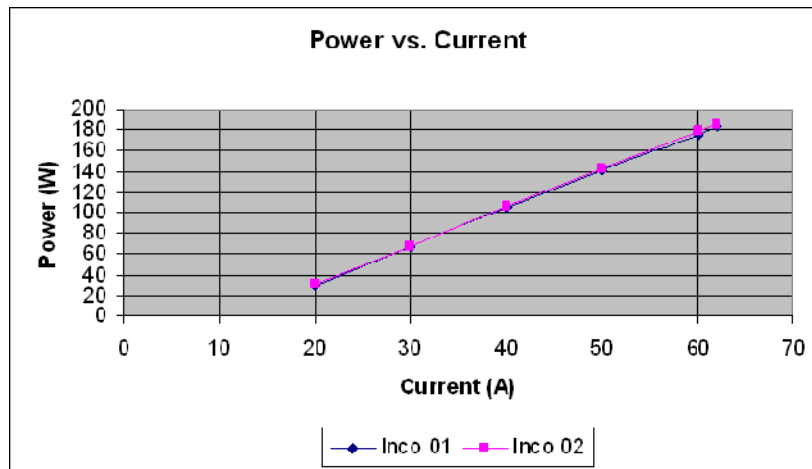
Figure 3.13 Manufacturer-supplied power calibration data for the Nuvonyx laser used in this work

3.4 Sample holder configurations

The sample holder was designed to provide a cross-flow configuration during the experiments, effectively dividing the deposition chamber into 2 parts: gas inlet side and gas exit side. The original sample opening had a circular shape with ~13 cm diameter, resulting in relatively low gas velocities (< 2cm/s) and significant inter-mixing occurring between the 2 sides of the chamber. In order to intensify the local flow conditions and provide laminar flow, the sample opening was decreased in size in several steps, until it assumed the final dimensions of 2x2 cm. Photographs of the sample holders used throughout the project are shown in Figures 3.14 to 3.19. Table 3.1 provides more information for each configuration, including the run numbers corresponding to commissioning of the new sample holders, basic geometry and flow parameters.

Phase I
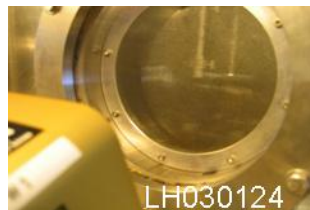
Figure 3.14 13 cm diameter sample holder, highly non-uniform flow.

Figure 3.15 4x15 cm sample holder, non-uniform flow.
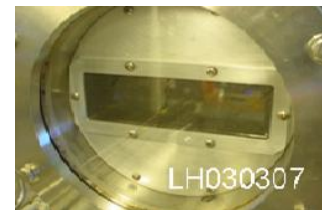
Figure 3.16   4x13 cm sample holder, non-uniform flow.

Phase II

Figure 3.17 2x10 cm sample holder,
improved flow uniformity
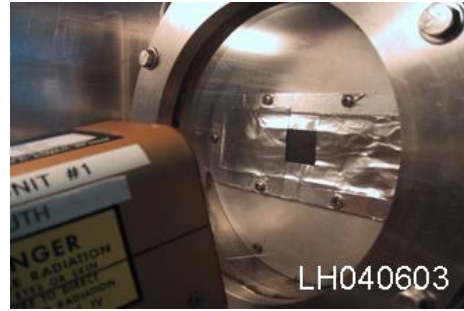
Figure 3.18 2x2 cm sample holder,
uniform uni-directional flow.

Phase III

Figure 3.19 Improved 2x2 sample holder, uniform uni-directional flow

Table 3.1 Average gas velocities in the sample opening

Figure #	First expt.	Sample area (cm²)	Aver. gas velocity (cm/s) @ 6 l/min flow	Comment
3.14	LH030124	133	0.75	circular opening / sample holder
3.15	LH030219	60	1.67	rectangular sample holder
3.16	LH030307	52	1.92	
3.17	LH040510	20	5.0	
3.18	LH040603	4	25.0	laser lenses removed
3.19	LH041006	4	25.0	improved version of 3.18

3.5 Reagent gases and substrate materials

Table 3.2 lists the gases used in the experiments, their purity and supplier. The nickel carbonyl was produced in the laboratory by reacting fine nickel powder (Inco S-grade) with carbon monoxide at ~70°C and ~100 psi pressure in a miniplant-scale carbonyl generator system designed for this purpose. The laser reactor was thoroughly purged before and after each experiment with nitrogen obtained from a laboratory liquid nitrogen central storage tank.

Table 3.2 Reagent gases used in experiments

Gas	Purity	Supplier
CO	99.9	Air Products
H_2S	99.9	Air Products
N_2	from liq. N_2 (<5ppm O_2)	Praxair
$Ni(CO)_4$	synthesized on-site using Inco carbonyl Ni powder	Vale Inco

The substrates used to prepare most of the Ni foam samples in this study were either open-cell, dark color, reticulated polyester polyurethane foam of grade "Bulpren S" produced by the Belgian company Recticel BLV, or Ni foam produced by electroplating at Vale Inco's IATM Dalian Foam plant in China. The polyurethane foam had ~90 ppi cell size (using North-American "pores per inch" scale, corresponding to approximately 500 μm 3-D cell diameter), and was 1.7 mm thick with an area density of 5.5 mg/cm^2 (55 g/m^2). In order to improve thermal absorption of the foam surface, the foam was pigmented to a charcoal-grey color by the supplier.

The thermal stability of the PU material is important in the pyrolytic CVD process. A thermal gravimetric analysis (TGA) of the PU foam material measured in helium atmosphere shows that it is thermally stable up to about 250°C (Figure 3.20).
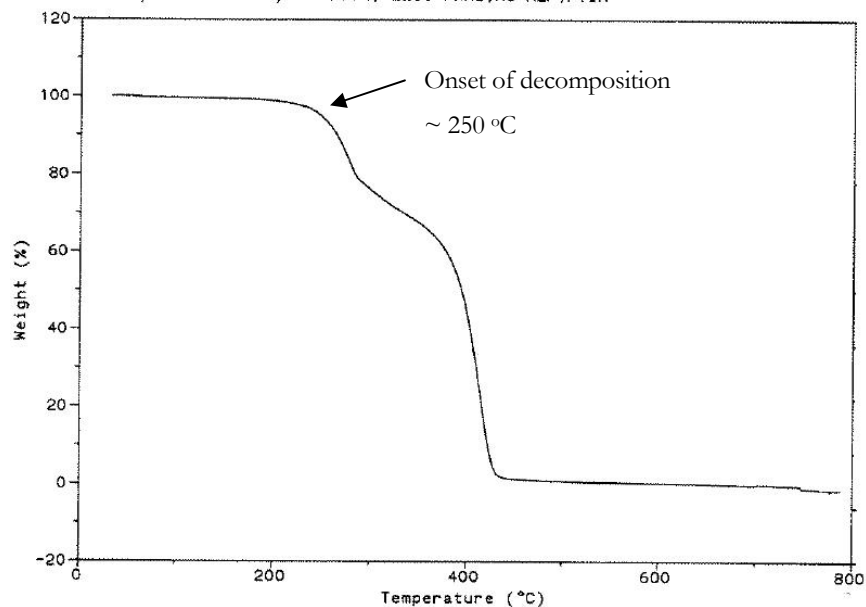
Figure 3.20   Thermal Gravimetric Analysis of PU foam sample in helium

The nickel foam substrate was a standard battery-grade foam with ~650 μm cells, 1.7 mm thick and ~420 g/m² nominal areal density.

Some experiments were done using a small selection of other specialty substrates and are discussed in Section 3.18.   A summary of all substrates used in the experiments is in Table 3.3.

Table 3.3 Substrate material data

Material	Sample ID	Typical size	Vendor
Polyurethane foam	VM4302M Bulpren S	4x13 cm	Recticel Belgium
Ultra-fine PU foam		4x13 cm	Corpura Corp. / Recticel
Ni foam		4x13 cm	IATM Dalian (Vale Inco China)
Carbon nanotubes			Univ. of Aveiro Portugal
Graphite foil	10832	4x13 cm sheet	Alfa –Aesar

3.6   Phase I experiments – polyurethane substrate

In a typical deposition experiment on PU substrate during Phase I experiments, the plating gas was introduced into the chamber and allowed to reach steady-state conditions by monitoring the exit gas concentration using the FTIR spectrometer. The laser was then set to a low power (25A or ~100 W) to produce an initial deposit (up to ~3 microns thick) on the polymer substrate. The surface temperature measured by the contact thermocouple reached approximately ~150°C at this stage. The pre-plate stage typically lasted 40 seconds.   At this point, the substrate was fully covered by nickel and the temperature was raised to a higher value to increase the deposition rate. The laser power was raised to ~200-280 W (depending on the gas flow and sample geometry used) and deposition continued until the desired density was reached (typically 60 seconds).   Graphs showing temperature, laser power profile and exit gas concentration during a typical deposition experiment starting with a PU foam substrate are shown in Figure 3.21.
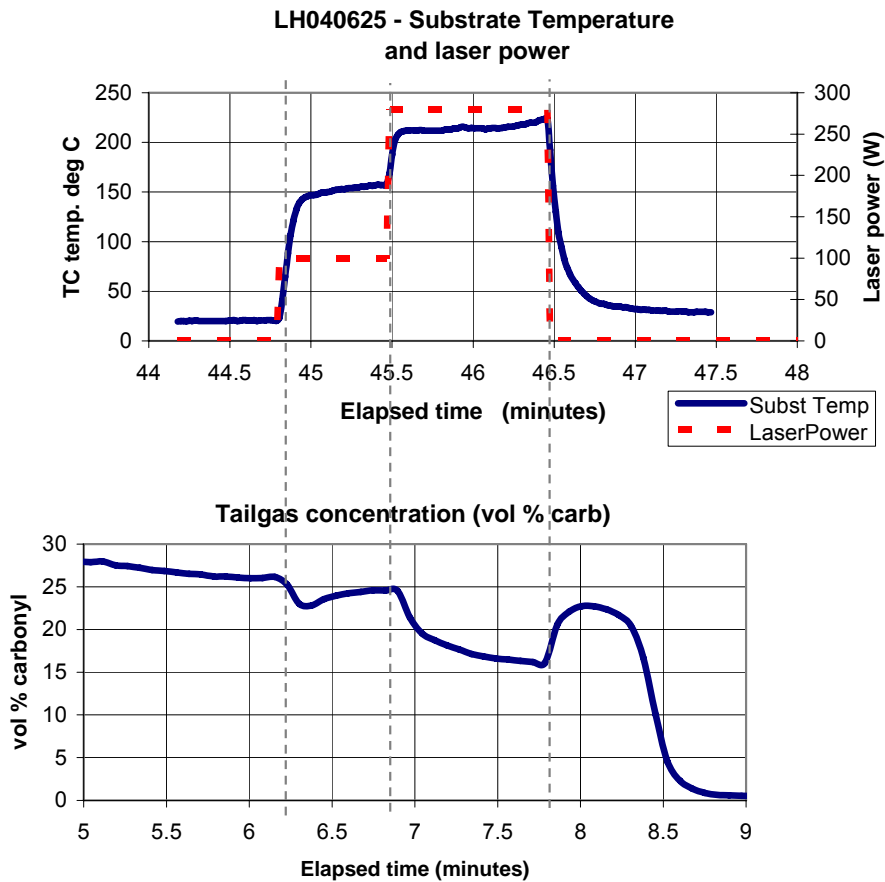
Figure 3.21 Temperature, laser power and exit gas concentration profile during a typical deposition experiment starting with PU substrate

Figure 3.22 shows the chamber with a 4 cm x 13 cm sample opening and the installed substrate before and after the deposition experiment. The uncooled quartz window was completely clear after the experiment, indicating that its temperature remained below the onset decomposition temperature of nickel carbonyl gas ($\sim100^{\circ}$C).
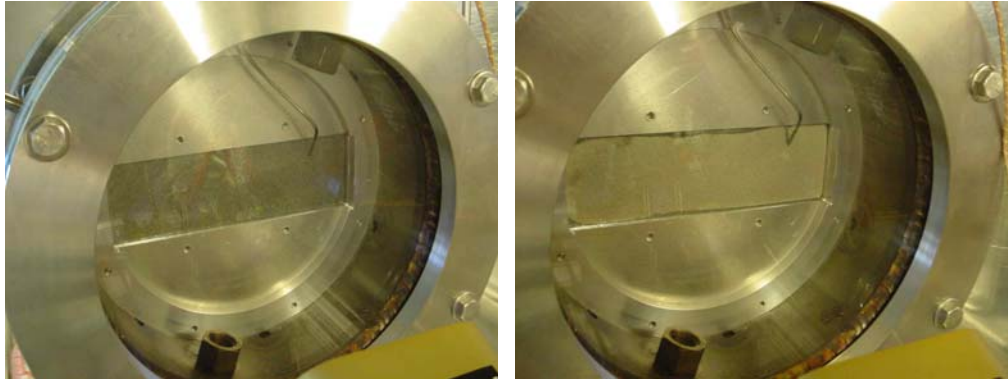
Figure 3.22   CVD chamber with 4x13 sample opening and PU substrate before (left) and after (right) Ni deposition experiment

3.7   Gas delivery system

In the conventional foam CVD process, the precursor gas is introduced in the deposition chamber with no provision to effectively reach the middle part of the porous substrate (Figure 3.23, left sketch).   The process thus becomes mass transport-limited at a relatively low deposition rate of ~1.5 μm/min, particularly within the foam interior.   A cross-flow gas delivery system was employed in the laser deposition experiments to enhance the delivery of unreacted nickel carbonyl throughout the 3-D foam structure.   In this regime, substantially all plating gas is passed through the porous substrate (Figure 3.23, right sketch).   The sample holder with adjustable sample opening effectively acts as a dividing wall.   The cross-flow arrangement is essential for achieving high deposition rates and contributes significantly to the across-thickness uniformity of samples prepared at high deposition rates.
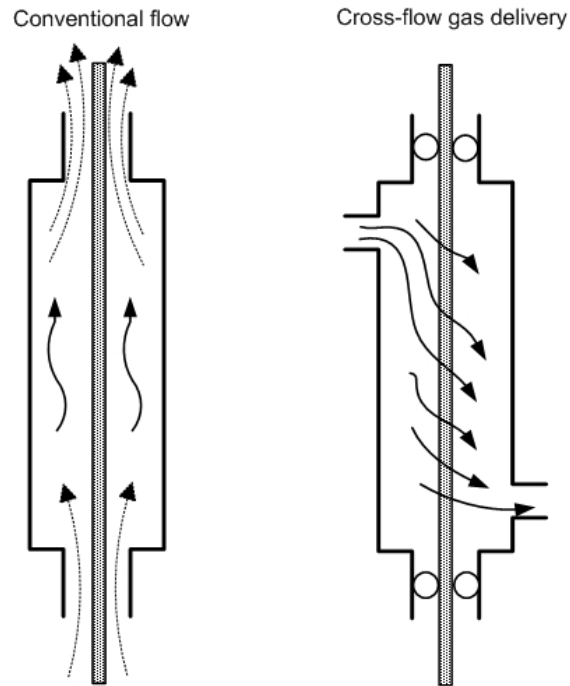
Figure 3.23 Conventional (left) and cross-flow (right) deposition chamber configuration

To maximize the deposition rate and to achieve acceptable 3-D deposit uniformity, the laser power (substrate surface temperature) must be balanced with adequate precursor gas flow to the chamber. An illustration of unbalanced conditions is shown in Figure 3.24 where a highly non-uniform deposit is visible on the gas inlet side. This sample was produced with a feed gas flow of 4.7 l/min (corresponding to 1.5 cm/s local gas velocity) and a final laser power of 220 W using the 4x13 cm sample opening. For this combination of gas flow and laser power, higher Ni density and nodular growth were observed on the gas inlet side of the sample, indicating that the gas was substantially depleted of Ni by the time it reached the second surface of the sample on the gas exit side. The average measured deposition rate was 2.1 μm/min.

Figure 3.25 shows a cross-section of a sample of Ni foam produced with a feed gas flow rate of 8.7 l/min (or 2.8 cm/s gas velocity, same gas concentration) and 220 W final laser power, using the same 4x13 cm sample opening. The average deposition rate obtained under these conditions was ~2.5 μm/min. In this case the deposit was uniform, indicating a sufficiently small concentration gradient across the sample thickness. The reaction remained in the kinetic control regime, while in the previous case (4.7 l/min gas flow or 1.5 cm/s gas velocity) the reaction became mass transport limited.
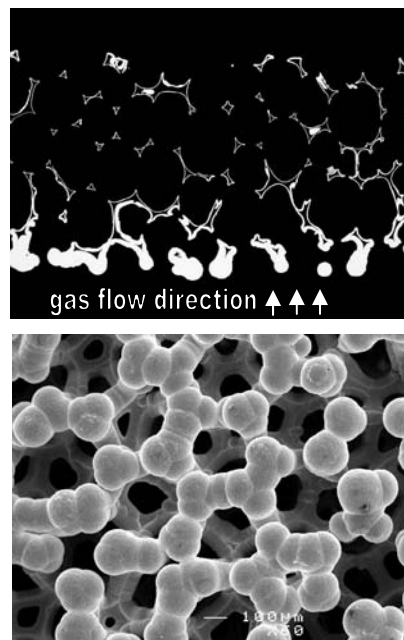
Figure 3.24 Highly non-uniform deposit produced at 220W and 4.7 l/min feedgas flow (expt. LH030321)
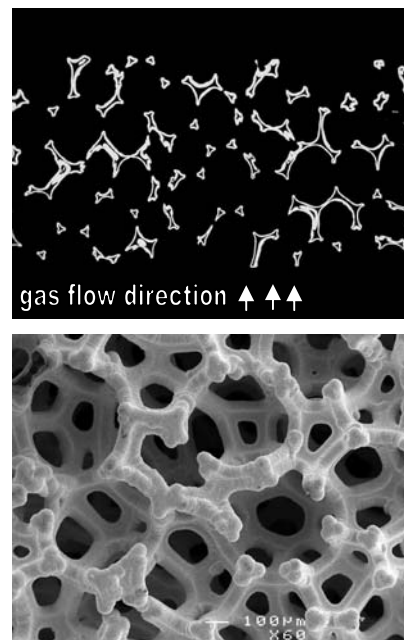
Figure 3.25 Uniform deposit at 220W and 8.7 l/min feedgas flow (expt. LH030328)

In both cases the deposit morphology showed a relatively smooth surface, suggesting that even higher rates were possible. An indication of a practical deposition rate limit is the onset of dendritic growth, signaling free-space decomposition of nickel carbonyl.

3.8 Phase II and III experiments – deposition system improvements

At this point, the benefits of precursor gas cross-flow and an external infrared laser energy source had been demonstrated by more than doubling the specific deposition rate as compared to the conventional process and by uniform deposit distribution in the foam samples. However, it was felt that the system was capable of considerably higher performance if both the mass transport and the delivered energy density could be further increased. This was accomplished by decreasing the size of the cross-flow sample opening (thus obtaining a higher gas velocity across the foam) and by removing the lenses designed to spread the beam (thus obtaining a smaller laser beam spot size). The evolution of modified sample holders was documented in Section 3.4, concluding with the final sample size of 2 x 2 cm^2. This sample opening was used in all experiments subsequent to experiment LH040603. The new gas velocity through the foam sample at a total inlet flow of 6 l/min was ~25 cm/s – more than 25 times higher than for the original sample holder design.

Since the diode laser radiation was outside of the visible spectrum (807 nm), the same View-it® ceramic plate used to visualize the diode pattern of the original rectangular beam (Figure 3.9), was used to project the beam shape and size with only the diffuser plate in place (the lenses were removed). The resultant beams are shown in Figures 3.26 and 3.27. The spot sizes were roughly spherical, with $1/e^2$ radius of approx. ~3 cm (beam area ~28 cm^2). The laser heads configured in this way provided a maximum power density of about 10 W/cm^2 near the centre of the beam (as measured by a laser power meter). For a 120x40 cm (4800 cm^2) conventional commercial plater window, this would correspond to 48 kW of IR energy. The commercial CVD plater with multiple chambers and short-wave IR lamps as the heat source used ~200 kW during standard operation.
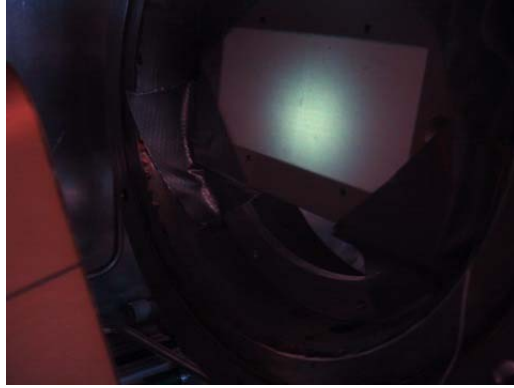
Figure 3.26 Beam shape with diffuser plate, lenses removed (South side)

Figure 3.27 Beam shape with diffuser plate, lenses removed (North side)

3.9   High-rate deposition on polyurethane substrate

After installation of a 2x2 cm^2 sample holder, the first set of experiments involved deposition on a PU substrate. As before, a complicating factor in these experiments was the requirement to start the process slowly, avoiding over-heating of the substrate. Such overheating could either completely destroy (melt and collapse) the PU foam if there was an insufficient metallic layer formed to maintain the original 3-D shape, or it could result in the presence of excessive amount of volatiles from the partial decomposition of polyurethane, which would interfere with the nickel deposition . The presence of a high concentration of volatiles during deposition typically resulted in an extremely brittle sample and sometimes patchy deposit (see Section 4.5.2). Typically, the deposit immediately adjacent to the PU foam was more brittle and discontinuous in some locations. This difference in the deposit structure is clearly visible on the etched cross-section of an as-deposited strut shown in Figure 3.28.
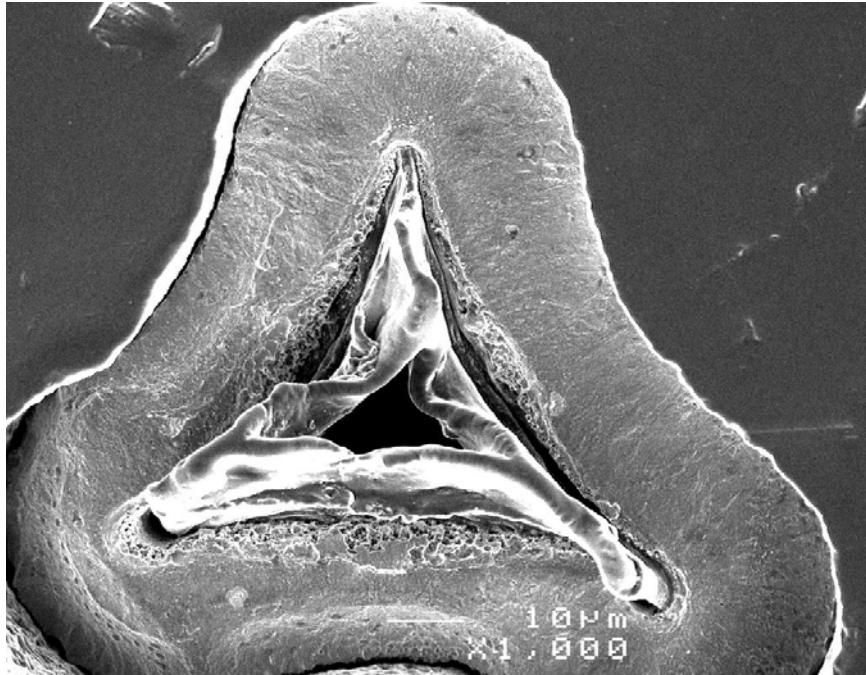
Figure 3.28   SEM cross-section image of etched (50/50 nitric/acetic acid) as-deposited Ni foam strut

The apparent opening in the middle of the PU strut is likely a result of the etching procedure. Fully dense, solid Ni deposit appears after about 1-3 micron initial thickness. It was found that deposition using the Phase I settings of 25A (~100W) for a period of 40 seconds provided sufficient base for the subsequent full-power, high rate deposition.

In one experiment (LH040628), the deposition was terminated following the pre-plate portion, and the sample was weighed and imaged in an SEM to confirm the amount of nickel deposited during this stage. Figure 3.29 shows SEM cross-sections of both the pre-plate (LH040628) and combined (LH040609) samples. The average thickness of the deposit after pre-plate was ~3 microns, providing

more than adequate coverage of the underlying polyurethane to allow rapid increase in temperature to ~ 210 °C, thus increasing the deposition rate. The issue of adequate coverage during the pre-plating step is important as it can impact the quality of the main deposit. Examples of incomplete coverage and its effects are further described and discussed in Chapter four, Sections 4.4.4 and 4.5.2.
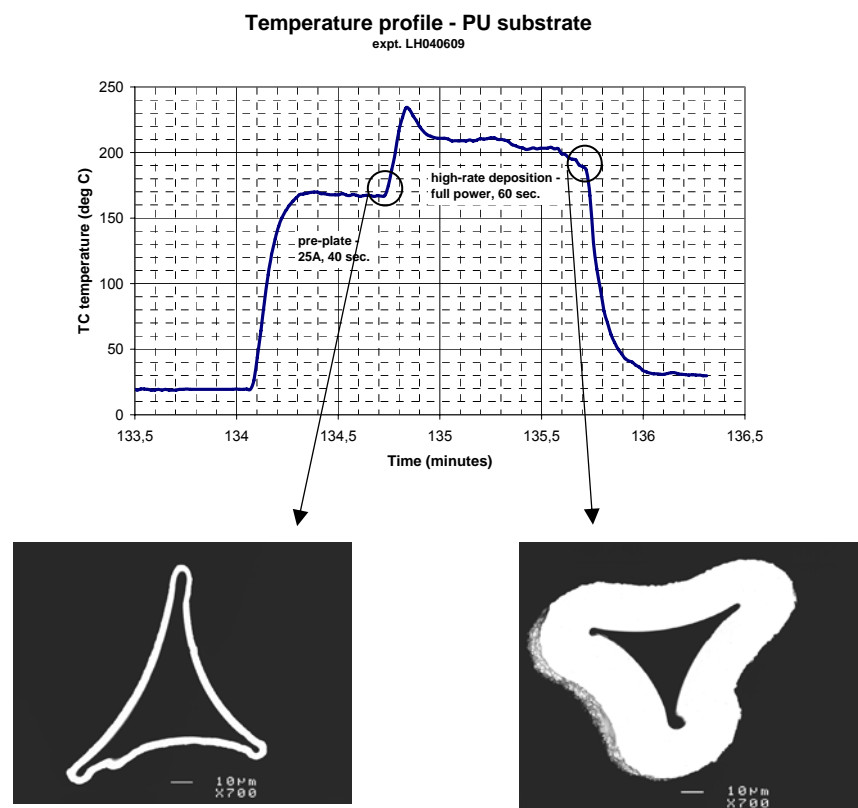
Figure 3.29 Temperature profile (test LH040609) and SEM cross-sections of a strut after pre-plating (40s at 25A, test LH040628) and combined pre-plating + high-speed deposition (40+60s, test LH040609)

The average deposition rate measured in experiment LH040609 was 10.2 μm/min or 1023 g/m²/min while the thermocouple position in the centre of the sample displayed an average temperature of ~170 °C during the pre-plate part

and ~210 ºC during high-rate deposition. Additional SEM images of the sample produced in this experiment are shown in Figures 3.30 to 3.35. The smooth morphology and uniform Ni distribution seen in these images confirm that it is possible to produce a high quality deposit on the polyurethane substrate at a rate of > 10 microns per minute. It is critical to provide continuous initial nickel coverage of the PU substrate without significant off-gassing of the polyurethane. Once the continuous layer of metal hermetically seals the polymer substrate, the deposition can proceed at a much higher rate.
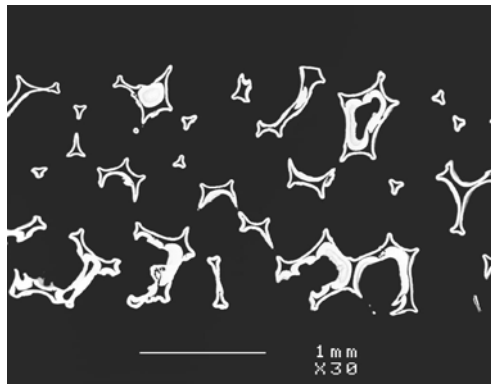
Figure 3.30 SEM cross-section of sample LH040609 (PU substrate)
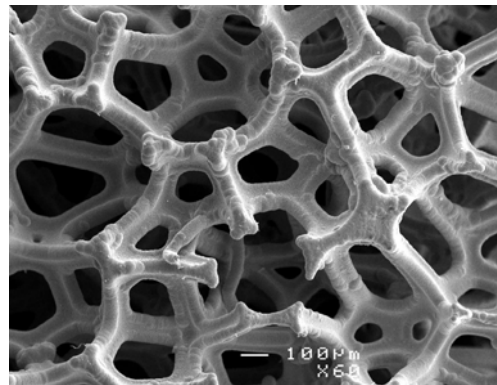
Figure 3.31 Surface morphology of sample from LH040609
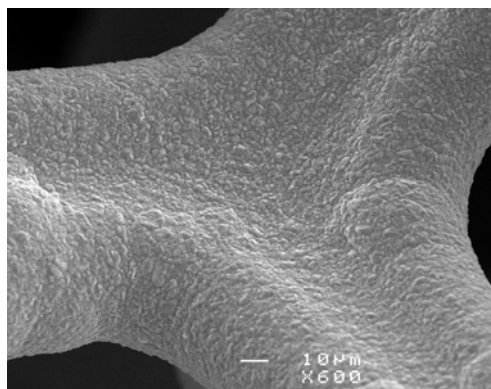
Figure 3.32 600x mag. of the surface morphology in LH040609)
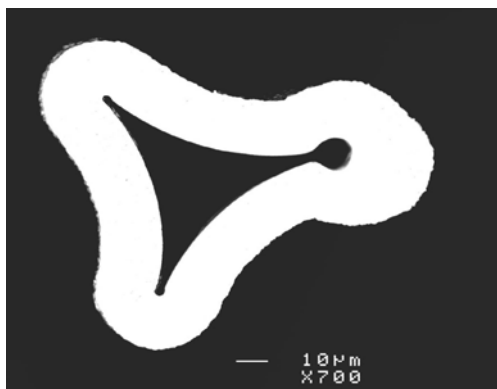
Figure 3.33 Strut cross-section detail in LH040609 showing uniform deposit on PU substrate
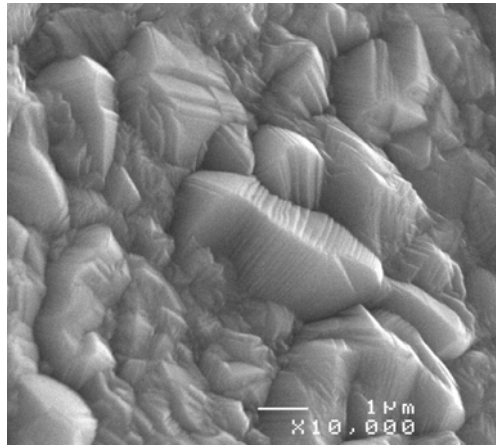
Figure 3.34 10,000x magnification of the surface detail - LH040609
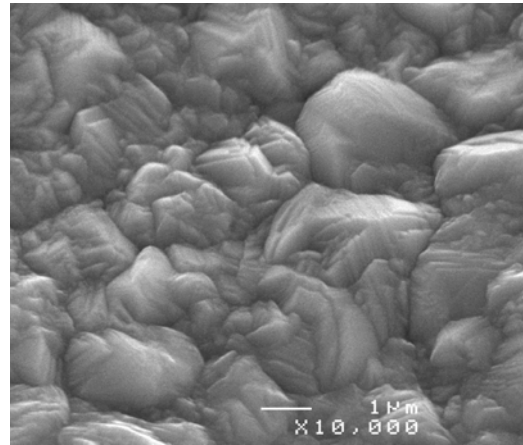
Figure 3.35 10,000x magnification of the surface detail - LH040609

3.10 Experiments starting with a Ni foam substrate

In order to simplify the quantification of high deposition rates, in some experiments the polyurethane substrate was replaced with a sintered electroplated nickel foam substrate, allowing the low-power pre-plate phase to be skipped. The final sample with the fresh nickel deposit thus represented only one set of process conditions during deposition. Typical temperature and laser power profiles of a high-rate experiment conducted with nickel foam substrates are shown in Figure 3.36. The thermocouple was located approximately at the centre of the laser beam spot and the standard deposition time was set to 30 seconds in these experiments. Note the rapid stabilization of the thermocouple temperature shortly after the onset of carbonyl decomposition. This onset is also clearly visible in the experiment video (page 99 in electronic version of this thesis) and occurs less than 1 second after the laser is turned on. The deposition rate measured in this particular test was 16.6 µm/min and the deposit was uniform based on SEM cross-sections.
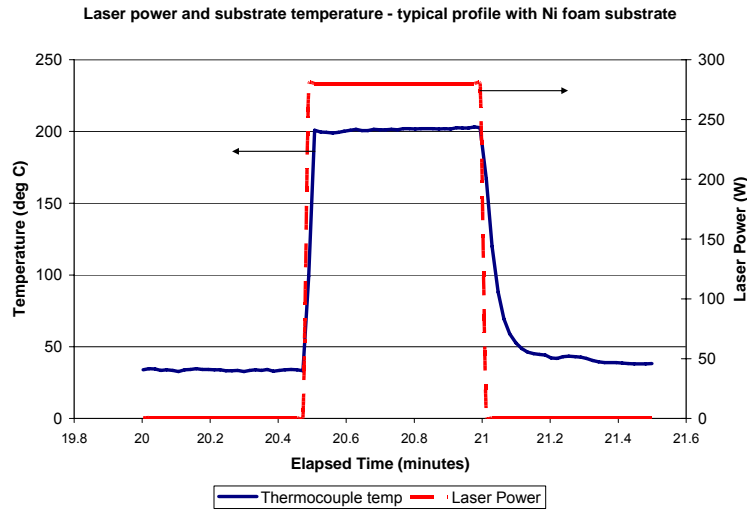
Figure 3.36 Temperature and laser power profile during a typical 30s deposition experiment starting with nickel foam substrate (expt. LH041110)

3.11 Process conditions study near homogeneous decomposition onset

To maximize the deposition rate and obtain desirable deposit morphology in the atmospheric pressure CVD process, it is necessary to control the process conditions so that the precursor decomposition proceeds exclusively heterogeneously on the substrate surface, without free space decomposition. The onset of homogeneous decomposition is accompanied by deposit morphology first becoming dendritic, followed by free-space powder formation. A series of tests was conducted to establish the necessary flow conditions for a given laser power setting that maximized the deposition rate in a purely heterogeneous regime. The maximum available laser power was used (~48 A with 7 bars operating) with the beam shaping lenses removed and the diffuser plate in place. The results of these tests are further discussed in Sections 3.12 and 3.13.

96

An example of a homogeneous decomposition onset taking place during a standard 30-second test is shown in the images of Figure 3.37 (the electronic version of this thesis also contains a ~40-second video documentation of this and two other experiments on page 99, Figure 3.38). The lower convection cooling due to the gas flow of 2.5 l/min resulted in the substrate exceeding the homogeneous reaction onset temperature under the given conditions. Figure 3.37 shows the temperature data recorded during this experiment. The developing rough substrate surface morphology darkened the surface within the first 5 seconds, enhancing the laser light absorption and causing further temperature increase. The sudden drop in temperature observed ~0.2 minutes into the test is due to the formation of Ni powder cloud, resulting in a partial blockage of the beam reaching the thermocouples. While neither of the two thermocouples (installed in the gas inlet side of the reactor and visible as 2 small dots near the bottom of the sample opening in Figures 3.37a and 3.37b) was located at the centre of the beam, based on other similar tests (notably test #LH041214, described later in this chapter) the maximum temperature in the centre of the beam exceeded ~220-230 °C, resulting in powder formation visible in Figures 3.37c-d. The gas transparency seemed to improve towards the end of the 30-sec. experiment as the circulating fine powder particles continued to agglomerate forming larger particle aggregates. The average gas concentration reached a lower equilibrium value (the concentration dropped from ~34% to ~22% in the first 15 seconds and stabilized at this value).

The combined hetero- and homogeneous decomposition process resulted in various 3-D structures on the surface formed from free-space nucleation of Ni particles and their assembly into filaments and web-like formations enveloping the struts. Some of these structures are further described later in this chapter (Section 3.13) and in Chapter four, Section 4.4.4.
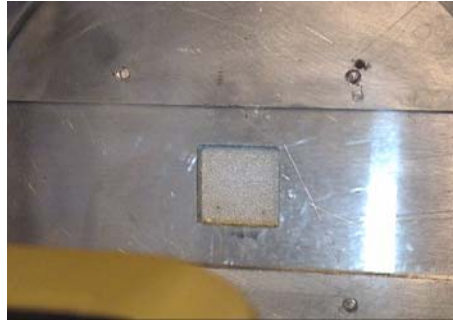
(a.) 0.5 seconds after laser-on
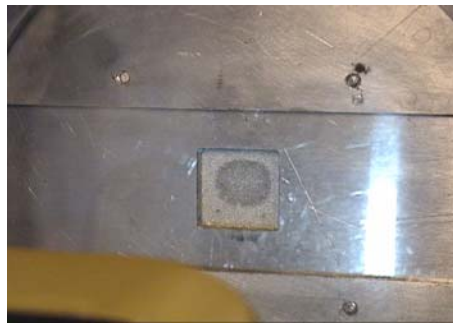
(b.) after 2 seconds
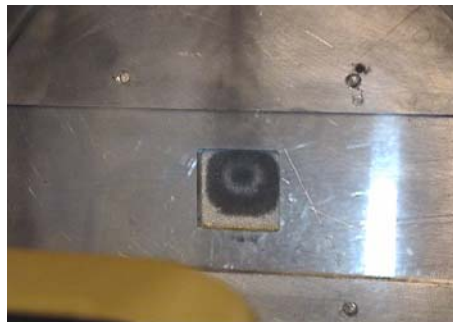
(c.) after 5 seconds – Ni powder plume is seen rising from the centre of the sample

(d.) after 20 seconds – agglomerating powder "flakes" are seen circulating in the chamber

Figure 3.37 Image sequence of a 30s experiment (LH050303) with onset of homogeneous decomposition

98
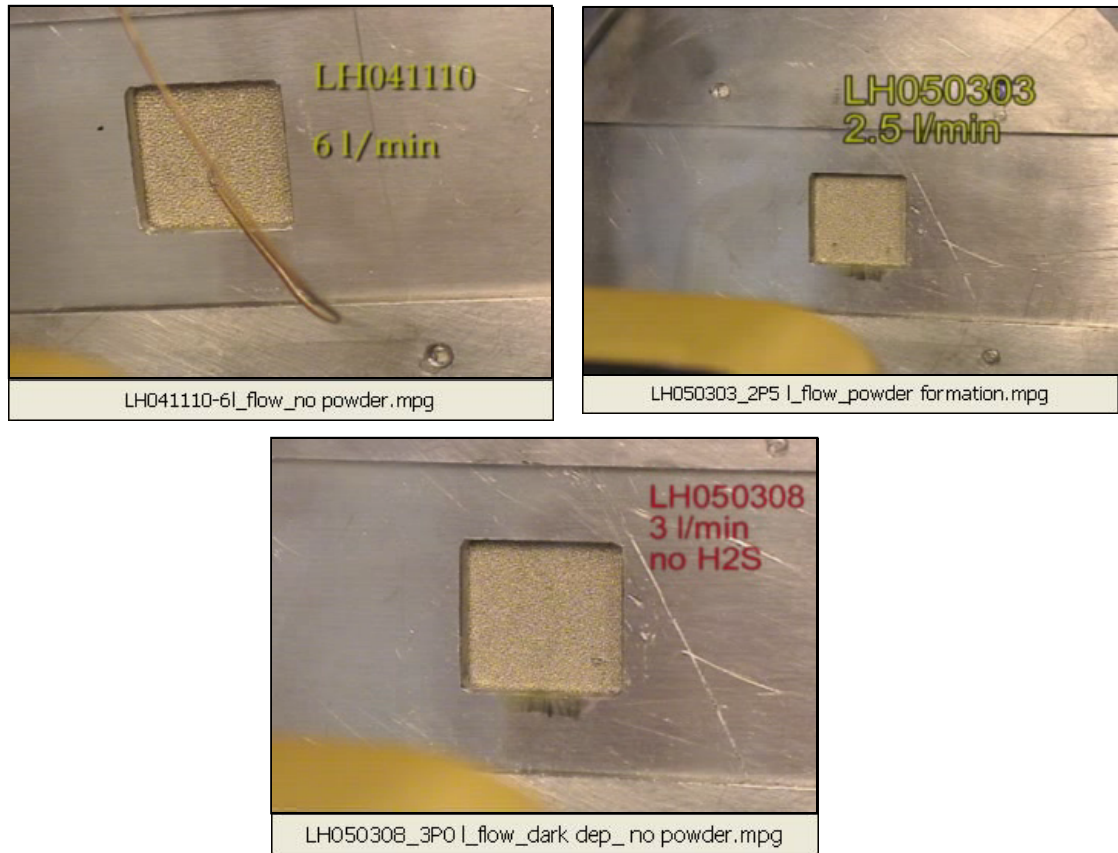
Figure 3.38 Video files of 3 selected experiments - click above images to play the file (e-version of the thesis)
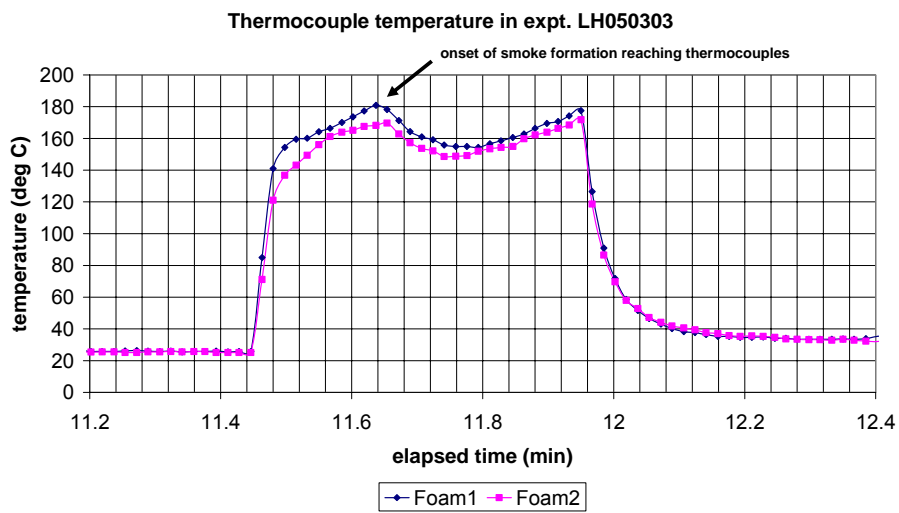
Figure 3.39 Temperature profile measured during experiment LH050303

3.12 Gas flow cooling effect

In pyrolytic CVD, temperature is the single most important variable controlling the deposition process. As shown by Steen [1977], convection and radiant surface losses can be significant in a temperature sensitive process. The cooling effect of a non-reacting gas flow was studied by measurement of the substrate temperature as a function of nitrogen gas flow at several laser power settings. A 1/16" thermocouple was inserted into the nickel foam substrate sample approximately in the middle of the 2 x 2 cm sample opening (Figure 3.41). The measured temperature variation confirmed that the nitrogen flow causes a significant cooling effect. For example, at 25 A laser current ($\sim$ 100 W of laser power), the temperature ranged from ~170°C at 7 l/min to ~430°C at 1 l/min flow. At full power (50A), temperatures as high as 560°C were measured with 5 l/min N_2, non-reacting flow.   More data points are shown in Figure 3.40.
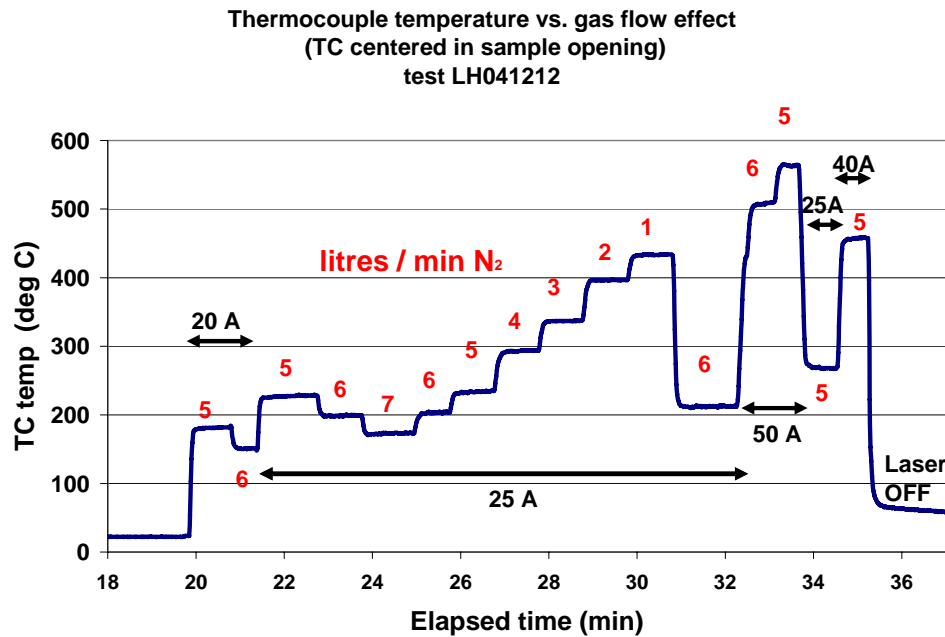
Figure 3.40 Temperature effect of a non-reacting gas flow (nitrogen)

3.13 Gas flow – laser power optimization

The significant cooling effect demonstrated with an inert gas flow implies that with the nickel carbonyl gas flow (which has nearly 5x higher heat capacity than nitrogen or CO), there will be some optimum flow setting that will result in the highest deposition rate with a uniform distribution of Ni at a given laser setting. This was investigated in two series of experiments where the deposition rate was measured as a function of the total gas flow at constant power, using the maximum available laser power setting.

3.13.1   Scoping test series

The first (scoping) series was done by conducting 30-second deposition tests at different gas flows without removing the sample from the reactor after each test. A thermocouple was positioned in the centre of the beam to acquire temperature data relevant to the observation of homogeneous carbonyl decomposition onset, initially always observed near the beam centre.   Figure 3.41 shows the thermocouple location and appearance of the sample after the test series as seen from the gas exit side of the chamber. A strong upward jet was clearly visible following the onset of homogeneous decomposition at 2 l/min total gas inlet flow. The fine Ni particles were carried upward in the stream of low density gas (due to higher local CO content of the heated gas originating from the decomposing carbonyl). Some of these particles were deposited on the sample holder wall providing visualization of the gas flow pattern, as seen in Figure 3.41.

Because the sample was not removed after each test, the incremental Ni deposition amount was not measured (this was done in the following tests series).
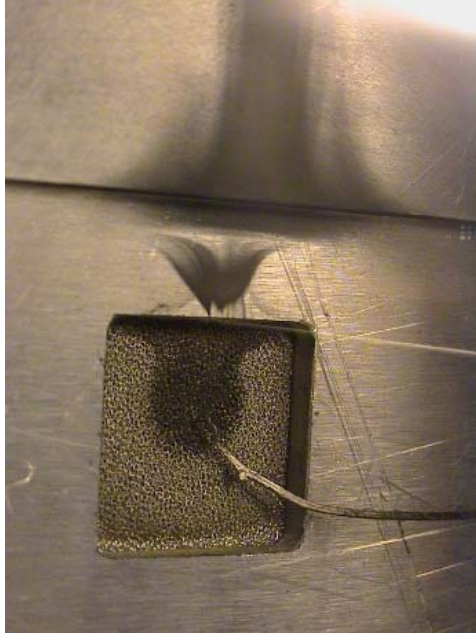
Figure 3.41 Thermocouple location during LH041214 tests series

The thermocouple data for this experiment is shown in Figure 3.42. The onset of powder formation was observed during the 5th deposition segment, with the thermocouple temperature rising up to 278°C. The powder formation started at approximately 230°C. During this stage the observed temperature was quite unstable in comparison with the pure film growth stage, owing to the changing absorbance of the foam surface (development of a rough, dark color surface visible in Figure 3.41) and due to the nucleating particles blocking some of the laser energy. In the last segment of this experiment, the feedgas nickel carbonyl concentration was dropped to about one half of that of the previous five segments.   As expected, this significantly reduced the deposition rate and consequently increased the thermocouple temperature, reaching about 280°C. Severe powder formation was observed during this segment as well.
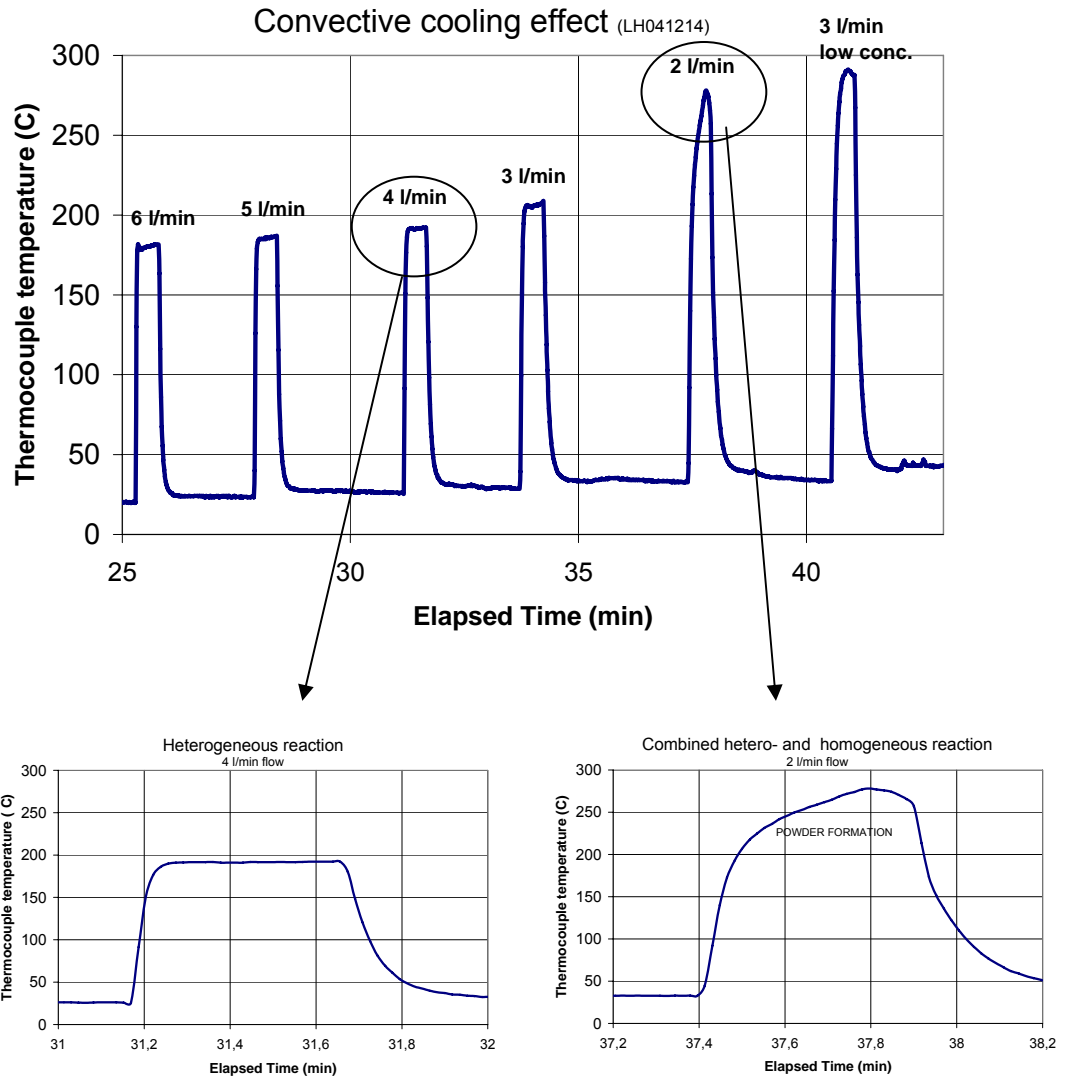
Figure 3.42 Temperature data in the variable gas flow experiment LH041214

Figure 3.43 shows examples of dendritic deposits formed following the onset of homogeneous decomposition.   Additional selected images of the variety of

surface morphologies, filaments and particle shapes formed during this test are included in the microstructure analysis part of Chapter four (Section 4.4).
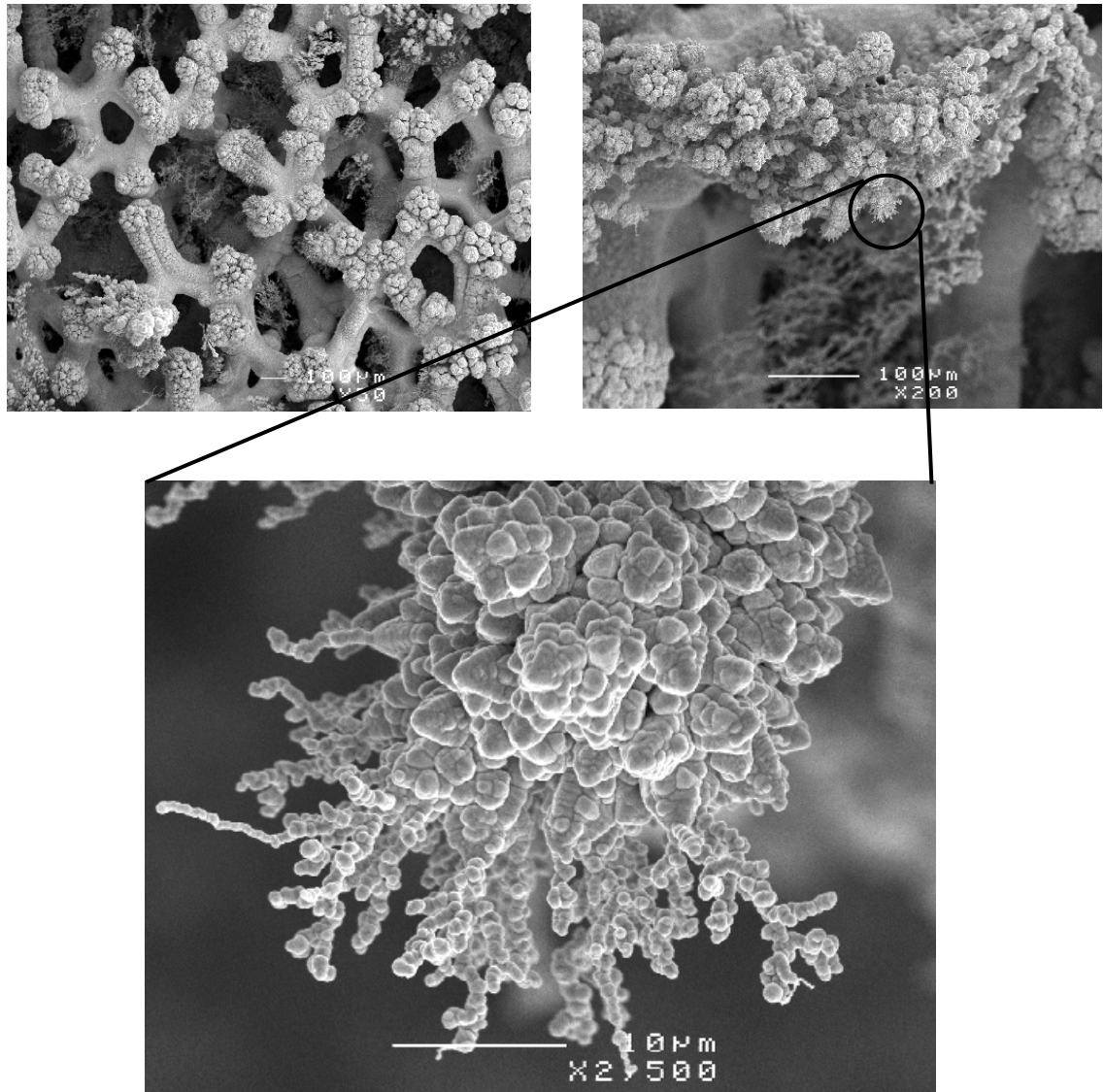
Figure 3.43 Dendritic morphology of a sample produced in expt. LH041214

3.13.2 Flow optimization with rate measurements

On the basis of the results from the variable flow experiment, selected test segments were repeated while removing the sample at the end of each test to accurately measure the deposition rate. A Ni foam substrate and the usual concentration of the H_2S catalyst (0.18%) were used in these tests. Figure 3.44 shows the results as a plot of deposition rate vs. total inlet gas flow rate. With constant laser power, there is an optimum gas flow value that balances the mass transport delivery and convection cooling effect, producing a uniform deposit at a high rate and without free space decomposition. A rate of 19.1 µm/min (or ~1,165 g/m^2/min for this particular substrate structure) was measured at a total gas flow rate of 3 l/min. This test was repeated with excellent reproducibility, giving a rate of 19.0 µm/min.

FLOW OPTIMIZATION TEST SERIES
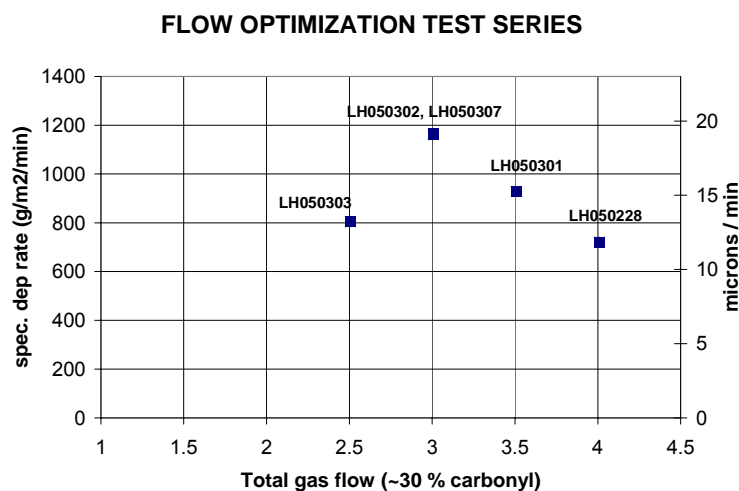
Figure 3.44 Deposition rate as a function of gas flow test series

Figure 3.45 is an SEM cross-section of one of the high-rate deposition samples (LH050307). The higher magnification detail on the right clearly shows the new

deposit on top of the original electroplated Ni foam substrate. The ~10 micron thick new layer was deposited in 30 seconds and was found to be uniform across the full substrate thickness.
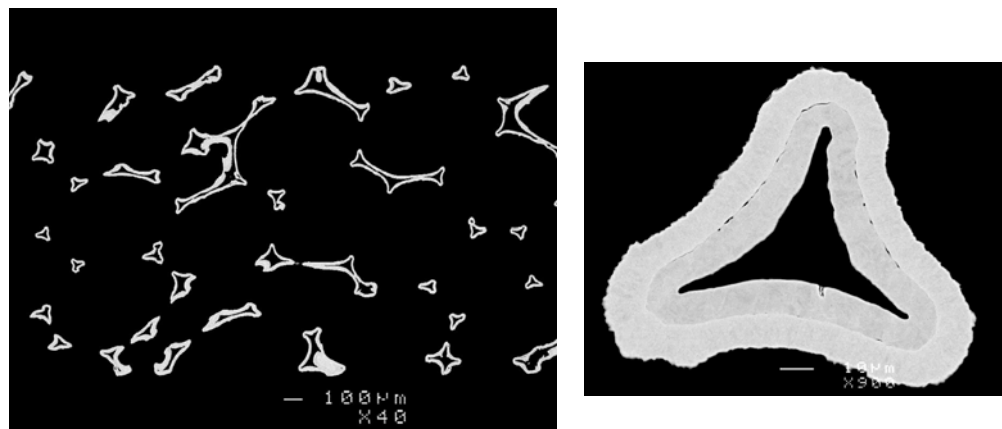
Figure 3.45 Uniform deposit on Ni foam substrate – experiment LH050307

3.14 Deposit thickness determination

In industrial practice and among commercial users of nickel foams, the density of the material (nickel content) is commonly described in units of grams of Ni per square meter of nominal Ni foam sheet area. Similarly, the deposition rate in both CVD and electroplating processes is often expressed in grams of Ni per m^2 of nominal foam area per minute. This unit is not practical for scientific purposes since for the given set of process parameters, the value will be strongly influenced by the overall thickness of the material and the foam cell size (i.e. the actual surface area available for deposition). In scientific literature, the deposition rate is most often expressed in the units of a deposit thickness per unit time, e.g. nm/s, μm/s or μm/min. In this work, we adopt the unit μm/min but also

provide the corresponding values in $g/m^2/min$ (m^2 of nominal foam sheet area) for comparison with industrial practice.

The deposit thickness was determined by cutting small coupons using a 7/16" diameter cutting die shown in Figure 3.46. The weight of the deposit was measured by weighing the coupon and subtracting the known weight of the PU substrate. Figure 3.46 also shows the method of density measurement on samples prepared using nickel foam substrates. Four control coupons surrounding the laser beam irradiated area were cut to determine the average Ni foam substrate density. This value was then subtracted from the measured coupon weight to determine the net deposited amount.

A known relationship between foam projected (nominal) area and the real surface area was then used to estimate the thickness of the deposit. This was verified by SEM imaging. For samples made on the Recticel PU foam, each 100 g/m^2 of areal density at 1.7 mm thickness corresponded to approximately 1 μm thickness of Ni deposit. The Ni foam substrate was somewhat coarser (~650 μm cell diameter), with a conversion factor between area density and Ni deposit thickness of 1 μm = 61 g/m^2.

Figure 3.46 Deposit thickness measurement

3.15 Differential Thickness Ratio Measurement

Differential Thickness Ratio (DTR) is a measure of nickel deposit thickness uniformity across the thickness of nickel foam sheet. It is determined by an optical or SEM imaging technique by dividing the foam cross-section into three equal layers (2 along the surfaces and one in the centre) and measuring the average thickness of the Ni layer in the three areas (Figure 3.47).

$$DTR = (A_1+A_3)/2A_2 \qquad\qquad (3.1)$$

where A_1 and A_3 are Ni areas along the 2 surfaces and A_2 is the area in the centre as determined from metallurgical cross-section. Perfectly uniform foam will have DTR = 1.0. Foam with a thicker deposit on the outside will have DTR > 1 and foam with a thicker deposit in the middle will have DTR < 1. This measure is only meaningful for symmetrical variation of Ni thickness.
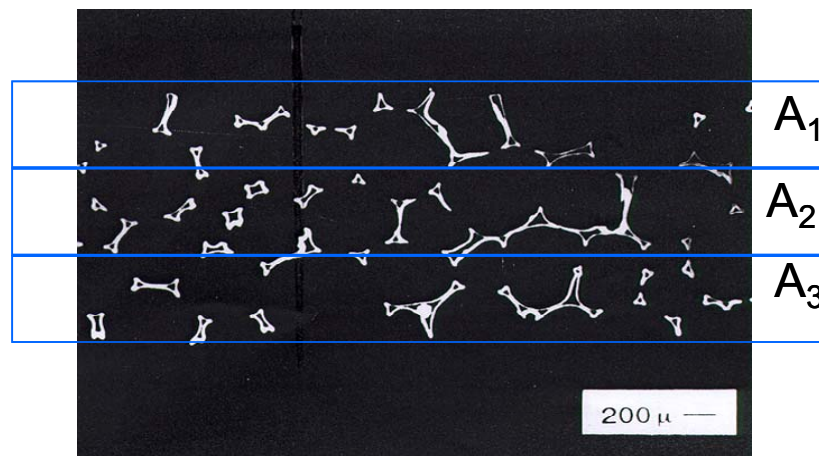
Figure 3.47 DTR measurement principle

For battery electrodes, foams with DTR values in the range ~1 < DTR < ~1.4 are preferred.

3.16 Temperature measurement

The substrate temperature can be considered the single most important parameter in the control of a heterogeneous CVD process. Accurate measurement of temperature, especially on porous, 3-D substrates such as nickel foam, presents a challenge. In this work, small-size (1/16" or smaller) K-type thermocouples were used to measure the temperature. Thermocouples were inserted into the foam structure, making multiple physical contacts with the foam struts. Figure 3.48 shows a picture of typical thermocouple locations. The thermocouple was located in the middle of the laser beam spot in the tests used for determination of the kinetic constants (upper center thermocouple in Fig. 3.48), while it was away from the main beam spot size (but still within the diffused beam radiation field) in other tests to minimize the Ni deposit on the thermocouple tip (lower left thermocouple in Fig. 3.48). The thermocouples were replaced periodically as they gradually built up nickel deposit.
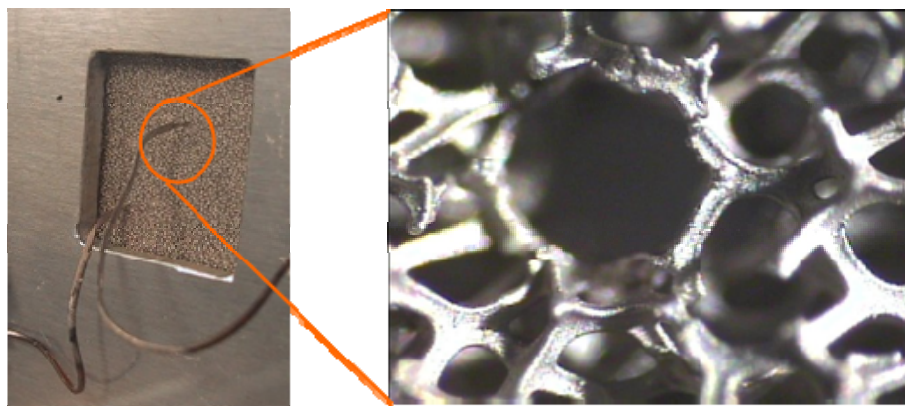
Figure 3.48 Location and a method of contact of a thermocouple (expt. LH050406)

Figure 3.49 shows temperature data illustrating that at high deposition rates, the dominant cooling effect on the substrate was the carbonyl decomposition reaction itself. In a test when 5 l/min non-reacting gas flow was used (nitrogen), the thermocouple positioned in the centre of the laser spot reached a temperature

of over 450ºC at 40A of laser current. The temperature was at ~270ºC at 25A current just prior to the laser current increase to 40A. With the reacting flow of CO and ~30% Ni(CO)$_4$, the temperature reached equilibrium of ~180ºC at full laser current of 50A within about 4 seconds after turning on the laser. The onset of Ni deposition was observed considerably earlier – well within ~1 second after turning on the laser beam (see experiment videos on page 99 (Figure 3.38) available in the electronic version of this thesis). The equilibrium temperature is thus the result of a combined cooling effect of the endothermic reaction, gas conducto-convective heat transfer to the flowing gas jet, and laser beam heating.

Sample temperature under reactive and non-reactive gas flows (5 l/min)
test LH041212 (non-reactive, part 15-16) and LH041214 (reactive, part 2)
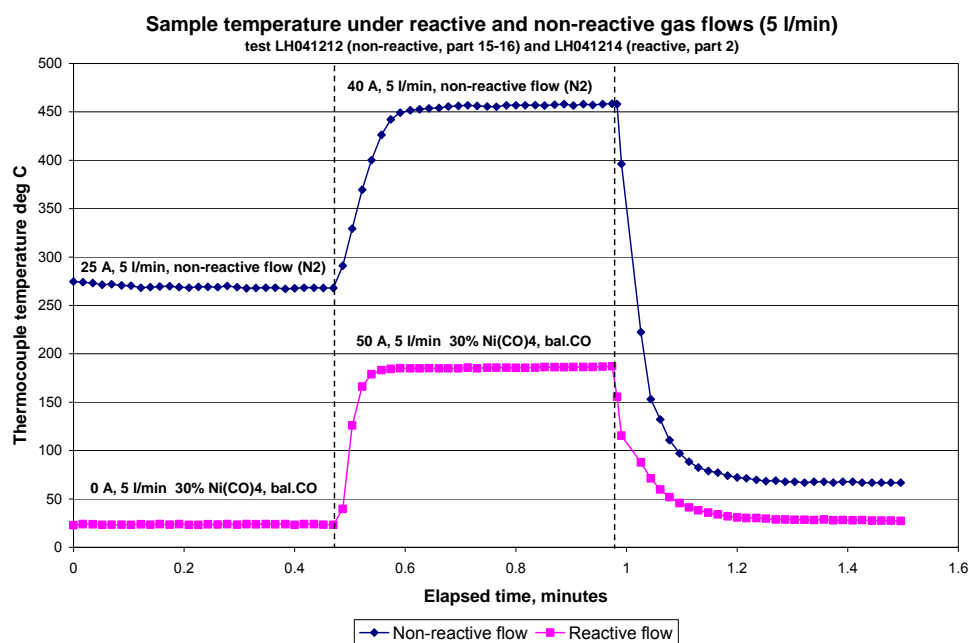
Figure 3.49 Centre-beam thermocouple temperature measurement during sample heating with reacting and non-reacting gas flow present

3.17 Window performance

The quartz window remained clean following most of the high-rate deposition experiments. However, localized window plating within the laser beam area was observed in several tests when Ni powder formed inside the reactor. It is likely that the onset of window plating originated from fine Ni particles colliding with and attaching themselves to the window internal surface, acting as IR absorption sites and subsequently plating with nickel in the laser beam area. An example of this situation is shown in Figure 3.50. Figure 3.51 shows the interior of the reactor exit side following this test (window removed). A significant amount of nickel powder was found on the reactor internal surfaces.
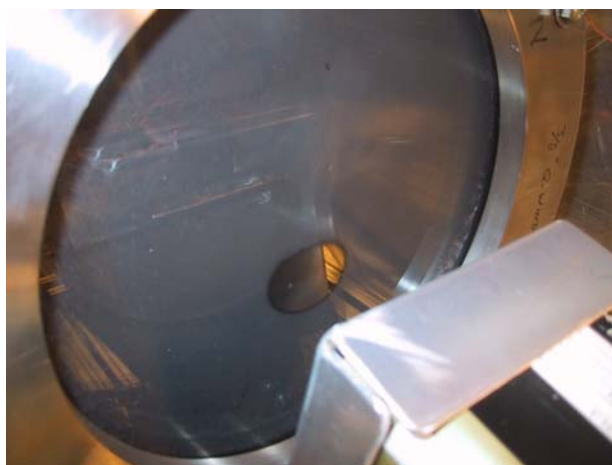
Figure 3.50 Ni deposit on the quartz window internal surface during experiment
when powder formation was observed (expt. LH040730)

While the experimental chamber used quartz windows, the near-IR laser wavelength of 807 nm should allow uncooled (or air-cooled) operation of regular borosilicate glass, which is more practical for large-scale reactor windows.
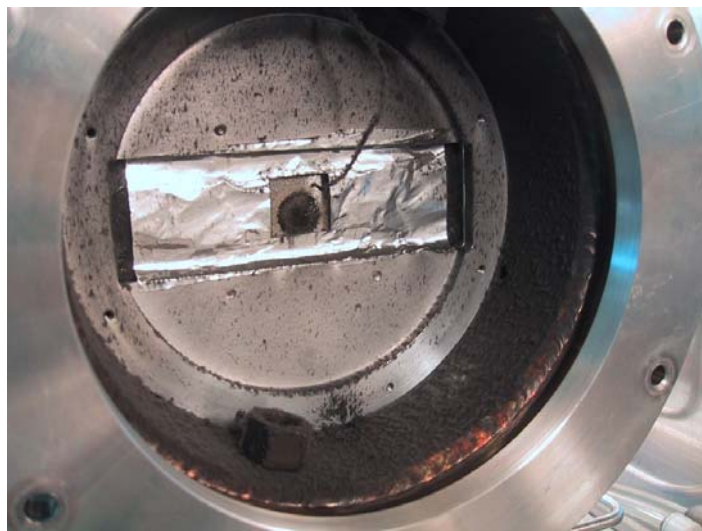
Figure 3.51 Reactor interior (gas exit side) following experiments with partially homogeneous reaction (expt. LH040730)

3.18 Laser CVD on other substrates

3.18.1 Carbon nanofoam

Carbon nanofoams are a new material with many of the properties of traditional aerogel material [Rode et al., 1999]. They are synthetic, lightweight foams in which the solid matrix and pore spaces have nanometer-scale dimensions and are available in the form of monoliths, granules, powders and papers. Prepared by sol-gel methods, nanofoams typically have a low density, continuous porosity, a high surface area, and fine cell/pore size. One form of carbon nanofoam is available commercially from Marketech International (www.mkt-intl.com). The structure is produced by a sol-gel process. An attempt to metalize the 3-D surface of a small C nanofoam sample purchased from Marketech was made in experiment LH050706.

Figures 3.52 and 3.53 show surface images of the nickel-coated C nanofoam substrate. It appears that the large cracks in the structure provided gas flow channels that effectively bypassed the relatively dense interior of the sample. This

resulted in most of the interior porosity being uncoated. Figure 3.54 is a polished cross-section of the same sample after Ni deposition, showing a detail of one of the larger channels spanning the full thickness of the sample.
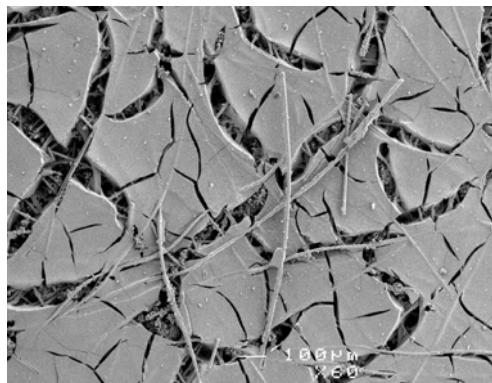
Figure 3.52 Surface SEM image of a metallized C nanofoam
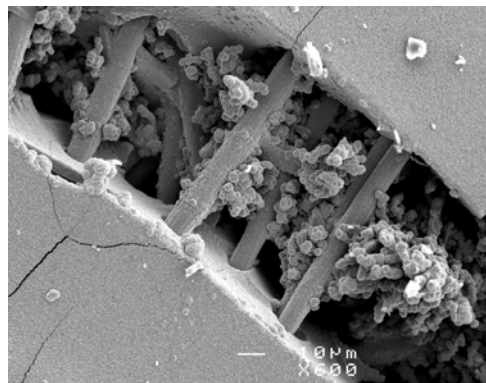
Figure 3.53 View into the interior of a metallized C nanofoam
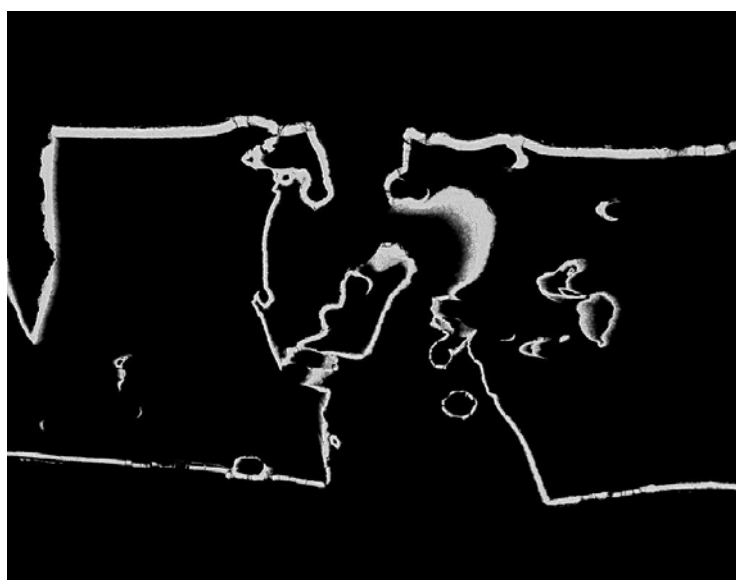
Figure 3.54 SEM cross-section of Ni-coated carbon nanofoam sample (expt. LH040706)

3.18.2 Phenolic foam

Phenolic foam was identified as a possible substrate for nickel CVD owing to its small cell size (high surface area) and good thermal properties. The material tested was found too dense for the given deposition conditions, and only limited coverage of the foam interior was observed. Figures 3.55 and 3.56 show a surface image and a cross-section (respectively) of the sample prepared in experiment LH050121.
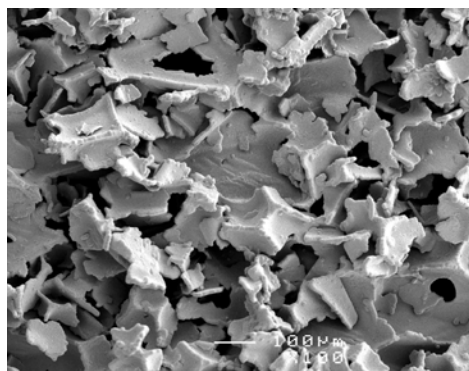
Figure 3.55 Surface SEM image of a metalized phenolic foam
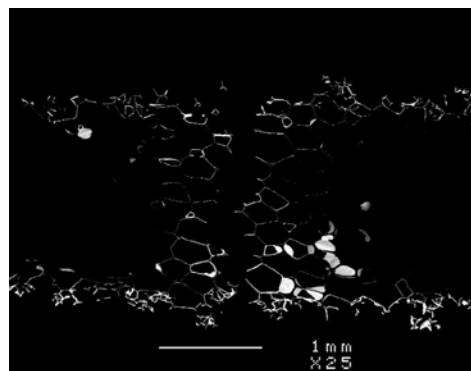
Figure 3.56 SEM cross-section of a metalized phenolic foam

3.18.3 Carbon nanotubes

The rapid heating rates and short exposure times possible with a laser heat source allow the preparation of ultra-thin nickel coatings on a variety of substrates. Recent interest in carbon nanotubes prompted the idea of using the carbonyl LCVD system to deposit a thin layer of nickel onto multi-wall carbon nanotubes. The devices made of ferromagnetically contacted carbon nanotubes are expected to exhibit giant magneto-resistance (GM) and their magnetic properties could be utilized for future spintronic applications [Mehrez, 2000]. The field has expanded significantly since the discovery of the GM effect in magnetic multilayers [Tsukagoshi, 1999] and has been the main driving force leading to the development of the present generation of high capacity magnetic storage devices.

114

The sample of carbon nanotubes used in this work was provided by the research group of Prof. J. Gracio at the University of Aveiro in Portugal [Titus et al., 2005]. Figures 3.57 and 3.58 show Ni-coated nanotubes with a very thin layer of Ni on the surface, produced by exposure of the sample to the laser beam at 25A (~100W) for 5 seconds in an atmosphere of ~30% nickel carbonyl and 70% carbon monoxide.
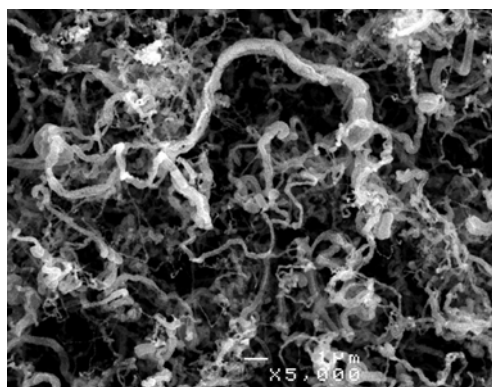
Figure 3.57 Surface SEM image of Ni-coated C nanotubes
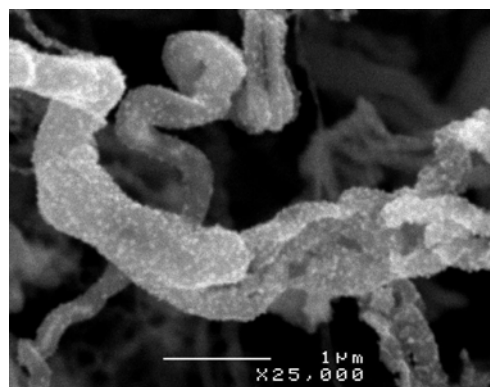
Figure 3.58 SEM detail of a C nanotube with deposited Ni particles

3.18.4   Deposition on white ultra-fine polyurethane foam

Very fine open-cell polyurethane foams that belong to the general category of hydrophilic foams recently became available in the PU foam market, driven mainly by cosmetic, medical (wound dressings) and inkjet printer cartridge applications. The average cell size of these foams is approximately 100 microns. A sample of this material produced by Corpura Corp. was metallized in the LCVD system with some limited success in obtaining uniform coverage of the ~ 5 mm thick sample. Figures 3.59 and 3.60 show the white foam sample inside the deposition chamber before and after the experiment (#LH050822), respectively. Figures 3.61 and 3.62 are surface SEM images of this sample before and after Ni deposition, respectively.

Figure 3.59 Surface SEM image of uncoated ultrafine PU foam sample
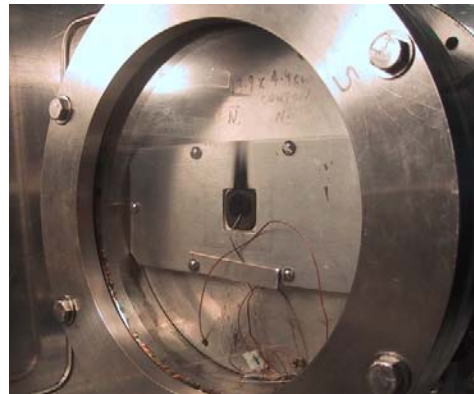
Figure 3.60 Surface SEM image of a metallized ultrafine PU foam sample
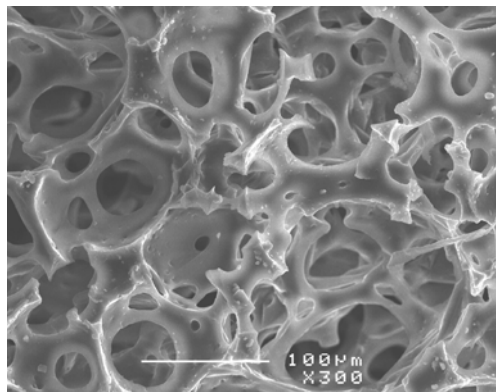
Figure 3.61 Surface SEM image of uncoated ultrafine PU foam sample
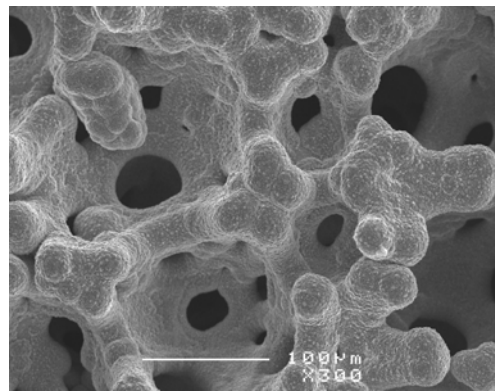
Figure 3.62 Surface SEM image of a metallized ultrafine PU foam sample

3.18.5 Graphite foil

In another series of experiments a graphite foil was used as a substrate for nickel LCVD. The sample holder was modified to provide flow of gas between inlet and exit parts of the chamber by drilling number of holes on either side of the sample area. The same 30-second deposition time was used to grow a nickel film on the surface of the graphite foil (Alfa Aesar product #10832). Figure 3.63 shows the deposit covering the laser beam area. Some swelling of the substrate,

116

visible in the photograph, was observed few seconds after the laser was turned on. At 40A laser current, the measured deposition rate obtained from the incremental weight of the sample was ~3 μm/min.
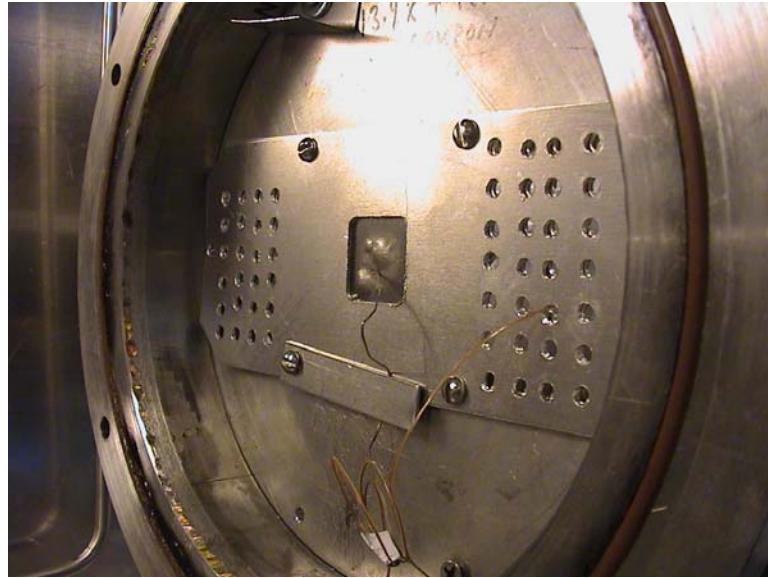
Figure 3.63 Modified sample holder for non-porous substrates - swelling of the graphite foil surface following 30 s deposition at 25A (expt. LH050819)

3.19 Pulsed laser deposition

A brief attempt was made to produce a nickel foam sample with the diode laser operating in a pulsed mode. For high productivity in mass production of conventional foams, this would not be a desired mode of operation as the overall deposition rate will be lower than in a CW mode. The interest in pulsed operation was motivated by the possibility of producing a deposit with much finer crystallinity, leading to a nanocrystalline structure. At certain grain sizes, such nickel deposits exhibit unique properties such as high tensile and compressive strength [Erb et al., 1993].

Figure 3.62 shows the surface morphology (at 10,000x magnification) obtained with the laser set to ~ 30% duty cycle and a pulse width of 0.3 ms (1 kHz). The measured deposition rate was rather low, about 0.2 μm/min. The pulsed deposit exhibited much smoother surface and very poor adhesion to the original Ni foam substrate. The inset image in Figure 3.64 is a high-resolution SEM micrograph of the same sample surface at 150,000x magnification, showing more detail. The surface consists of about 50-70 nm grains. The smooth surface of the pulsed sample contrasts with the much coarser surface of a sample produced using CW laser beam (grain size of the order of 1 micron), shown in Figure 3.65 at the same magnification of 10,000x.
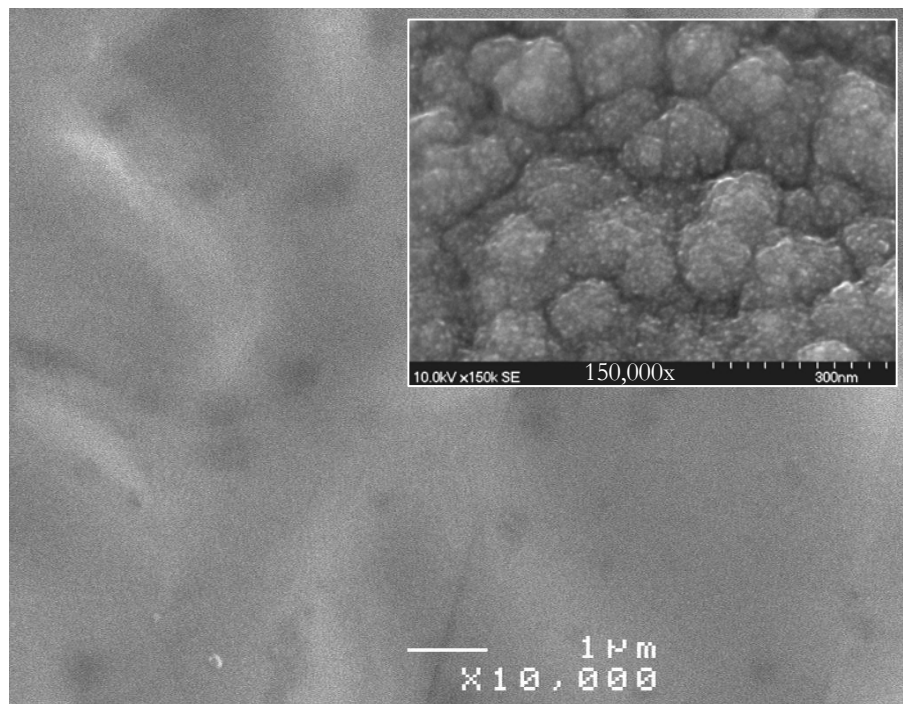
Figure 3.64 Surface morphology of a sample produced with pulsed laser beam (expt. LH050916)
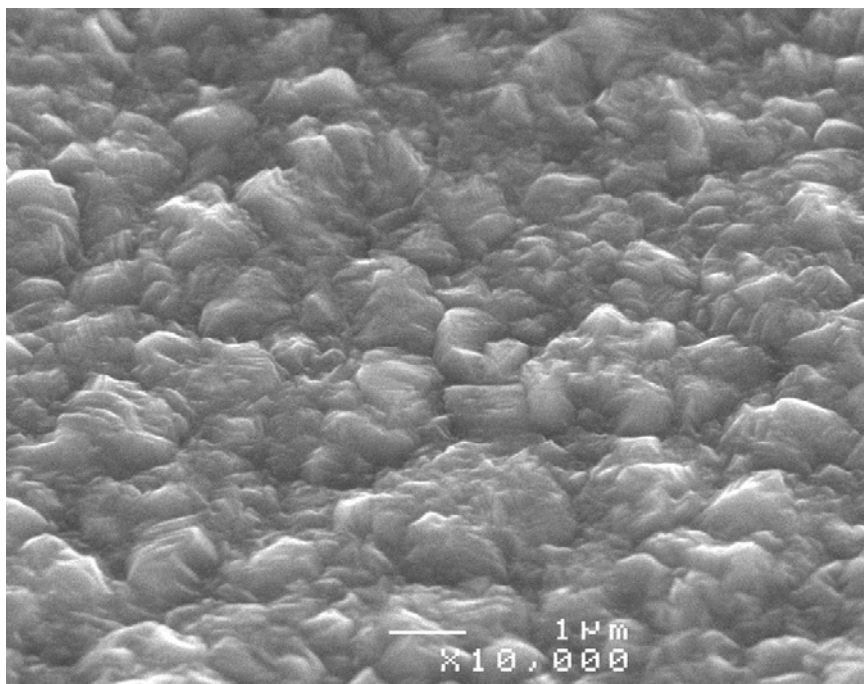
Figure 3.65 Surface morphology of a sample produced with CW beam (expt. LH040628)

In Figure 3.66 (SEM cross-section of a foam strut), the pulsed laser deposit is seen as a distinct, thin nickel layer separated from the underlying annealed (electroplated) nickel foam substrate. This could be due to the large difference in grain size between the 2 deposits. The pronounced separation of the pulsed laser deposit likely occurred during the vacuum out-gassing of the sample, which is a part of the SEM sample mounting procedure.

Further work using pulsed operating mode of the diode laser is recommended. This process can lead to an efficient method of preparation of 3-dimensional nanocrystalline deposits, facilitating the production of ultra-light porous foam structures with high tensile and compressive strength. Another application could be the production of ultra-thin nickel foils. Foils that are presently made by

electroforming are limited to a minimum thickness of about 10 micrometers[5]. The sample shown in Figure 3.66 shows a fine-grained nickel deposit that appears mechanically strong at a thickness of about ~1 micron. This points to the possibility of producing ultra-thin nickel foils with unique mechanical properties by tailored grain size and film growth control using the pulsed laser nickel carbonyl CVD process. A possible application area could be the production of nanostructured multi-layer reactive foils, which often involve nickel as one of the reactive elements [Wang et al., 2004].
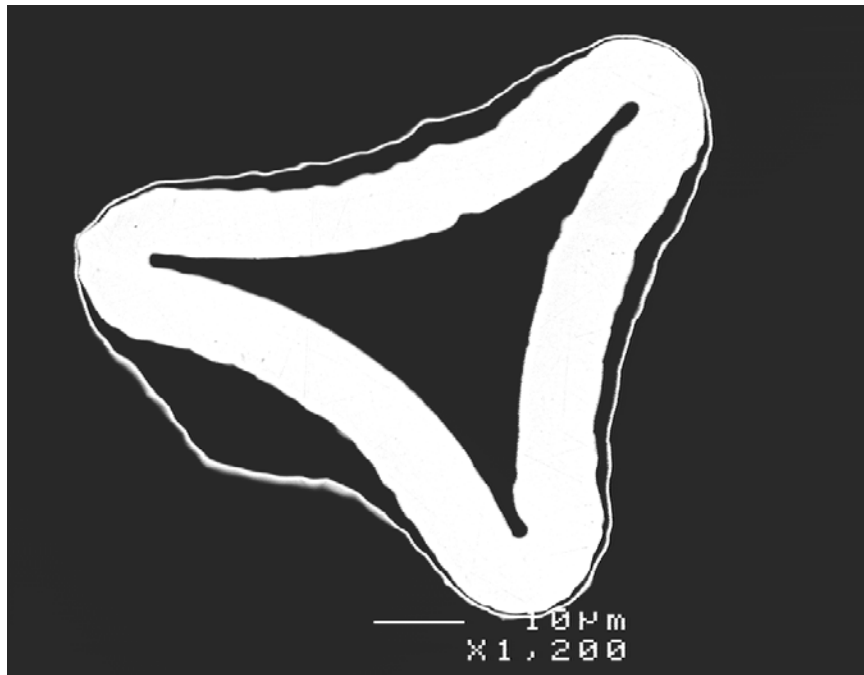
Figure 3.66 Cross-section of a strut with a thin pulsed laser deposit seen separating from the underlying electroplated Ni foam substrate (expt. LH050916)

---

[5] See for example Special Metals Corporation catalogue,
http://www.smcwv.com/documents/Electroformed%20Nickel%20Foil.pdf

4   RESULTS AND DISCUSSION

This chapter discusses the physical and chemical processes affecting the deposition process and the observed deposit morphology. The results of an earlier kinetics study using conventional IR lamps are presented and compared with the data obtained in the present LCVD process.

4.1   Measurement of kinetic constants

An earlier study on the kinetics of polyurethane foam plating was conducted at Vale Inco using a conventional chamber and heat sources (IR lamps) [Coley, 2003]. The chamber was a vertical rectangular reactor with the sample suspended on a sensitive strain gauge, monitoring weight gain during deposition. The temperature was measured on another sample located immediately below the strain gauge-mounted sample (thermocouple contact would affect the accuracy of the strain gauge measurement) and the assumption was made that the temperature and deposition rate differences between the two samples were negligible. The reactor used in this study is shown in Figure 4.1 and a sample mounting arrangement including the thermocouple location is shown in Figure 4.2. Note that no provision was made in these tests for cross-flow of gases, resulting in a good approximation of the conventional process.

The data obtained in this work provided a good illustration of the mass transport limitation encountered in nickel CVD on 3-dimensional substrates. The experimental configuration employed in this earlier work had no provision for enhancing the precursor gas supply inside the 3-D foam structure. Figure 4.3 shows the nickel distribution observed at temperatures as low as 140 $^{\circ}$C,

illustrating severe precursor depletion of the foam sample interior and causing excess nickel to deposit on the two outer surfaces.
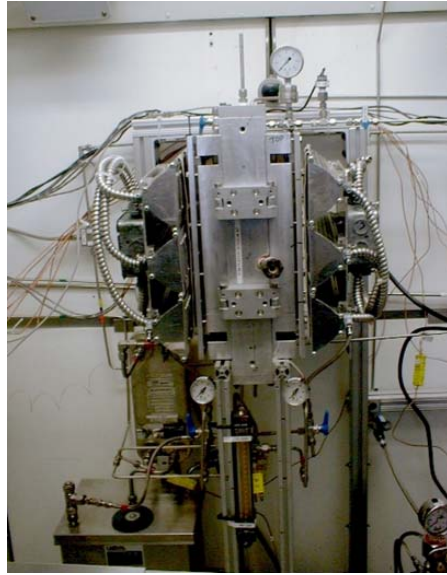
Figure 4.1 Rectangular reactor used in earlier kinetic study of conventional foam plating
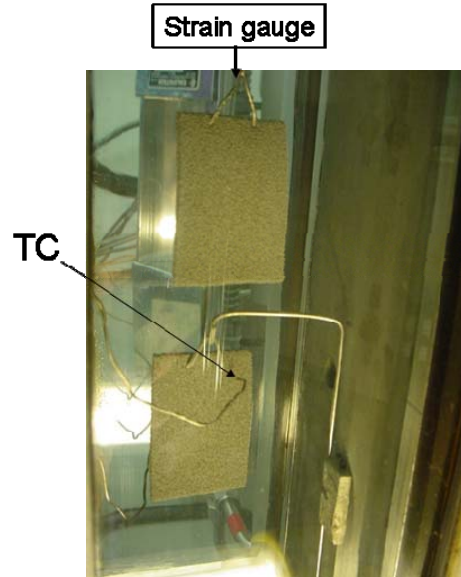
Figure 4.2 Sample mounting in a test reactor with conventional heating and gas supply

One of the objectives of this earlier study was a confirmation of the order of the carbonyl decomposition reaction. Based on the measured data at 110 $^{\circ}$C, the reaction appeared to be first order with respect to carbonyl concentration. Several other researchers arrived at the same conclusion regarding the order of reaction, e.g. Tsylov [1971], and Boettger et al. [1962], although others concluded that the reaction was of a higher order, notably Carlton & Oxley [1967].

The 110 $^{\circ}$C temperature was chosen because good deposit uniformity was obtained at this temperature (Figure 4.4), confirming that the process was in a kinetic control regime under the conditions present in the experimental apparatus shown in Figures 4.1-4.2.
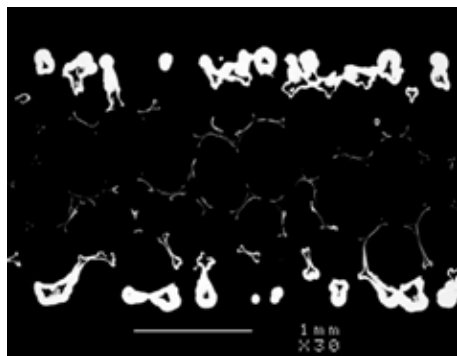
Figure 4.3 Poor nickel distribution obtained at 140°C in a conventional apparatus
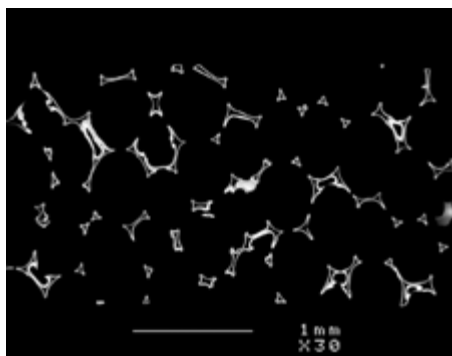
Figure 4.4 Uniform nickel distribution obtained at 110°C in a conventional apparatus

The deposition rate as a function of average gas concentration is shown in Figure 4.5. This data also shows that the concentration of the H_2S catalyst did not have a significant effect on the deposition rate at different concentrations of nickel carbonyl.
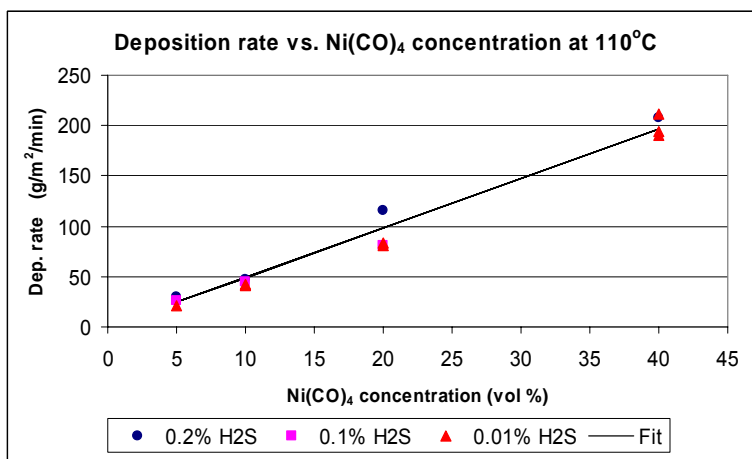
Figure 4.5 Deposition rate as a function of nickel carbonyl concentration – first order reaction

As discussed earlier in Sections 1.18 and 3.7, the main benefit of changing the flow configuration to provide forced flow across the foam sample should be the extension of the kinetically-controlled deposition regime to higher temperatures,

and thus to higher deposition rates. Data based on uniform deposits measured in the laser system at higher temperatures were combined with the low-temperature data from the earlier kinetic study to produce an Arrhenius plot for concentration-normalized nickel carbonyl decomposition rates on 3-D foam substrates. In order to highlight the pronounced effect of temperature on deposition rate, the data is plotted in Figure 4.6 using a linear temperature scale. Small changes in temperature in the upper temperature range of heterogeneous decomposition process change the deposition rate markedly – for example the rate can be approximately doubled by increasing the temperature by 30 degrees from 450K to 480K.
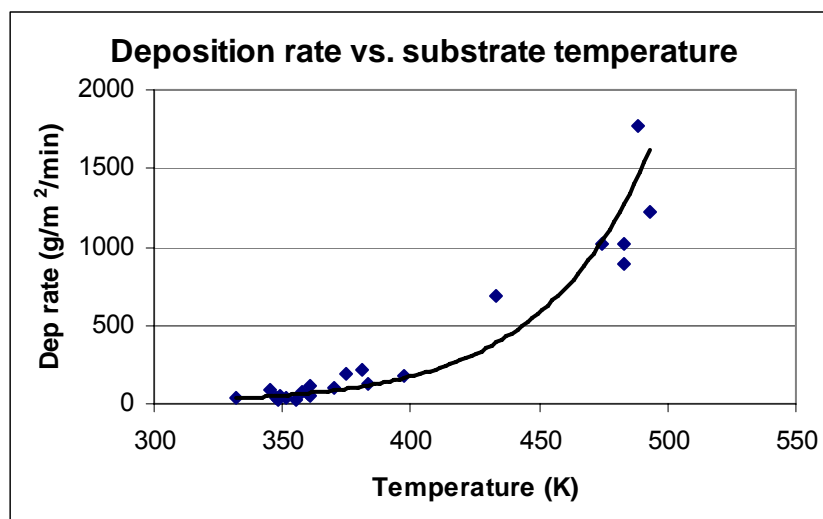
Figure 4.6 Combined kinetic data shown on a linear deposition rate vs. temperature scale

Figure 4.7 shows the combined data in a standard Arrhenius form along with the calculated slope and intercept values used in the calculation of the kinetic constants.

124

The measured kinetic constants obtained from this data gave the pre-exponential factor k_0 = 2160.5 cm/s and activation energy E = 37.0 kJ/mol. This activation energy value is at the low range of values reported in literature, which vary in a wide range from about 37 to over 180 kJ/mol [Smith, 1978].
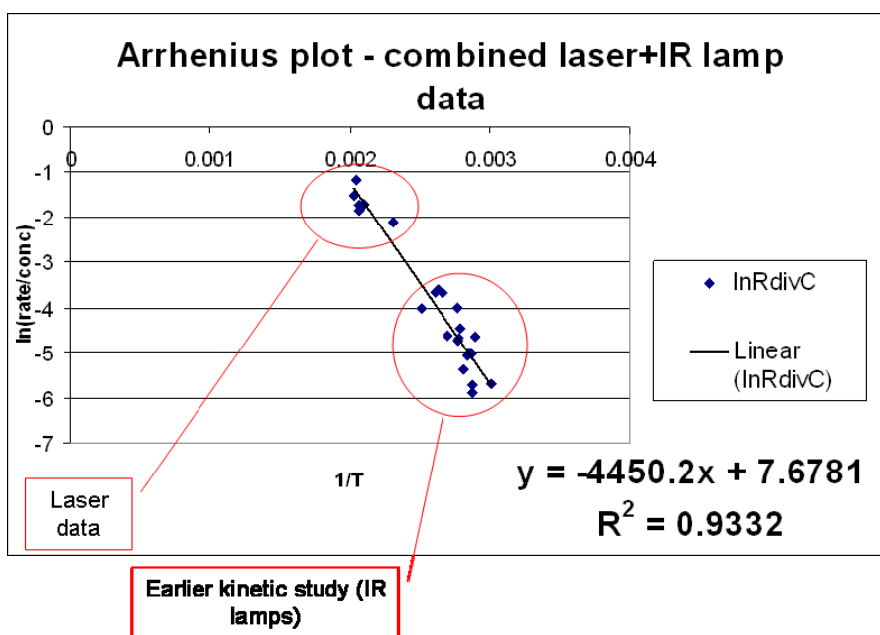
Figure 4.7 Arrhenius plot with combined IR lamp/conventional flow and laser/forced flow data points

To maximize the film deposition rate, it is clearly beneficial to operate at higher temperatures as long as one can prevent the onset of homogeneous decomposition.   Based on experimental observations and for intermediate concentrations of nickel carbonyl (20-40 vol.%) at or near atmospheric pressure, purely heterogeneous decomposition on a three-dimensional porous substrate appears to take place at temperatures up to about 220°C.

4.2　Modeling of local deposition rates

In the cross-flow reactor with the 2x2 cm^2 sample holder configuration, the plating gas formed a jet passing through the sample from the inlet side to the exit side of the chamber. In the following discussion, the volume of the foam sample irradiated by the laser beam will be treated as a small plug-flow reactor. Observation of the gas flow in experiments where a small amount of nickel powder forming in the gas phase allowed visualization of the gas flow pattern confirmed that (at least on a macroscopic scale) there was no visible gas re-circulation in the area of the reactor occupied by the foam. The macroscopic flow was always in one direction (from the inlet side to the exit side). However, due to the tortuous 3-D path of gas streams as they traversed the foam sample, local eddy currents enhanced the delivery of unreacted carbonyl molecules to the foam strut surfaces. This is demonstrated by the excellent uniformity of the nickel film coverage of all strut surfaces (for example see Figure 1.30 in Chapter one).

In the absence of free space decomposition and powder formation, the reaction was limited to the part of the reactor occupied by the foam sample. Thus the "active reactor" geometry can be approximated as a ~2 mm deep cylinder with the diameter of the laser beam. Also due to this geometry, the "active-reactor" gas flow pattern can be approximated by unidirectional, ideal plug-flow. Figure 4.8 illustrates the geometry considered in this simplified reactor kinetics model for calculation of local deposition rates.
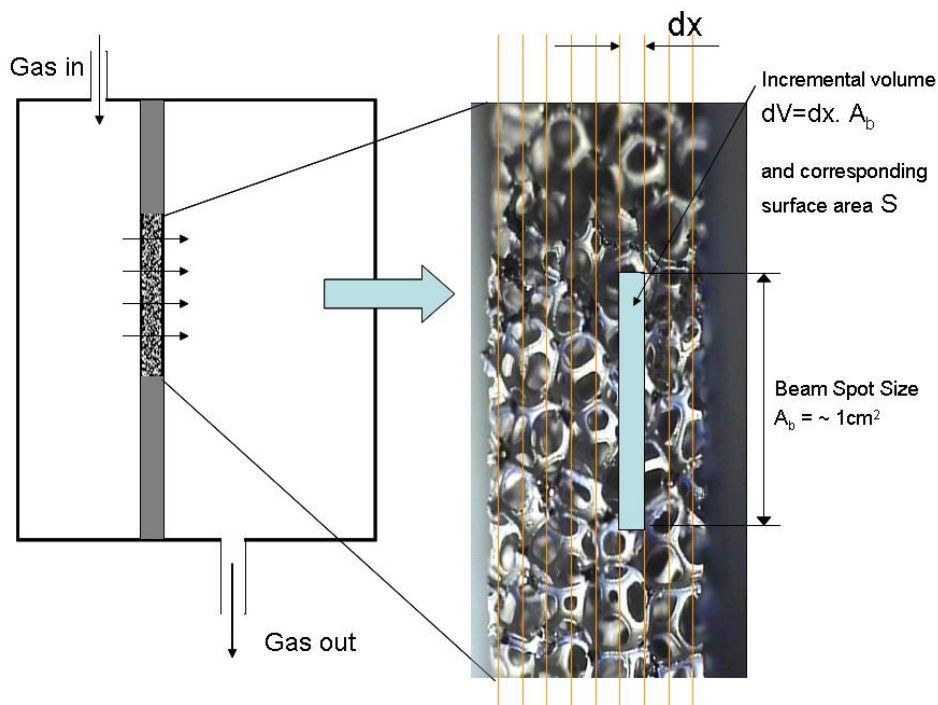
Figure 4.8 Reactor kinetics model – sample and flow geometry

4.2.1   Concentration gradient within the sample

The mass balance calculation will be now used to derive an expression for the variation of local gas concentration across the foam sample. The convection term due to the plug-flow approximation is $-u \cdot \dfrac{\partial c}{\partial x}$, where

$u =$ gas velocity (cm s^{-1})

$c = \mathrm{Ni(CO)}_4$ concentration (mol cm^{-3})

$dV = dx \cdot A_b$ incremental reactor volume (cm^3), $A_b =$ beam spot size

The surface reaction rate is: $r_s = -k_s \cdot c$, where k_s = surface reaction constant (cm s^{-1}). The gas-phase reaction rate is: $r_g = -k_g \cdot c$, where k_g = gas-phase reaction constant (cm s^{-1}).

Mass balance:

$$\frac{\partial c}{\partial t} = \frac{\partial N}{V \partial t} = -u\frac{\partial c}{\partial x} + D\frac{\partial^2 c}{\partial x^2} - k_g c - k_s c \qquad (4.1)$$

at steady state: $\frac{\partial c}{\partial t} = 0 \;\rightarrow\; -u\frac{\partial c}{\partial x} + D\frac{\partial^2 c}{\partial x^2} = k_g c + k_s c \qquad (4.2)$

For pure heterogeneous decomposition (no gas-phase reaction), $k_g c \rightarrow 0$

$$-u\frac{\partial c}{\partial x} + D\frac{\partial^2 c}{\partial x^2} = k_s c \quad \text{(dispersed plug-flow reactor approximation).}$$

Assuming ideal plug flow in the area of the reactor occupied by foam, the diffusion term can be set to zero: $D\frac{\partial^2 c}{\partial x^2} \rightarrow 0$. Hence, the concentration will vary with distance into the foam simply as follows:

$$-u \cdot \frac{\partial c}{\partial x} = k_s c \qquad (4.3)$$

If u is assumed to be a constant gas velocity through the sample and L is the foam total thickness, the equation can be solved in a simple way:

$$-u \cdot \int_{c_0}^{c} \frac{1}{c} dc = k_s \cdot \int_{0}^{L} dx \;\rightarrow\; c = c_0 \cdot e^{\frac{-k_s \cdot L}{u}} \qquad (4.4)$$

The concentration thus decays exponentially within the foam sample at a rate dependent on the deposition rate constant (which is a strong function of temperature), sample thickness L and gas flow rate (velocity). To achieve a uniform deposit across the thickness, it is important to minimize the concentration decay. Such a situation will be favored by a high gas flow, a low deposition rate and for thin samples.

4.2.2 Local deposition rate calculation

To evaluate the model numerically, we divide the foam sample into small volumes as illustrated in Figure 4.8 and treat these as individual small reactors. The output from one reactor is used as input to the next reactor (assuming surface reaction only), and so on. The Reynolds number at 25 cm/s gas velocity (common setting during the high-rate tests) is ~300, confirming a laminar flow condition within the sample opening, as also observed visually in tests where powder formation occurred (see videos in Figure 3.38 on page 99 in the electronic version of this thesis). The local deposition rate can be calculated from mass balance as a function of average concentration c_{av} (mol$_{Ni(CO)4}$/cm^3) (assuming first order reaction), flow rate F (mol/min) and effective surface area S (cm^2), given the rate constant k_s.

Mass balance:

carbonyl vapor in = surface reaction rate + carbonyl vapor out (approximated as c_{av})

$$F_{in} \cdot c_{in} = k_s \cdot S \cdot c_{av} + F_{in} \cdot c_{av} \rightarrow c_{av} = \frac{F_{in} \cdot c_{in}}{F_{in} + k_s \cdot S} \qquad (4.5)$$

Using the output (flow, concentration) from one incremental volume as the input to the next (assuming a purely surface or heterogeneous reaction), the local deposition rate profiles within the foam interior can be calculated. In the

following figures (4.9-4.12), various scenarios are included to illustrate the results of the model. The 2 mm foam thickness is divided into 10 segments for the purpose of the calculation.

1. constant temperature of 177 ^{o}C (450K), 20% carbonyl fed, 2x2 cm^2 sample opening, varying total gas flow (Case 1, Figure 4.9)

2. constant temperature of 230 ^{o}C (503K), 20% carbonyl feed, 2x2 cm^2 sample opening, varying total gas flow (Case 2, Figure 4.10)

3. constant total inlet flow 3 l/min, 20% carbonyl feed, 2x2 cm^2 sample opening, varying temperature (Case 3, Figure 4.11)

4. constant total inlet flow 3 l/min, constant temperature of 202 ^{o}C, 20% carbonyl feed, varying sample opening / gas velocity (Case 4, Figure 4.12)
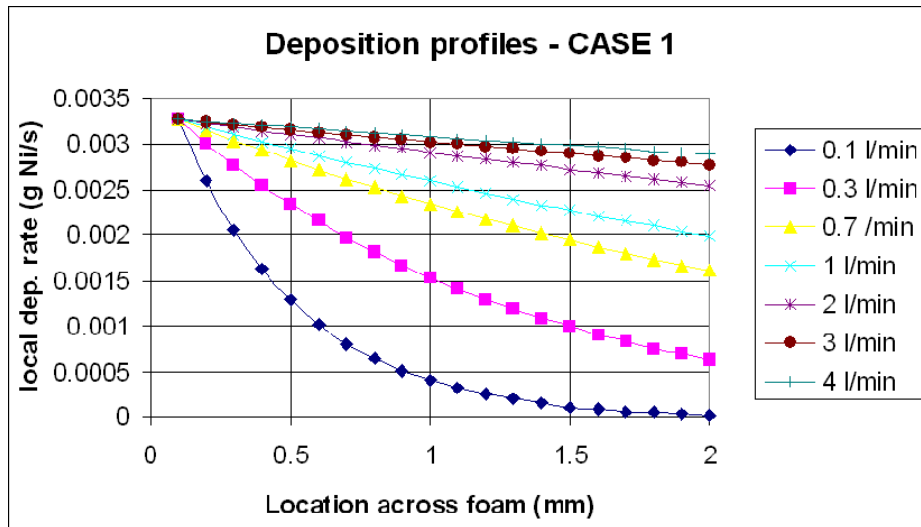
Figure 4.9 Deposition profile – T=450K, 2x2cm sample, 20% carb., vary total flow

130
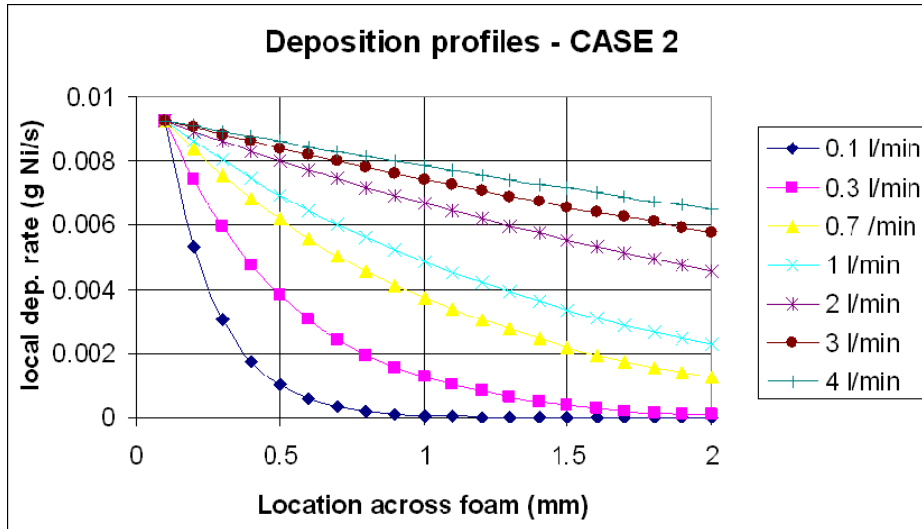
Figure 4.10 Deposition profile – T=503K, 2x2cm sample, 20% carb., vary total flow
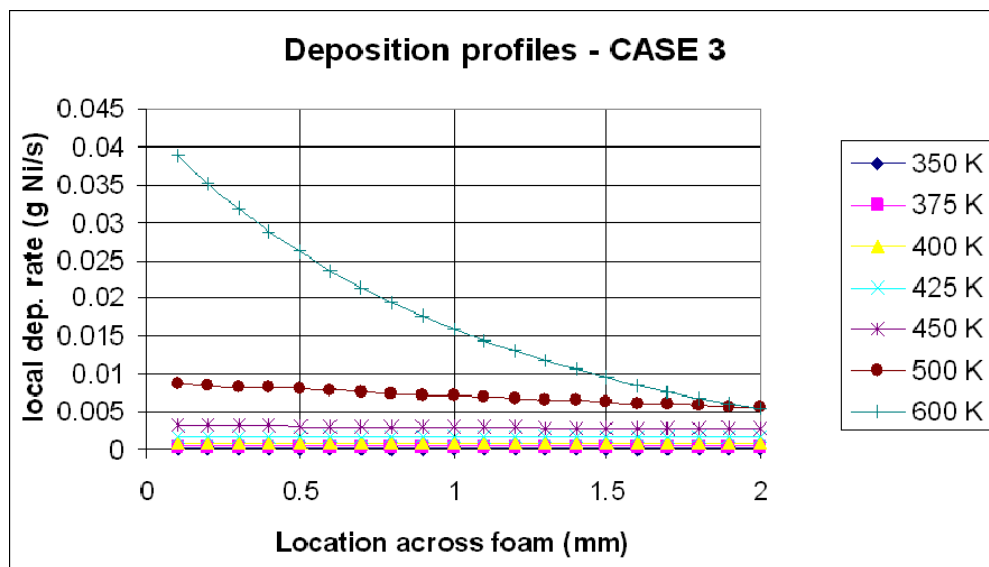
Figure 4.11 Deposition profile – flow 3 l/min, 2x2cm sample, 20% carb., vary temperature
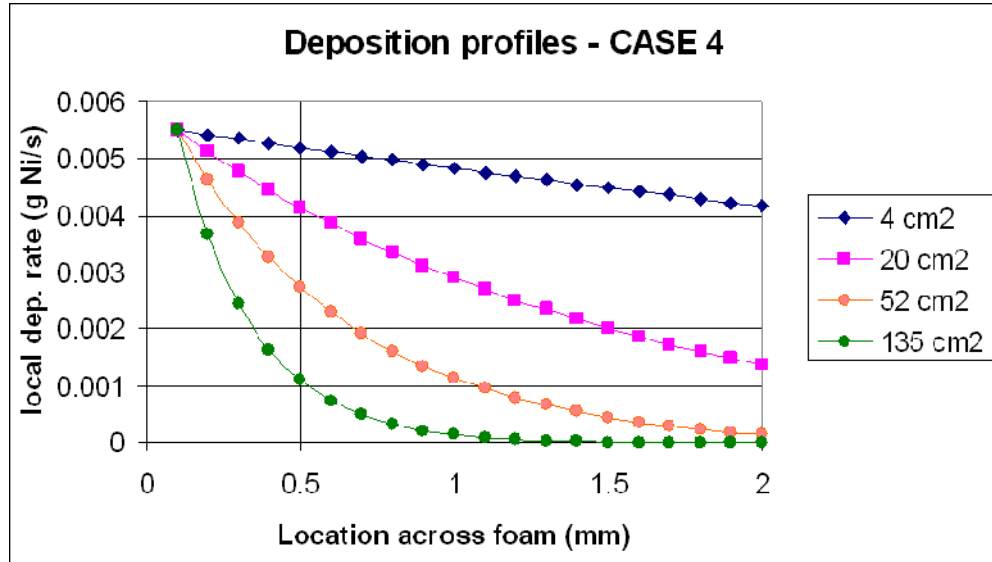
Figure 4.12 Deposition profile – flow 3 l/min, T=475K, 20% carb., vary sample opening (gas velocity)

4.3 Examples of experimental results

Two extreme cases are presented below along with experimental observation of deposit uniformity for both sets of conditions. In the first test (expt. # LH030131), the large sample opening of 135 cm^2 (almost fully open cross-section of the cylindrical chamber, see Figure 3.14 in Chapter three) resulted in an average gas velocity of < 1 cm/s across the foam. At an average temperature of 450 K, the model predicts an average deposition rate of 167 g/m^2/min, while the measured rate (coupon method, see Figure 3.46 in Chapter three) was 124 g/m^2/min. A typical optical microscope cross-section of one of the coupons from this test is shown in Figure 4.13 and the calculated deposition rate profile is in Figure 4.14, showing reasonable agreement. On the other hand, Figures 4.15 and 4.16 show a case of a uniform deposit produced at 435 K with the 4 cm^2 sample holder, a gas velocity of 16 cm/s, measured deposition rate of 720 g/m^2/min and calculated average deposition rate of 718 g/m^2/min.

132

Optimization of the deposition process thus involves careful selection of the operating conditions (gas flow regime and temperature in particular).

Figure 4.13 Sample LH030131 optical cross-section
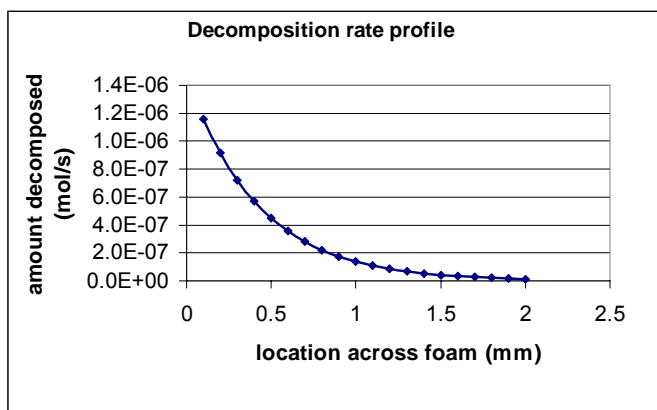
Figure 4.14 Calculated nickel distribution for conditions used to produce sample in Figure 4.13

Figure 4.15 Sample LH030328 optical cross-section
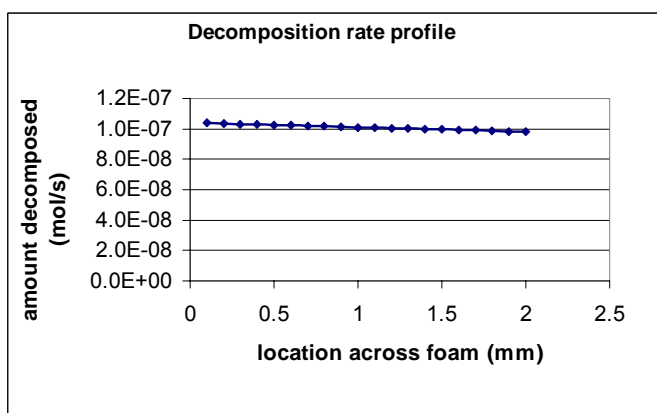
Figure 4.16 Calculated nickel distribution for conditions used to produce sample in Figure 4.15

4.4 Deposit microstructure analysis

Selected as-deposited samples were examined by SEM, high-resolution SEM, XRD and optical microscopy. This section also references high-resolution TEM and focused ion beam work done on as-deposited and sintered CVD foam samples by the CANMET/NRC[6] Materials Technology Laboratory, suggesting a possible reason for the inherent brittleness of the as-deposited foams.

4.4.1 Mechanism of structure formation

CVD deposit microstructures reflect the uni-directional transfer of atoms from the gas phase to the substrate and later to the growing deposit surface. In early stages of film growth, clusters form on the substrate surface and depending on the combination of diffusional (mass transport) and reaction kinetic factors, these develop into a variety of thick film structures ranging from single crystal, epitaxial deposits through large grain, columnar structure to nanocrystalline and even amorphous films. Shadowing effects, substrate temperature and energy of depositing atoms are among the influential factors that affect grain morphology.

In addition to Monte Carlo and molecular dynamics modeling [Müller, 1987] of film structure formation, several analog models were developed to describe the observed film growth phenomena. In the following discussion we will follow the growth dynamics model due to Bates et al. [1989] in interpreting the deposit morphologies observed in this work.

The following three elements of deposit formation are involved in a pyrolytic CVD process: 1) mass transport of the precursor molecules to the surface, driven by the bulk gas flow followed near the substrate surface by vapor phase diffusion; 2) incorporation of the mass into the deposit surface by thermally activated kinetic processes; and 3) mass transport *along* the deposit surface driven by capillary forces. Figure 4.17 defines the model parameters.

---

[6] CANMET Materials Technologies Laboratory / Natural Resources Canada

A bulk, fixed concentration of reactants c_b is maintained by an external vapor source. Diffusion D drives the molecules toward the surface where the reactant thermal decomposition takes place characterized by a kinetic mass-transfer coefficient k when new material is incorporated into the deposit. At steady state, the diffusive flux equals the incorporation flux and

Figure 4.17 Schematic view of the CVD process [Bates et al., 1989]

the instantaneous concentration field is given by

$$\Delta^2 c = 0 \tag{4.6}$$

$$c(z = \delta) = c_b \tag{4.7}$$

$$k[c(s) - c_{eq}(s)] = D\mathbf{n} \cdot \nabla c\big|_s \tag{4.8}$$

were s is a point on the surface and $\mathbf{n}$ is a unit vector normal to the surface. The equilibrium concentration of reactant molecules just above the surface is given by the Gibbs-Thompson formula:

$$c_{eq} = c_{flat} + \Gamma\kappa(s) \tag{4.9}$$

where Γ is proportional to the surface tension and $\kappa(s)$ is the local surface curvature.

Equations 4.6-4.8 are solved for any given morphology of the lower surface. The new surface is grown at a rate

$$v(s) = \Omega k[c(s) - c_{eq}(s)] \tag{4.10}$$

in the direction to the local normal (where Ω is the atomic volume of the solid) and the process is repeated.

135

There are three lengths scales that characterize the CVD process in this model: 1.) the width of the stagnant boundary layer δ, 2.) a capillary length $\xi = \Gamma /(c_b - c_{flat})$, and 3.) an effective maximum distance $d = D/k$ over which different parts of the surface "communicate" by evaporation (or volatization), gas-phase diffusion and re-decomposition (or re-condensation).

Flat surfaces grow at a steady-state velocity

$$v = \Omega D(c_b - c_{flat})/(d + \delta) \qquad (4.11)$$

However, the surface becomes unstable against small morphology perturbations with wavelength greater than

$$\lambda_c = 2\pi[\xi\delta(1 + d/\delta)]^{1/2} \qquad (4.12)$$

In order for this dimension to be greater than the characteristic dimension of the sample (to maintain flat/smooth deposit), one must operate the process sufficiently far into the surface kinetic-limited regime $(d/\delta \rangle\rangle 1$, i.e., at slow deposition rate.

Figures 4.18 is an example of a surface which started flat with small random fluctuations but fast kinetics $(\dfrac{d}{\lambda_c} \to 0$, or large k), and evolved into a finger-like morphology. Some fingers overtake their neighbors and their growth continues faster as the lower parts are "screened from nutrient" – the asymptotic growth patterns thus gradually consist of fewer, larger fingers.

Figure 4.19 illustrates the growth at slow kinetics $(\dfrac{d}{\lambda_c} = 2.5)$. The reactant molecules "pile up" near the surface and have time to form a layer of uniform concentration. Since at early stages the local surface curvatures are small, the growth occurs everywhere at similar rates and the surface features are less pronounced.

136
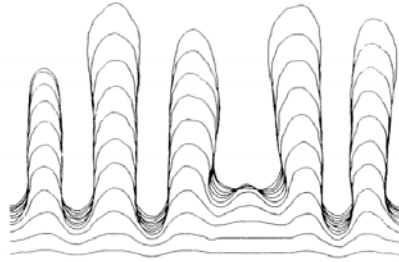
Figure 4.18 surface morphology with fast surface kinetics regime, λ_c is 1/10 of the figure width [Bates et al., 1989]
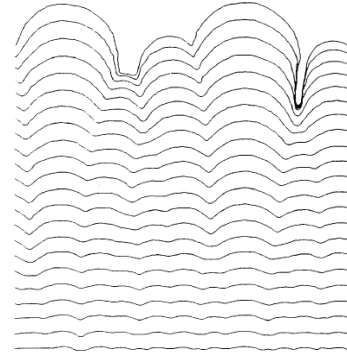
Figure 4.19 Surface morphology with slow kinetics regime, λ_c is 1/32 of the figure width [Bates et al., 1989]

These competing forces of reaction kinetics and mass transport are common to all vapor-based processes (PVD and CVD) and therefore the deposits share common morphological features.   The most common type of structure is columnar grain growth, normal to the substrate plane.

The local conditions (concentration of Ni atoms and temperature) may therefore favor the deposition at the ends of crystallites extending from the main deposit, and starve the areas near the main body of the deposit, between the protruding crystallites. Different parts of the deposit are thus subjected to a different degree of mass transport and kinetic control regimes. At higher substrate temperatures and in the presence of "buffer" gas (see Section 2.2.4), the deposit becomes more textured and exhibits various micron- and submicron-sized surface structures such as cones, pyramids, ridges and faceted planes. In the case of carbonyl nickel, the deposit surface is dominated by protruding, highly regular, 5 sided pyramid-shaped single crystal formations, representing situation depicted in Figure 4.18 (commonly referred to as a "spiky nickel" in industrial jargon). Since these crystal formations are of sub-micron dimensions, they are effective in trapping light in the visible wavelength range, causing the dark appearance of the deposit.

137

4.4.2 SEM surface imaging

The two surface morphology extremes are shown in Figures 4.20 and 4.21, respectively. The main difference in deposition conditions for these two samples was the substrate surface temperature: 160ºC (smooth surface sample, Figure 4.20) and 230ºC (spiky sample, Figure 4.21). Both samples were produced in the absence of H_2S additive. The use of additives such as H_2S produces much finer grain size deposits, and spiky surface of the extent produced in sulfur-free atmosphere is not observed. The H_2S effect is further discussed in Section 4.5.

The surface darkening effect is best observed on the experiment video included on page 99 of the electronic version of this thesis (Figure 3.38). The tips of the pyramid-shaped crystallites are extremely sharp and the structure has the right dimensions for trapping electromagnetic radiation of visible wavelengths. This morphology is also found on the surface of regular (sulfur-free) nickel pellets, the dominant form of bulk carbonyl nickel.

One can envision utilizing nickel foam with this surface morphology as a substrate for photovoltaic coatings to produce 3-D solar cells. It could be also used to produce additional functionalized surface utilizing e.g. carbon nanotubes [Paserin et al., 2008].
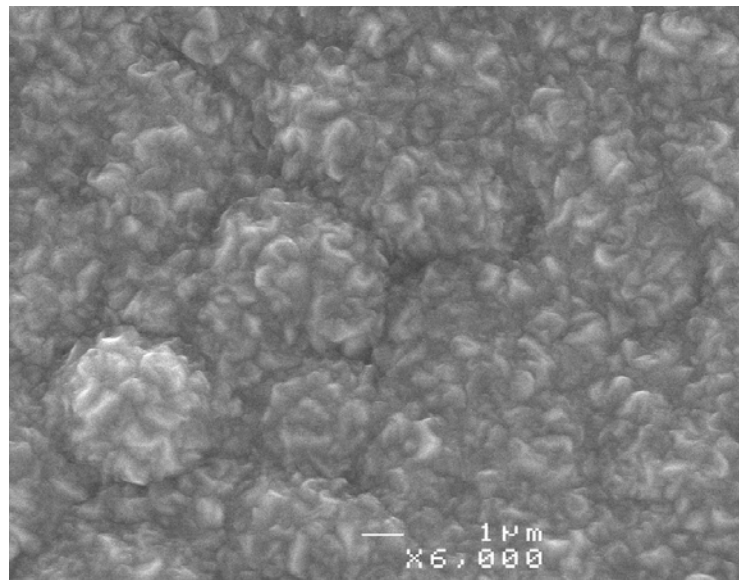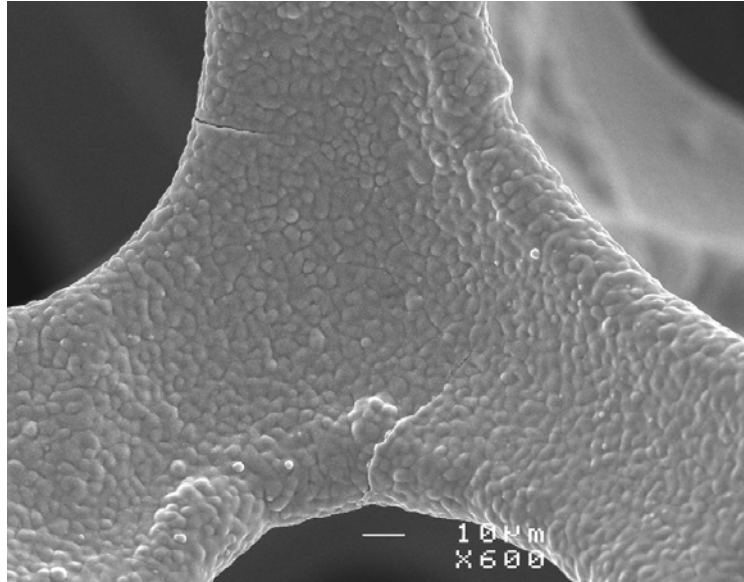
Figure 4.20 Surface morphology of a foam sample produced at 160ºC substrate temperature imaged at 600x and 6000x magnification (expt. LH050310)
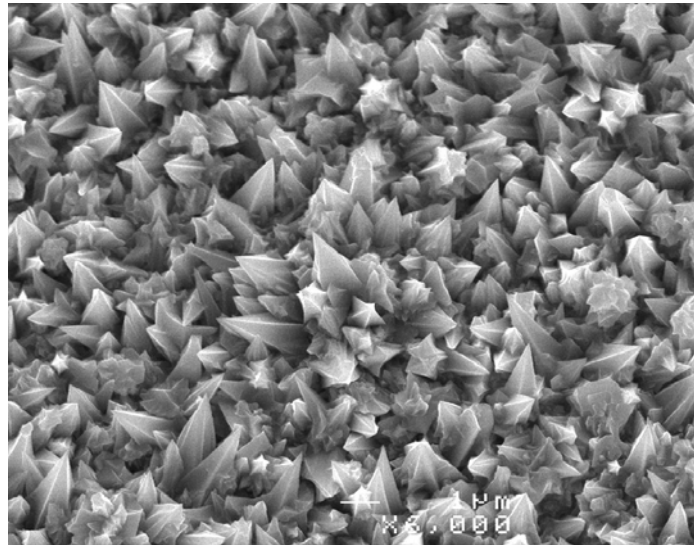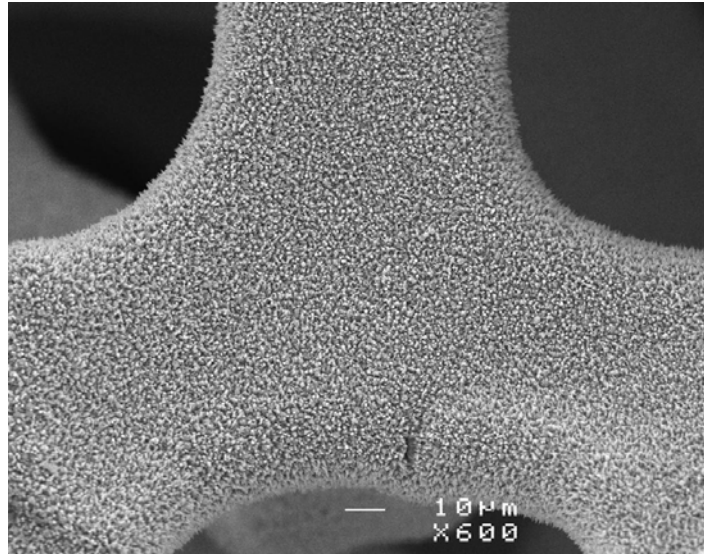
Figure 4.21 Surface morphology of a foam sample produced at 230°C substrate temperature, imaged at 600x and 6000x magnification (expt. LH050308)

4.4.3 Focused Ion Beam microscopy

A suitable technique for imaging the grain size of as-deposited and annealed nickel foams is focused ion beam (FIB) microscopy [Carpenter et al., 2004]. FIB systems use a finely focused beam of gallium ions that can be operated at low beam currents for imaging or high beam currents for site specific sputtering or milling. The images in Figures 4.22 – 4.23 and 4.24 show a foam strut of as-deposited and annealed nickel foam samples, respectively, after stress-free sectioning using the ion beam. Due to the pronounced grain orientation FIB sectioning and imaging reveal grain structure and porosity difficult to observe using traditional techniques. Prior to taking the image, the sample surface was sputtered in such a way as to preferentially etch grain boundaries on the "sides" of the strut and to minimize grain boundary etching on the "top" surface of the sectioned portion of the strut. As-deposited samples exhibit sub-micron grain size, while the annealed sample image shows that the grains grew to several microns during the annealing process. The annealed sample image in Figure 4.24 also shows some internal porosity typically present in annealed samples. As discussed in Section 1.6.2, the organic vapors migrate to the surface during the high temperature treatment and most of them leave the structure upon reaching the surface of the deposit. The pores visible in the sectioned specimen are likely caused by trapped gases evolving during the vaporization of the PU foam substrate that did not make it to the surface. The largest pores are found at the grain boundary nodes where three or more grain boundaries meet.
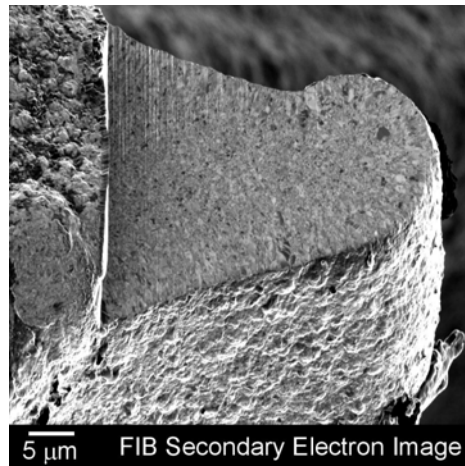
Figure 4.22 Focused Ion Beam image of as-deposited nickel foam sample
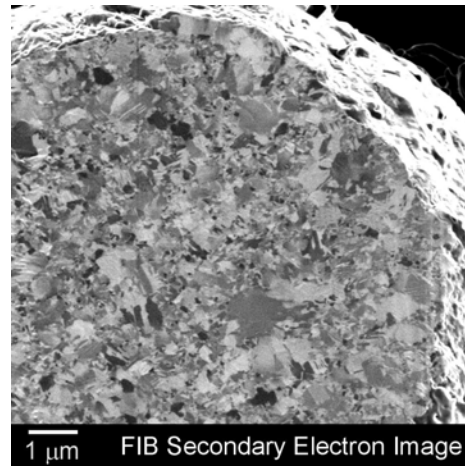
Figure 4.23 Detail of as-deposited nickel foam structure showing sub-micron grain sizes
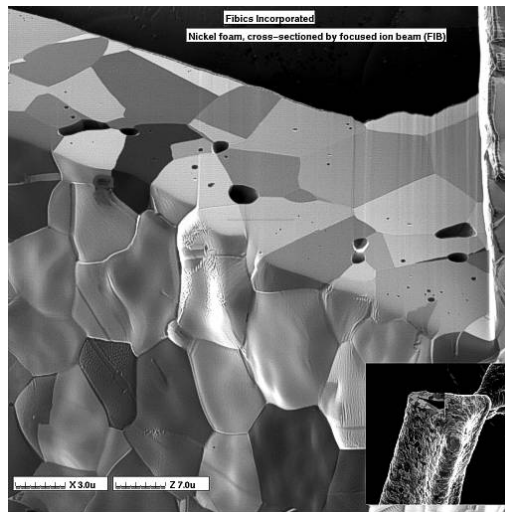
Figure 4.24 Focused ion beam image of a portion of a Ni foam strut after polymer burn-out and high temperature anneal, showing grains several microns in size

4.4.4   Study of microstructures formed in transient regime

In addition to the spiky morphology described above, the onset of free-space decomposition observed in the course of some experiments yielded a variety of interesting microstructures. Nickel filaments, wires and agglomerated particles were found either loosely on the surface of the foam or attached to the surface. These structures form by gas-phase nucleation of Ni atoms, agglomeration into clusters and particles that eventually attach to each other and, likely due to the magnetic properties of nickel, self-assemble to form filaments (the process operates well below the Ni Curie point of 354ºC). The size of the primary particles forming the majority of the filaments, which appeared quasi-spherical in shape, was of the order of 1 micron.   An SEM micrograph at 12,000x magnification capturing some of these particles in the initial stages of forming new branches on existing filaments is shown in Figure 4.25.   These initial particles were much smaller, of the order of ~50-100 nm in diameter.
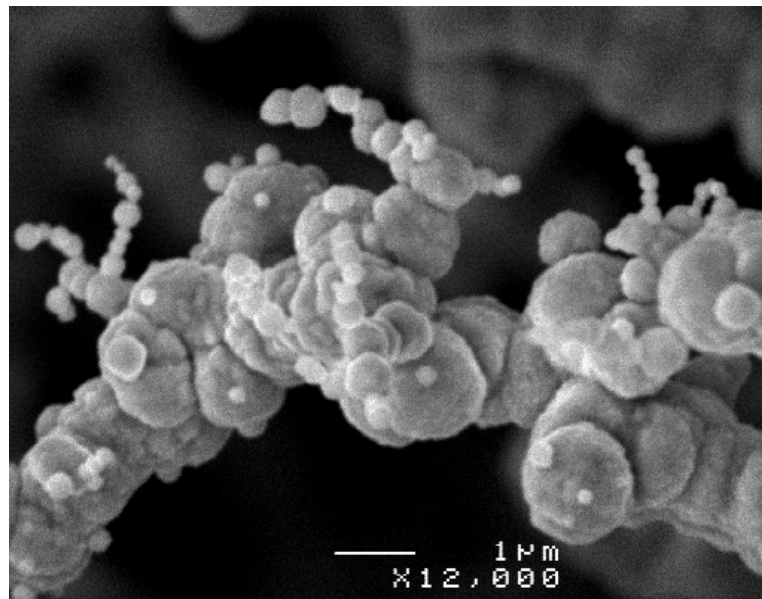
Figure 4.25 SEM micrograph of primary particles being assembled into filaments
(expt. # LH041214)

143

Figure 4.26 shows an example of interlinked nickel filaments of relatively consistent size (~1 micron wide) forming a complex filamentary network. The individual filaments span distances of few tens of microns before contacting other filaments to form a common node. An image of such node is shown at 10,000x magnification in the left part of Figure 4.26.
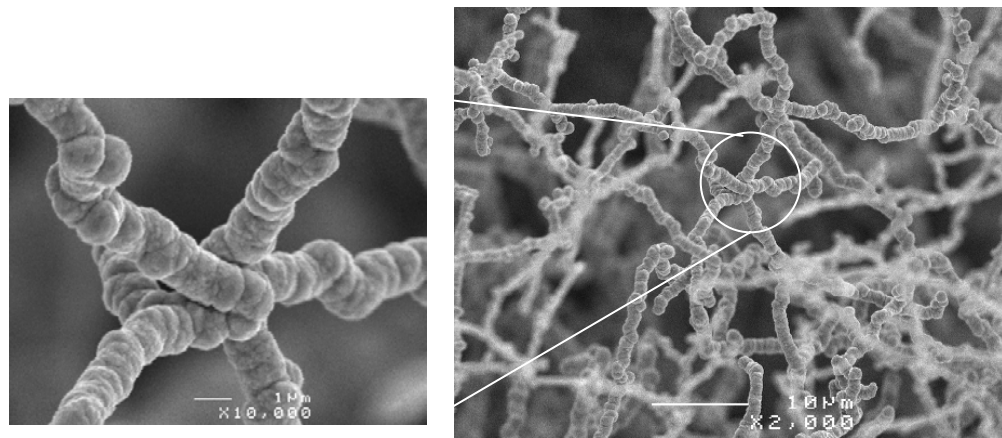
Figure 4.26 A network of filaments ~1 micron in diameter (expt. # LH041214)

It is possible to design enhanced surface area nickel foam structure by controlling the process in pure heterogeneous mode during the main deposition on the PU substrate, and finishing the deposition process by entering the filamentary powder forming conditions at the end. The filaments are found forming "nickel web" wrapped around the nickel foam struts as shown in Figure 4.27. Such structure may find applications in the use of Ni foam as a catalyst support, low pressure drop "superstructure" providing additional surface area and customizable flow characteristics.
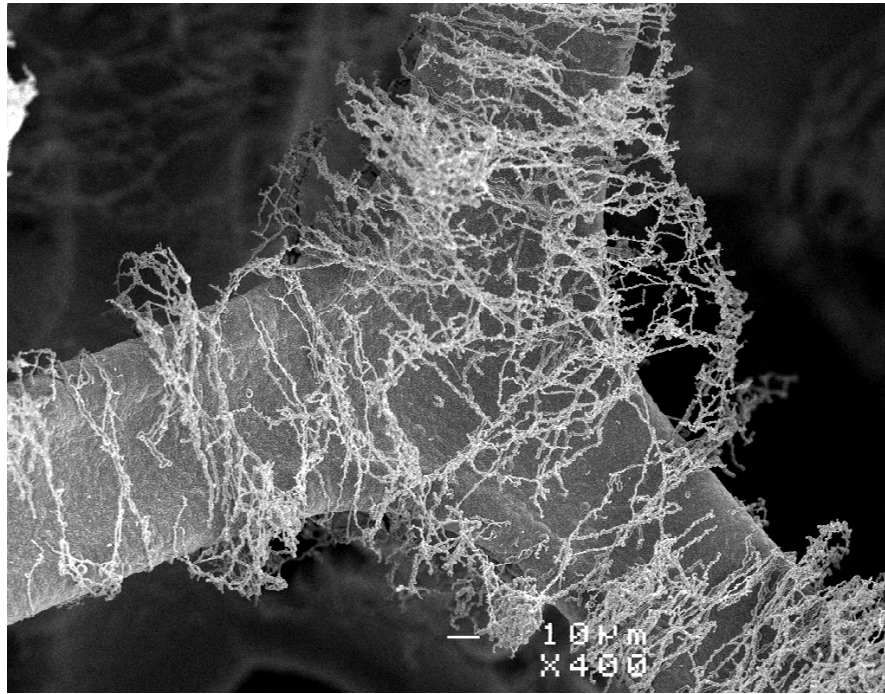
Figure 4.27 Nickel web enveloping a foam strut (expt. # LH041214)

Another example of a microstructure formed by the interplay of the local homogeneous and heterogeneous decomposition conditions is shown in Figure 4.28. The space between struts was filled with loose powder, providing seeds for the growth of dendritic "Ni grass" in the area between struts. Cauliflower-shaped nodules were found growing on the struts themselves. This is an example of the variety of deposit forms caused by different local mass transport conditions due to the shape of the substrate at each location, the proximity to the main gas flow area, and local temperature effects. As discussed in Section 4.4.1, the area near the bottom of this cell would experience particularly strong depletion of the precursor molecules, as these are consumed by the surrounding cauliflower-shaped nodules. The deposit morphology is thus highly irregular, in the form of thin Ni columns or whiskers.

145
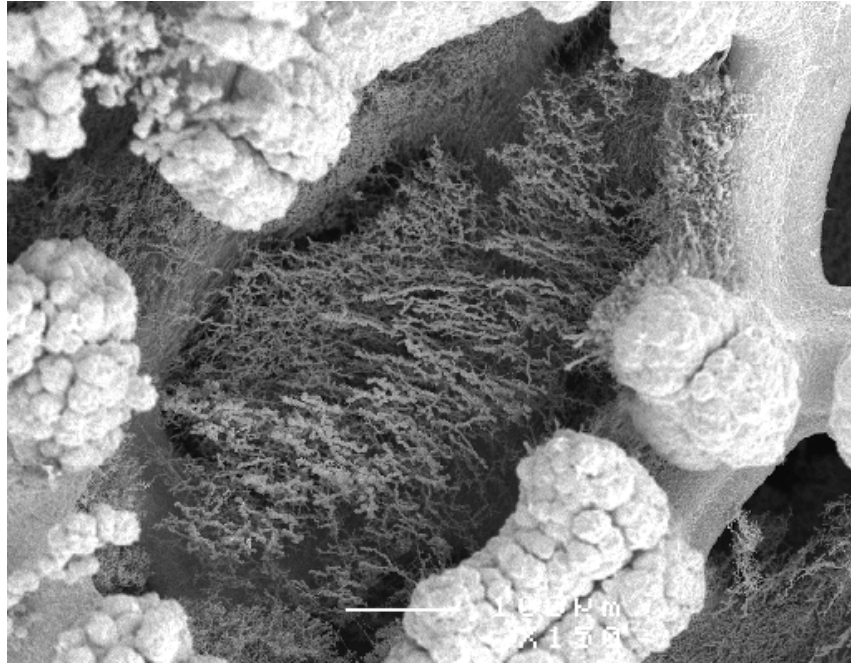
Figure 4.28 A growth of "Ni grass" between the struts of foam cells
(expt. # LH041214)

4.4.5 Etched deposit imaging

Etching of a sample cross-section prepared for SEM imaging uniquely reveals the microstructure and the density of the deposit. This was done on a sample using a PU substrate plated by the standard 2-step process (40 seconds – low power pre-plate, 60 seconds – main deposition at full power). The etched cross-section of this sample is shown in Figure 4.29. The etching solution used was a 50/50 nitric/acetic acid. The image revealed different structure in the first 2-3 microns of the initial deposit, likely caused by the presence of organic vapors due to partial decomposition of the PU substrate. The surface SEM image of the pre-plate sample taken in a thin area adjacent to the substrate surface confirms the

146
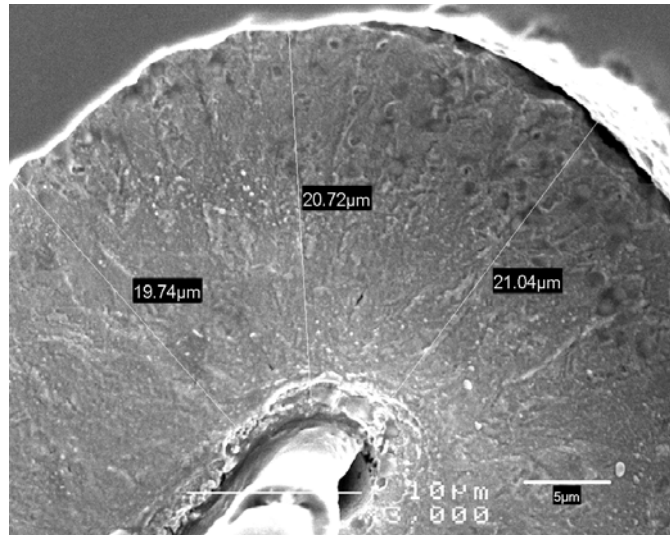
Figure 4.29 Etched (50/50 nitric/acetic acid, 30 second immersion time) cross-sectional view in high contrast SE mode showing fine structure – sample LH040625

difference in morphology in the PU-Ni deposit interface layer (Figure 4.30, left image). The thin cross-section (Figure 4.30, right image) shows that in some areas, the deposit adjacent to the PU substrate is not continuous during the early stages of deposition (initial 1-2 microns).
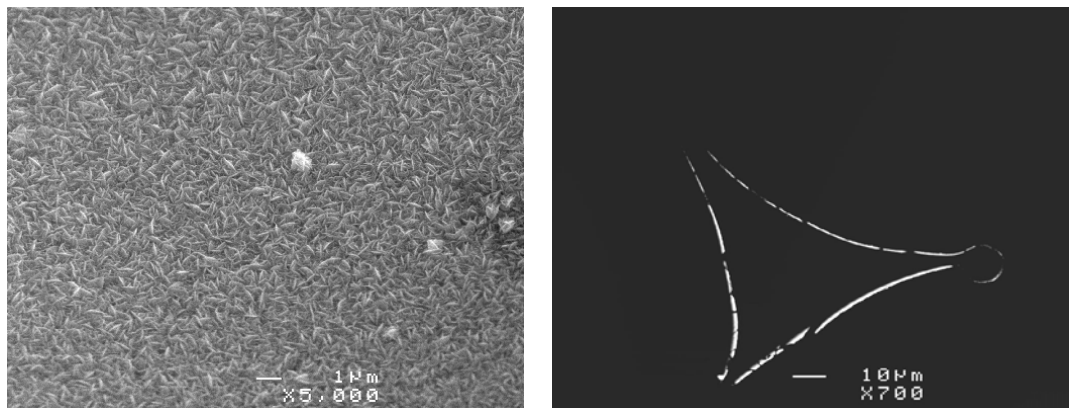
Figure 4.30 SEM surface (left image) and cross-section (right image) of a thin Ni film deposited on the PU substrate during sample pre-plate step

147

4.5   Deposition without H₂S

4.5.1   Use of sulfur-containing gas additives in carbonyl CVD

H_2S or other sulfur-containing gas additives (e.g. COS) are commonly used in the nickel carbonyl CVD process to enhance the deposit uniformity and to produce a smooth surface morphology. In the commercial Ni foam CVD process, a typical H_2S concentration used was 0.2 vol%. This resulted in approximately 0.2 wt% sulfur in the as-deposited foam (i.e. about 80% of the added sulfur was incorporated in the deposit). The subsequent high-temperature anneal (~900 ºC) in the presence of hydrogen brought the sulfur content in the final product to <50 ppm.

The sulfur containing gas additives are often referred to as "catalyst", even though they are at least partially consumed in the CVD reaction. While the actual mechanism of sulfur action is not fully understood, it is generally regarded as a "poison" preventing growth of larger single-crystal areas during Ni deposition (selective poisoning). A possible mechanism leading to the deposit creating uniform coverage (smooth morphology) assumes the formation of localized patches of sulfur on the growing nickel surface, temporarily blocking nickel deposition at such sites. The further deposition of nickel alongside the contaminant would eventually wrap around the "poisoned" region until the nickel closed over to form a nano-size pore. Such nanopores were observed in a TEM study of as-deposited Ni foams [Carpenter et al., 2004].

Another possible explanation originates in the study of carbonylation effects. In nickel carbonyl formation, sulfur species are thought to act as a catalyst in forming adsorbed, activated $Ni(CO)_x$ complexes on the reduced nickel surface, with a characteristic IR absorption at 2082 cm⁻¹. These subsequently participate in the formation of a stable nickel carbonyl molecule by reacting with physically

adsorbed CO from the gas phase. This conclusion was made on the basis of experimental study using gas adsorption isotherms and IR spectroscopy in carbonylation of freshly reduced and sulfided nickel surfaces [O'Neill, 1961]. Similar mechanism could be active in the process of "stripping" the carbonyl molecule of the CO ligands by a catalytic action of adsorbed sulfur.

The sulfur-free deposition process is of interest due to simplified post-processing requirements and greater stability of the nickel deposit (lower nickel activity), opening the possibility for the material use *without* the subsequent heat treatment. Sulfur-free foams are also easier to sinter since the material does not go through a temperature phase with poor mechanical properties due to liquid-phase sintering responsible for removal of the sulfur species.

4.5.2   Sulfur-free deposition on polyurethane substrate

Figures 4.31 and 4.32 show the surface morphology and the cross-section of a sample prepared on a PU substrate *without* H_2S, respectively (at 3.8 l/min total gas flow, expt. LH050407). This was a 30-second experiment (15s pre-plate and 15s high rate part) attempting to minimize the pre-plate period of low rate deposition on the PU substrate (earlier established at 40 seconds at 25A laser current). The temperature during the high-rate portion of the deposition did not exceed about 150ºC, however, visible off-gassing of the PU substrate was observed in the initial stages and some Ni powder formation toward the end of the experiment. Both images clearly show areas where the deposition was inhibited, and the growth continued only in selected areas. It is hypothesized that this phenomenon is caused by the formation of a passive layer due to the deposit of contaminants (from the PU foam) that inhibit further nickel growth. H_2S was found to act as a catalytic agent helping to overcome this phenomenon (see Figures 1.30 or 3.29, H_2S and longer pre-plate times were used in these cases). It should be possible to avoid such patchy morphology in high-rate deposition by careful control of the

149

pre-plate process without H_2S, encapsulating the PU substrate with a continuous Ni deposit without significant off-gassing (also evidenced by the fact that the thin pre-plate deposit appears continuous). This remains to be demonstrated experimentally and is one of the suggestions for future work.
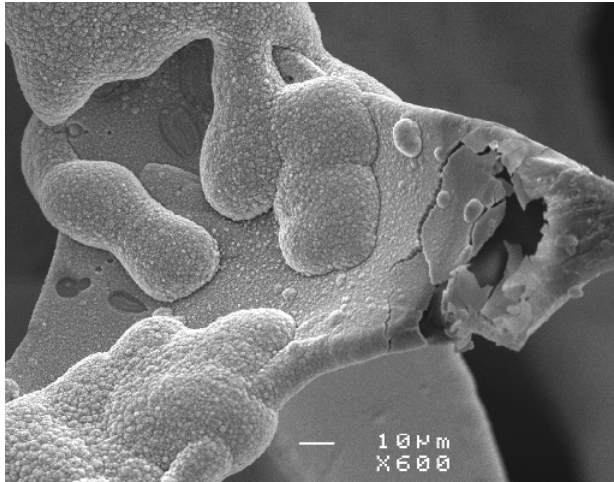
Figure 4.31 Surface morphology of a foam sample produced without H_2S at 3.8 l/min gas flow (expt. LH050407)
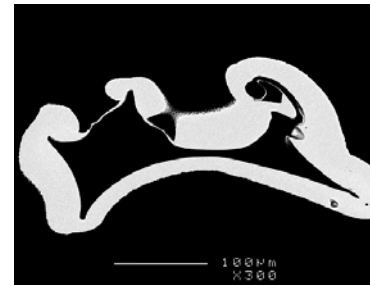
Figure 4.32 Cross-sections of the same sample, showing passivated areas

4.5.3   Nickel foam substrate

H_2S-free deposition was also done on nickel foam substrate to confirm whether the same high deposition rates are achievable as in the catalyzed process. Figure 4.33 shows the cross-sections of the sample produced in this test. A slight gradient in the deposit thickness is measured from one side to the other, likely caused by the depletion of carbonyl within the foam sample. The average deposition rate was 12.04 µm /min, somewhat higher than the rate measured on PU substrate. As in other tests on nickel foam substrate, a clear boundary is visible between the original electrodeposited and sintered nickel and the new CVD deposit.
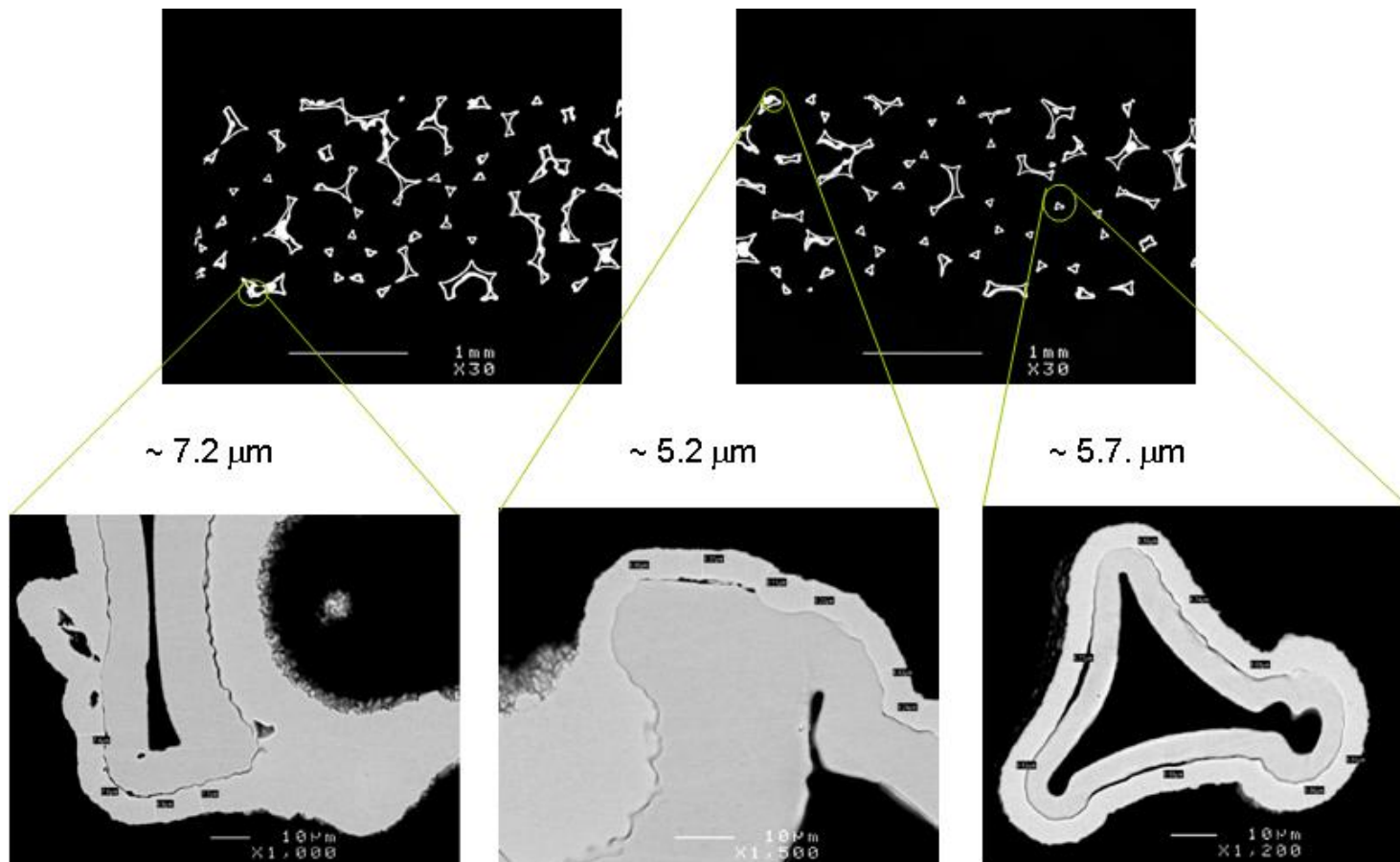
Figure 4.33 Deposit thickness determination by image analysis – expt. LH050406 (H_2S-free deposition on Ni foam substrate)

151

4.6   XRD analysis of as-deposited and annealed Ni foam

The average crystallite size in typical, as-deposited foam samples measured from SEM images and consistent with the XRD pattern was estimated at approximately 1 μm. During the high-temperature sintering step, the grain size typically grows to a final size of 5 to 10 μm, depending on the sintering conditions and the initial sulfur content. Figure 4.34 shows a typical XRD pattern of as-deposited (broader peaks) and sintered (narrow peaks) nickel foams.
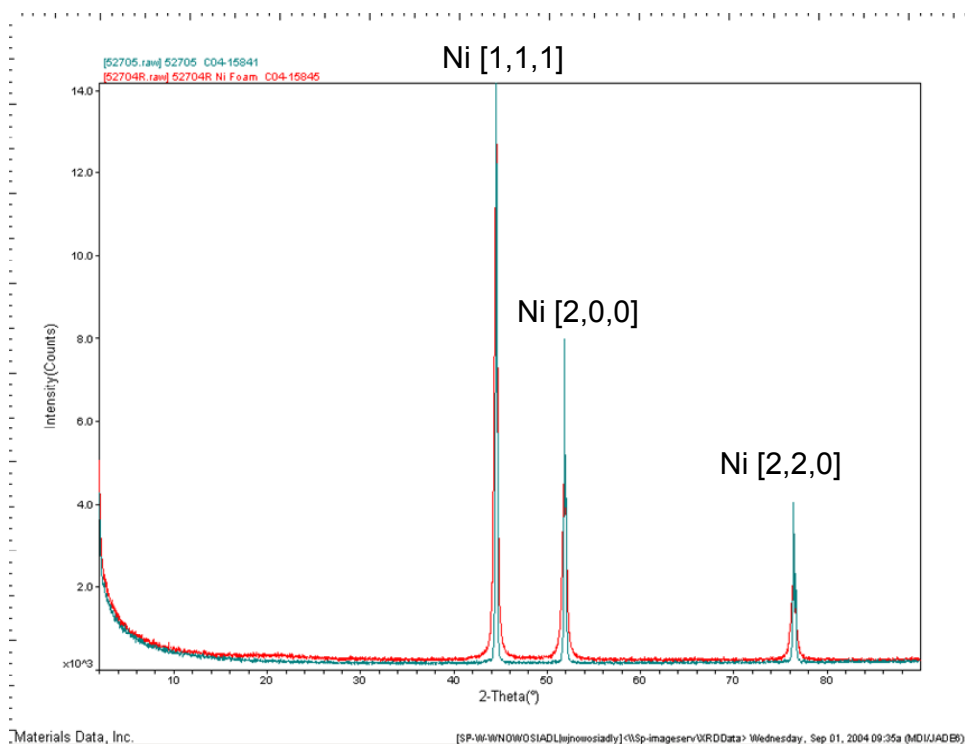
Figure 4.34 XRD of as-deposited (red, broader peaks) and annealed Ni foam (green, narrow peaks)

5 CVD PROCESS MODELING AND SCALE-UP CONSIDERATIONS

5.1 Three-dimensional Computational Fluid Dynamics modeling

Gas flow patterns and thermal effects have been studied by modeling the reactor chamber and deposition process using commercial Computational Fluid Dynamics (CFD) software package Ansys® CFX, version 5.7. The main goal of this work was to confirm the flow patterns inside the CVD chamber and to demonstrate how these depend on the configuration of the sample holder and facilitate the flow-through geometry.

5.1.1 CFD principles

CFD is based on a sequence of iterative calculations that predict the internal states in a complex flow by a numerical solution of the following conservation equations of mass, momentum and energy [AEA Technology, 2000]:

Mass balance or continuity equation:

$$\frac{\partial \rho^g}{\partial t} + \frac{\partial \left(\rho^g \, u_i^g \right)}{\partial x_i} = 0 \tag{5.1}$$

where ρ^g and u_i^g are gas density and velocity, respectively, and index i represents the three directions of the Cartesian coordinate system.

Momentum transport equation in direction i for a turbulent flow is given by:

$$\frac{\partial}{\partial t}\left(\rho^g u_i^g\right)+\frac{\partial}{\partial x_j}\left(\rho^g\ u_i^g u_j^g\right)=-\frac{\partial p}{\partial x_i}+\frac{\partial \tau_{ij}^g}{\partial x_j}-\frac{\partial}{\partial x_j}\left(\rho^g\overline{v_i'^g v_j'^g}\right)+\rho^g g_i+F_i \quad (5.2)$$

where p is pressure, τ_{ij}^g are viscous stresses, $\rho^g\overline{v_i'^g v_j'^g}$ are turbulent or Reynolds stresses, g_i is gravity along direction i, and F_i represents other body forces exerted on the fluid in this direction.

Buoyancy, or a body force acting on a fluid in which there are density gradients, is described by $B=\rho g$, where density variation with temperature for an incompressible (or weakly compressible) fluid follows the Boussinesq approximation:

$$\rho = \rho_0\left[1-\beta\left(T-T_0\right)\right] \quad (5.3)$$

where T_0 is the buoyancy reference temperature, and β is the gas thermal expansion coefficient.

In **energy or heat transfer,** the enthalpy transport equation for a turbulent flow, assuming the turbulence is modeled with an eddy viscosity, μ^t, can be written as follows:

$$\frac{\partial}{\partial t}\left(\rho^g h^g\right)+\frac{\partial}{\partial x_j}\left(\rho^g\ u_j^g h^g\right)=\frac{\partial}{\partial x_j}\left[\left(\frac{\mu^t}{\sigma_h}+\frac{\lambda^g}{C_p}\right)\frac{\partial h^g}{\partial x_j}\right]+\frac{\partial p}{\partial t} \quad (5.4)$$

Since the fluid is assumed to be thermally perfect, the enthalpy h^g can be written in terms of the specific heat and temperature:

$$h^g = \overline{C}_p(T)T-\overline{C}_p\left(T_{ref}\right)T_{ref} \quad (5.5)$$

where

$$\overline{C}_p(T)=\frac{1}{T}\int_0^T C_p(T')dT' \quad (5.6)$$

Here T_{ref} is the enthalpy reference temperature. Equation 5.4 assumes Fourier's conduction law and a thermally perfect fluid with negligible work due to body forces and negligible viscous dissipation.

Turbulence model

The Reynolds stresses, $\rho^g \overline{v_i'^g v_j'^g}$, in the momentum equations are unknown and require a closure model. The eddy viscosity hypothesis is used to model the Reynolds stresses. The eddy viscosity hypothesis states that the Reynolds stresses can be linearly related to the mean velocity gradients, as given below:

$$\rho^g \overline{v_i'^g v_j'^g} = -\mu^t \left(\frac{\partial \overline{v_i^g}}{\partial x_j} + \frac{\partial \overline{v_j^g}}{\partial x_i} \right) + \frac{2}{3} \left(\rho^g k^g + \mu^t \frac{\partial \overline{v_m^g}}{\partial x_m} \right) \delta_{ij} \qquad (5.7)$$

Here, k is turbulent kinetic energy, defined as:

$$k^g = \frac{1}{2} \sum \overline{\left(u_i'^g \right)^2} \qquad (5.8)$$

A $k - \varepsilon$ turbulence model is used to determine the values of k and μ^t. The eddy viscosity in the $k - \varepsilon$ model is related to the turbulent kinetic energy, k, and dissipation rate, ε as given below:

$$\mu^t = \rho^g C_\mu \frac{k^{g2}}{\varepsilon^g} \qquad (5.9)$$

The dissipation rate of the turbulent kinetic energy, ε^g is defined by the following expression:

$$\varepsilon^g = v \left(\overline{\frac{\partial u_i'}{\partial x_i} \frac{\partial u_i'}{\partial x_i}} \right) \qquad (5.10)$$

where v is the kinematic viscosity.

The transport equations for the turbulent kinetic energy and dissipation rate are:

$$\frac{\partial}{\partial t}\left(\rho^g k^g\right)+\frac{\partial}{\partial x_j}\left(\rho^g \overline{v_j^g} k^g\right)=\frac{\partial}{\partial x_j}\left[\left(\mu^g+\mu_T^g/\sigma_k\right)\frac{\partial k^g}{\partial x_j}\right]+\tau_{ij}^g\frac{\partial \overline{v_i^g}}{\partial x_j}-\rho^g \varepsilon^g \quad (5.11)$$

$$\frac{\partial}{\partial t}\left(\rho^g \varepsilon^g\right)+\frac{\partial}{\partial x_j}\left(\rho^g \overline{v_j^g}\varepsilon^g\right)=$$

$$=\frac{\partial}{\partial x_j}\left[\left(\mu^g+\mu_T^g/\sigma_\varepsilon\right)\frac{\partial \varepsilon^g}{\partial x_j}\right]+C_{\varepsilon 1}\frac{\varepsilon^g}{k^g}\tau_{ij}^g\frac{\partial \overline{v_i^g}}{\partial x_j}-\rho^g C_{\varepsilon 2}\frac{\varepsilon^{g^2}}{k^g} \qquad (5.12)$$

where C_μ, $C_{\varepsilon 1}, C_{\varepsilon 2}, \sigma_k$ and σ_ε are constants with default values described in the CFX software solver manual.

The solution of these calculations is a complete spatial description of the fluid states (temperature, velocity, density, turbulence) within the domain of interest.

A CFD model divides the region of interest (in our case the internal volume of the cylindrical reactor), into a large number of small cells (control volumes), forming a mesh or a grid covering the area of interest.   The above partial differential equations describing the fluid flow are re-written as algebraic equations that relate the local pressure, velocity, temperature, reaction rates and reactant concentrations to the values in the neighboring cells. These equations are then solved numerically yielding a complete picture of the flow fields, local temperatures and local reaction rates. The results can be visualized by 3-D color-coded plots showing fluid streamlines, velocity vectors and contours representing values of various process variables of interest. The solutions of the multiple equations are often computationally intensive and require significant computing resources.

5.1.2   CFD model setup

The first stage in a CFD model development is the creation of a geometry which represents the object being modeled.   This was done using Ansys Design

Modeler software. From this point, a mesh is generated which creates the cells and control volumes. The CFD software can automatically optimize the mesh to concentrate analysis on points of interest. Figure 5.1 shows the overall geometry with the reactor interior shown in a mesh format to illustrate the size of the individual cells. The entire reaction chamber consisted of 313,500 elements (about 72% tetrahedrons, 27% prisms and 1% pyramids). Figure 5.2 shows the sample opening area with a denser mesh, providing more detailed description of the reactor area of interest. This is where most of the nickel carbonyl decomposition takes place (100% in case of purely heterogeneous decomposition). Because of the complex 3-D structure of the foam surface and its high porosity (>97 vol. %, therefore high gas permeability), the foam sample opening was modeled as a single-phase sub-domain of the main reactor containing volumetric energy source, located within the foam (in reality the energy was absorbed by the foam from an external laser source). The energy transfer to the gas was modeled utilizing the CFD solver "isotropic loss model", which is appropriate for isotropic porous regions. The model specifies coefficients for permeability and loss, in generalized form of Darcy's law:

$$\frac{\partial p}{\partial x_i} = \frac{\mu}{K_{perm}} u_i + K_{loss} \frac{\rho}{2} |u| u_i \tag{5.13}$$

Where μ is the dynamic viscosity, K_{perm} is the permeability and K_{loss} is the empirical loss coefficient. The model parameters were selected so that the model predicts temperatures in the sample opening area close to those measured by the thermocouple on the foam surface. The transferred energy is then used to drive the decomposition of nickel carbonyl gas above a certain temperature (373 K was set as the reaction extinction temperature). The reaction rate was modeled using the Arrhenius relationship and constants described in Chapter four.

157
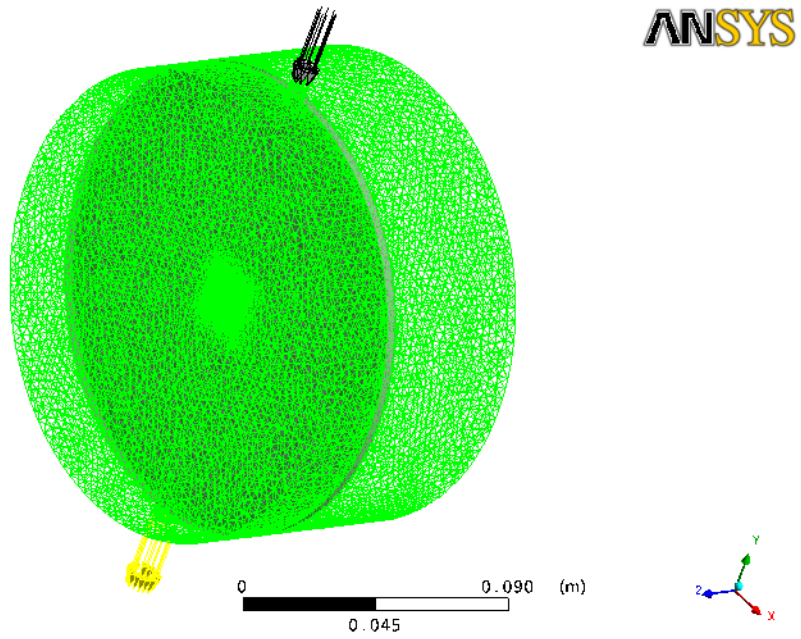
Figure 5.1 View of the complete CFX mesh containing 313,500 elements
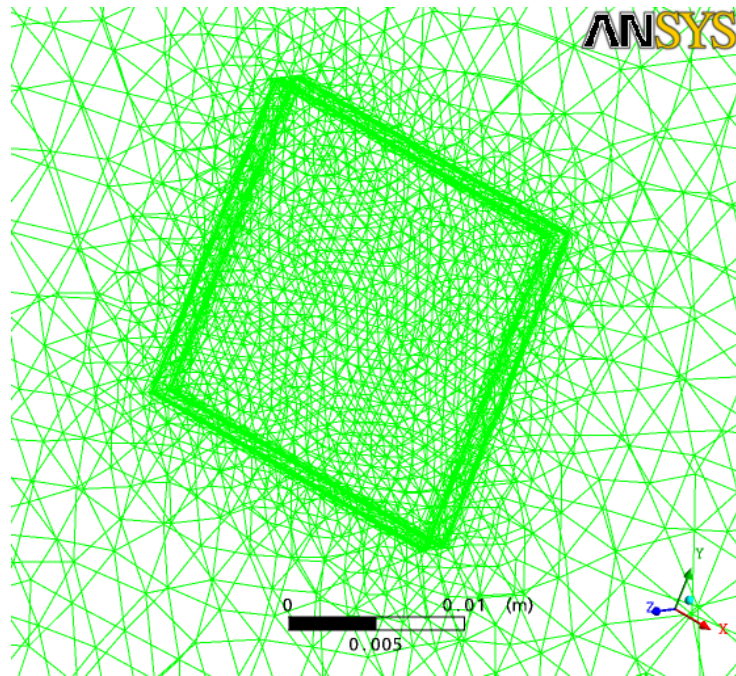
Figure 5.2 Mesh detail showing smaller volume elements in the sample opening area

158

5.1.3 Boundary conditions

The model boundary conditions were applied as follows:

- Specified flow of the nickel carbonyl and carbon monoxide mixture was set at the gas inlet near the top of the reactor.

- The temperature of the entering gas as well as the reactor walls was set at 300K. The walls in the domain were treated as adiabatic, smooth, no-slip surfaces.

- The foam sample was treated as high-porosity energy source with specified power to obtain temperature of the sample area comparable to observed values

5.1.4 Simulation results

Once the mesh is complete, the model boundary conditions, fluid properties and reaction parameters are specified and the software proceeds to solve the equations of state for each cell until an acceptable convergence is achieved. This can be a time consuming process, often taking several hours to reach convergence even on today's fast computers. The Ansys Workbench™ collection of programs was used for the complete process of geometry and mesh formation, solving the reactor chamber flow distribution and post-processing.

Early chamber configuration – large sample opening

The initial geometry model was based on a 4x15 cm^2 sample opening designed to match the original expanded laser beam pattern. The modeling confirmed earlier experimental results showing that the gas flow pattern in the sample area was highly non-uniform, resulting in varying deposition conditions depending on the location on the sample. The flow crossed back-and-forth between the inlet and outlet parts of reactor, creating some areas where the flow was almost parallel with the sample, causing poor delivery of the carbonyl precursor to the internal

parts of the foam. Thus, a highly non-uniform deposition profile across the foam thickness was observed for rates as low as 200-300 $g/m^2/min$ or 2-3 $\mu m/min$ (see Figure 3.24). Modeling work with this geometry was limited to the study of non-reactive flow patterns.

Figure 5.3 shows a typical flow pattern modeled on the exit side of the chamber with inlet at the top (far side of the sample holder), outlet at the bottom and a 4x15 cm^2 sample opening. While substantially all gas was forced to flow through the substrate, the flow was not uni-directional and was found to cross the substrate from the inlet to the exit side multiple times. Large re-circulation flow patterns were observed on the sides of the sample opening, with a higher velocity gas jet crossing the foam in the middle, directed towards the chamber exit at the bottom of the exit side of the sample holder (Figure 5.4). The uneven flow pattern caused varying degree of cooling on the substrate, with high temperature areas in the "eye" of the recirculation flow and cooler region (less deposit) near the centre of the chamber, affected by the high velocity jet.
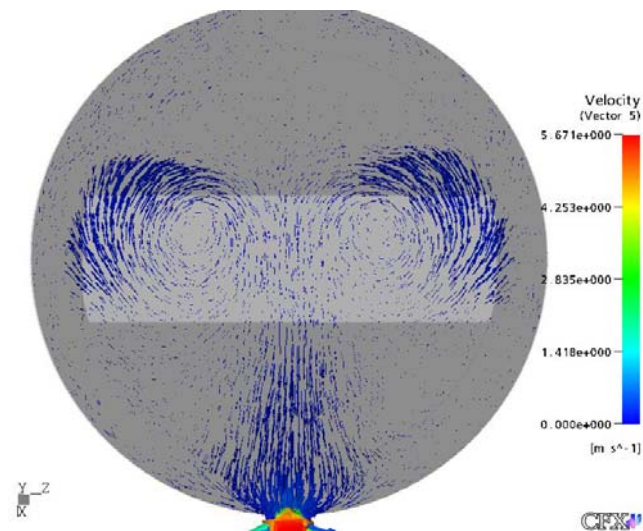
Figure 5.3 Gas flow pattern with the 4x15 cm² sample opening
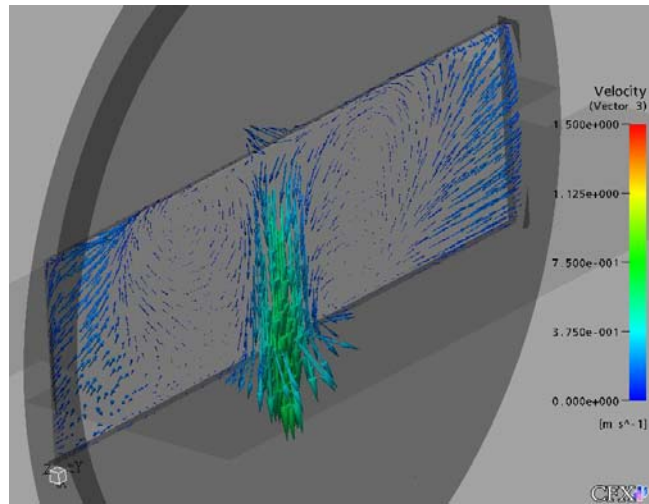
Figure 5.4 Gas flow pattern on exit side of chamber with 4x15 cm² sample opening

The cross-flow and circular flow pattern of the gases were even more severe for the original design of the sample holder (13 cm diameter circular opening). This was also evident from the deposit color and distribution as shown in Figure 5.5. The darker areas indicate more textured deposit, enhancing the IR absorption and resulting in a higher local temperature.

Figure 5.5 Flow patterns visible on Ni deposits prepared with 4x13 cm² sample opening

Reduced size sample opening

As described earlier in Chapter three, in order to eliminate the gas flow non-uniformity problem and to facilitate improved mass transport, the sample opening was modified in several steps to eventually cover a 2x2 cm^2 area in the centre of the reactor. The CFD model confirmed that the flow was uni-directional across the reduced-size opening, as shown in Figure 5.6.

Figure 5.7 shows the calculated temperature profiles of the model based on a local energy source located in the sample area sub-domain and CFX isotropic loss heat transfer model. The top part is an overall view of the chamber with three horizontal cross-sectional planes colored based on the local temperature calculated in each plane. The lower part of Figure 5.7 is a close-up of the sample area. The localized high temperature area (~ 550 K in this simulation run) is the energy source sub-domain representing the foam sample. Figure 5.8 is an overall view of the chamber showing uni-directional flow across the sample area and re-circulating flows in both the inlet and exit parts of the reactor. These flow patterns were confirmed in experiments with partial homogeneous decomposition (powder formation) where they became visible due to ultra-fine nickel particles following the gas flow streamlines. The buoyancy effects are also correctly predicted by the model showing upflow gas stream rising towards the top of the chamber past the sample opening (even though the gas exit is in exactly opposite direction, at the bottom of the reactor). This is consistent with the observation of visible particle jet rising past the sample opening e.g. in experiment LH050303, Figure 3.37(c) or in the video included in Figure 3.38 in the electronic form of this thesis.
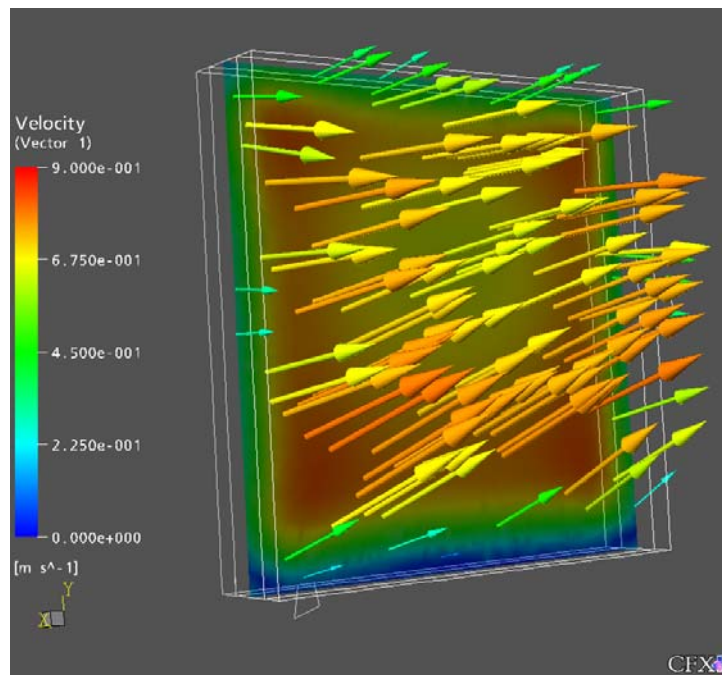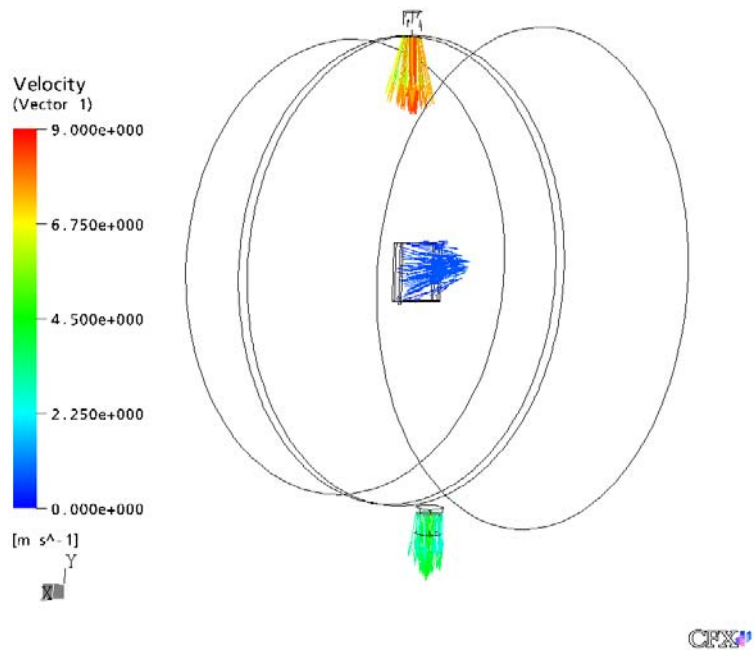
Figure 5.6 Flow patterns in the chamber with 2x2 cm² sample holder configuration

163
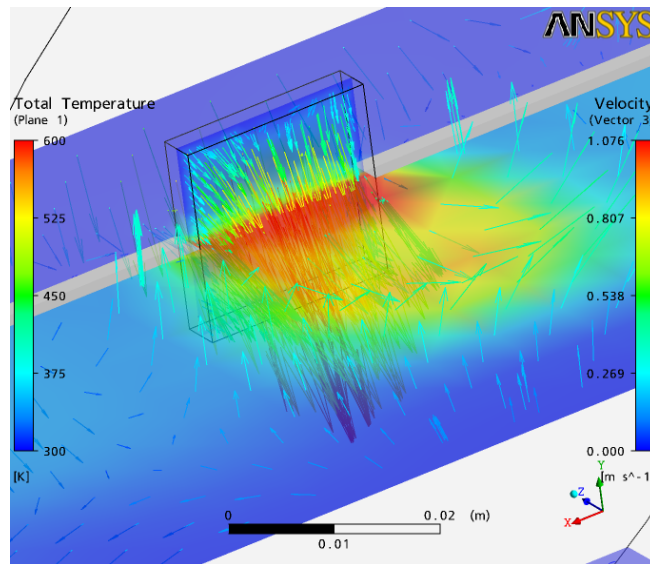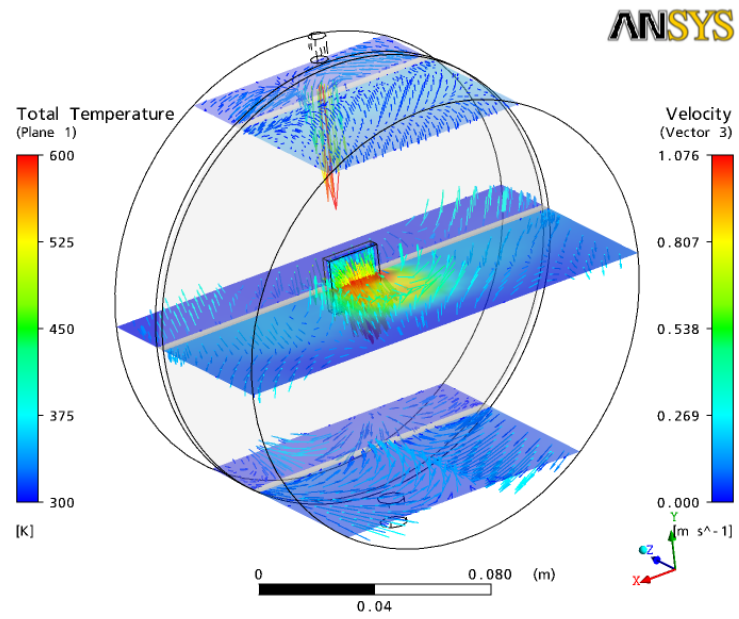
Figure 5.7 Cross-sectional planes color-coded by temperature
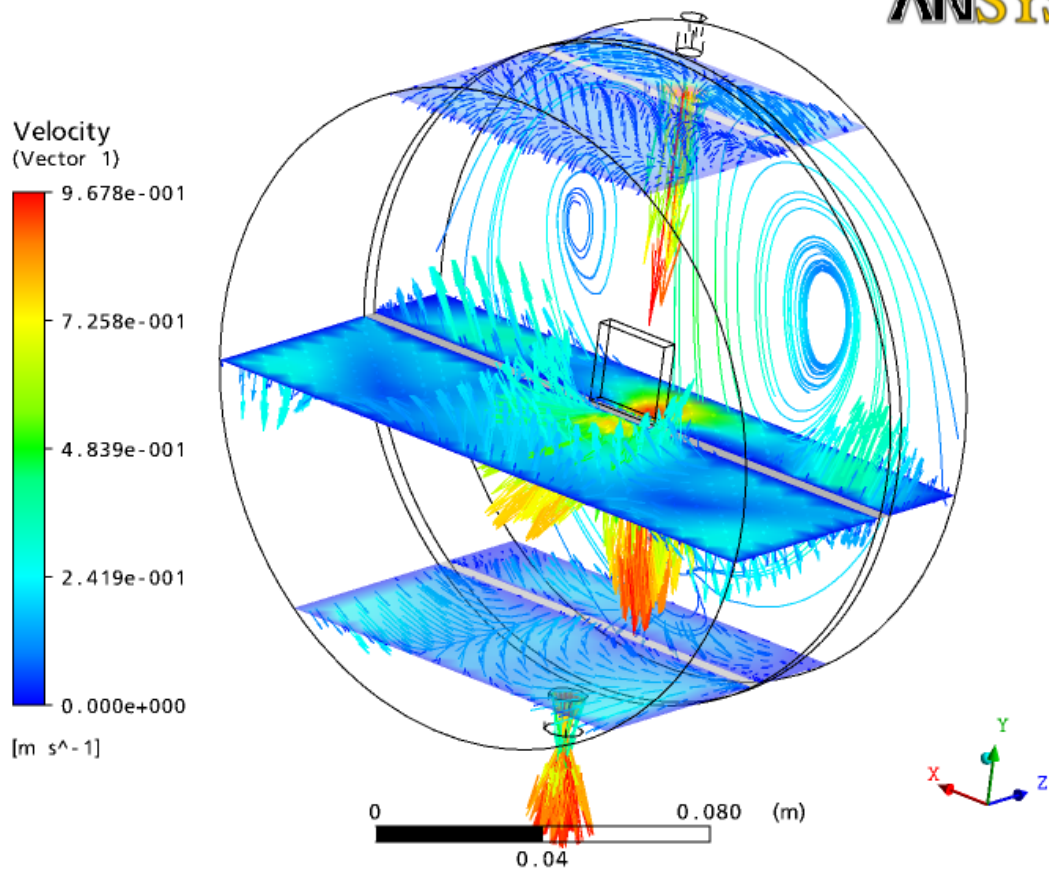
Figure 5.8 Cross-sectional planes and flow vectors color-coded by local gas velocity

5.1.5   CFD model summary

The CFD model confirmed that the gas flow pattern with the reduced sample opening of 2 cm x 2 cm results in a uni-directional, laminar flow in the sample area, while the flow is highly turbulent on either side of the dividing wall containing the sample. With larger sample openings employed initially the flow was not laminar in the sample area leading to local mass transport limitation in parts of the sample. The model used a simplified energy source in the sample area and did not attempt to model the details of the decomposition reaction on

the complicated foam sample surface. Including a physical model of the foam surface and modeling of the local flow and heat transfer process to the foam surface (from a radiation source), and subsequently to the gas, is a recommended future extension of this work. Several researchers have done work in this area, utilizing various idealized periodic structures to simulate the foam surface [Boomsma et al., 2003, Dillard et al., 2005 and Daxner, 2006]. An example of the work of Thomas Daxner that led to a detailed finite element model describing the topology of metal foams with significant detail is shown in Figure 5.9. The geometry was modeled with the program 'Surface Evolver', which minimizes surface energies and was developed by Ken Brakke of Susquehanna University [Brakke, 1992]. This program is capable of calculating the shape of surfaces of minimal surface energy under periodicity constraints by means of a triangular discretization. Daxner's model reproduces the topology of CVD-produced INCOFOAM® remarkably close (Figure 5.9).
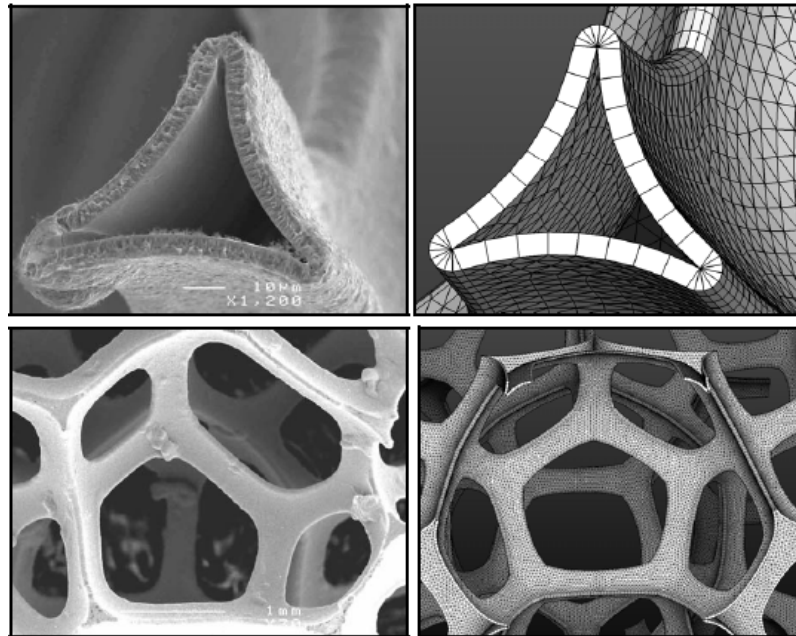
Figure 5.9 Comparison of INCOFOAM® sample SEM images on the left with sub-sections of a finite element unit cell of generic, open cell foam on the right [Daxner et al., 2006]

166

5.2 Conventional process – industrial scale

During the original process development and following the laboratory trials in a 7 cm-wide deposition chamber (shown in Figure 4.1 in Chapter four), the INCOFOAM® CVD production process was scaled up to a miniplant scale utilizing three 40x40 cm^2 chambers and a reel-to-reel, semi-continuous operation in the early 1990's. Conventional IR lamp energy sources were installed and tested in various configurations, as shown in Figure 5.10. The first commercial scale-up involved using the same chamber design, but increasing the number of chambers from 3 to 14 and thus increasing the throughput of the system by a factor of ~ five (Figure 5.11).

This unit was built and commissioned by Vale Inco in 1992 in the Copper Cliff Nickel Refinery in Sudbury, Ontario and operated between 1992 and 2001. By providing an uncoiler and recoiler ("terminal equipment") of sufficient size, the unit was capable of producing about 1,000 linear meters of ~35 cm wide foam in a single batch.

Figure 5.10 Miniplant-size Ni Foam plater (cca 1990)

In 1999, a similar production system with 14 chambers, three times wider than the Copper Cliff unit (i.e. 120 x 40 cm), was built in the Vale Inco Europe refinery in Clydach, Wales, UK (Figures 5.12, 5.14 and 5.16). In addition to wider windows, the scale-up included another step-up in terminal equipment size. However, the operation was still semi-continuous, involving a closed system with the need to completely purge the unit between batches.
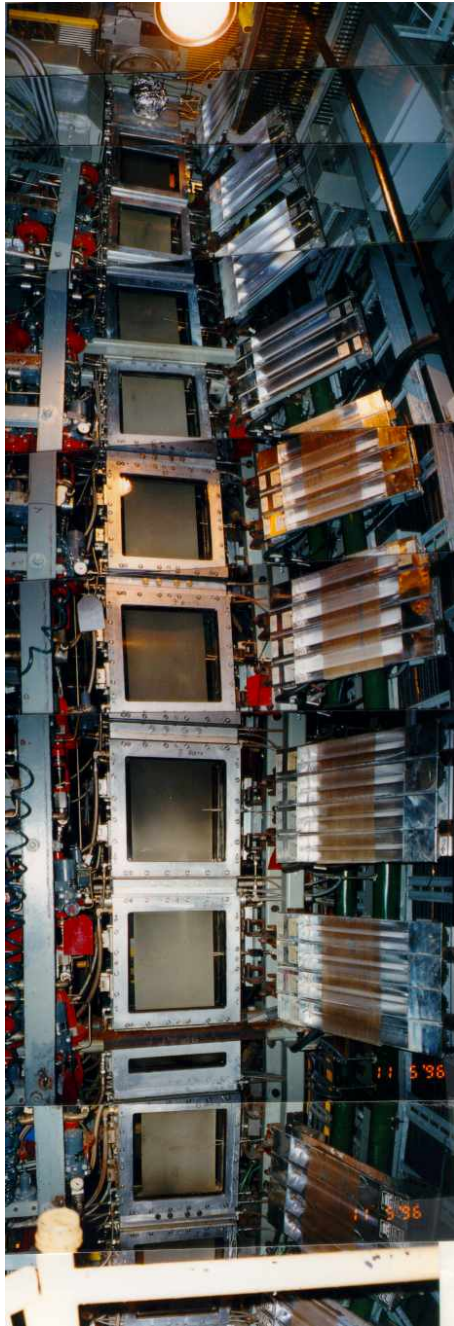
Figure 5.11 First commercial Ni Foam plater at Copper Cliff Nickel Refinery, Ontario (1992 - 2001)

Until late 2006, two plating units were in operation at the Vale Inco Europe Foam plant, with an annual capacity of approximately half a million square meters of battery-grade nickel foam. The semi-continuous deposition process used ~2,500 m long coils of thin (~1.3-3 mm), 1.1 meter wide polyurethane foam which was metallized in a closed, reel-to-reel CVD plating system (Figures 5.14 and 5.16). The plated spools were then thermally treated in a separate conveyorized high temperature furnace to burn-off the polyurethane substrate and sinter the metallic nickel deposit. The result was a high purity, pliable nickel foam product with excellent mechanical and electrical properties. The sintered foam was slit to a customer-specified smaller width and packaged as 200-300 meters long spools of final product. Photographs of semi-automated slitting machines producing coils to customer-specified widths are shown in Figure 5.15.
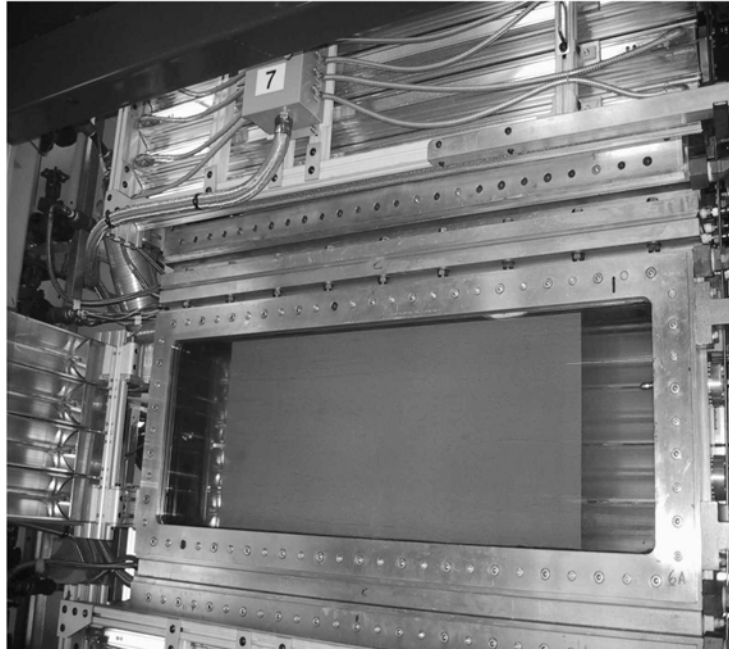
Figure 5.12 One of the 120 cm wide deposition chambers in the Vale Inco Europe Foam plant

Figure 5.13 Large production spool of Ni foam being transported between sintering and slitting operations

Figure 5.14 View of the Clydach Foam plant plating column
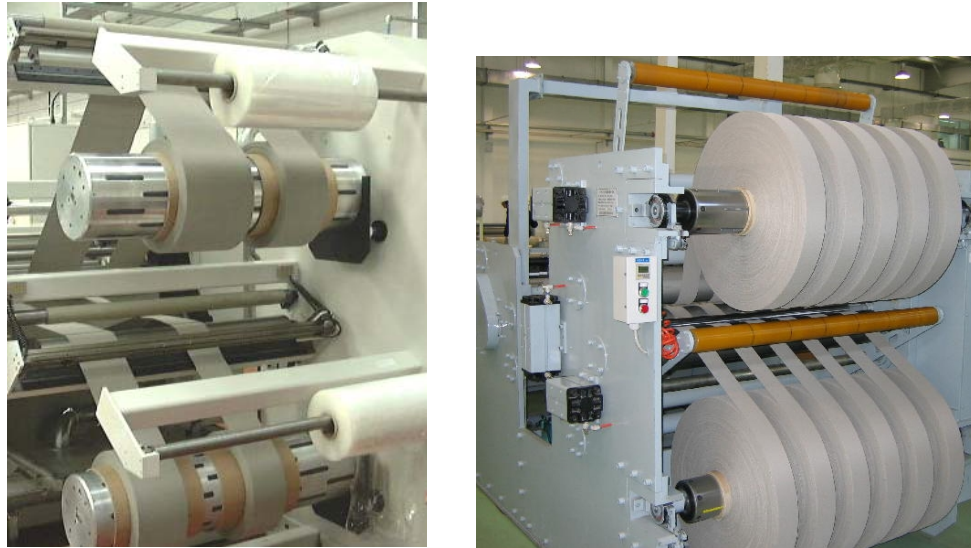
Figure 5.15   Slitting machines producing foam coils to customer-specified widths

Figure 5.16 shows the lower part (uncoiler and the lower deposition chambers with banks of IR lamps) of the commercial plater in operation.

The economics of the U.K. operation was negatively impacted by the extended unit purge times and turn-around times. A switch from batch to continuous operation would be essential for long-term viability of this process.

Figure 5.16   Uncoiler and the lower chambers of the commercial foam plater in operation (Vale Inco Europe Nickel Refinery 1999-2006)

5.3   Use of diode laser heating in foam sintering

In the commercial process, the polymer substrate burnout and high temperature (~1000 °C) annealing of nickel foam are done in conventional electric or gas-fired belt furnaces. Because of the low thermal mass of Ni foam, this process is quite

inefficient (the furnace conveyor belt represents higher thermal load than the foam itself). The polymer burnout process is enhanced by rapid heat-up of the as-deposited foam, which facilitates formation of multiple "blow holes". These are utilized as escape passages for the organic vapors from inside of the Ni foam struts (see Figure 1.5). A laser beam would provide a possibility for a much more rapid heat-up of the un-sintered foam, facilitating better control of the number of PU vapor escape sites. Furthermore, the energy could be delivered directly to the foam structure rather than via hot furnace walls and the conveyor belt.

5.4   Laser-driven process scale-up

In the conventional production units, the window area can be as large as 0.5 m^2 (120 x 40 cm^2). Covering such a large area with a uniformly distributed laser beam may present a challenge. The generation of large-area, uniform beams that would enter the deposition chamber through windows of comparable size (~ 120 cm wide to accommodate the standard ~110 cm wide foam) will thus present the most challenging part of the laser-driven process scale-up. The length of the chamber will depend on the design of the multi-bar diode laser source and on the requirement to provide a uniform, laminar cross-flow across the foam substrate to enhance mass transport. A practical dimension might be ~5-10 cm. The window material can be either regular borosilicate glass or a quartz plate of sufficient thickness to meet the required deposition chamber pressure rating, with appropriate anti-reflective coating. A single pane window should be adequate owing to the low absorption of diode laser radiation in glass or quartz. External air cooling may be necessary to provide added control of the window temperature.

In principle, it is possible to build arbitrarily large stacked arrays of laser diodes (Figure 5.17). With the recent efforts to increase wall-plug efficiency to ~80%, [Hitz, 2005] and decreasing unit costs of mass-produced diode modules, such large area diode laser sources could be economically available in a not too distant future.
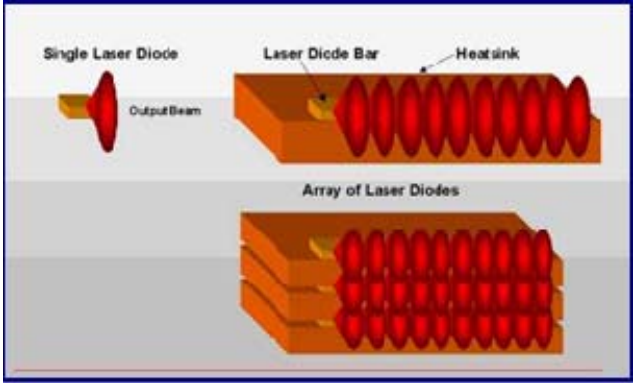
Figure 5.17 Stacking of laser diode arrays to build large-area sources

5.4.1 Beam homogenization options

In addition to the beam homogenization technique using a diffuser plate (employed in this work), there are several other methods to obtain uniform, lage-area beam profiles. A top-hat power distribution profile with a flat plateau and steep edges was developed by a group at Fraunhofer Institute for Laser Technology in Aachen, Germany [Traub, 2003]. The beam shaping was accomplished by a waveguide and microstep mirror imaging system (Figure 5.18). The first microstep mirror divided
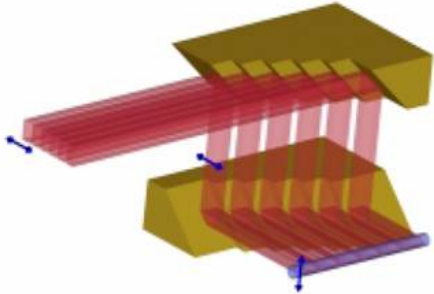
Figure 5.18 Microstep mirror principle

173

the beam into a number of sub-beams along the slow axis. The slow and fast axes were then swapped by the reflection of these sub-beams on the second microstep mirror. Beam distributions of the type shown in Figure 5.19 were obtained by a combination of microstep mirror technology and a waveguide with the same aspect ratio as the final desired beam shape. In the lighting application described by Traub et al. the homogenized beam had a respectable size of 43 x 30 cm^2.
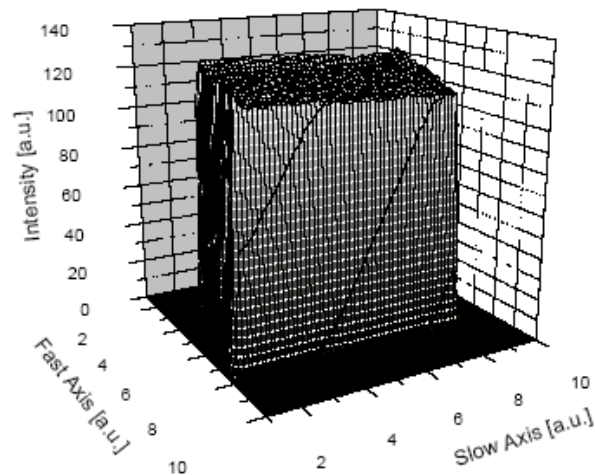
Figure 5.19 Homogenized beam pattern utilizing waveguide

Figures 5.20 and 5.21 show another example of intensity distribution as a function of slow axis position before and after homogenization, developed for a laser metal cutting application. Figure 5.20 also shows the effect of defective emitters (dashed line). The edge steepness of the corrected beam reached <5% and homogeneity of the main plateau was better than 90%. The optical efficiency (compared to un-homogenized beam) amounted to ~78% at a laser power of 680W.
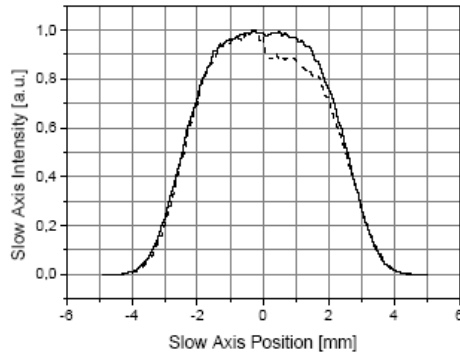
Figure 5.20 Slow axis un-homogenized intensity profile for stack without defects (solid line) and with 50% defect emitters (dashed line)
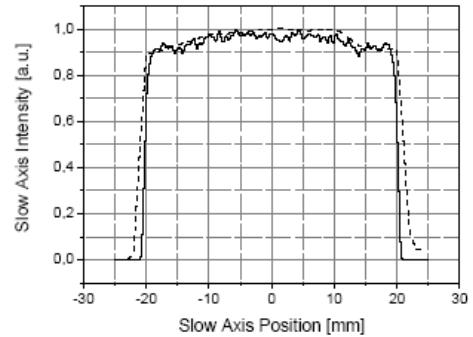
Figure 5.21 Homogenized beam: measured (solid line) and calculated (dashed line)

One drawback of the homogenization techniques described above is the significant increase in system weight and size. Further developments in applying micro-optics for beam homogenization are expected to improve this aspect.

5.4.2   High power CW Direct Diode Arrays

Ongoing development of the diode arrays leads to increasing power levels and more reliable, longer lifetime diode arrays. Power levels in the tens of kW were available as of 2009. Lensed versions of such high-power arrays can provide uniform illumination of large work piece areas. An example of a 45 kW system manufactured by Coherent Inc. (previously Nuvonyx) is shown in Figure 5.22. The assembly consists of 19 arrays with 24, 100W bars in ach array. The system uses 125 A per array and achieves electrical to optical efficiency of better than 60%. The diodes operate at a wavelength of 808 nm +/- 7.5 nm [Coherent Inc. Preliminary product announcement].
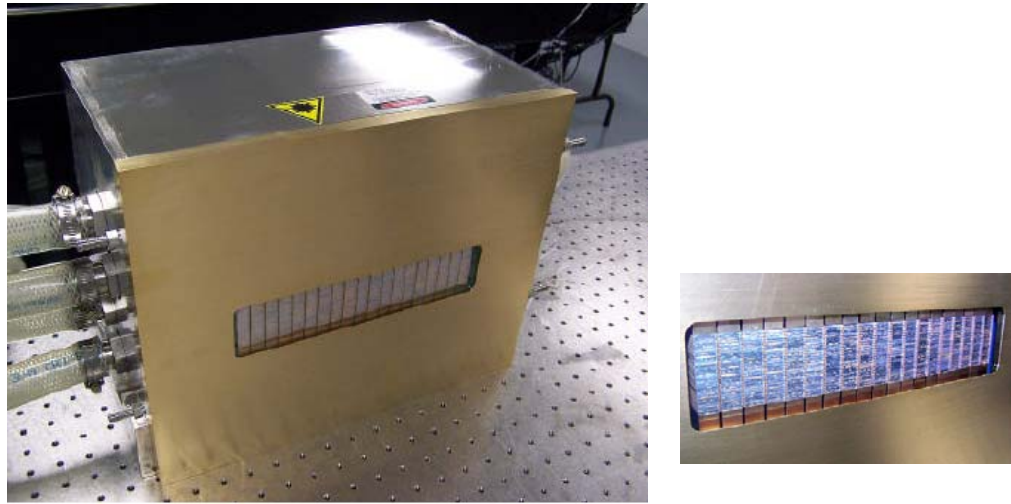
Figure 5.22 Coherent Inc. 45 kW laser diode array (left) and the same array in operation (right)

An example of a homogenized, lensed beam providing ~10x10 mm^2 work piece illumination produced by the Coherent Inc. system is shown in Figure 5.23.
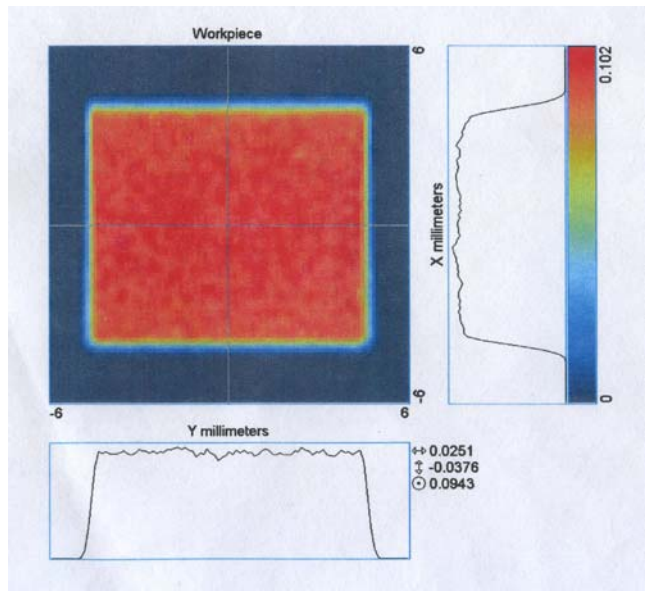
Figure 5.23 Homogenized 10x10 mm^2 beam

5.4.3   Continuous system design

A new production line concept based on the diode laser arrays, pre-plate and high-rate deposition zones and a continuous, open-ended design with gas interlocks at either end and between zones is illustrated in Figure 5.24.
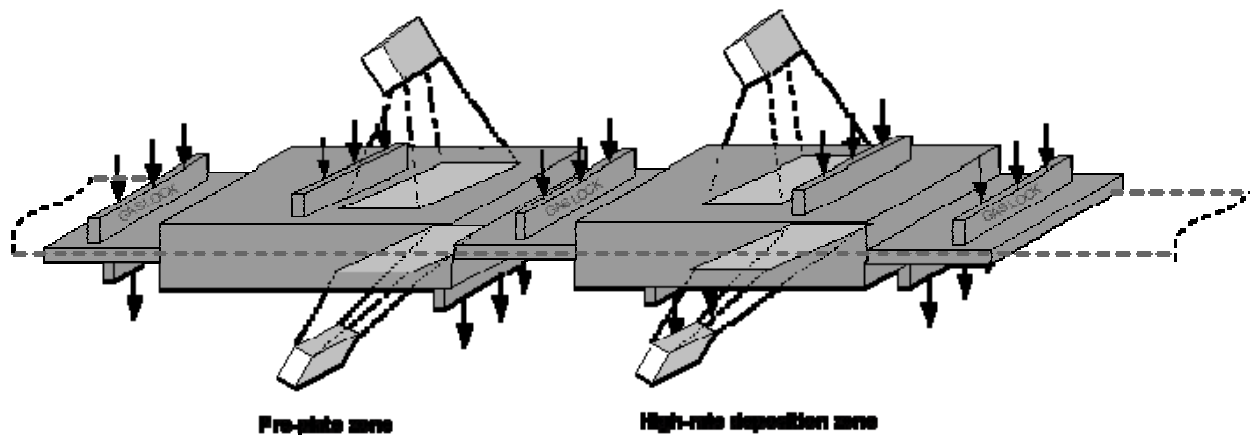
Figure 5.24 Key components of a foam production line utilizing HPDL technology and a forced flow gas delivery system

 The system orientation could be either horizontal or vertical. A vertical system may provide better symmetry of conditions on the two sides of the foam and easier maintenance of deposition chamber windows, whereas keeping the bottom window free of particulates over extended operation may require special cooling or a purging provision.   Integration of the combined nickel deposition process, PU burn-out chamber and a high-temperature sintering chamber based on the same technology can be also envisioned (Figure 5.25). The gas lock technology could take advantage of the compressible nature of the polyurethane substrate on the entry side, and could employ a labyrinth-type gas seal between chambers and at the exit, utilizing the low profile of the substrate. Because of the toxic nature

177

of nickel carbonyl, careful pressure and flow balancing would be required to make this successful. Such technology for continuous operation with toxic gas precursors has been demonstrated in the past, for example in the design of commercial atmospheric pressure CVD furnaces commonly used in the semiconductor industry [Bartholomew, 1989] and at Vale Inco's continuous carbon fibre nickel coating system. In order to further increase the line speed and thus productivity, there may be more than one high-rate deposition zone in series. Since there will always be a slight deposit thickness gradient due to depleting carbonyl concentration from inlet side to the exit site (as exemplified by the thickness measurements in Figure 4.33), the direction of the forced flow gas supply should alternate. Using an even number of high-rate deposition chambers (minimum of 2) would maximize the deposit uniformity, resulting in DTR values near unity.
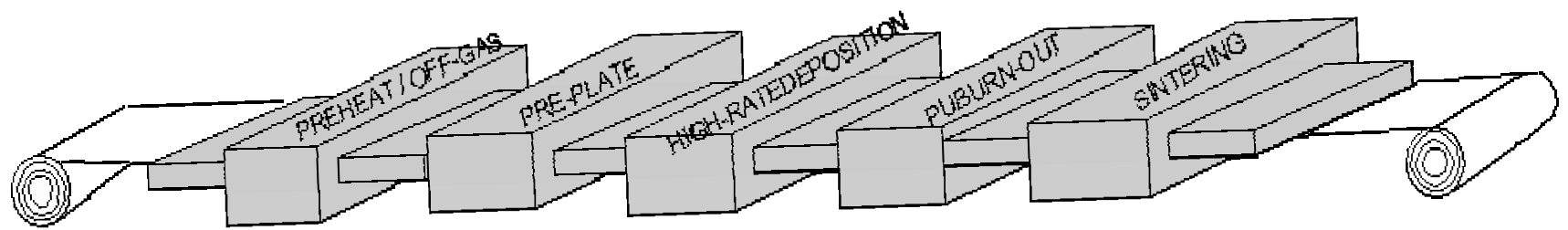
Figure 5.25 Integrated, reel-to-reel continuous Ni foam production line

6 CONCLUSIONS AND RECOMMENDATIONS

High-power diode lasers are being increasingly used in materials processing in a variety of ways. The work described in this thesis proposes the use of HPDL as unique heat sources driving CVD reactions of precursors such as nickel carbonyl on the surface of relatively thermally sensitive, 3-dimensional polymer substrates. The use of HPDL heat sources for such a quasi-large area deposition process is a novel approach aiming at intensifying the nickel carbonyl CVD reaction and enabling a development of a more compact and efficient production equipment. This is an extension of an existing process developed at Vale Inco in the 1990's, which utilizes short-wave quartz infrared lamps as conventional IR heat sources. Due to the laser operating wavelength being just outside the visible spectral range (~807 nm), HPDLs offer the ability to deliver the required energy to the substrate surface via regular glass or quartz windows without appreciable absorption in these common window materials. At the same time, the absorptivity of HPDL radiation (especially on metal surfaces) is better than that of YAG or CO_2 lasers. Excellent directional and power level control (including the possibility of pulsed operation), stability and continued, rapid development of the HPDL technology towards mass-scale production show good promise for commercial deployment of these devices.

While the HPDL-driven CVD processes have been historically applied to the selective deposition of microstructures and patterned thin films, the 3-dimensional structure of metal foam based on the polyurethane foam template offers some of the same fundamental attributes as other, more conventional microstructures. In terms of enhanced mass transport, the foam struts, which

are few tens of microns thick, are surrounded by openings with dimensions of several hundred microns, enabling 3-dimensional access of gas molecules to the strut surfaces. Using forced-flow configuration, it was possible to drive the decomposition reaction of nickel carbonyl on the foam surface at a relatively high rate of ~19 microns/min using two 240W HPDL power sources. This rate is about 16 times higher than typical rates achieved in the commercial CVD deposition system. This reported deposition rate limit was reached due to the limited power available in the experimental equipment and the given objective to prepare samples of a certain minimum size (~1 cm diameter coupons). It is reasonable to expect even significantly higher rates simply by providing higher power density and gas flow.

By optimizing gas delivery and power setting conditions during the pre-plate and main deposition processes, it was possible to produce uniform 3-D deposits on nickel foam substrate *without* the use of an H_2S catalyst. Operation without the sulfur-based catalyst simplifies the subsequent high-temperature processing step due to superior mechanical properties of sulfur-free as-deposited foam. However, a sample produced without H_2S on a PU foam substrate exhibited poor uniformity. Further work on optimization of pre-plate conditions using PU substrate and H_2S-free gas compositions is therefore required.

The diode laser heating technique can be extended to the high-temperature PU foam burn-out and nickel film sintering, typically done at ~ 1,000ºC. A possible design of an integrated foam production line enabling continuous operation with efficient, small modules connected by a common channel and separated by gas locks is outlined.

6.1   Recommendations for future work

The deposition rates measured in the course of this work were ultimately limited by the available laser beam power density. Further increase of the rate should be

possible by further intensifying both the laser power and the forced flow gas delivery. The ultimate practical limit will be probably reached due to the mechanical strength of the lightly coated substrate and its ability to withstand the unidirectional force applied by the flowing gas precursor. Further investigation of operating conditions with more powerful diode laser beams is expected to yield considerably higher deposition rates than those reported in this work. Rates in excess of 100 microns per minute are quite reasonable and consistent with observations of other researchers working on LCVD of nickel microstructures using nickel carbonyl.

The forced flow configuration should allow thicker and denser 3-D substrates to be metallized uniformly. Investigating materials such as woven and non-woven felts, carbon fibers, cellulose fibers (various forms of paper) and similar structures could yield new 3-D nickel based porous materials. For example, a sample of nickel-coated paper produced by slow deposition with nickel carbonyl using conventional IR lamps is shown in Figure 6.1. The cross-flow LCVD process could result in a better nickel coverage and significant improvement in deposition rate on such dense structures. A potential application of such inexpensive metallized substrates involves their use in deposition of synthetic diamond films. A sample of nickel-coated packaging paper such as the one shown in Figure 6.1 was used in a hot-filament CVD process to deposit a layer of diamond crystals [Cabral et al., 2006]. Figure 6.2 shows optical and SEM images of the diamond-coated sample.
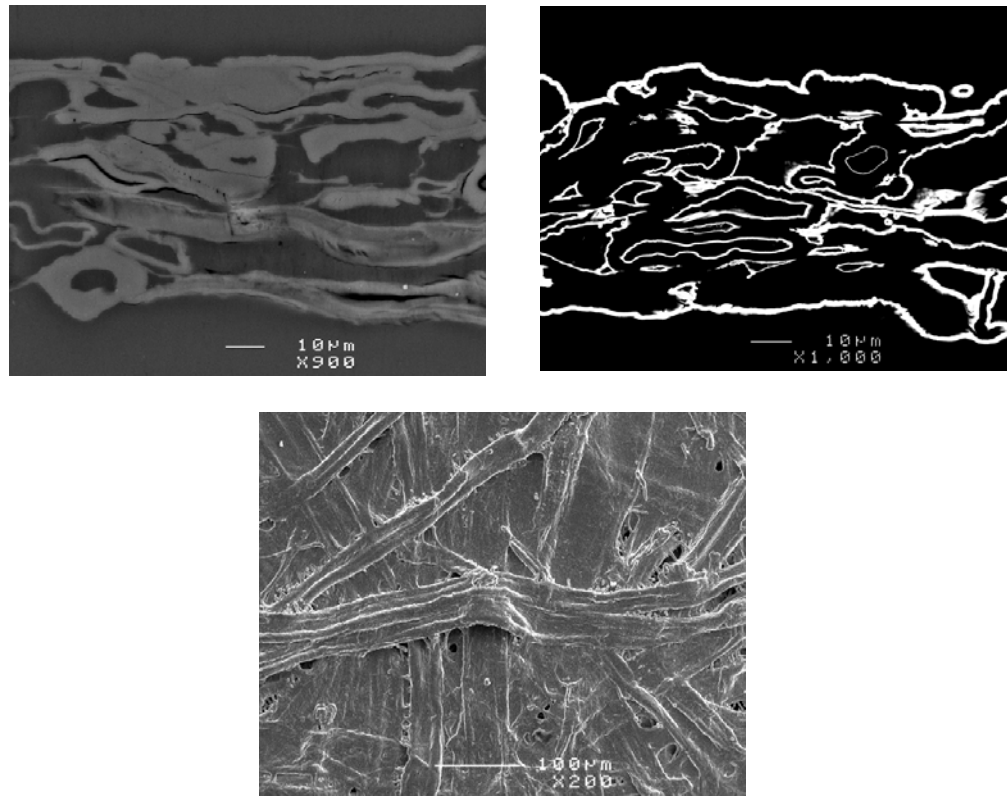
Figure 6.1 Ni-coated paper sample – SEM images of uncoated cross-section (upper left), Ni-coated cross-section (upper right) and Ni-coated surface morphology (lower image)
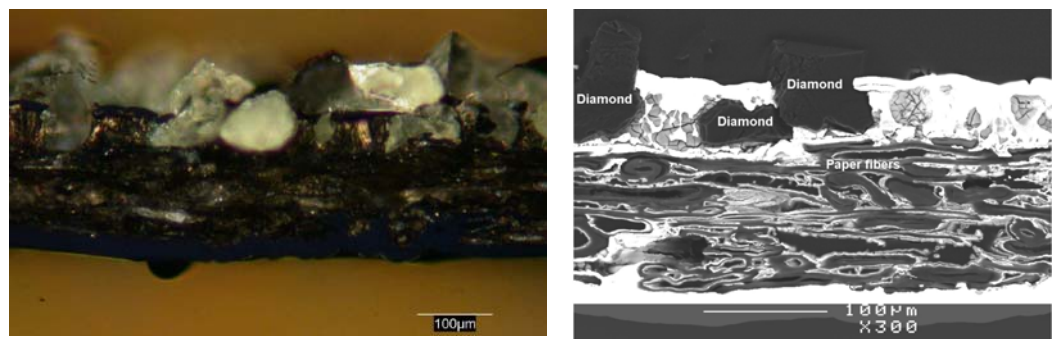
Figure 6.2 Optical (left) and SEM (right) cross-sections of diamond film on Ni-coated paper[7]

183

Beam homogenization and delivery of uniform laser radiation to large-area substrate require further development. Since the energy densities are much lower than those used in other laser materials processing applications, use of conventional materials should be possible. Similarly, the use of recently developed high-power fibre lasers operating at wavelengths between 1 and 1.5 μm should be fully applicable to this system. The fibre lasers, which are readily available in multi-kW versions, are emerging as a strong candidate in materials processing applications.

Pulsed laser operation could be investigated as a means to control deposit crystallinity, with the possibility of producing nanostructured deposits.

The work on catalyst-free deposition should be extended to temperature-sensitive substrates such as PU foam directly. The use of other nucleating agents such as oxygen and ozone could be investigated. Diode laser beam heating can be also envisioned for coating of pre-nucleated particles via CVD by passing them through the precisely defined area of the beam inside a CVD chamber, on their way to a particle collection system. The combination of such precise energy delivery and availability of the nickel CVD precursor on industrial scale may further facilitate the development leading to the mass production of nickel-based nanomaterials [Paserin et al., 2008].

6.2   Nickel foam surface morphology and materials of nature

Cellular solids appear widely in nature and form an integral part of various natural systems. The structure of cancellous bone, wood, cork, and coral all involve intricate 3-dimensional networks of interconnected cells [Gibson, 1997]. The ability to duplicate such structures in man-made materials and precisely control their structural and surface properties provides us with a tool and building

material that the Nature has already been using extensively. Production of such materials in metallic form further widens the possible fields of use, benefiting mainly from the high temperature and corrosion resistance of materials like nickel. The open-cell structure is well suited as a low differential pressure flow medium with available functionalized contact surface to promote a specific flow medium – surface interaction. The control of surface morphology by means of more sophisticated production systems such as cross-flow reactors and diode lasers further enhances the ability to customize the properties of metal foams and to develop more efficient production processes.

Figure 6.3 shows the structure of a sea coral resembling that of the spiky nickel foam produced by deposition conditions bordering between heterogeneous and homogeneous decomposition reaction of nickel carbonyl. Similar to the role of such morphologies in natural systems, the synthesized 3-D metallic structure could serve as a base for porous, low-pressure drop functionalized surface with unique capabilities, such as precise temperature control utilizing the electrical conductivity of the underlying metal foam.
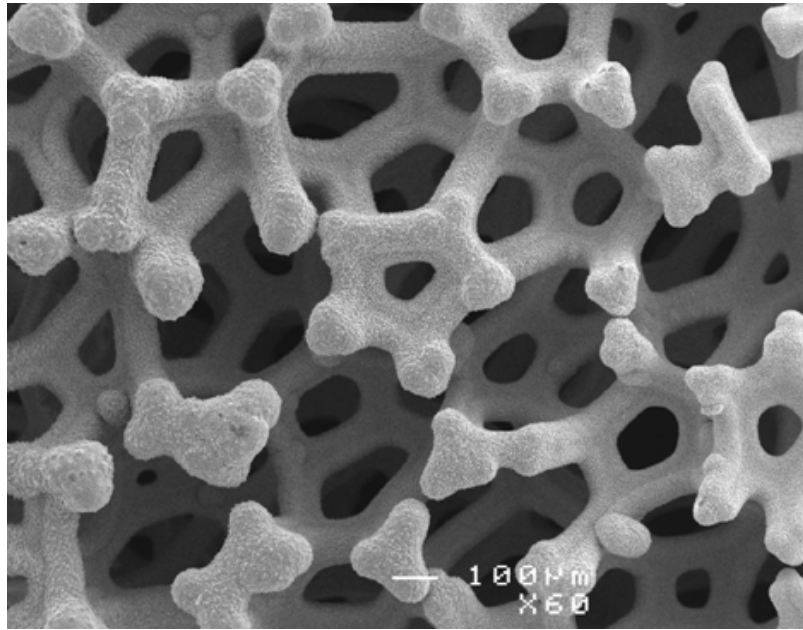
Figure 6.3 Images of a sea coral (top) and spiky nickel foam (bottom image, expt. LH050308)

BIBLIOGRAPHY

AEA Technology, *"CFX-4 Documentation"* for Ansys / CFX software, AEA Technology Software Engineering Inc., 2000.

Allen, S.D., *"Laser Chemical Vapor Deposition: A Technique for Selective Area Deposition"*, J. Appl. Phys. 52 (11), pp. 6501-6504, 1981.

Allen, L.B., Koenig, H.G., Stacy, R.A., Meyer, D.D., *"Laser Diode with Double Sided Heat Sink"*, US patent 4,393,393, July 1983.

Ashby, M.F., Evans, E.G., Fleck, N.A., Gibson, L.J., Hutchinson, J.W., and Wadley, H.N.G., *Metals Foams: A Design Guide*, Butterworth, 2000.

Babjak J., Ettel V.A. and Paserin V., *"Method of Forming Nickel Foam"*, US Patent 4,957,543, September 1990.

Bale R.A. and Chapman E.T. *"INCO's Pressure Carbonyl Refining of Nickel"*, in Proc. Nickel Metallurgy Vol.1, No.3, p. 532-551 (25th Annual Conference of Metallurgists), 1986.

Ball, B.B., *"Method of Making Porous Material"*, US Patent 3,111,396, November 19, 1963.

Bartholomew, L.D., Gralenski, N.M., Richie, M.A., Hersh, M.L., *"Atmospheric Pressure Chemical Vapor Deposition Apparatus"*, US Patent 4,834,020, Watkins Johnson Company, May 30, 1989.

Bates, G.S., Redfield, A.C. and Zangwill, A., *"Growth Dynamics of Chemical Vapor Deposition"*, Phys. Rev. Lett. Vol 62, No. 7, p. 776-779, 1989.

Bäuerle, D., *"Production of Microstructures by Laser Pyrolysis"*, Mat. Res. Soc. Symp. Proc. Vol 17, p. 19-28, 1983.

Bäuerle, D., *Laser Processing and Chemistry*, 3rd edition, Springer-Verlag, 2000.

Bezuk, S.J., Baseman, R.J., Kryzak, C., Warner, K. and Thomas, G., *"Pyrolytic Laser Direct Writing of Nickel over Polyimides"*, Mat. Res. Soc. Symp. Proc. Vol. 75, p. 75-81, 1987.

Bi, X. and Kambe, N., *"Efficient Production of Particles by Chemical Reaction"*, US Patent 6,248,216 B1, June 19, 2001.

Boettger, G. Fetting, F., Chem. Ingr. Tech. 384, 34, 1962.

Bookham Inc. press release, January 26, 2009 http://www.bookham.com/pr/20090126a.cfm, January 2009.

Boomsma, K., Poulikakos, D., and Ventikos, Y., *"Simulations of the flow through open cell metal foams using an idealized periodic cell structure"*, in Int. J. of Heat and Mass Transfer 24, p. 825-834, 2003.

Boomsma, K., Poulikakos, D., and Zwick, F., *"Metal Foams as Compact High Performance Heat Exchanger"*, Mechanics of Materials 35, p. 1161-1176, 2003.

Boughaba, S. and Auvert, G., *"Growth Kinetics of Micron-size Nickel Lines Produced by Laser-assisted Decomposition of Nickel Carbonyl"*, in J. Appl. Phys. 73 (12), June 15, 1993.

Bradley, D., *"Metal with Wings"*, New Scientist, 14 April 1988, p. 38-41.

Brakke, K.A., *"The Surface Evolver"* in Experimental Mathematics Vol. 1, No. 2, p. 141-165, 1992.

Cabral, G., Madaleno, J.C., Titus, E., Ali, N., Gracio, J., *"Diamond Chemical Vapor Deposition on Seeded Cemented Tungsten Carbide Substrates"*, Thin Solid Films 515, p. 158-163, 2006.

Calmidi, , V.,V., and Mahajan, R.L., *"Forced Convection in High Porosity Metal Foams"*, Journal of Heat Transfer, Vol 122, p.557-565, 2000

Carlton, O. and Oxley, J., *"The Heterogeneous and Homogeneous Decomposition of Nickel Carbonyl"*, AIChE Journal, Vol. 13, No. 1, p. 86-91, 1967.

Carpenter, G.J.C., Wronski, Z.S., Phaneuf, M.W., *"TEM Study of Nanopores and the Embrittlement of CVD Nickel Foam"*, Materials Science and Technology, Vol. 20, p. 1421-1426, Nov. 2004.

Chan, R., *"The Heterogeneous and Homogeneous Decomposition of Nickel Carbonyl"*, PhD Thesis, University of Wisconsin, 1954.

Coley K.S., Ambrose, J., Robinson, F.J.R., Nguyen, N., *"Kinetics of Nickel Deposition onto Polyurethane Foam from Nickel Carbonyl"*, Inco internal technical report (unpublished), April 2004.

Cushnie K., Campbell S., *"Process for Removal of Polymer Foams from Nickel-coated Substrates"*, US Patent 5,735,977, April 7, 1998.

Daxner, T., Bitsche, R.D. and Bohm, H.J., *"Micromechanical Models of Metallic Sponges with Hollow Struts"*, THERMEC 2006, Materials Science Forum, 539-543, p. 1857-1862, 2007.

Degischer, H.-P., Kriszt, B. (editors), *"Handbook of Cellular Metals: Production, Processing, Applications"*, Wiley-VCH, 2002.

Diehl, R. (ed.), *High-Power Diode Lasers – Fundamentals, Technology, Applications*, Springer-Verlag, 2000.

Dillard, T., N´Guyen, F., Maire, E., Salvo, L.,Forest, S., Bienvenu, Y., Bartout, J.-D.,Croset, M., Dendievel, R. and Cloetens, P., *"3D Quantitative Image Analysis of Open-cell Nickel Foams under Tension and Compression Loading using X-ray Microtomography"*, Phil. Mag. 85, Issue 19, p. 2147-2175 (2005).

Duley, W. W., *"CO_2 Lasers: Effects and Applications"*, Academic Press, 1976.

Duley, W. W., *"UV Lasers: Effects and Applications in Materials Science"*, Cambridge University Press, 1996.

Duty, C.E., Jean, D. and Lackey, W. J., *"Laser Chemical Vapor Deposition: Materials, Modeling, and Process Control"*, International Materials Reviews, Vol. 46 No. 6, p. 271-287, 2001.

Duty, C.E., *"Design, Operation and Heat and Mass Transfer Analysis of a Gas-Jet Laser Chemical Vapor Deposition System"*, PhD Thesis, Georgia Institute of Technology, 2001.

Erb, U., El-Sherik, A.M., Palumbo, G., and Aust, K.T., *"Synthesis, Structure and Properties of Electroplated Nanocrystalline Materials"*, J. of Nanostructured Materials, 2, 383-390, 1993.

Gibson, L.J. and Ashby, M.F., *"Cellular Solids – Structure and Properties"*, 2nd edition, Cambridge University Press, 1997.

Grove, A.S., *"Physics and Technology of Semiconductor Devices"*, 1st edition, John Wiley & Sons Inc., 1967.

He, H., Heist, R.H., McIntyre, B.L. and Blanton, T.N., *"Ultrafine Nickel Particles Generated by Laser-Induced Gas Phase Photonucleation"*, Nanostructured Materials, Vol. 8, No. 7, p. 879-888, 1997.

He, Y., Li, X., Swihart, M. T., *"Laser-driven Aerosol Synthesis of Nickel Nanoparticles"*, Chemistry of Materials, 17(5), 1017-1026, 2005.

Herman, I.P., Hyde, R.A., McWilliams, B.M., Weisberg, A.H., Wood, L.L., *"Wafer-scale Laser Lithography: I. Pyrolytic Deposition of Metal Microstructures"*, Mat. Res. Soc. Symp. Proc., Vol. 17, p. 9-18, 1983.

Hitz, B., *"Military Project Aims to Improve Diode Laser Efficiency"*, Photonics Spectra, Vol. 39, Issue 1, p. 89 (January 2005), also see SHEDS program webpage http://www.darpa.mil/mto/sheds/.

Howard-White, F.B., *"Nickel – An Historical Review"*, D. Van Nostrand Co., 1963.

Jenkin, W.C., *"Method of Depositing Metals and Metallic Compounds Throughout the Pores of a Porous Body"*, US Patent 3,160,517, December 8, 1964.

Jenkin, W.C., personal communication, 1990.

Jarah, N., *"Nanostructured Catalyst Support based on Carbon Nano-Fibres"*, PhD Thesis, University of Twente, 2004.

Jervis, T.R., *"Metal Film Deposition by Gas-phase Laser Pyrolysis of Nickel Tetracarbonyl"*, J. Appl. Phys. 58 (3), 1984.

Jervis, T. R. and Newkirk, L.R., *"Metal Film Deposition by Laser Breakdown Chemical Vapor Deposition"*. J. Mater. Res. 1(3), May/June 1986 p. 420-424, 1986.

Jones, L. H., *"Vibrational Spectrum of Nickel Carbonyl"*, J. Chem. Phys. 28(6), June 1958 p. 1215-1219, 1958.

Kavecky, S. and Sajgalik, P., *"Carbon Nanotubes Produced by CVD"*, Key Engineering Materials Vol. 290, p. 230-233, July 2005.

Kleijn, C.R., *"Transport Phenomena in Chewmical Vapor Deposition Reactors"*, PhD Thesis, Technical University Delft, 1991.

Kodas, T.T., Baum, T. H., Comita, P. B., *"Gold Crystal Growth by Photothermal Laser-Induced Chemical Vapor Deposition"*, Journal of Crystal Growth, Vol. 87, p. 378-382, 1988.

Kodas, T.T. and Comita, P. B., *"Role of Mass Transport in Laser-induced Chemistry"*, Acc. Chem. Res. Vol. 23, p. 188-194, 1990.

Koltsakis, G.C., Katsaounis, D., Samaras, Z.C., Saberi, S., Boehm, A., Naumann, D., *"Filtration and Regeneration Performance of a Catalyzed Metal Foam Particulate FIlter"*, SAE 2006 World Congress and Exhibition, Detroit, MI, USA, April 2006.

Kräuter, J., Bäuerle, D., Fimberger, F., *"Laser-induced Chemical Vapor Deposition of Ni by Decomposition of Ni(CO)$_4$"*, Applied Physics A: Solids and Surfaces, A31(1), p. 13-18, 1983.

Lackey, W.J., Rosen, D., Duty, C., Jean, D., Bondi, S., Elkhatib, T., Johnson, R., Jiang, M., Mi, J., Gillespie, J. and Harvey, R., *"Laser CVD System Design, Operation, and Modeling"*, Ceramic Engineering and Science Proceedings 23(4) p. 23-33, 2002.

Lide, D.R. (editor), *"CRC Handbook of Chemistry and Physics"*, 75th edition, CRC Press, 1994.

Linden, D. (editor), *"Handbook of Batteries"* McGraw-Hill, 1995.

Matsumoto I.; Iwaki T.; Yanagihara N., *"Battery electrode"*, US Patent # 4,251,603, February 17, 1981.

Mazumder, J. and Kar, A., *"Theory and Application of Laser Chemical Vapor Deposition"*, Plenum Press, 1995.

Maxwell, J., Pegna J. and Hill E., *"Gas-Phase Laser-Induced Pyrolysis of Tapered Microstructures"*, Solid Freeform Fabrication Symp. Proc., Pub. University of Texas at Austin, p. 143-150, 1995.

Maxwell, J., Boman, M., Williams, K., Larsson, K., Jaikumar, N. and Saiprasanna, G., *"High-Speed Laser Chemical Vapor Deposition of Amorphous Carbon Fibers, Stacked Conductive Coils, and Folded Helical Springs"*, SPIE Conf. on Micromachining and Microfabrication Process Technology V, 3874, p. 227-235, 1999.

Mehrez, H., Taylor, J., Guo, H., Wang, J. and Roland, C., *"Carbon Nanotube Based Magnetic Tunnel Junctions"*, Physical Review Letters 84, 2682, 2000.

Mittasch, A., Z. Phys. Chem., 40, 1, 1902.

Mondry, M., Rudy, P., Zhou, H., *"Improving the Performance of High-Power Diode Lasers"*, Photonics Solutions for the Design Engineer, April 2005.

Müller, K-H., *Ion-beam-induced Epitaxial Vapor-phase Growth: a Molecular Dynamics Study*, Phys. Rev. B, Vol 25, No 15, p. 7906-7913, 1987.

Nelson, D., *"A Kinetic Study of the Formation and Decomposition of Nickel Carbonyl"* PhD Thesis, University of Wisconsin, 1952.

NIST Chemistry Webbook, NIST Standard Reference Database Number 69, http://www.webbook.nist.gov/chemistry, June 2005.

O'Neill, C.E., *"The Role of Nickel - Carbon Monoxide Surface Complexes in the Formation of Nickel Carbonyl"*, PhD. Thesis, Columbia University, 1961.

Olurin, O.B., Wilkinson, D.S., Weatherly, G.C., Paserin, V. and Shu, J., *"Strength and Ductility of As-plated and Sintered CVD Nickel Foams"*, Composite Science and Technology, 63 p. 2317-2329, 2003.

Paserin, V., Shu J., Marcuson, S. and Wilkinson, D.S. *"The Chemical Vapour Deposition Technique for Inco Nickel Foam Production – Manufacturing Benefits and Potential Applications"* in Cellular Metals: Manufacture, Properties and Applications, Proc. 3rd Int. Conf. on Cellular Metals and Metal Foaming Technology (MetFoam 2003), Verlag MIT Publishing, 2003.

Paserin, V., Babjak, J., Ettel, V., Adams, R.S., *"Infrared Window"*, US Patent 5,145,716, September 1992.

Paserin, V., Stromness, S. and Duley, W., *"High-rate, Large Area Laser Deposition of Nickel on Polymer Substrates"*, Proc. 22nd Int. Congress on Applications of Lasers and Electro-Optics (ICALEO 2003), Oct. 13-16, 2003.

Paserin, V., Shu J., Marcuson, S., *"Superior Nickel Foam Production: Starting from Raw Materials Quality Control"* in Porous Metals and Metal Foaming Technology, Proc. 4[rh] Int. Conf. on Porous Metals and Metal Foaming Technology (MetFoam 2005), Japan Institute of Metals, 2006.

Paserin, V., Baksa S., Zaitsev, A., Shu, J., Shojai, F., Nowosiadly, W., *"Potential for Mass Production of Nickel-Based Nanomaterials by Carbonyl Process"*, J. Nanosci. Nanotechnol. , Vol. 8, No. 8, p. 4049-4055, 2008.

Powell, C.F., Oxley, J.H., Blocher jr., J.M. (ed.), *"Vapor Deposition"*, John Wiley & Sons Inc., 1966.

Rode, A.V., Hyde, S.T., Gamaly, E.G., Elliman, R.G., McKenzie, D.R., Bulcock, S., Appl. Phys. A69, S755-S758, 1999.

Ruiz, E.C., *"Modeling of Heat Transfer in Open Cell Metal Foams"*, M.Sc. Thesis, University of Puerto Rico, 2004.

Sahoo, Y., He, Y., Swihart, M.T., *"An Aerosol Mediated Magnetic Colloid: Study of Nickel Nanoparticles"*, J. Appl. Phys. 98, 054308, 2005.

Scouby, D.C. and Jensen, F.., *"Modeling of Pyrolytic Laser-assisted Chemical Vapor Deposition: Mass Transfer and Kinetic Effects Influencing the Shape of the Deposits"*, J. Appl. Phys. 63 (1), p.198-206, 1988.

Smith, A., *"Reaction Kinetics for the Decomposition of Nickel Carbonyl"*, Inco Europe Technical Report #252, December 1978.

Stedman, D.H., Hikade, D.A., Pearson, Jr. R., Yalvac, E.D., *"Nickel Carbonyl Decomposition in Air and Related Studies"*, Science, Vol. 208, p. 1029-1031, 1980.

Steen, W.M., *"The Thermal History of a Spot Heated by a Laser"*, Letters in Heat and Mass Transfer 4, p.167, 1977.

Sturney, A.C. *"The Story of Mond Nickel"* The Curwen Press, England, 1951.

Titus, E., Ali, N., Cabral, G., Gracio, J., Ramesh-Babu, P. and Blau, W.J., *"Ferromagnetic Contacts onto Carbon Nanotubes for Spintronics Applications"*, Proceedings of the International Conference on Surfaces, Coatings and Nanostructured Materials (nanoSMat 2005), University of Aveiro, p. O-45-47, Sept. 2005.

Tonneau, D., Auvert, G., Pauleau, Y., *"Growth Kinetics of Nickel Microstructures Produced by Laser-induced Decomposition of Nickel Tetracarbonyl"*, J. Appl. Phys., 64 (10), p. 5189, Nov. 15 1988.

Tonneau, D., Auvert, G., Pauleau, Y., *"Deposition of Nickel Microstructures by CO_2 Laser-assisted Decomposition of Nickel Tetracarbonyl"*, J. Appl. Phys., 66 (1), p. 165, July 1989.

Traub, M., Plum, H.-D., Hoffmann, H.-D., Loosen, P., Poprawe, R., *"Homogenized High Power Diode Laser Systems for Material Processing and Illumination"*, Proceedings of the Second International WLT Conference on Lasers and Manufacturing 2003, Munich, June 2003.

Tsukagoshi, K., Alphenaar, B.W. and Ago, H., *"Coherent Transport of Electron Spin in a Ferromagnetically Contacted Carbon Nanotubes"*, Nature 401, 572, 1999.

Tsylov, B.A., *"Heterogenous and Homogeneous Decomposition of Nickel Carbonyl"*, Poroshkovaya Metallurgiya No. 5 (101), p. 21-26, May 1971.

Wadley, H.N.G., "*Cellular Metals Manufacturing: an Overview of Stochastic and Periodic Concepts*", Proc. Int. Conf. Cellular Metals and Metal Foaming Technology, Editors: Banhart, J., Ashby, M.F., Fleck, N., p. 137-146, Verlag-MIT-Publishing, 2001.

Wadley, H.N.G., *"Cellular Metals Manufacturing"*, Advanced Engineering Materials 2002, 4, No.10 p 726-733, 2002.

Wadley, H.N.G. and Groves, J.F., *"Directed Vapor Deposition of Electron Beam Evaporant"*, US Patent #5,534,314, July 1996.

Wang, J., Besnoin, E., Duckham, A., Spey, S.J., Reiss, M.E., Knio, O.M., Weihs, T.P., *"Joining of stainless-steel specimens with nanostructured Al/Ni foils"*, J. Appl. Phys., 95 (1), p. 248-257, January 2004.

Wasmund, E.B., *"A Study of Powder Making by the Decomposition of Nickel Carbonyl in an Aerosol Tube Reactor"*, PhD Thesis, McMaster University, 2005.

Weber, R. and Sheppard, R., *"Method and Apparatus for Producing Nickel Shell Molds"*, US Patent 5,407,487, April 1995.

A brief history and additional properties of nickel carbonyl

This appendix contains a brief historical note describing the discovery of nickel carbonyl and a summary of selected chemical and physical properties. References used to source this information are included in the Bibliography.

A brief history of the "metal with wings"

$Ni(CO)_4$ was first synthesized in 1888 by Ludwig Mond (1839-1909) and Carl Langer (†1935) in their laboratory in London, England. Like many other significant discoveries, the existence of this compound was discovered by accident, when Mond realized that a small amount of carbon monoxide present in his chlorine plant in Winnington was likely reacting with the nickel valves and causing black carbon deposits to affect their operation. Mond summoned Langer to study the reaction of carbon monoxide and nickel in some detail. The evidence of nickel carbonyl formation came one evening when Langer was concluding his experiments of flowing CO over finely divided nickel powder at temperatures of several hundred degrees Celsius. The flame used to incinerate the

Ludwig Mond
(1839-1909)

Carl Langer
(†1935)

reactor exit gas suddenly turned luminous as the temperature dropped below the boiling point of water.   To confirm formation of nickel-containing gas, Langer inserted a cold porcelain tile into the luminous flame and found that it was

immediately coated with a shiny mirror that analyzed as pure nickel with a small quantity of carbon. In the words of the investigators - "when a finely divided nickel ..... is allowed to cool in a slow current of carbon monoxide, this gas is readily absorbed as soon as the temperature has descended to about 100 degrees and ..... a mixture of gases is obtained which contains ..... nickel-carbon-oxide". Thus – as stated by Lord Kelvin, nickel had been "given wings" [Sturney, 1951 and Bradley, 1988].

Nickel carbonyl structure

The molecular structure of $Ni(CO)_4$ is reproduced in Figure A1.1. The carbon and oxygen atoms surround the central Ni atom forming a tetrahedral symmetry. Since the C-O bond (length 1.141 Å) is much stronger than the Ni-C bond (length 1.838 Å), the decomposition of $Ni(CO)_4$ is
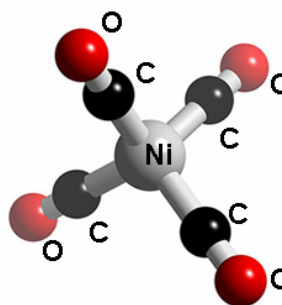
Figure A1.1 $Ni(CO)_4$ molecule structure

understood to occur by sequential breaking of the Ni-C bonds to give the overall reaction $Ni(CO)_4$ (g) $\rightarrow$ Ni (g) + 4 CO (g) via four elementary steps:

(1) $Ni(CO)_4$ (g) $\rightarrow$ $Ni(CO)_3$ (g) + CO (g)
(2) $Ni(CO)_3$ (g) $\rightarrow$ $Ni(CO)_2$ (g) + CO (g)
(3) $Ni(CO)_2$ (g) $\rightarrow$ Ni(CO) (g) + CO (g)
(4) Ni(CO) (g) $\rightarrow$ Ni (g) + CO (g)

Data given in The CRC Handbook of Chemistry and Physics [Lide, 1994]:

$Ni(CO)_4$, CAS #13463-39-3
Molecular weight: 170.734 amu
Melting point: –19.3°C
Boiling point: 43°C
Density 1.31 g/cm^3
Insoluble in water
Soluble in ethanol, benzene, acetone, CCl_4

Thermochemical Properties (at standard conditions of 298.15 K and 1 bar):

Standard heat of formation as a liquid: $\Delta H_f(l)$ = -633 kJ/mol

Standard heat of formation as a gas: $\Delta H_f(g)$ = -602.9 kJ/mol

Standard (Gibbs) free energy of formation as a liquid: $\Delta G_f(l)$ = -588.2 kJ/mol

Standard (Gibbs) free energy of formation as a gas: $\Delta G_f(g)$ = -587.2 kJ/mol

Standard entropy as a liquid: $S(l)$ = 313.4 J/(mol K)

Standard entropy as a gas: $S(g)$ = 410.6 J/(mol K)

Constant pressure heat capacity as a liquid: $C_p(l)$ = 204.6 J/(mol K)

Constant pressure heat capacity as a gas: $C_p(g)$ = 145.2 J/(mol K)

Molecular Structure

  Ni-C bond length = 1.838 Å
  C-O bond length = 1.141 Å
  Tetrahedral symmetry (all C-Ni-C angles are 109.4712°, all Ni-C-O angles are 180°)

Additional Data Given in the NIST Chemistry Webbook [NIST, 2005]:

  Heat of reaction for $Ni(CO)_4(g) \rightarrow Ni(cr) + 4\ CO(g)$ is 160.4 kJ/mol (equivalent to 0.759 kWh/kg$_{Ni}$).

  Heat of reaction for $Ni(CO)_4(g) \rightarrow Ni(CO)_3(g) + CO(g)$ is 104 ± 8 kJ/mol

Ni carbonyl absorption spectra [Jones, 1958]
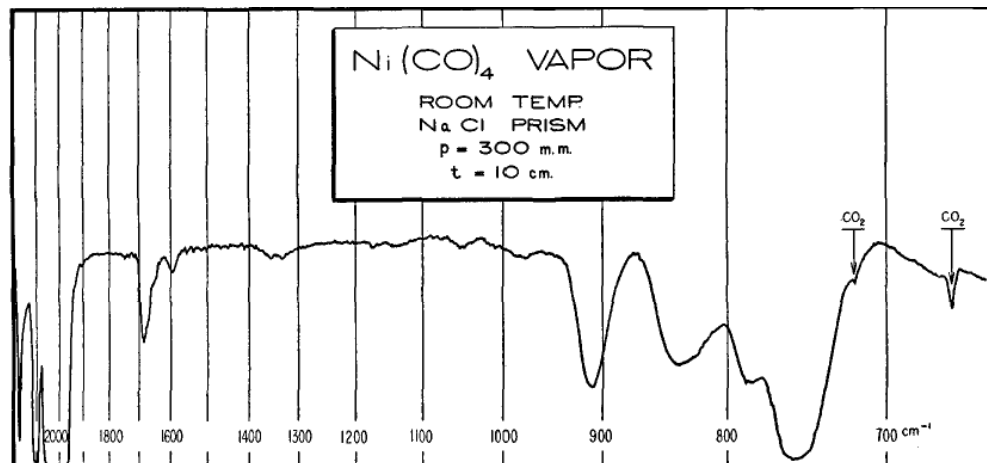
Figure A1.2 Ni carbonyl IR spectrum 2000-700 cm^{-1}
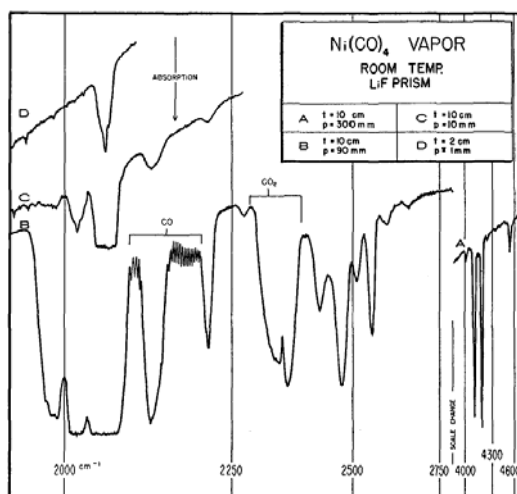
Figure A1.3 Ni carbonyl IR spectrum 2000-4600 cm^{-1}
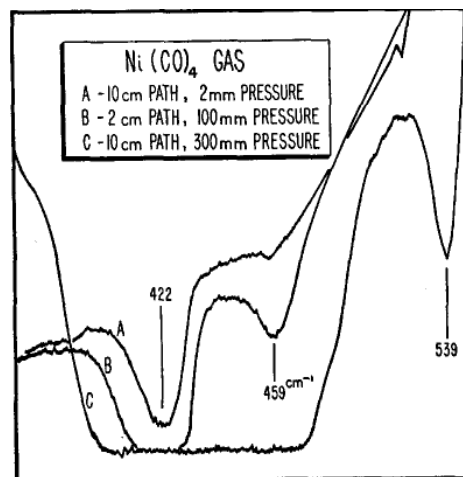
Figure A1.4 Ni carbonyl IR spectrum 400-550 cm^{-1}
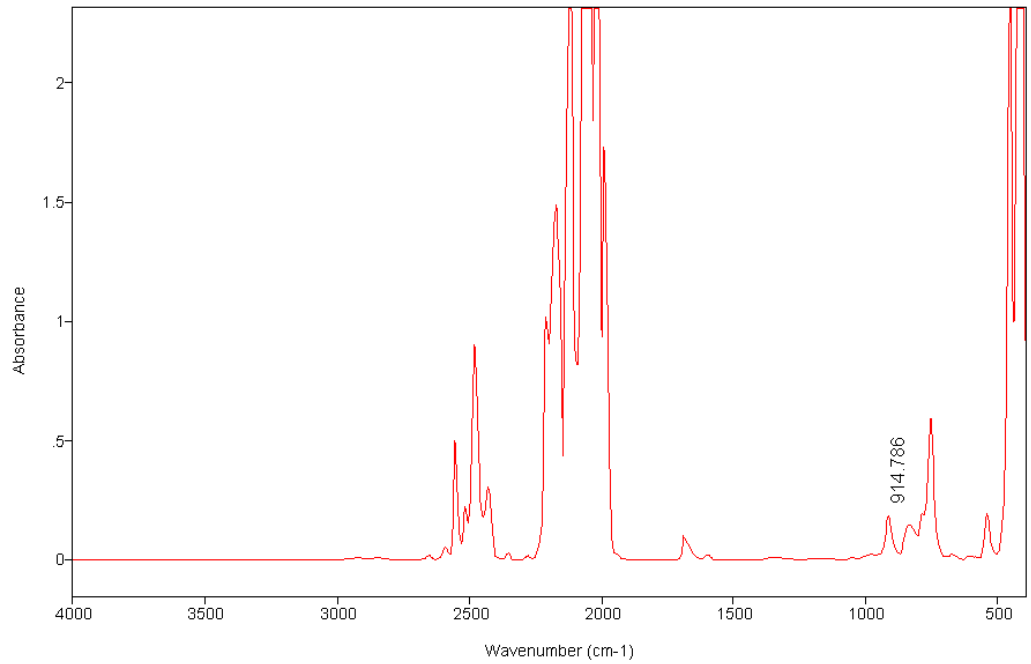
Figure A1.5 Ni carbonyl IR spectrum 400-4000 cm^{-1}, 19cm path length, ~10 vol% concentration, measured by the Bomem FTIR analyzer. The peak at 914.78 nm was used to quantify the concentration in intermediate range
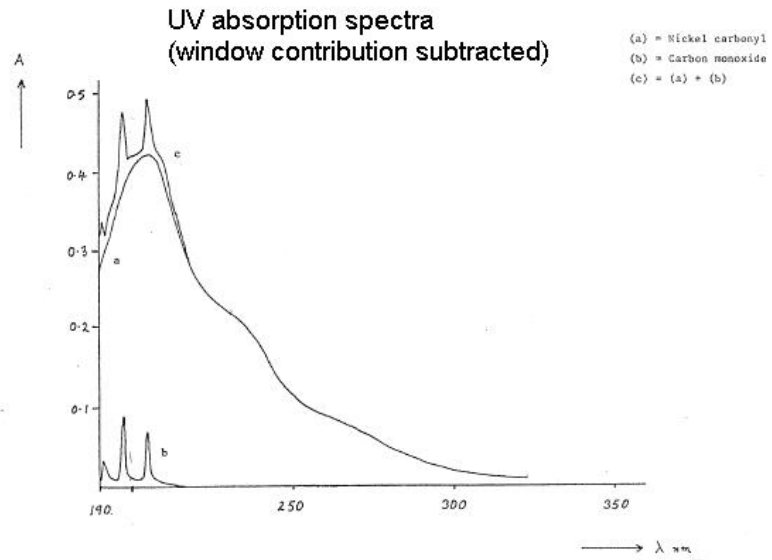
Figure A1.6 Ni carbonyl UV spectrum 190-350 nm [Vale Inco data]

199

Summary of experiments

Table A2.1   Summary of experiments

#	Expt #	Part #	Length of time	Substrate	Sample opening size cm²	Laser current Amps	Gas flows Total l/min	Gas flows % carb	Gas flows % H₂S	Gas vel. through opening cm/s	Average meas. deposition rate microns/min	Comment
1	**LH030124**	1	28	PU foam Recticel VM4302M 1.9 mm thick	135	18	1.3	38	0.21	0.2	0.63	
		2	300			25	1.3	38	0.21			
2	**LH030131**	1	30	PU foam	135	Low	3.5	28	0.21	0.44	1.24	
		2	38			32	3.5	28	0.21			
		3	136			35	3.5	28	0.21			
3	**LH030207**	1	21	PU foam	135	35	13.4	14	0.24	1.7	1.96	
		2	80			42	13.4	14	0.24			
4	**LH030219**	1	20	PU foam	52	Low	5.1	29	0.02	1.6	2.06	masked areas not heated by the beam with Al tape
		2	60			25	5.1	29	0.02			
		3	22			25-42	5.0	28	0.02			
		4	180			42	5.0	28	0.02			
5	**LH030307**	1	15	PU foam	52	Low	9.4	32	0.15	3.0	2.08	
		2	60			25	9.4	32	0.15			

#	Expt #	Part #	Length of time	Substrate	Sample opening size cm^2	Laser current Amps	Gas flows Total l/min	% carb	% H_2S	Gas vel. through opening cm/s	Average meas. deposition rate microns/min	Comment
		3	20			25-42	9.4	32	0.15			
		4	5			42	9.4	32	0.15			
		5	175			42	10.6	32	0.15			
6	**LH030321**	1	23	PU foam	52	Low	4.7	25	0.32	1.5	2.11	- use new mounting plate, same flow-through area (4x13 cm) - highly non-uniform deposit
		2	155			25	4.7	25	0.32			
		3	22			25-49	4.7	25	0.32			
		4	180			49	4.7	25	0.32			
7	**LH030328**	1	11	PU foam	52	Low	8.7	33	0.18	2.8	2.44	- uniform deposit
		2	60			25	8.7	33	0.18			
		3	17			25-49	8.7	33	0.18			
		4	180			49	8.7	33	0.18			
												rates to-date based on total Ni deposited
LH030404 ---> LH040423 Laser Head Failure - repairs by Nuvonyx + specialty substrate plating in Nov / 03 - Jan /04 period (TEMBEC cellulose substrates)												
8	**LH040423**	1	45		52	25	10.0	33	0.18	3.2		re-commision system with PU foam substrate soft pre-plate + main high-rate deposition
		2	180	PU foam		49	10.0	33	0.18		3.22	

#	Expt #	Part #	Length of time	Substrate	Sample opening size cm^2	Laser current Amps	Gas flows			Gas vel. through opening cm/s	Average meas. deposition rate microns/min	Comment
							Total l/min	% carb	% H$_2$S			
												Dep. rates from here onward are based on ~1cm dia. coupon density
9	**LH040507**	1	30	PU foam	52	25	10.0	33	0.18	3.2	4.77	moved laser heads closer to reactor (as close as possible) - sample overheated at full power (powder formation)
		2	120			49	10.0	33	0.18			
10	**LH040510**	1	30	PU foam	20	25	10.0	33	0.18	8.4	4.40	further masking of the flow-through area with Al tape to give 2x10cm opening
		2	60			49	10.0	33	0.18			
12	LH040520	1	30	PU foam	20	25	10.0	33	0.18	8.4	4.47	added horiz. plate to deflect inlet flow
		2	60			49	10.0	33	0.18			
13	LH040603	1	30	PU foam	4	25	10.0	33	0.18	41.8	3.65	mask sample further to give 2x2 cm area first test with removed lenses from laser (except for diffuser plate)
		2	60			49	10.0	33	0.18			

#	Expt #	Part #	Length of time	Substrate	Sample opening size cm²	Laser current Amps	Gas flows			Gas vel. through opening cm/s	Average meas. deposition rate microns/min	Comment
							Total l/min	% carb	% H$_2$S			
14	**LH040609**	1	30	PU foam	4	25	5.0	33	0.18	20.9	10.23	reduced gas flow
		2	60			49	5.0	33	0.18			excellent sample, uniform, no dendrites
15	**LH040610**	1	30	PU foam	4	25	2.5	33	0.18	10.4		further reduction in flow (50%), temp > 450 C, lots of powder, dendrites
		2	60			49	2.5	33	0.18			sample extremely brittle, mass not measurable
16	LH040624	1	30	PU foam	4	25	4.0	33	0.18	16.7	1.91	temp > 350 C, powder, dendrites
		2	60			49	4.0	33	0.18			sample brittle, mass not accurate
17	LH040625	1	40	PU foam	4	25	6.0	33	0.18	25.1	17.05	excellent sample, uniform, no dendrites
		2	60			49	6.0	33	0.18			
18	LH040628	1	40	PU foam	4	25	6.0	33	0.18	25.1	2.30	pre-plate only, 40 seconds
19	LH040629	1	30	PU foam	4	49	6.0	33	0.18	25.1		attempt to eliminate pre-plate powder formation

#	Expt #	Part #	Length of time	Substrate	Sample opening size cm²	Laser current Amps	Gas flows Total l/min	% carb	% H₂S	Gas vel. through opening cm/s	Average meas. deposition rate microns/min	Comment
												sample brittle, mass not measurable
20	**LH040630**	1	10	PU foam	4	25	5.9	34	0.00	24.6		attempt to eliminate H2S powder, test aborted
		2	30			49	5.9	34	0.00			
21	**LH040706**	1	15	carbon nanofoam	4	25	6.0	33	0.18	25.1		C nanofoam some powder on feed side
		2	30			49	6.0	33	0.18			
22	**LH040716**	1	15	PU foam	4	25	7.0	33	0.18	29.2	9.49	back to PU foam plating smoke visible on exit side
		2	30			49	7.0	33	0.18			
23	**LH040721**	1	15	PU foam	4	25	7.0	33	0.18	29.2	2.81	sample overheated, significant amount of powder found on exit side, very brittle
		2	30			49	7.0	33	0.18			
24	**LH040730**	1	15	PU foam	4	30	6.0	33	0.18	25.1	10.07	examine sample after 15 and 30-sec pre-plates powder formation on exit side
		2	30			30	6.0	33	0.18			
		3	30			49	6.0	33	0.18			
25	**LH040917**	1	40	PU foam	4	25	6.0	33	0.18	25.1	2.08	repeat of LH040625 – used nitrogen instead of CO+H2S
		2	60			49	6.0	33	0.18			

#	Expt #	Part #	Length of time	Substrate	Sample opening size cm^2	Laser current Amps	Gas flows			Gas vel. through opening cm/s	Average meas. deposition rate microns/min	Comment
							Total l/min	% carb	% H$_2$S			
26	**LH040921**	1	30	electroplated Ni foam	4	25	6.0	33	0.18	25.1	7.36	repeat of LH040625 (flows) but use Ni foam substrate lasers pointing too low, lots of powder observed gradual increase in power from 25 -> 50A
		2	120			49	6.0	33	0.18			
27	**LH041006**	1	60	PU foam	4	25	6.0	33	0.18	25.1	8.34	repeat of LH040625 (flows) but use Ni foam substrate new Al sample holder installed lasers pointing too low, lots of powder observed gradual increase in power from 25 -> 50A
		2	30			30	6.0	33	0.18			
		3	10			40	6.0	33	0.18			
		4	60			46.3	6.0	33	0.18			
28	**LH041025**	1	90	PU foam		30	6.0	33	0.18	25.1	8.39	lasers alligned by visual observation slight puff of smoke at the beginning of test repeat of LH040625 gas flows
		2	30			46	6.0	33	0.18			

#	Expt #	Part #	Length of time	Substrate	Sample opening size cm²	Laser current Amps	Gas flows Total l/min	% carb	% H₂S	Gas vel. through opening cm/s	Average meas. deposition rate microns/min	Comment
29	**LH041103**	1	56	electroplated Ni foam	4	48	6.0	33	0.18	25.1	15.49	repeat of LH040625 gas flows preheat at 28A for 5 min in N2, no smoke gradual increase of power to FULL over few seconds
30	**LH041110**	1	30	electroplated Ni foam	4	48	6.0	33	0.18	25.1	16.61	repeat of LH040625 gas flows uniform deposit, no smoke preheat at 28A for 5 min (to offgas)
31	**LH041112**	1	30	electroplated Ni foam	4	49	6.0	33	0.18	25.1	14.57	LH040625 gas flows used, full power, no pre-heat, NO POWDER observed no preheat in this test
32	**LH041114**	1	30	electroplated Ni foam + LH041112	4	20		0	0	20.8	N/A	no carbonyl used, test substrate temperature vs. gas (N₂) flowrate following test
		2	30			30	5.0	0	0			
		3	30			40	5.0	0	0			

#	Expt #	Part #	Length of time	Substrate	Sample opening size cm^2	Laser current Amps	Gas flows			Gas vel. through opening cm/s	Average meas. deposition rate microns/min	Comment
							Total l/min	% carb	% H$_2$S			
		4	30	sample		48	5.0	0	0			LH041112 (thermocouple at the same location, centered in the beam spot) max temp reached 660 deg C at 2l/min N2 flow
33	**LH041203**	1	30	electroplated Ni foam	4	50.6	7.0	33	0.18	29.2	1.23	higher flow, also new (full) autoclave used
34	**LH041209**	1	30	electroplated Ni foam	4	50.6	6.0	33	0.18	25.1	2.57	repeat of LH040625 gas flows, second run with new autoclave
35	**LH041210**	1	30	electroplated Ni foam	4	50.6	4.8	14	0.23	19.9	4.96	flows adjusted to get ~14% feedgas conc
36	**LH041212**	1		electroplated Ni foam	4	variable	variable	0	0	variable	N/A	temperature vs. N2 flow test (no deposition)
37	**LH041214**	1	30	electroplated Ni foam	4	50.6	6.0	33	0.18	25.1	not measured	variable flowrate test (with deposition)
		2	30				50.6	5.0	33	0.18	20.9	

#	Expt #	Part #	Length of time	Substrate	Sample opening size cm²	Laser current Amps	Gas flows			Gas vel. through opening cm/s	Average meas. deposition rate microns/min	Comment
							Total l/min	% carb	% H₂S			
		3	30			50.6	4.0	33	0.18	16.7		smoke observed in this segment
		4	30			50.6	3.0	33	0.18	12.5		smoke observed in this segment
		5	30			50.6	2.0	33	0.18	8.4		
		6	30			50.6	3.1	22	0.12	12.7		slight amount of smoke,
38	**LH050121**	Special test with phenolic foam										
39	**LH050123**	1	30	PU foam	4	48.4	3.0	33	0.18		6.10	try PU foam substrate again, thermocouple came off after first few seconds, lots of smoke, extremely brittle sample
40	**LH050211**	1	10	Carbon nanotubes		25	3.0	33	0.18			C nanotubes
41	**LH050217**	1	8	Copper and Graphite		25	3.0	33	0.18			Cu & graphite substrate
42	**LH050219**	1	10	copper plate substrate		25	3.0	33	0.18			Cu substrate

#	Expt #	Part #	Length of time	Substrate	Sample opening size cm^2	Laser current Amps	Gas flows			Gas vel. through opening cm/s	Average meas. deposition rate microns/min	Comment
							Total l/min	% carb	% H$_2$S			
43	**LH050226**	1		electroplated Ni foam							N/A	Laser power vs. temperature test - no deposition, 2 new thermocouples installed
44	**LH050228**	1	30	electroplated Ni foam	4	49	4.0	33	0.18	16.7	11.28	start of flow series, 4 l/min total flow, no smoke
45	LH050301	1	30	electroplated Ni foam	4	49	3.5	33	0.18	14.6	15.21	3.5 l/min total flow, no smoke
46	**LH050302**	1	30	electroplated Ni foam	4	49	3.0	33	0.18	12.5	19.11	3.0 l/min total flow, no smoke
47	**LH050303**	1	30	electroplated Ni foam	4	49	2.5	33	0.18	10.4	13.18	2.5 l/min total flow, Ni smoke 3 sec after laser turned on
48	**LH050307**	1	30	electroplated Ni foam	4	49	3.0	33	0.18	12.5	19.03	repeat of 0302 - 3 l/min total flow, no smoke, excellent reproducibility
49	**LH050308**	1	30	electroplated Ni foam	4	49	3.0	34	0	12.3	20.05	3 l/min total flow, no H$_2$S
50	**LH050310**	1	30	electroplated	4	49	3.8	35	0	15.8	11.26	4 l/min total flow, no H$_2$S

#	Expt #	Part #	Length of time	Substrate	Sample opening size cm^2	Laser current Amps	Gas flows Total l/min	Gas flows % carb	Gas flows % H$_2$S	Gas vel. through opening cm/s	Average meas. deposition rate microns/min	Comment
				Ni foam								
51	**LH050406**	1	30	electroplated Ni foam	4	48.4	3.8	35	0	15.8	12.05	Repeat of LH050310 3 min pre-heat in N$_2$ @ 28A
52	**LH050407**	1	15	PU foam	4	0→48.4	3.8	35	0	15.8	11.54	Severe powder formation
		2	15			48.4	3.8	35	0	15.8		
53	**LH050603**	1	40	PU foam	4	0→30	3.8	35	0.18	15.8		
Tests LH050719 to LH050721 are special project- deposition on carbon nanotubes												
54	**LH050810**			Graphite foil Alfa-Aesar part #10832	4	25	4	35	0.18	N/A	N/A	Solid substrate, sample holder modified with perforations (Fig. 3.61)
55	**LH050812**			Graphite foil Alfa-Aesar part #10832	4	30	4	35	0.18	N/A	N/A	Increased laser current, light deposit
56	**LH050816**			Graphite foil Alfa-Aesar part #10832	4	35	4	35	0.18	N/A	N/A	Further increased in laser current, light deposit

#	Expt #	Part #	Length of time	Substrate	Sample opening size cm^2	Laser current Amps	Gas flows			Gas vel. through opening cm/s	Average meas. deposition rate microns/min	Comment
							Total l/min	% carb	% H$_2$S			
57	**LH050817**			Graphite foil Alfa-Aesar part #10832	4	40	4	35	0.18	N/A	N/A	Higher laser current
58	**LH050818**			Graphite foil Alfa-Aesar part #10832	4	40	4	35	0.18	N/A	3	Repeat of LH050817, net. dep. 1.4 mg
59	**LH050819**			Graphite foil Alfa-Aesar part #10832	4	45	4	35	0.18	N/A	2.1	Possible re-carbonylation by CO following deposition, net. dep. 1.0 mg
60	**LH050822**			Ultra-fine PU "SENSO SSF.02"	4	0→30	4	35	0.18			White, ultrafine PU foam substrate from Huntsman / Recticel
61	**LH050829**			Ultra-fine PU "SENSO SSF.02"	4	0→30	4	35	0.18			White, ultrafine PU foam substrate from Huntsman / Recticel
	LH050916			PU foam	4	37 ("on" current)	3	35	0.18	12.5	0.2	Pulsed laser operation, 1000Hz, 30% duty cycle

Appendix 3

Safety of working with nickel carbonyl and lasers

A3.1 Nickel carbonyl safety

With a TLV of 50 ppb in Canada and 1 ppb in the United States, nickel carbonyl is considered one of the most toxic substances in industrial use today. Combining the use of nickel carbonyl with high-power laser beams may thus seem as a clear path to trouble, even in a laboratory environment. Furthermore, proposing to use such a system industrially may sound over-ambitious. At the same time, Vale Inco has been producing and processing literally tons of this substance daily for many decades, with an excellent safety record. Standard engineering and laboratory safety measures derived from the long industrial practice with nickel carbonyl at Vale Inco were employed in this work.

Central to the safe operation of carbonyl equipment is the verification of the system integrity (leak-free status), and continuous environmental monitoring for trace amounts of nickel carbonyl. The deposition system was leak-checked prior to each experiment by pressurizing it to 5 psi and verifying that no significant pressure loss occurred over a 1-hour period.
The short half-life of nickel carbonyl (~60 seconds in air [Stedman, 1980]) also helps in mitigating the consequences of minor equipment leaks.

The experimental deposition system was housed inside a laboratory fumehood with ~2000 scfm of constant air flow. The fumehood exhaust was continuously monitored for traces of nickel carbonyl. A chemiluminescent analyzer with a nickel carbonyl detection limit of ~1 ppb provided early warning to the operator in case of even a minor system leak.

A3.2 Class IV diode laser safety

Since the system represented the first installation of a Class IV laser at Inco's Carbonyl Technology laboratory in Mississauga, it was initially decided to locate the reactor and the two laser heads inside a full metal enclosure. The enclosure cover was equipped with a safety interlock connected to the laser power supply. Later in the project (after obtaining more laser operating experience as well as a formal Laser Safety Officer training), the system was modified to allow operation with the enclosure front panel removed in order to be able to visually monitor the progress of experiments. The use of the laser safety goggles with an optical density of at least 6.0 was of course mandatory for everyone present in the room. A flashing "Class IV laser operation" sign was installed above the laboratory entrance door and interlocked with the laser power supply. Probably the most serious laser-related incident during the ~3 years of system operation was the burning of a cardboard target used for initial alignment of the 2 laser heads. This event was captured on camera, featuring Randy Shaubel as the principal operator (Figure A3.1).

Figure A3.1 Randy Shaubel and "overheated" cardboard target

INDEX